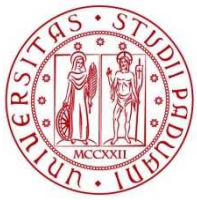

UNIVERSITÀ DEGLI STUDI DI PADOVA

TÉCNICO LISBOA

Università degli Studi di Padova

Centro interdipartimentale "Centro Ricerche Fusione"

Universidade de Lisboa

Instituto Superior Técnico (IST)

JOINT RESEARCH DOCTORATE IN FUSION SCIENCE AND ENGINEERING

Cycle XXVIII

Design of electric and magnetic components of a negative ion accelerator in view of application to ITER Neutral Beam Injectors

Coordinator: Prof. Paolo Bettini

Supervisor: Prof. Giuseppe Chitarin

Candidate: Daniele Aprile

Padua, January 2016

Abstract

The work of this PhD thesis has been developed inside the framework of magnetic confinement thermonuclear fusion and is connected in particular to the major worldwide experiment in this context, the future tokamak ITER. A very important component of ITER and of tokamaks in general is the Neutral Beam Injector (NBI), a device whose purpose is the production of an energetic beam of neutral particles capable to sustain the fusion reactions inside the reactor vessel. The prototype of the NBI for ITER, called MITICA, has been designed and will be constructed at Consorzio RFX, Padua, and its main requirement is the achievement of a Deuterium beam with 1 MeV of energy, 17 MW of power and 3600 s of duration.

This thesis is focused on the design of one of the crucial components of MITICA, the electrostatic accelerator, in which the electric and magnetic fields play a decisive role in determining the final performances. The work developed is chronologically collocated during the final three years of MITICA accelerator design, which is now finished.

The design activities carried out on electric and magnetic components of MITICA accelerator will be here presented together with the results of the experimental activities on prototypes and other existing accelerators.

A chapter will be dedicated to the results of code improvement activities.

This work can be read as the closure of MITICA accelerator design, in which all the remaining design issues have been faced and solved, and the operating scenario has been finalized.

Sommario

I contenuti di questa tesi di dottorato sono stati sviluppati nell'ambito della fusione termonucleare a confinamento magnetico, e sono connessi in particolare al maggiore degli esperimenti in questo campo a livello mondiale, il futuro tokamak ITER. Un componente molto importante di ITER e dei tokamak in genere è l'iniettore di neutri, un dispositivo il cui scopo è produrre un fascio di particelle neutre ad alta energia in grado di sostenere le reazioni di fusione all'interno della camera di reazione. Il prototipo degli iniettori di ITER, chiamato MITICA, è stato progettato e sarà costruito presso il Consorzio RFX a Padova, e il suo obiettivo principale è il conseguimento di un fascio di Deuterio con energia di 1 MeV, potenza di 17 MW e durata di 3600 s.

Questa tesi è incentrata sul progetto di uno dei componenti fondamentali di MITICA, l'acceleratore elettrostatico, nel quale i campi elettrici e magnetici giocano un ruolo chiave nel determinarne le prestazioni. Il lavoro sviluppato si colloca cronologicamente durante i tre anni finali del progetto dell'acceleratore di MITICA, che è adesso concluso.

Le attività di progetto svolte su componenti elettrici e magnetici dell'acceleratore di MITICA saranno qui presentate assieme ai risultati delle attività sperimentali svolte su prototipi o altri acceleratori esistenti.

Un capitolo a parte sarà dedicato ai risultati delle attività di sviluppo codici.

Questo lavoro può essere letto come la chiusura del progetto dell'acceleratore di MITICA, in cui i problemi ancora aperti sono stati affrontati e risolti, e in cui lo studio dello scenario operativo è stato completato.

Outline

Chapter 1 introduces the background of the thesis activities starting from the very general and progressively moving to the particular. First, the global energy scenario will be presented, introducing the motivations of nuclear fusion, then the magnetic confinement thermonuclear fusion, tokamaks and ITER will be discussed, leading to the description of a Neutral Beam Injector and MITICA. Finally, the magnetic configuration of MITICA accelerator, that is the specific background of the thesis, will be described.

Chapter 2 is a long chapter summarizing the most important design activities carried out on MITICA accelerator, including a new magnetic configuration developed for eliminating the ion deflection due to the electron-suppression magnetic field, a new magnetic configuration developed for performing the accelerator horizontal aiming instead of the traditional mechanical solution, the update of the design of the Transverse Magnetic Field Coils, for performance enhancement of MITICA, and a series of magnetic measurements activities carried out on prototypes and on other accelerators with the purpose of investigating the feasibility of the studied solutions and of checking the uniformity of the magnetic field.

Chapter 3 summarizes the most relevant code improvement activities carried out on the 3D magnetic code NBImag, previously developed at Consorzio RFX and used so far during the design of MITICA accelerator.

Chapter 4 presents the results of the non ideal, off-normal and failure conditions analysis of MITICA accelerator and represents the closure of the design of the accelerator itself. In this chapter the effects of mechanical tolerances of the grids, of real orientation of Beam Groups, of demagnetization of permanent magnets, of failure of PG current power supply, of non-uniform extracted current and gas density and of breakdowns between grids, have been analyzed and simulated, and finally some indications on possible fault protection strategies have been given.

Chapter 5 reports the design activities on a flux-gate type magnetic sensor, for application on MITICA and ITER HNB. The sensor has been first simulated by a FEM model and by a more complex numerical model including the dynamic behavior of ferromagnetic materials, and then a prototype has been realized and tested at Consorzio RFX. The preliminary results obtained are presented.

Chapter 6 consists of some of the design activities carried out on an Extraction Grid designed and realized at Consorzio RFX and to be tested on the experiment NITS at JAEA Naka, Japan, under the framework of a scientific cooperation agreement recently signed between the two laboratories. This Extraction Grid will feature the new magnetic configuration developed at Consorzio RFX for ion deflection cancellation and presented in chapter 2. Results of magnetic analysis, electrostatic analysis, mechanical design and preliminary experimental setup will be presented in this chapter. The experiments at NITS will take place in February 2016.

Chapter 7 consists of a summary of the main results obtained during the thesis activities, conclusions and future works.

Contents

ABSTRACT **3**

SOMMARIO **5**

OUTLINE **7**

CONTENTS **9**

1. INTRODUCTION **13**

1.1. GLOBAL ENERGY SCENARIO 13
1.2. NUCLEAR FUSION 15
1.3. MAGNETIC CONFINEMENT FUSION 16
1.4. ITER 17
1.5. AUXILIARY HEATING AND CURRENT DRIVE 19
1.6. NEUTRAL BEAM INJECTION 20
1.7. THE PADUA NEUTRAL BEAM TEST FACILITY 21
1.8. MITICA 22
1.8.1. Magnetic configuration of MITICA accelerator *24*

2. DESIGN ACTIVITIES ON MITICA ACCELERATOR **27**

2.1. CANCELLATION OF THE ION DEFLECTION DUE TO ELECTRON-SUPPRESSION MAGNETIC FIELD IN A NEGATIVE-ION ACCELERATOR 27
2.1.1. Introduction *27*
2.1.2. One-sided flux magnetic structures *27*
2.1.3. Asymmetric magnetic grid concept and deflection cancellation *28*
2.1.4. Asymmetry adjustment, optimization and uniformity *31*
2.1.5. Magnetic measurements on a grid prototype *32*
2.1.6. Assembly *33*
2.1.7. Conclusions *35*
2.2. GG AIMING 36
2.2.1. Horizontal aiming requirements and reference solution *36*
2.2.2. Possible layout *38*
2.2.3. Preliminary evaluation of Grounded Grid Steering Magnets on a single beamlet group *40*
2.2.4. Preliminary model of a complete Grounded Grid *44*
2.2.5. Alternative layout using ferromagnetic yokes *45*
2.2.6. Conclusions *47*
2.3. UPDATE OF THE DESIGN OF TRANSVERSE MAGNETIC FIELD COILS (TMFC) FOR MITICA ACCELERATOR 48
2.3.1. Introduction *48*
2.3.2. New PG busbar layout PG_24 ..... *48*
2.3.3. Recall of TMFC design parameters and constraints *49*
2.3.4. Description of the optimization algorithm *51*
2.3.5. TMFC optimization results *53*
2.3.6. Uniformity analysis *55*
2.3.7. Final TMFC Design solution *57*
2.3.8. Thermal analysis *58*
2.3.9. Power load scan of TMFC operating point *58*
2.3.10. Conclusions *61*
2.4. MAGNETIC TESTS ON MULTI CHANNEL PROTOTYPE 62
2.4.1. Introduction *62*
2.4.2. MCP configuration #1 - CESM only *64*
2.4.3. Magnetic characterization of single magnets *69*

2.4.4. MCP configuration #2 - CESM + ADCM 75
2.4.5. Conclusions 81
2.5. MAGNETIC TESTS ON NIO1 82
2.5.1. Introduction 82
2.5.2. Magnetic configuration of NIO1 82
2.5.3. Axial Profile of By along the accelerator 83
2.5.4. Measurements of Bx and By cusp field 84
2.5.5. Axial profile of Bx along the accelerator 86
2.5.6. Check on the orientation of rear cover magnets 87
2.5.7. Simulations with NBImag 87

3. CODE IMPROVEMENT ACTIVITIES 89

3.1. INTRODUCTION AND PROBLEM DESCRIPTION 89
3.2. FORMULATION OF FORCE AND INDUCTANCE CALCULATION 89
3.3. VALIDATION OF FORCE CALCULATION BETWEEN PERMANENT MAGNETS 90
3.4. VALIDATION OF FORCE CALCULATION BETWEEN COILS 92
3.5. VALIDATION OF SELF-INDUCTANCE CALCULATION 93
3.6. VALIDATION OF MUTUAL INDUCTANCE CALCULATION 94
3.7. CONCLUSIONS 94

4. NON IDEAL, OFF-NORMAL AND FAILURE CONDITIONS ANALYSIS OF MITICA ACCELERATOR 97

4.1. INTRODUCTION 97
4.2. NON IDEAL OPERATING CONDITIONS 99
4.2.1. Cumulative effects of permanent magnets in the 16 BG grid model 99
4.2.2. Comparison between single Beam Group model and 16 Beam Groups model using EAMCC 107
4.2.3. Effect of mechanical tolerance of grid grooves 110
4.2.4. Effect of real orientation of Beam Groups 118
4.3. OFF-NORMAL OPERATING CONDITIONS 126
4.3.1. Effect of demagnetization of permanent magnets 126
4.3.2. Effect of wrong PG current value 128
4.3.3. Clarification on transmitted electrons calculation 130
4.3.4. Non uniform gas density and extracted current 132
4.3.5. Effect of breakdowns between grids 133
4.3.6. Off normal operating conditions of thermo-mechanical nature 133
4.3.7. Detection and protection strategies 135
4.4. CONCLUSIONS 135

5. DEVELOPMENT OF A FLUX-GATE MAGNETIC SENSOR 137

5.1. INTRODUCTION 137
5.2. FLUX-GATE OPERATING PRINCIPLE 138
5.3. DESCRIPTION OF NUMERICAL MODEL 140
5.4. DESCRIPTION OF FEMM MODEL 144
5.5. CONSTRUCTION OF THE PROTOTYPE 145
5.6. EXPERIMENTAL SET-UP 147
5.7. EXPERIMENTAL RESULTS 148
5.8. CONCLUSIONS 151

6. DESIGN OF AN EXTRACTION GRID TO BE TESTED ON NEGATIVE ION TEST STAND (NITS) 153

6.1. INTRODUCTION 153
6.2. DESCRIPTION OF NITS ACCELERATOR 153
6.3. EXPERIMENTAL SETUP OF FIRST JOINT EXPERIMENTS 154
6.4. MAGNETIC ANALYSIS OF NEW EG 155

6.5. ELECTROSTATIC ANALYSES AND OPTICS OPTIMIZATION OF NEW EG 158
6.6. ELECTROSTATIC ANALYSES OF ORIGINAL EG OF NITS 164
6.7. COMPARISON BETWEEN SLACCAD AND BEAMORBIT 165
6.8. CALCULATION OF ION DEFLECTION AND ADCM OPTIMIZATION 169
6.8.1. Calculation of ion deflection using an analytical formula 169
6.8.2. Calculation of Ion deflection calculation using OPERA 171
6.9. MECHANICAL DESIGN 173
6.10. CONCLUSIONS 175
7. CONCLUSIONS AND FUTURE WORK 177
REFERENCES 179
ACKNOWLEDGEMENTS 183

1. Introduction

In this introductive chapter the background and motivations of this PhD thesis will be presented, starting from the global energy scenario, introducing nuclear fusion and ITER, and arriving to Neutral Beam Injectors and negative ion accelerators, the main topic of this work.

1.1. Global energy scenario

In this section the world energy scenario will be briefly summarized. Fig. 1, obtained with data from [1], shows the world energy consumption by fuel and gives us two important information: first, the world energy consumption is constantly increasing and is today more than the triple of fifty years ago. This fact is due to the increase of global population and to the rapid development of big countries like China and India.
The second information is that 85% of the consumed energy comes from fossil fuels, i.e. coal, oil and natural gas. This fact has in turn other two important consequences.

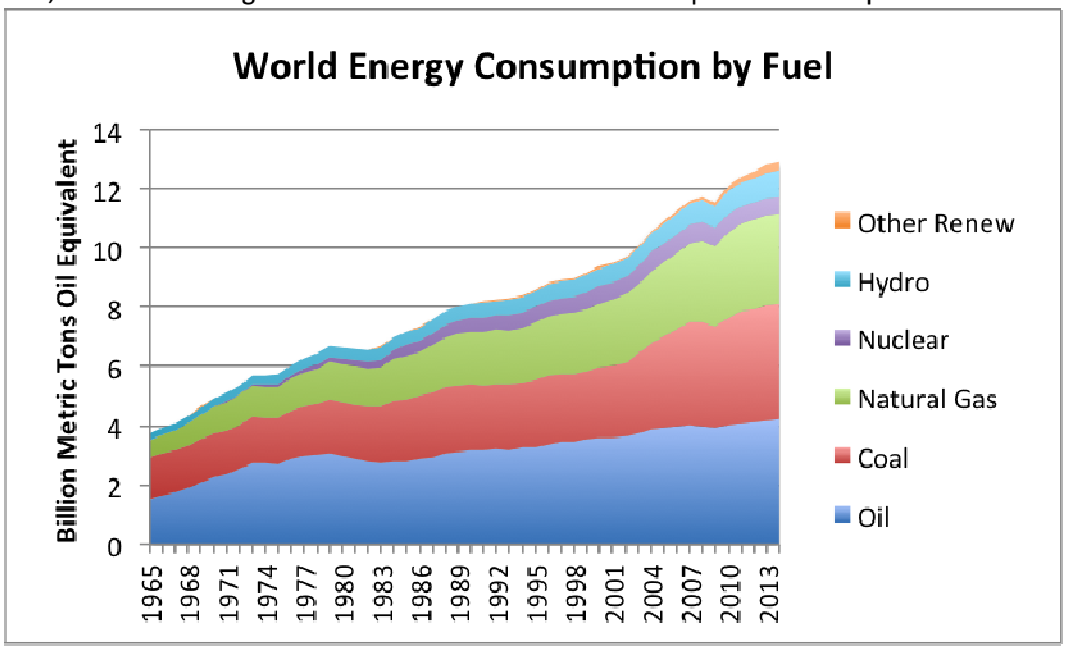

Fig. 1 World energy consumption by fuel.

The first consequence is that, since fossil fuels are practically non renewable, their global reserve is going to deplete, soon or later.
The second and more important consequence regards the greenhouse gas emission into the atmosphere and it's immediately clear if looking at Fig. 2, taken from [2]. This Fig. shows the greenhouse gas emission by fuel (averaged on twenty different studies on this subject), and shows how the consumption of fossil fuels generates high levels of greenhouse gas with respect to hydroelectric, renewable, and nuclear energy.

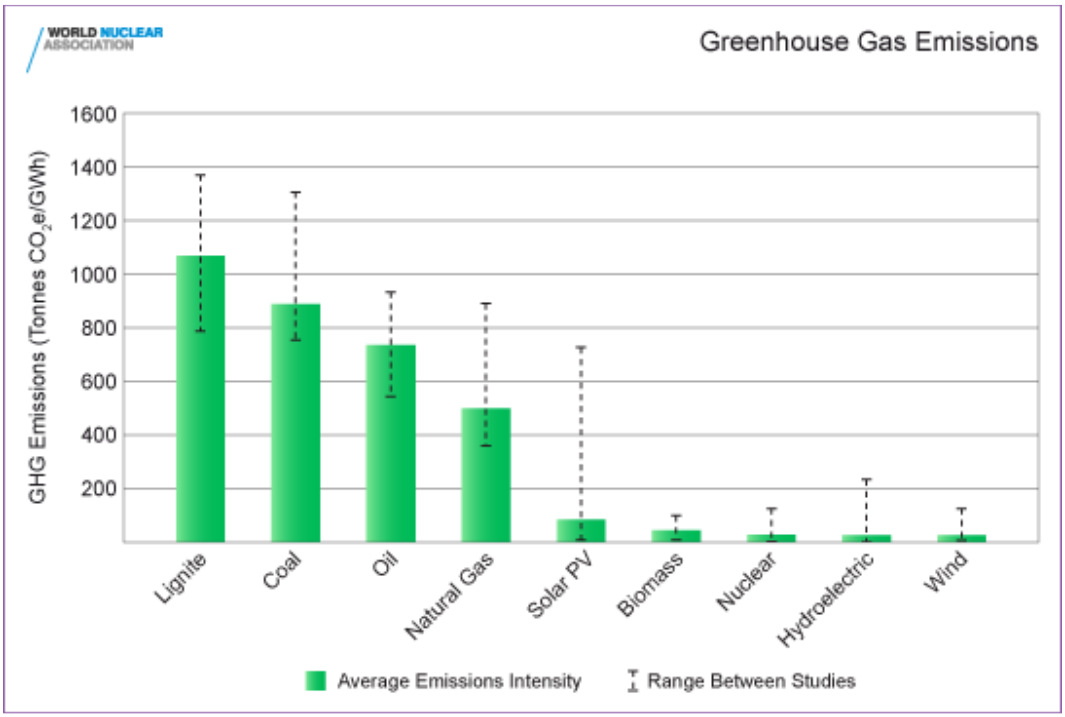

Fig. 2 Greenhouse gas emission by fuel.

Fig. 3, taken from [3], shows the annual anthropogenic greenhouse emission by sector. The power generation sector is the one that more contributes to the total, with more that 20% of the annual word greenhouse gas emission. Strongly reducing this contribute, together with the contribution from fossil fuel retrieval, processing and distribution, and part of the transportation fuels (imagining a future dominated by electric cars), the global greenhouse gas emission could be reduced by approximately 40%.
Now, greenhouse gas is mostly constituted by carbon dioxide (72%, see [3]), that is also more persistent in the atmosphere with respect to Methane and Nitrous oxide, the other two major contributors.
A study made in [4] estimates that the natural Earth carbon cycle is able to absorb about half of the anthropogenic carbon dioxide emitted per year, while the other half is accumulated in the atmosphere, where it persists for hundreds years, causing global warming with a series of adverse effects.
So, an energy scenario where consumption of fossil fuels is largely reduced could be almost compatible with the Earth natural carbon dioxide absorption, solving in turn the problem of anthropogenic global warming.

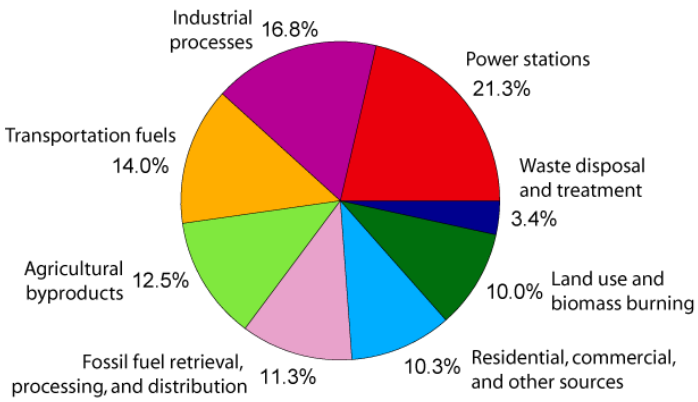

Fig. 3 Annual anthropogenic greenhouse gas emission by sector.

Among the energies with low greenhouse gas emission there are the renewable, hydroelectric and nuclear. The first two are unfortunately unable to meet the global energy demand, due to their limited and not well space and time distributed power density, so, only nuclear power is left at present day options. Nuclear power is subdivided into nuclear fission and nuclear fusion, but at present day only the first one is available. Nuclear fission, despite being "clean" from the greenhouse gas point of view, has its non negligible drawbacks, like the risk of serious accidents, the problem of wastes, and the limited global amount of nuclear fission fuels (^{235}U and ^{239}Pu).
Nuclear fusion, on the other hand, has no problem of depletion of fuels (Deuterium, extremely abundant, and Tritium, which can be produced), it's intrinsically much safer than nuclear fission and the problem of waste is much easier to treat.
In conclusion, nuclear fusion could be the answer to the world energy problem, being its fuel practically infinite, its power density enough to satisfy the global energy demand and its environmental impact very limited.
Nuclear fusion will be explained with more details in the next section.

1.2. Nuclear Fusion

Nuclear fusion is a nuclear reaction in which atomic nuclei collide at a very high energy and fuse together to form a new nucleus. In this process some matter is not conserved and is directly transformed into energy according to the Einstein relation $E = mc^2$.
This process, naturally happening in stars, can be reproduced and exploited to produce energy, but there important difficulties to overcome:

1) Very high energy is required for the reactants to fuse. Fig. 4 shows the cross-section (a parameter measuring the reaction rate) of the three most relevant fusion reactions from the point of view of energy production on Earth, reported below, involving Deuterium (D or H^2), Tritium (T or H^3), Helium (He^4) and its isotope He^3.

D-T reaction: $H^2 + H^3 \rightarrow He^4\ (3.5\ MeV) + n\ (14.1\ MeV)$

D-D reaction: $H^2 + H^2 \rightarrow He^3\ (0.8\ MeV) + n\ (2.5\ MeV)$ (50%)
$H^2 + H^2 \rightarrow H^3\ (1.0\ MeV) + p\ (3.0\ MeV)$ (50%)

D-He^3 reaction: $H^2 + He^3 \rightarrow He^4\ (3.7\ MeV) + p\ (14.7\ MeV)$

From Fig. 4 it appears that the D-T reaction has the highest reaction rate peak, which corresponds also to a lower energy with respect to the peaks of the D-D reaction and the D-He^3 reaction. Anyway, the necessary energy for achieving the highest D-T reaction cross-section is still ~10 keV, corresponding to ~100 million Kelvin. At this temperature, the matter is at the state of plasma.

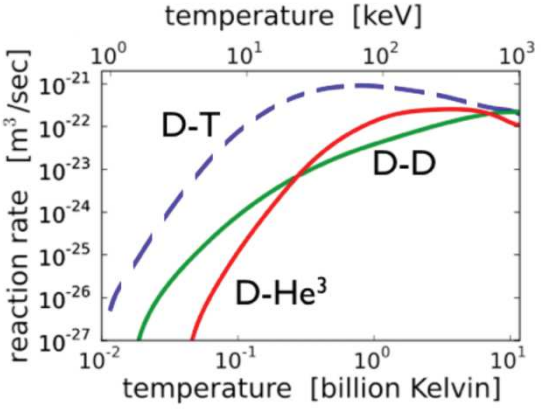

Fig. 4 Cross-section of the three most interesting fusion reactions from the point of view of energy production.

2) The second problem is the confinement of a plasma with such a high energy. Inside the stars, the confinement is provided by the gravity, while on Earth

two main methods are under research and development:

- **Magnetic confinement fusion** (see [5]), in which the hot plasma is confined by strong magnetic fields;
- **Inertial confinement fusion** (see [6]), in which the confinement of a small volume of solid matter is achieved by the action of high power focused lasers that heats up the matter to critical conditions.

In this thesis, only magnetic confinement fusion is considered, more details are given in the next section.

1.3. Magnetic confinement fusion

Magnetic confinement fusion exploits strong magnetic fields to confine the hot D-T plasma contained in the reaction chamber. This approach is more developed with respect to inertial confinement fusion, and more promising.

There are two main kind of device able to achieve magnetic confinement fusion, the stellarators (see [7]), and the tokamaks (see [8]).

In this thesis, only the tokamaks are considered.

The word *tokamak* comes from a Russian acronym meaning *Toroidal Chamber with Magnetic Coils*, in fact, a tokamak consists of a torus shaped vacuum chamber with two sets of coils, the toroidal magnetic field coils and the poloidal magnetic field coils, as shown in Fig. 5:

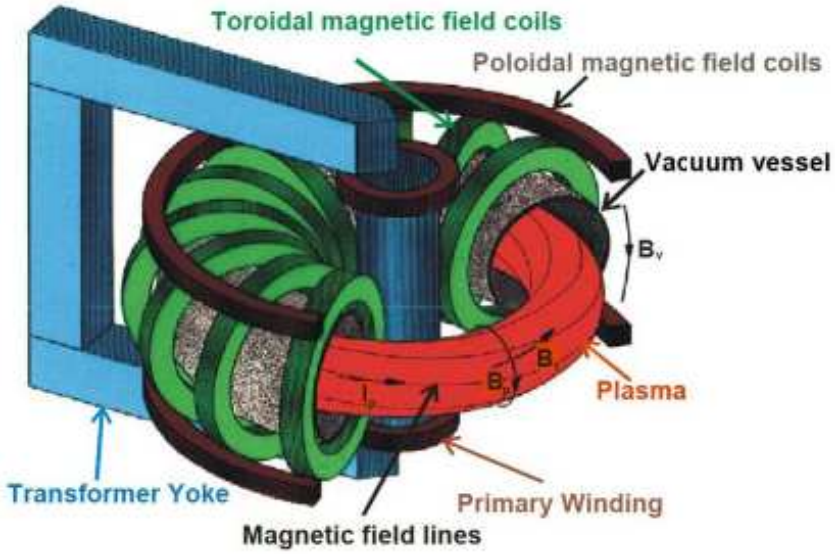

Fig. 5 Scheme of a tokamak.

The combination of toroidal and poloidal magnetic field, confines the plasma inside the vacuum vessel, following helical lines. The transformers induce a current flowing into the plasma, which generates the confinement poloidal magnetic field. The poloidal magnetic field coils are used to produce additional poloidal field for plasma shaping and stabilization.

Fusion D-T reaction happens in the confined plasma and release energetic Helium and neutrons. The neutrons are not affected by magnetic field so the travels across the plasma and impinge on the vessel wall, releasing their energy, that can be gathered and used as hot source for producing electric energy in the traditional way.

The produced Helium, on the contrary, is suddenly ionized (becoming α-particles, ${}_2^4He$) and releases its energy to the D-T plasma.

If the plasma density, temperature and confinement time are high enough, the α-particles heating is enough to sustain the fusion reaction, and the reactor has reached the so called *ignition.*
The ignition condition is usually expressed using the following figure of merit, called *triple product*:

$$n\tau_E T \geq 3 \cdot 10^{21}\ [m^{-3}\ keV\ s]$$

where n is the plasma density, τ_E the energy confinement time and T the plasma temperature.
Ignition has not been reached so far by any of the existing tokamaks and is one of the main goals on the future tokamak ITER, described in the next section.
Fig. 6 shows the values of the triple product reached by various tokamaks since the beginning of fusion research. The next step is represented by ITER, which is designed to reach the ignition.

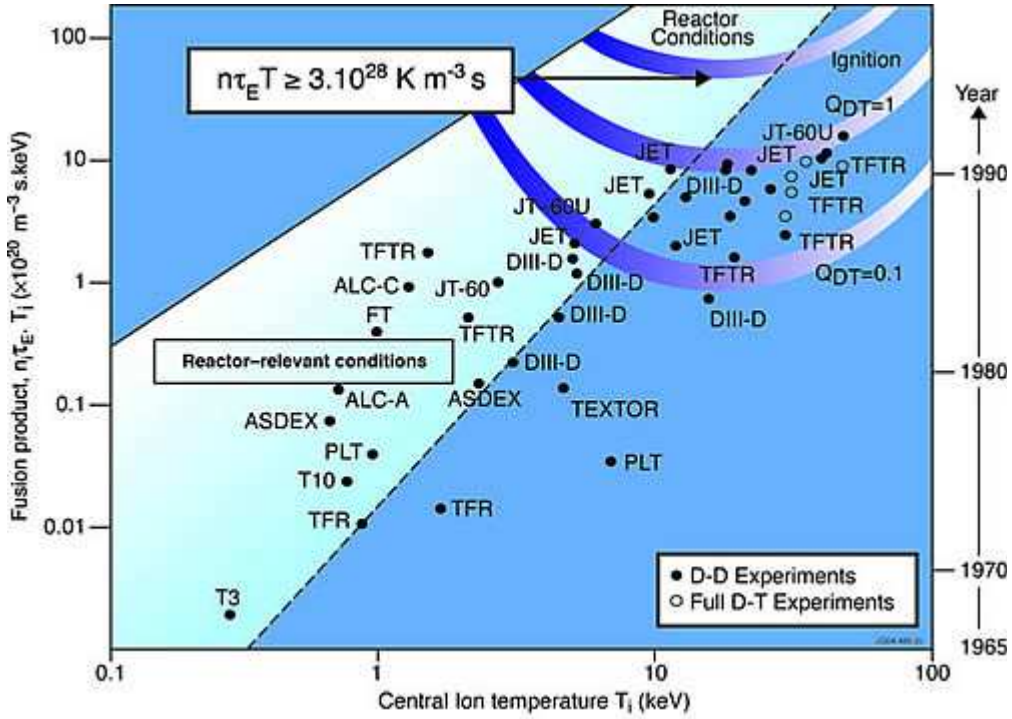

Fig. 6 Values of triple product as a function of ion temperature for the existing tokamaks operating with D-T or D-D reactions.

In all the present tokamaks and also in a future reaction before reaching the ignition point, additional heating systems are required to maintain the fusion reactions.
Another important figure of merit of a tokamak is the power amplification factor Q, defined as the ratio between the fusion power and the additional heating power.

1.4. ITER

ITER is an international nuclear fusion project which will be the world's largest tokamak and nuclear fusion experiment. ITER is under construction in France, near Cadarache, and its members are European Union, United States, Russia, Japan, China, India and South Korea, for a total cost of about 15 billion dollars.
The main goals of ITER are:

- To momentarily produce ten times more thermal energy from fusion heating than is supplied by auxiliary heating ($Q = 10$);
- To produce a steady-state plasma with non inductive plasma current and $Q > 5$;
- To maintain a fusion pulse for up to 480 seconds;
- To develop technologies and processes needed for a fusion power plant (advanced materials, superconducting magnets, remote handling,…);
- To verify tritium breeding concepts;
- To refine neutron shield/heat conversion technology.

The main ITER parameters are summarized in Tab. 1:

ITER parameter		
Fusion power	500	MW
Power amplification factor, Q	≥ 10	
Major radius	6.2	m
Minor radius	2	m
Machine height	26	m
Machine diameter	29	m
Plasma volume	837	m^3
Max. toroidal field	5.3	T
Plasma current	15	MA
Pulse duration	≥ 480	s

Tab. 1 Main ITER parameters.

A cutaway view of ITER is given in Fig. 7. For more information about ITER, see [9].

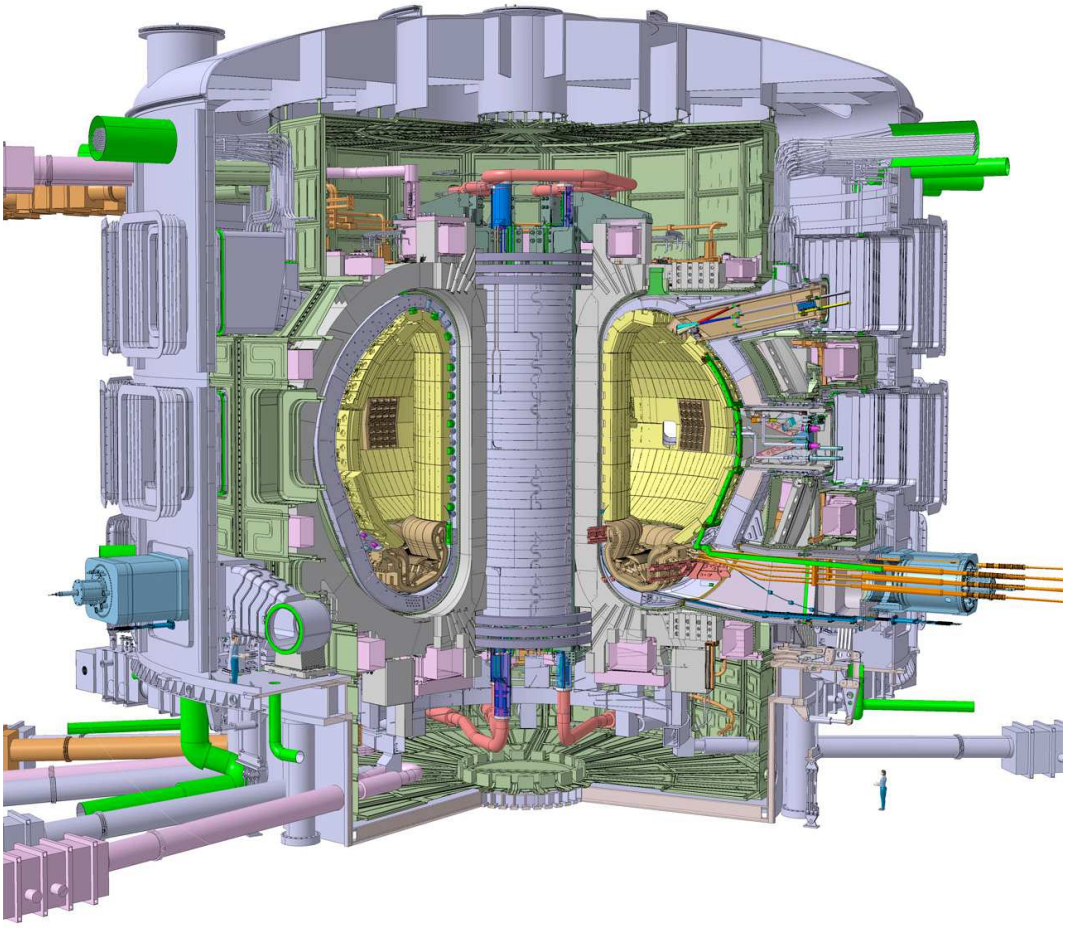

Fig. 7 Cutaway view of ITER.

1.5. Auxiliary Heating and Current Drive

As mentioned in Par. 1.3. , except in the case of ignition, auxiliary heating is necessary to compensate the power losses and keep the fusion plasma at the required temperature. Moreover, electric current flowing through the plasma is fundamental for plasma confinement (see again Par. 1.3.), and must be kept at the required level as well.

For this reason, several Heating and Current Drive systems have been developed and play a very important role in a tokamak.

Initially, a current is induced in the plasma exploiting the principle of the transformer (see Fig. 5), but this system can be adopted only in a transient phase.

Similarly, the initial plasma heating is rather simple to obtain, exploiting the ohmic heating due to the plasma current, according to $P_{Ohm} \propto I_P^2 R_P$, P_{Ohm} being the power produced, I_P the plasma current and R_P the plasma resistance. Unfortunately, above a certain plasma temperature, about 2keV, R_P decreases and ohmic heating is not effective anymore.

To further increase the plasma temperature and to maintain and control the plasma current, two different strategies are adopted:

- Radiofrequency Heating and Current Drive;
- Neutral Beam Injection (NBI).

The first strategy exploits microwaves with a frequency equal to charged particles oscillation frequency, in order to transfer energy to ions or electrons which in turn heat up all the plasma by collisions.
The second strategy consists on firing an energetic beam of neutral particles which transfer their energy and momentum to the plasma.
With both the strategies is possible to perform both plasma heating and current drive.
Fig. 8 shows a scheme of Heating and Current Drive systems used in tokamaks but also in stellarators.

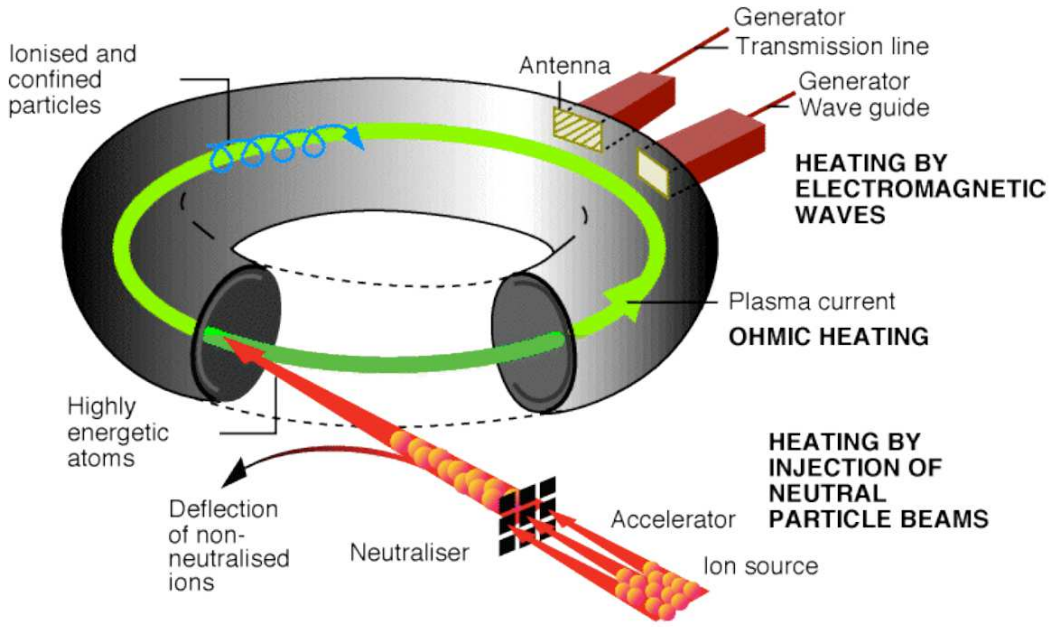

Fig. 8 Scheme of Heating and Current Drive systems used in magnetic confinement fusion.

This thesis will focus on Neutral Beam Injection systems only, whose principles are explained in the next section.

1.6. Neutral Beam Injection

As mentioned, a Neutral Beam Injector (NBI) is a device able to produce an accelerated beam of neutral particles with the purpose of heating and driving current in a fusion plasma. The beam must be neutral, otherwise it would be deflected by the strong magnetic fields produced by the tokamak coils.
Neutral particles are not subjected to electric or magnetic field, so the beam has to be initially constituted by charged particles, positive or negative, which are then electrostatically accelerated and then neutralized before entering the tokamak vessel.
Once inside the hot plasma, the neutral particles are ionized and release their energy and momentum through collisions. One important fact is that the penetration distance inside the plasma is proportional to the beam energy, and so, the proper beam energy has to be chosen in order to deposit the beam power in the plasma center, without losing it in the plasma edge. This fact is very important in the case of large plasma volumes, as in ITER, because in this case the optimal beam energy can be very high, with consequent complications in NBI operation (voltage holding, heat loads on NBI components, overall efficiency).
Depending on beam energy, there is also the choice between positive or negative ions, as shown in Fig. 9. Positive ions are in fact much easier to produce but their

neutralization efficiency becomes very low for beam energies higher than 100 keV for Deuterium and 40 keV for Hydrogen.
In ITER, for example, the plasma volume is very large, so a beam energy of 1MeV is required and the use of negative ions is a mandatory choice.

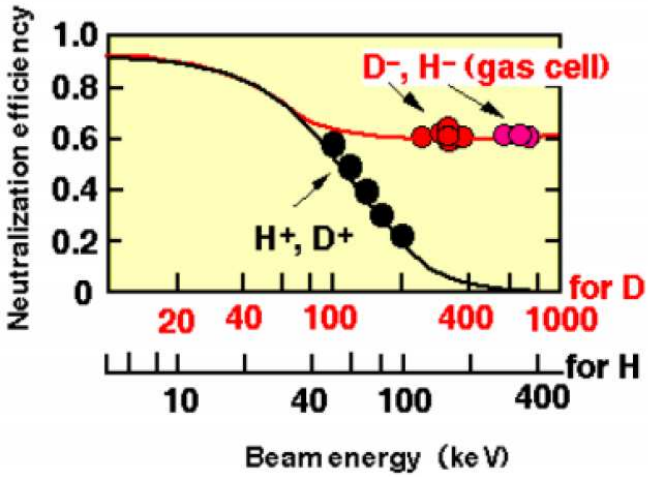

Fig. 9 Neutralization efficiency as a function of beam energy, for positive and negative Hydrogen and Deuterium ions.

Two NBIs are foreseen in ITER, each one having a beam energy of 1 MeV and beam power of 17 MW.
This thesis will focus on negative ions NBI, better explained in Par. 1.8. .

1.7. The Padua Neutral Beam Test Facility

The Padua Neutral Beam Test Facility (NBTF) is an ITER test stand in Padua, in the area of National Research Council, in cooperation with Consorzio RFX, with the purpose of realizing the full scale prototype of ITER NBI, see [10].
The NBTF is composed by PRIMA (Padua Research on ITER Megavolt Accelerator), the facility that will host the experiments, SPIDER (Source for the Production of Ions of Deuterium Extracted from an RF plasma), an experiment for testing the negative ion extraction from an ITER size ion source, and MITICA (Megavolt ITER Injector and Concept Advancement), the final full scale, full performance prototype of the Heating Neutral Beams (HNB) for ITER.
The facility PRIMA is now completed (see Fig. 10), the experiment SPIDER is under construction, and the design of MITICA has been completed by Consorzio RFX.
This thesis is focused on MITICA and its design.

Fig. 10 Aerial view of PRIMA facility in Padua.

1.8. MITICA

MITICA (see [11]) is the full scale prototype of ITER Heating Neutral Beams (HNB, see [12]) and it has been designed at Consorzio RFX in the framework of NBTF project.
Fig. 11 shows a sketch of MITICA and its components. MITICA is constituted by a negative ion source and accelerator, a neutralizer, an electrostatic residual ion dump for deflecting the non neutralized particles, and a calorimeter for diagnostic purposes. The total length of the device is more than 20 meters.

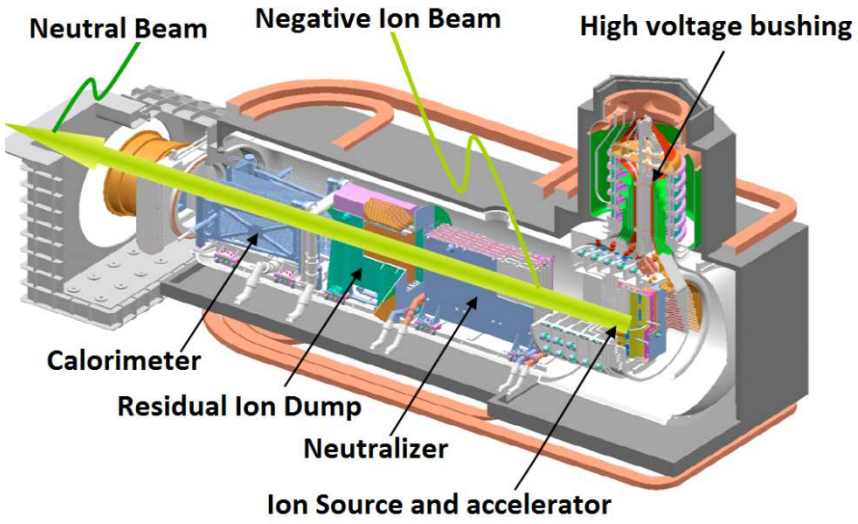

Fig. 11 Sketch of MITICA.

The main MITICA parameters are summarized in Tab. 2:

Parameter			
Ion species	**D-**	**H-**	
Beam energy	1	1	MeV
Beam power	17	17	MW
Pulse length	3600	3600	s
Acceleration current	40	60	A
Extracted current density	285	355	A/m^2
Extracted electron to ion ratio	1	0.5	
Source pressure	0.3	0.3	Pa

Tab. 2 Main MITICA parameters.

This thesis is focused on MITICA electrostatic accelerator, shown in Fig. 12. The purpose of the accelerator is to accelerate and focus the negative ions produced by the radiofrequency ion source. For more details on negative ion production inside the ion source, see [13] and [14].
The accelerator is constituted by seven copper grids, each one made of four parts called grid segments with 1280 apertures in total, divided in 16 beam groups 16x5, as shown in Fig. 13 together with the main dimensions.
The first is the Plasma Grid (PG), which is a molybdenum-coated copper plate with 1280 apertures. This grid faces the Ion source and is kept at the electric potential of -1009 kV. The second grid is the Extraction Grid (EG), biased at about -1000 kV, which has the purpose of shaping the electric potential so that 1280 well-focused ion beamlets are produced and extracted from the source through the PG.

The EG also includes permanent magnets which produce a magnetic field for deflecting the electrons that are extracted together with the negative ions (co-extracted electrons).
Downstream of the EG, there are the four Acceleration Grids (AG1 – AG4) and the Grounded Grid GG, which have a potential of -800, -600, -400, -200 and 0, respectively, and accelerate the negative ions at the required energy of 1 MeV.

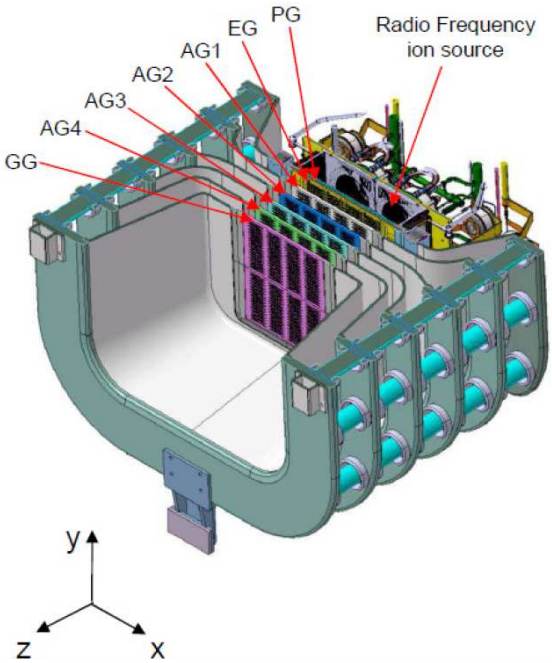

Fig. 12 Cut view of the MITICA ion source and accelerator: PG=plasma grid, EG=extraction grid, AG1-AG4 acceleration grids, GG= grounded grid.

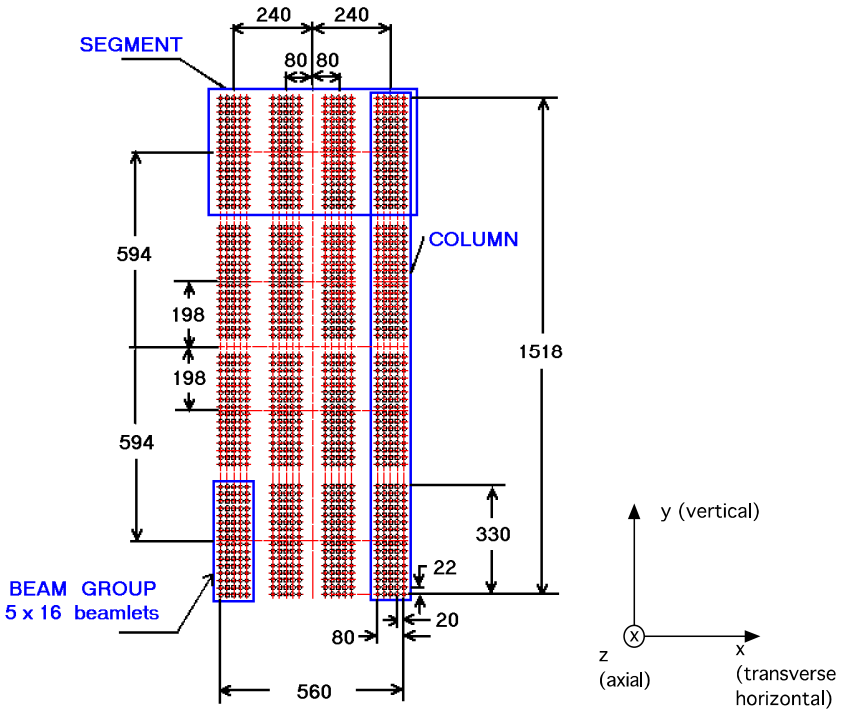

Fig. 13 Front view of a MITICA accelerator grid, showing main dimensions, grid segments and the 16 beam groups, each constituted by 16x5 apertures, for a total of 1280 apertures.

The most important issues for the MITICA accelerator design are the following:

- reaching an optimized beam optics in terms of divergence and aiming of the negative ion beam;
- minimizing the heat loads on the accelerator grids, with an efficient dumping of co-extracted and stripped electrons given by an optimized magnetic and electrostatic configuration;
- designing a cooling system capable of maintaining the alignment among the grids in all foreseen operating scenarios, at the same time satisfying all the structural verifications according to the ITER criteria;
- guaranteeing the voltage holding among the grids and between the source and the vacuum vessel.

1.8.1. Magnetic configuration of MITICA accelerator

The magnetic fields represent a critical issue of the design optimization of the MITICA beam source, as they influence several crucial aspects of its operation, like the accelerator efficiency, beam optics and beam uniformity.

The principal function of magnetic field inside MITICA accelerator is to suppress both the electrons which are extracted from the source together with the ions (co-extracted electrons) and those generated by stripping reactions inside the accelerator, when an accelerated negative ion collides with the background gas or with the electrodes and one or two electrons are detached.

The deflection of the co-extracted electrons is performed by a set of magnets called Co-extracted Electron Suppression Magnets (CESM) embedded in the EG. Namely, these magnets generate a field mainly along the y direction and alternated from row to row, that is able to deflect nearly all the co-extracted electrons onto the EG itself.

After several optimization stages, see [15], [16], [17] and [18], it was found that the most efficient setup for removing the stripped electrons without spoiling the beam optics was a combination of:

- a "local" field along the transverse vertical direction (y), produced by the Stripped Electrons Suppression Magnets (SESM) located in the AGs;
- a "long-range" field along the transverse horizontal direction (x), produced by the current flowing through the PG and the related conductors.

In this way, a transverse diagonal magnetic field is generated, which deflects the electrons directly on the parts of the grids that are more efficiently cooled by internal cooling channels, thus minimizing the peak copper temperature and the related thermal stresses.

Fig. 14 shows the arrangement of the permanent magnets of a Beam Group. CESM and SESM are described above, ADCM (Asymmetric Deflection Compensation Magnets) will be explained in Par. 2.1. . The short range vertical magnetic field produced by CESM, SESM and ADCM is shown in Fig. 15.

The Plasma Grid and its related conductors, with the indication of the electric current path, are shown in Fig. 16, together with the resulting magnetic field. These conductors have been designed so as to produce both the "long-range" magnetic field inside the accelerator (for suppression of stripped electrons, as mentioned above), and also the so called Filter Field in the ion source region, that is necessary for helping the negative ion production, see [13] and [14].

Additional information about PG busbar configuration can be found in Par. 2.3.2. and in [19].

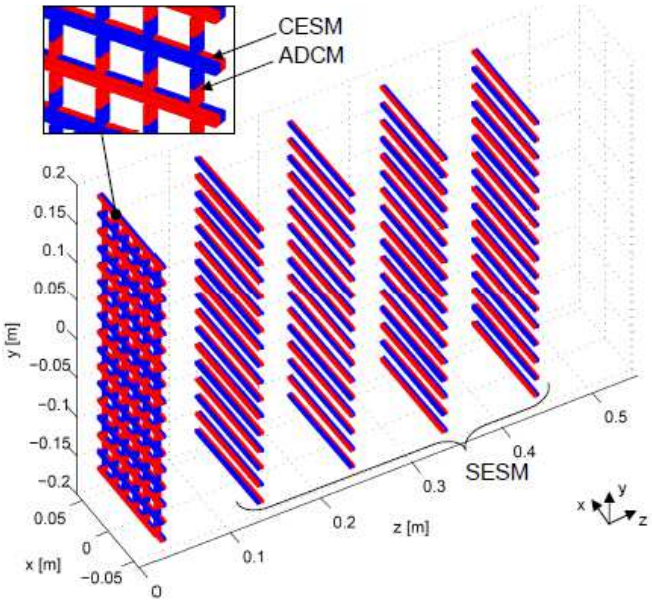

Fig. 14 Permanent magnets of a beam group.

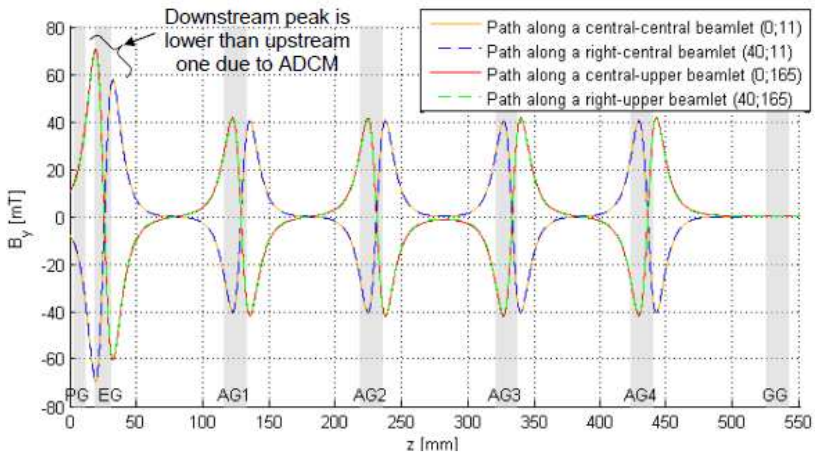

Fig. 15 Short range vertical magnetic field produced by CESM, ADCM and SESM.

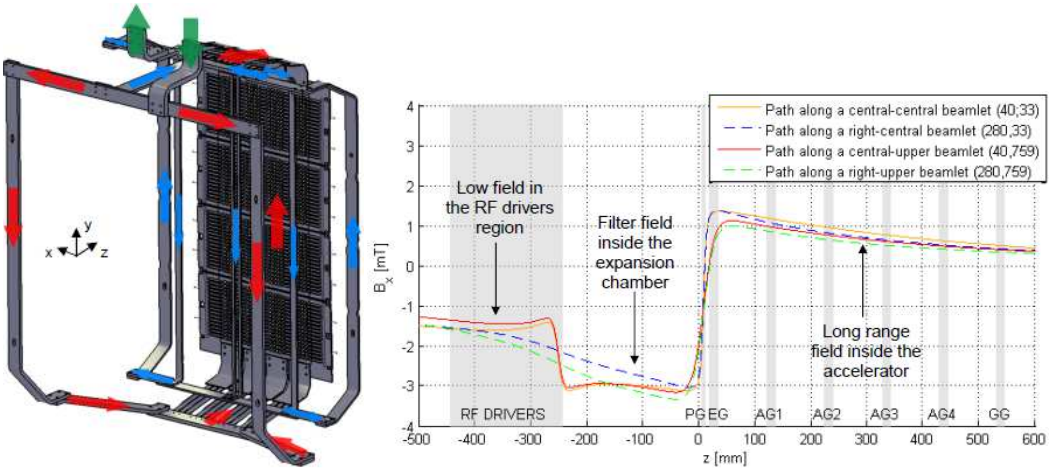

Fig. 16 Electric current flowing through the Plasma grid and its related conductors (left) and the resulting magnetic field (right).

2. Design activities on MITICA accelerator

In this chapter the most important design activities carried out on MITICA accelerator will be presented. The first two involve the study of alternative magnetic configurations for the accelerator in order to solve some existing issues, then there is a section dedicated to the update of the design of the Transverse Magnetic Filed Coils, and finally the last two sections show the results of magnetic measurement campaigns on Multi Channel Prototype and on NIO1 accelerator.

2.1. Cancellation of the ion deflection due to electron-suppression magnetic field in a negative-ion accelerator

A new magnetic configuration has been proposed for the suppression of co-extracted electrons in a negative-ion accelerator. Such configuration is produced by an arrangement of permanent magnets embedded in the Extraction Grid (see Fig. 14) and creates an asymmetric local magnetic field on the upstream and downstream sides of this grid. Thanks to the "concentration" of the magnetic field on the upstream side of the grid, the resulting deflection of the ions due to magnetic field can be "intrinsically" cancelled by calibrating the configuration of permanent magnets. At the same time, the suppression of co-extracted electrons can be improved.

2.1.1. Introduction

As explained in Par. 1.8.1. , negative ion electrostatic accelerators require a transverse magnetic field for the "suppression" of co-extracted and stripped electrons. This transverse field improves the accelerator efficiency by diverting the electrons before they are accelerated and substantially reduces the heat loads on subsequent grids and beam-line components, but typically has a negative impact on beam optics, due to resulting undesired deflection of the ion trajectories.
A novel magnetic configuration has been proposed, which provides effective electron suppression and avoids at the same time the ion deflection, see [20].
This configuration has subsequently become the reference solution for MITICA.

2.1.2. One-sided flux magnetic structures

One-sided magnetic flux structures are somehow conflicting with "intuitive" concepts, but have been used in various applications. The idea was first described in 1973 by J. C. Mallinsons of Ampex Corp. [21] but was never applied in the industry of audio recording tapes, where it was conceived. The concept was independently developed in a paper published in 1980 by K. Halbach [22], showing that permanent magnet bars arranged around a cylindrical cavity can produce a "pure" dipole (or multipole) magnetic field inside the cavity and negligible field outside (Fig. 17). Halbach applied the concept to the realization of efficient magnetic dipoles and quadrupoles for particle deflection in high-energy accelerators [23]. By changing the orientation of the magnets, a multipole magnetic field outside the cavity and zero field inside can also be produced. This concept has wide application in "brushless" synchronous electric motors and generators.

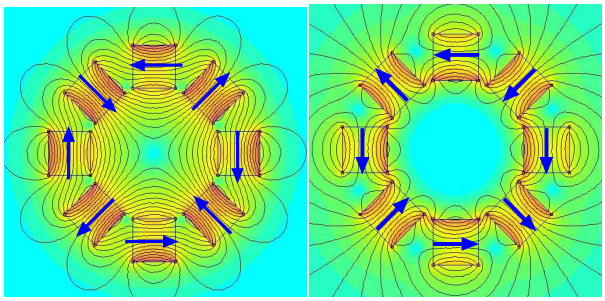

Fig. 17 2D maps of quadrupole magnetic field produced by permanent magnet bars arranged around a cylindrical cavity (cross-section view, arrows indicate the magnetization direction, colors indicate field strength).

The same concept has been applied to planar 2D structures (called Halbach arrays) in linear electric motors, see Fig. 18.

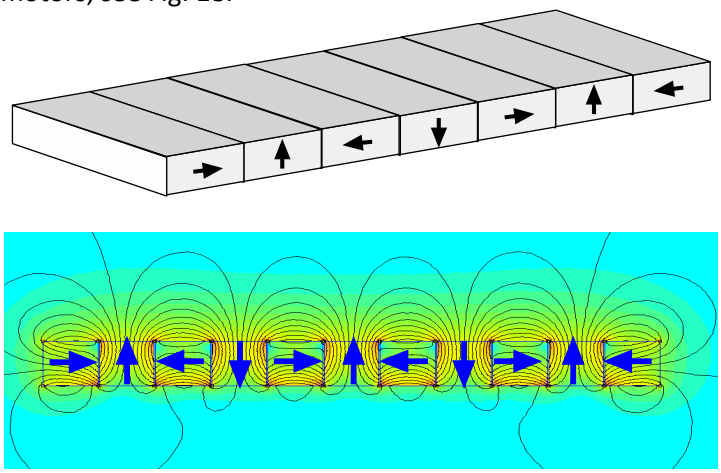

Fig. 18 Sketch of a planar Halbach array and corresponding 2D map of magnetic field showing the flux asymmetry (cross-section view).

The interesting feature of the planar Halbach array is that, even if the structure is geometrically symmetric with respect to the plane where the structure lies, it produces a strong magnetic field only on one side of a plane.

2.1.3. Asymmetric magnetic grid concept and deflection cancellation

In negative ion accelerators for Heating Neutral Beam Injectors, the main electron-suppression field is produced along the first acceleration stage by magnets embedded in the Extraction Grid (EG). These magnets, which have been called "Co-extracted Electron Suppression Magnets" (CESM, see Par. 1.8.1.), are arranged in horizontal arrays and are magnetized along the acceleration direction z, as shown in Fig. 14, Fig. 19, and Fig. 21. The transverse (vertical) component of the magnetic field (By) along a beamlet axis exhibits a typical symmetric double-swing profile (continuous blue line in Fig. 20).

This field assures that most of the co-extracted electrons will be deflected and will impinge on the upstream side of the EG. In multi-stage accelerators, such as MITICA, magnets having the same arrangement but smaller size, can be embedded in the acceleration grids (AGs) in order to produce a vertical field, whose purpose is to deflect the electrons produced by stripping reactions with the background gas, as explained in Par. 1.8.1.

According to the present design of MITICA, Sm2Co17 magnets having a remanence of 1.1 T, a cross-section of 4.6 x 6.6 mm and a vertical pitch of 22 mm will be used and symmetric peaks of ± 64 mT are obtained along the beamlet axis (Fig. 20).

As a first approximation, the deflection can be estimated as the ratio of transverse velocity vx and axial velocity vz, according to the "paraxial approximation" formula:

$$\delta = \frac{v_{x,exit}}{v_{z,exit}} = \frac{q\int_{z_0}^{z_{exit}} B_y\, dz}{m_{D^-}\sqrt{\frac{2qU_{exit}}{m_{D^-}}}} = \sqrt{\frac{q}{m_{D^-}}} \cdot \frac{\int_{z_0}^{z_{exit}} B_y\, dz}{\sqrt{2U_{exit}}}$$

(q and m are the ion charge and mass, U_{exit} is the electrostatic acceleration potential and z_0, z_{exit} are the initial and final axial coordinates of the ion trajectories).

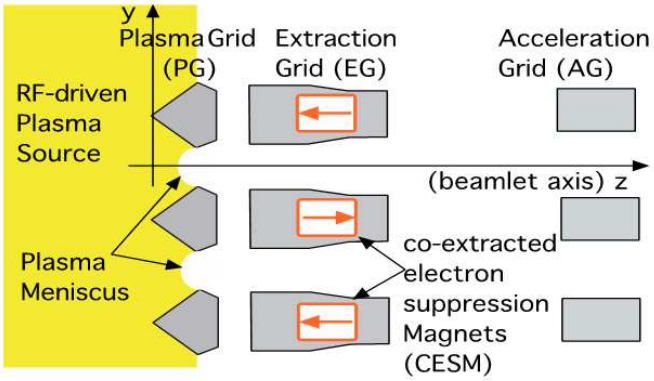

Fig. 19 Vertical cross-section of the first stages of a negative-ion accelerator, showing the Plasma Grid and CESM embedded in the Extraction grid. Ions are extracted from the RF-driven plasma source and accelerated along the z direction.

Anyhow, the horizontal deflection of ion beamlets due to the vertical field By is a major issue in the optics design of multi-beamlet accelerators [24].
The beamlet horizontal deflection at the accelerator exit is thus related to a non-zero integral of By. As a matter of fact, the negative ions are formed mainly at the border of the Plasma Source region and the magnetic deflection of the ion beamlets is commonly ascribed to the ion trajectories (and integral of By) starting at a virtual surface called plasma meniscus (see yellow and blue areas in Fig. 20). This deflection has a typical "zig-zag" pattern, due to the fact that the By field is reversed row by row.

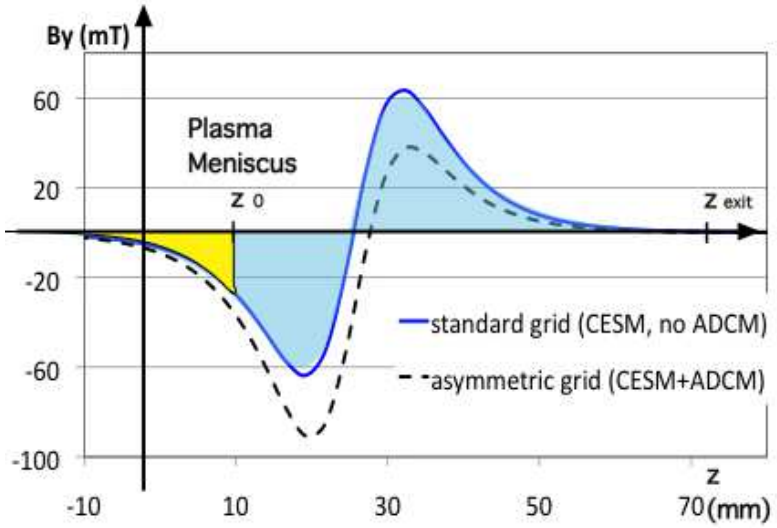

Fig. 20 Profiles of transverse magnetic field By along a beamlet axis: standard symmetric grid (continuous blue line) and asymmetric grid (dashed black line).

This magnetic deflection can be non-linearly amplified by the electrostatic "divergent-convergent" lens effect, which is stronger on the upstream side of the EG with respect to the downstream side. On the basis of the present MITICA design, the expected

deflection is of the order of ± 3 mrad at accelerator exit. Being the deflection alternate row by row, its compensation is necessary in order to obtain a well focused beam. It is worth noticing that magnets located inside the subsequent acceleration grids (AG) cannot modify the deflection due to CESM, since their contribution to the integral of By is null. Compensation by electrostatic means (aperture offset) has been considered and tested so far, but its adjustment is very delicate, see [25] and [26].
The new grid configuration proposed here combines the features of a standard Extraction Grid used in negative-ion accelerators (based on CESM) with those of a planar Halbach array, so that an asymmetric By profile is produced. The concept is shown in Fig. 21 and Fig. 22.
Essentially, the new grid is constituted by an additional set of permanent magnets inserted just in between the CESM of a standard EG. These magnets are alternately magnetized along the vertical direction and are called "Asymmetric Deflection Compensation Magnets" (ADCM) because they enhance the vertical component By on the upstream side of the EG and diminish it on the downstream side. Therefore the By profile becomes asymmetric, as shown by the dashed line in Fig. 20, which refers to the case of standard CESM (same cross-section and pitch as above) plus ADCM having a tentative thickness of 3 mm in the horizontal direction.

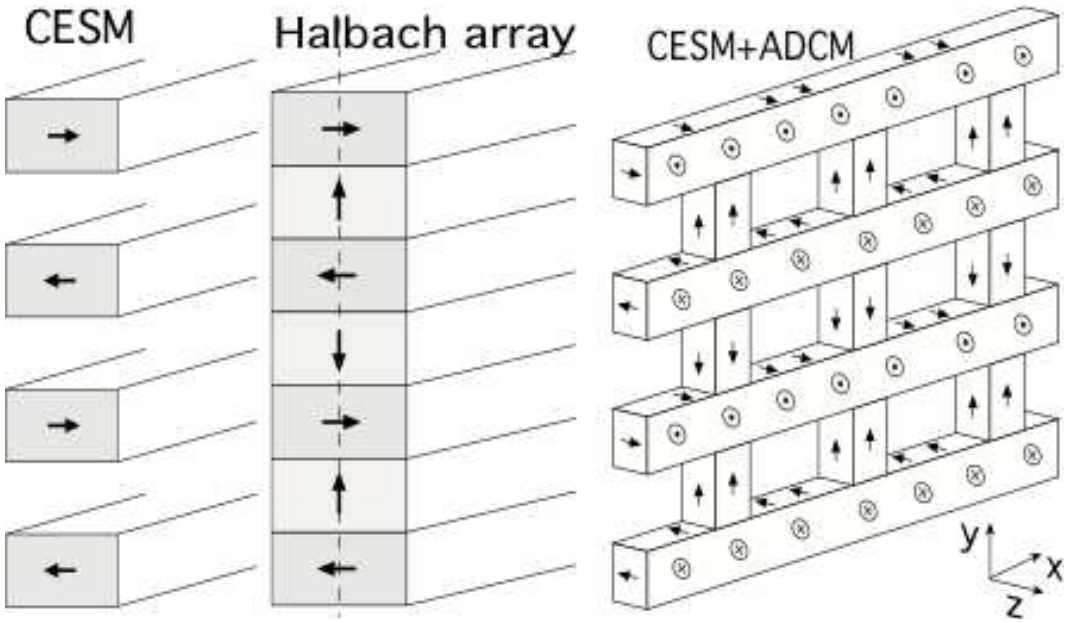

Fig. 21 Sketch of magnet layout and orientation in a standard extraction grid (left), in a Halbach plane array (centre), and in the proposed asymmetric grid (right).

The main features of this new configuration are the following:

- contrary to the planar Halbach array (which produces an asymmetric flux, but has no "holes"), the asymmetric magnet grid is compatible with the typical accelerator grid geometry. If all magnets have the same size along z (as in Fig. 21) and a rectangular lattice of channels is machined inside the grid, both the CESM and ADCM magnets can be assembled by inserting them in proper sequence into the grid;
- the asymmetry of the By profile along z can be adjusted by choosing the thickness (t) of the ADCM along the horizontal direction (x), so that the integral of By and the magnetic deflection can be precisely cancelled out. Adjustment by using materials having different magnetic remanence is also possible;

- thanks to the ADCM, the magnetic flux is concentrated on one side of the grid and can be cancelled on the other.

This implies that the asymmetric grid produces a higher field on the upstream side than the standard one. Therefore, for a given electron-suppression field on the upstream side, the size of CESM can be reduced. This is generally beneficial to the design of the EG.

2.1.4. Asymmetry adjustment, optimization and uniformity

On the basis of the above considerations, a complete cancellation of the magnetic deflection can be achieved by an appropriate choice of the ADCM thickness. A first optimization was carried out using the NBImag code [18] for the calculation of the By profile and the above mentioned By integral for the estimation of the magnetic deflection, obtaining that a thickness of just 0.73 mm was required for the ADCM. Then a more precise calculation of the ion trajectory deflection was made using an OPERA 3D model [10], which also takes into account the nonlinear amplification effect of electrostatic lenses and space charge. It has been found that these effects tend to require a more asymmetric By profile for the complete cancellation and that the optimum is achieved with thicker ADCM (thickness of about 2 mm) and CESM having slightly reduced cross-section (4.2x6.6 mm) (see Fig. 22).

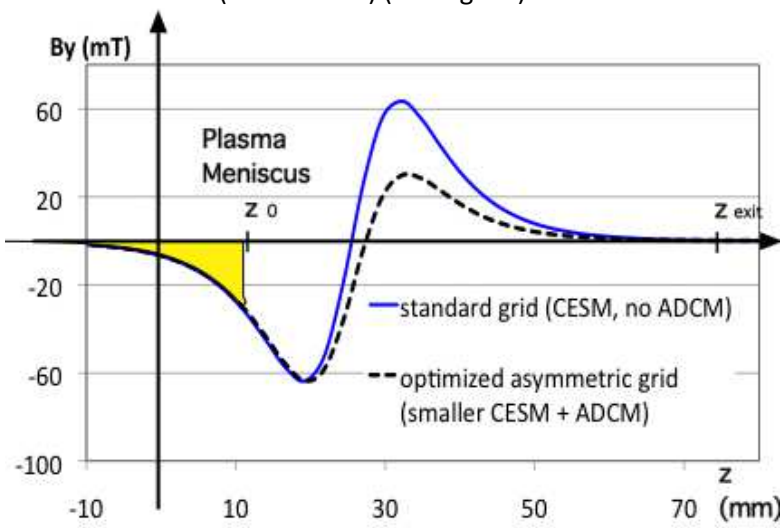

Fig. 22 Profiles of transverse magnetic field By along a beamlet axis: standard symmetric grid (continuous blue line) and optimized asymmetric grid (dashed black line).

It is worth noticing that the first part of the By profile is identical to the one produced by the standard grid, hence no effect on plasma source can be expected.

Using the same NBImag code, the uniformity of the optimized configuration has been evaluated along horizontal paths located across the beamlet aperture on the front side and on the back side of the grid (10 mm upstream and downstream from the EG). The results show that the non-uniformity of the By field is smaller than 5%, which is well acceptable (Fig. 23) so that the effect of the cancellation of the deflection is effective across the whole beamlet cross-section.

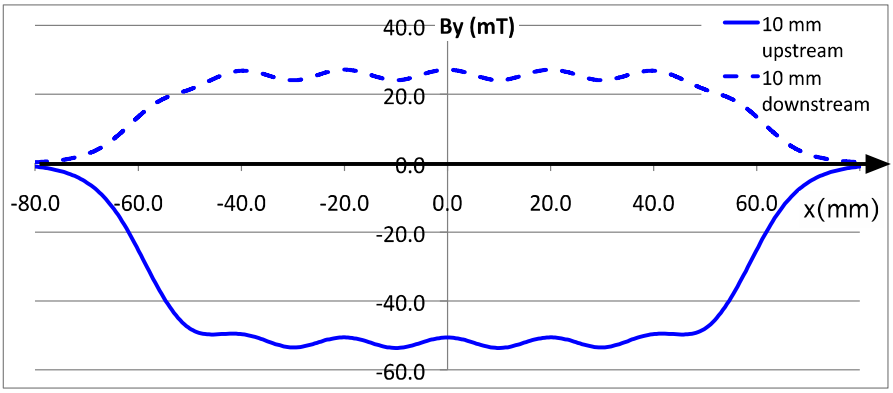

Fig. 23 Profiles of transverse magnetic field By along horizontal paths located 10 mm upstream and downstream of the EG (optimized asymmetric grid).

2.1.5. Magnetic measurements on a grid prototype

As a preliminary test, the asymmetric grid has been implemented and benchmarked on the already existing Multi Channel Prototype (MCP) [27], which is a grid made of electrodeposited copper, having 8x5 apertures of 13 mm diameter (see Fig. 24).
This grid was already provided with Sm2Co17 CESM having a remanence of 1.1 T and a cross-section of 4.6 x 5.6 mm, arranged in horizontal arrays in grooves having 22 mm vertical pitch.

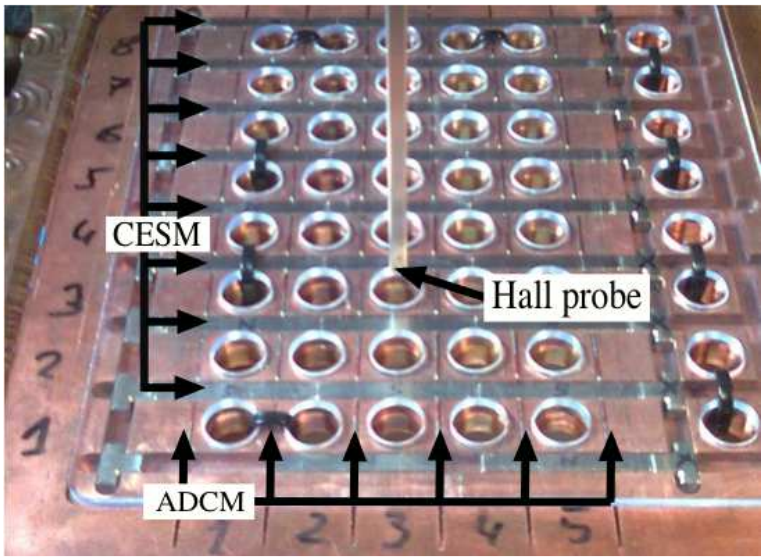

Fig. 24 Picture of the MCP prototype, showing CESM and ADCM inserted in the copper grid. The magnetic Hall probe is also visible in the centre.

After machining the additional vertical grooves, ADCM having remanence of 1.1 T and thickness of 0.73 mm (as resulting from the first optimization above described) were inserted between the CESM magnets in the grid. For easier realization and visualization the magnets were kept in position inside the grooves by means of a transparent polycarbonate lid fixed to the copper grid.
The transverse magnetic field By along several apertures was mapped using a FW Bell 6010 Gaussmeter with the same setup and adjustable support frame used for LHD BL2 source mapping [28]. The experimental results are plotted in Fig. 25 and show very good agreement with the NBImag numerical simulations.

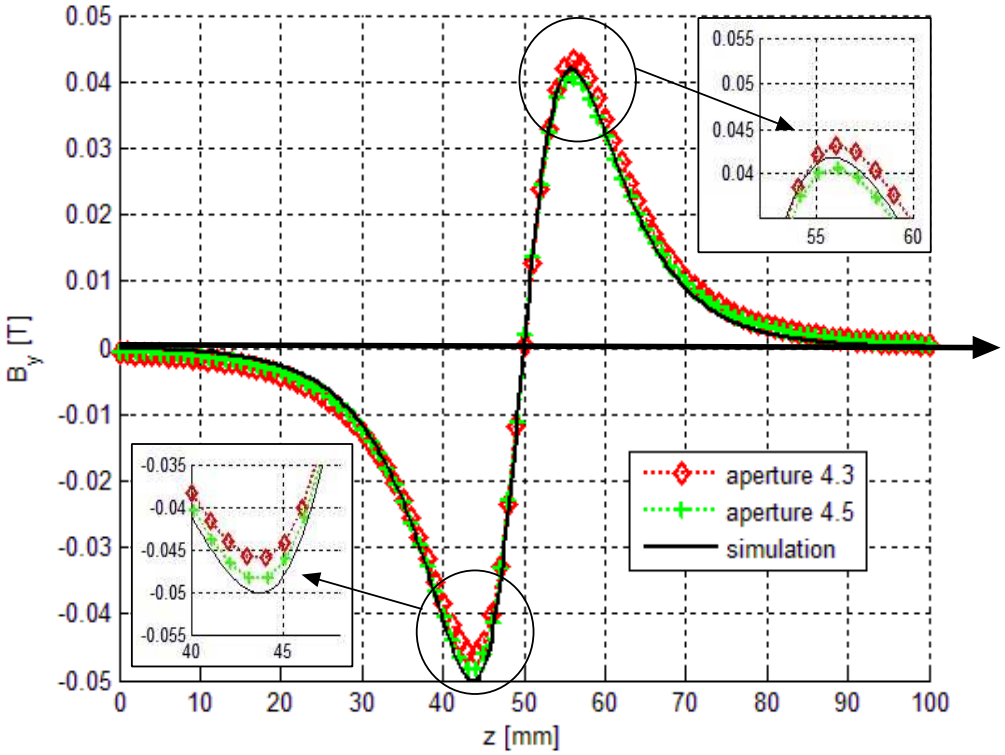

Fig. 25 Measurements of By profiles on MCP (different colors for different apertures, black for NBImag simulations).

The small non-uniformities among the profiles measured in different apertures have been related to the mechanical tolerance in the positioning of the magnets inside the MCP grooves (clearance was 0.4 mm) and are considered anyhow acceptable.

2.1.6. Assembly

For the assembly of the real MITICA grid (where removable lid is not foreseen and magnets will have to be inserted in channels accessible only from the sides of the grid) numerical simulations were carried out with the software NBImag with the new routines for magnetic forces calculation described in Chapter 3.

In parallel, a practical test of magnet insertion in the MCP grooves (with the lid closed) has been performed in order to compare the results of the simulation and to have a final proof of the assembly feasibility and ease.

A first simulation has been carried out with the first row of CESM and ADCM magnets in their nominal position, showing a zero acting force (because of symmetry). A second one has been carried out with the first two rows of CESM and ADCM, and in this case there was a repulsive force (about 1 N) acting on the ADCM, thus complicating the assembly procedure, see Fig. 26:

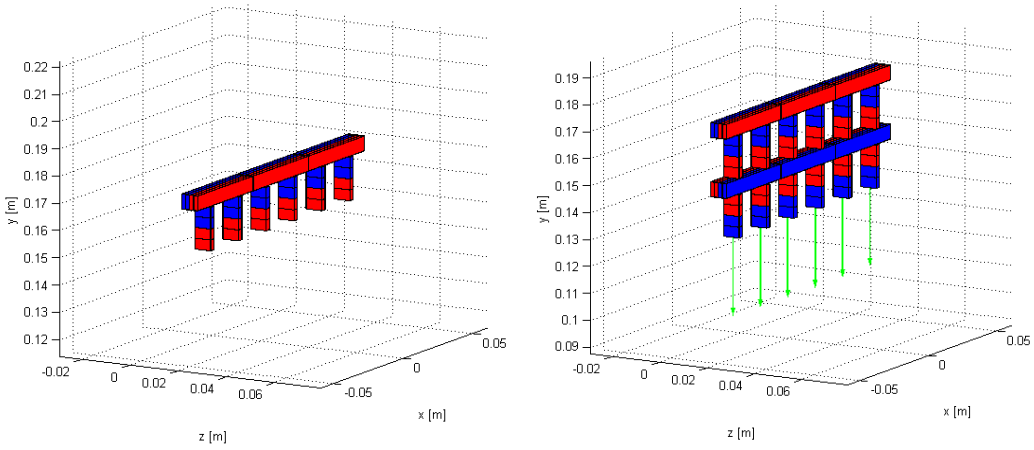

Fig. 26 Forces acting on the first two rows of ADCM (nominal position).

However, first practical assembly attempt on the MCP grid prototype, whose geometry is similar to a MITICA beamlet group, showed the opposite results, that is an attractive force between CESM and ADCM, in any row. This qualitative difference can be easily understood in terms of the real position of the magnets along the grooves, this last ones having a tolerance of some tenth of millimeters with respect to the magnets.
Another simulation has been made with the magnets in the actual position observed from the prototype, that is with a little shift (0,4 mm) in the z-direction (see Fig. 27 and Fig. 28) and the results were this time in agreement with the experiment.

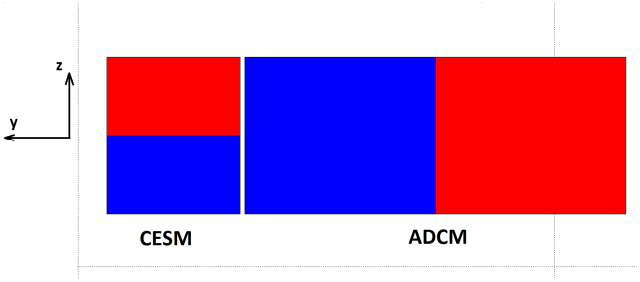

Fig. 27 CESM and ADCM in nominal position (no resulting force on ADCM along y-direction)

Fig. 28 CESM and ADCM in real position (attractive force on ADCM along y-direction).

Exploiting this tolerance in our favor, a sequence has been proposed for the assembly of a beamlet group, using an external magnet for moving the CESM and the ADCM to their positions.

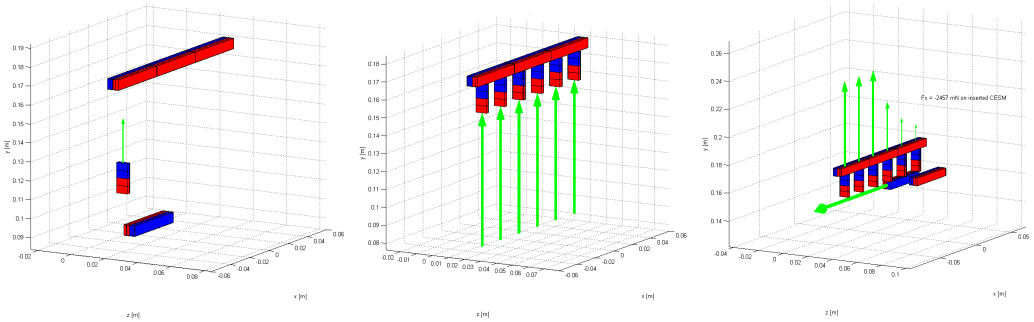

Fig. 29 Assembly step 1 (F~127 mN), step 2 (F~750 mN) and step 3.

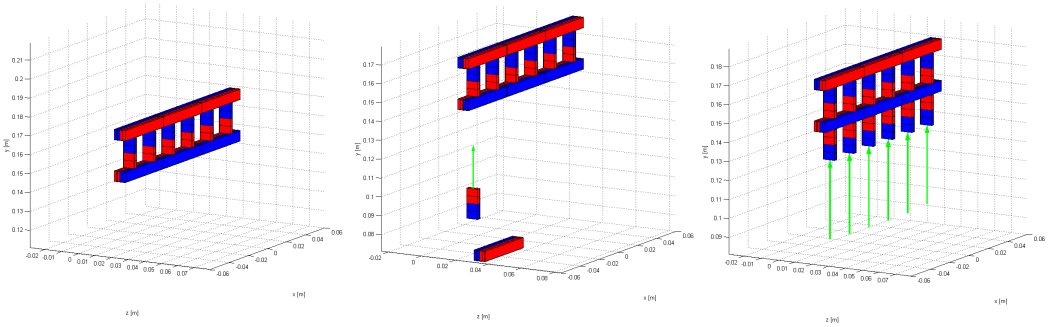

Fig. 30 Assembly step 4, step 5 and step 6 (F~430 mN).

The same external magnet used for the assembly can be also used for disassembling the beamlet group, as proved on the prototype and shown in Fig. 31:

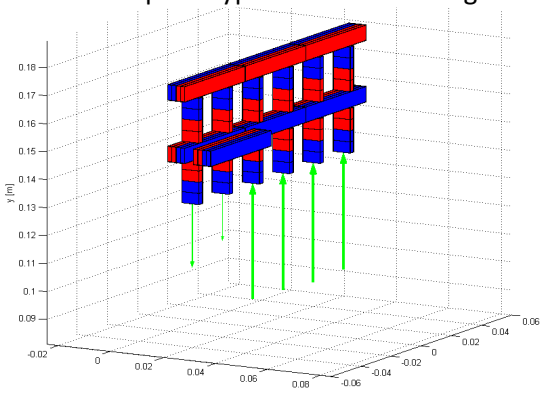

Fig. 31 Disassembly of two ADCM using an external magnet.

2.1.7. Conclusions

An asymmetric configuration can be produced by an arrangement of permanent magnets embedded in one accelerator grid. The asymmetry can be calibrated so that the resulting deflection of the ions due to magnetic field is "intrinsically" cancelled. Thanks to the "concentration" of the magnetic field on the upstream side of the grid, the suppression of co-extracted electrons is improved. As a preliminary test, the new magnetic configuration has been implemented and experimentally mapped on a prototype, showing good agreement with the calculated asymmetric field profiles and also good uniformity. A feasible assembly procedure has also developed and experimented.

After proving its validity, this solution has been accepted to be the reference solution for MITICA accelerator.

Experimental test of this solution in an existing accelerator are foreseen for the future, see Chapter 6.

2.2. GG aiming

A preliminary evaluation for the implementation of a "magnetic aiming" on the MITICA accelerator has been carried out as a "proactive" measure for risk reduction, in case of difficulties in the realization of double dihedral grids (explained below) with the required mechanical tolerances.

This evaluation shows that a steering angle (magnetic deflection of ions) of the order of ~ 10 mrad is feasible and can be implemented relatively easily by magnets embedded in the Grounded Grid. An increase in the thickness of the grounded grid from 17 to ~ 24 mm would be required to this purpose.

The non-uniformity of the steering angle due to edge effects of the magnetic field has been evaluated to be of the order of ~ 2 mrad, and could be further reduced if ferromagnetic yokes are introduced.

2.2.1. Horizontal aiming requirements and reference solution

Horizontal aiming at 25,4 m is required for MITICA, as can be seen in Fig. 32. Considering the accelerator geometry of Fig. 13, the required steering angles are directly evaluated:

- Outer beamlet groups: 240 mm / 25.4m = 9.4 mrad
- Inner beamlet groups: 80 mm / 25.4 m = 3.2 mrad

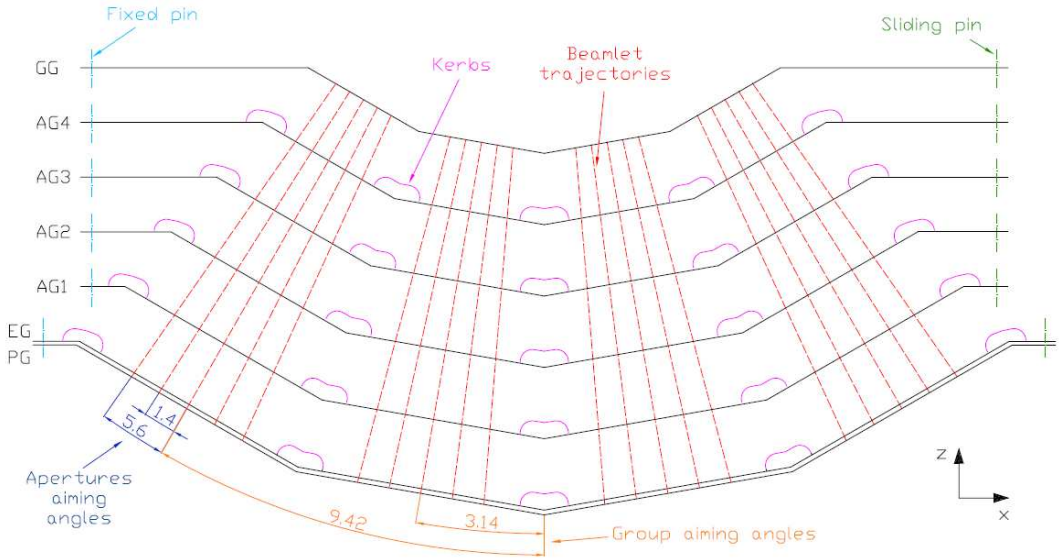

Fig. 32 Horizontal aiming scheme of MITICA.

The reference solution foreseen for obtaining these angles is the mechanical bending of all the grid segments, resulting in the so called double dihedral configuration, schematically shown in Fig. 33.

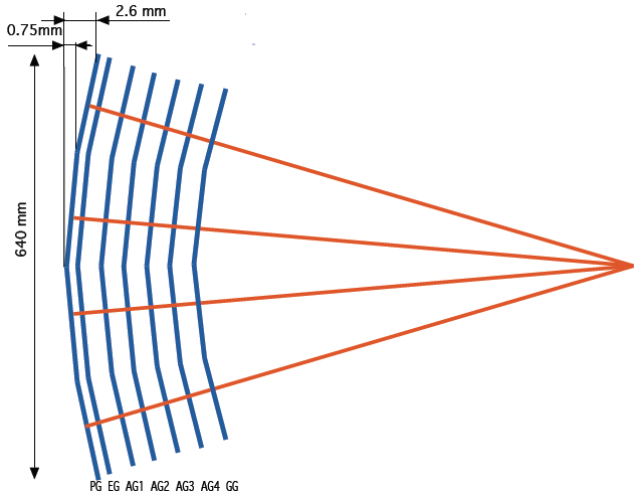

Fig. 33 Horizontal aiming by double dihedral grids.

In this configuration all the grids are bent with a very small deviation from the flatness (0.75 – 2.6 mm over a span of 640 mm), therefore the construction and the assembly of this solution is very complicate, with no possibility of adjustment.
For these reasons, a backup solution has been analyzed, in which the steering takes place only at the Grounded Grid by means of permanent magnets, so without needing anymore the grid bending. The concept is shown in Fig. 34.

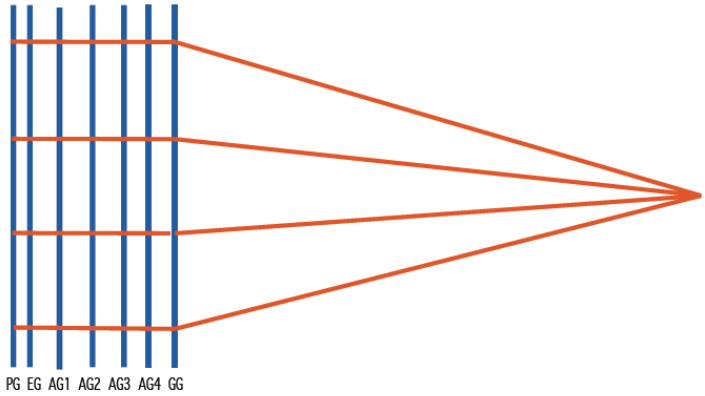

Fig. 34 Horizontal aiming at Grounded Grid.

This configuration has the great advantage of having flat grids. This brings several beneficial effects: easier machining, no spring-back effect, easier positioning and dimensional verifications before and after assembly, possibility of adjustment.
A feasibility study of this solution has been carried out by mean of the usual formula for magnetic deflection in paraxial approximation, here reported:

$$\delta = \frac{v_{x,exit}}{v_{z,exit}} = \frac{q\int_{z_0}^{z_{exit}} B_y\, dz}{m_{D^-}\sqrt{\frac{2qU_{exit}}{m_{D^-}}}} = \sqrt{\frac{q}{m_{D^-}}} \cdot \frac{\int_{z_0}^{z_{exit}} B_y\, dz}{\sqrt{2U_{exit}}}$$

Considering charge and mass of D- ions and $U_{exit} = 1\,MV$, in order to have a horizontal deflection of ~10 mrad, a "concentrated" vertical magnetic field (By) in the GG can be used, whose integral has to be:

$$\int_{z_0}^{z_{exit}} B_y \, dz \sim 2 \cdot 10^3 \, (mTesla \cdot mm) \approx \mathbf{140\ mT \cdot 14\ mm}$$

A magnetic field of the order of 140 mT produced by permanent magnets seems to be feasible, so, different magnetic layouts for obtaining this value have been analyzed.

2.2.2. Possible layout

A first possible layout for the aiming at GG is an array of horizontal magnets magnetized in vertical direction with same orientation as the required magnetic field, as shown in Fig. 35.

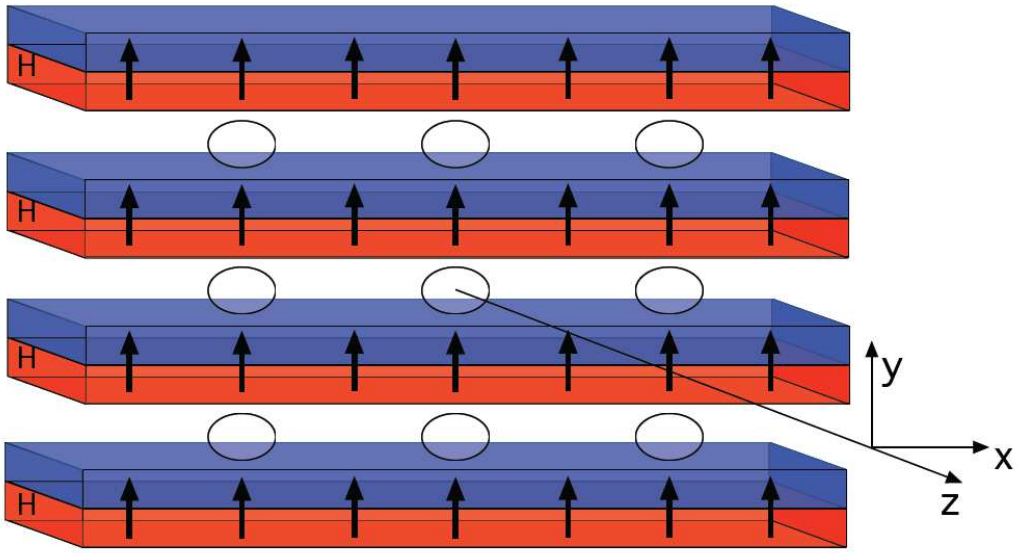

Fig. 35 First layout: horizontal magnet array.

The initial size of the magnet has been chosen as: 12x4x120 mm, with Bresidual = 1.1 T
Another possible layout is an array of vertical magnets with vertical magnetization but opposite orientation to the required magnetic field, see Fig. 36.

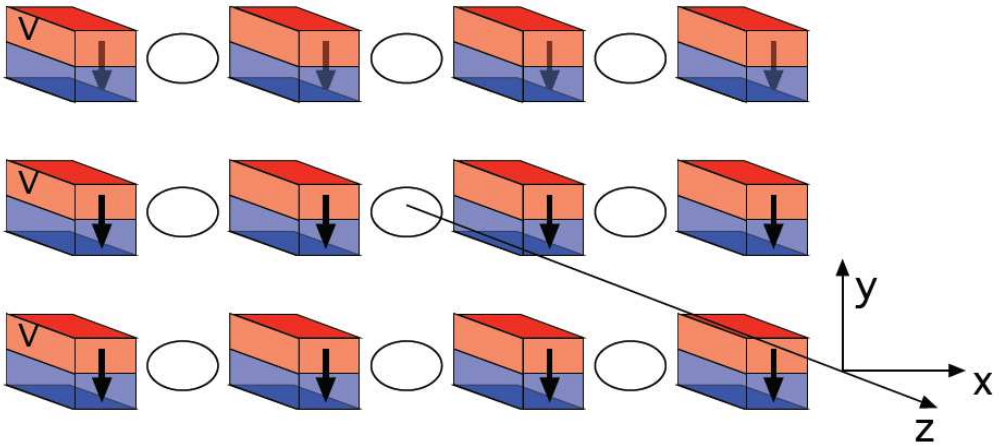

Fig. 36 Second layout: vertical magnet array.

Magnets' size is in this case: 12x4x18 mm, with the same Bresidual = 1.1 T
The magnetic field profile has been calculated along the central aperture and the result is shown in Fig. 37:

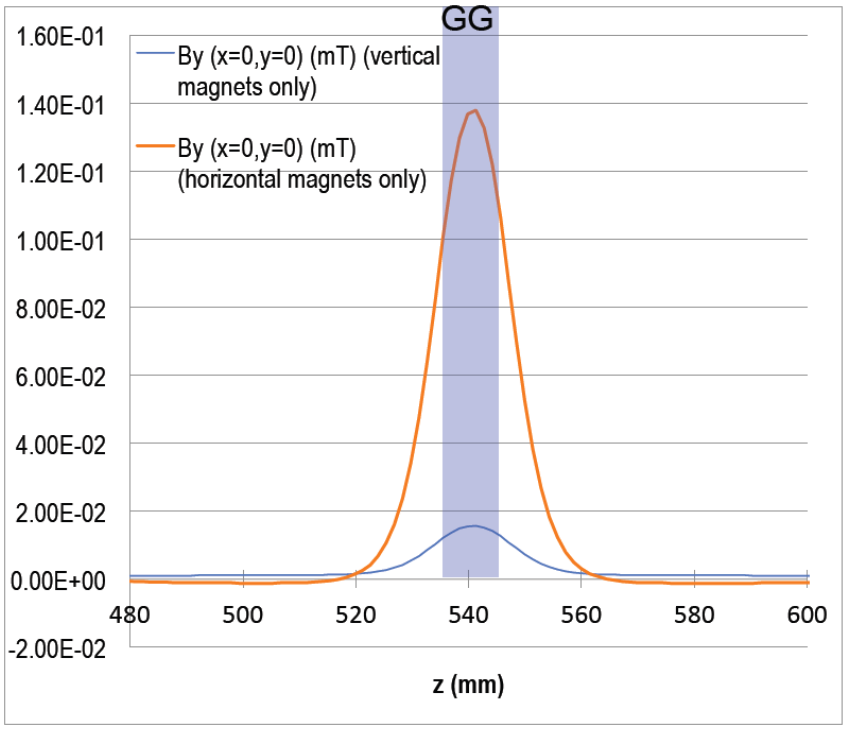

Fig. 37 Magnetic field profile along the central aperture for the two possible layout.

It can be noticed that:

- the horizontal magnet array has a large strength of By (140 mT), but stray field (some mT) having opposite orientation upstream and downstream;
- the vertical magnet array has a weak By field, but having same orientation both inside and outside the GG.

For these reasons, hereafter a combined and improved layout has been considered, having both the horizontal and the vertical magnet arrays. The new layout is shown in Fig. 38. And the resulting magnetic field profile compared to the one produced by the horizontal array only is shown in Fig. 39.

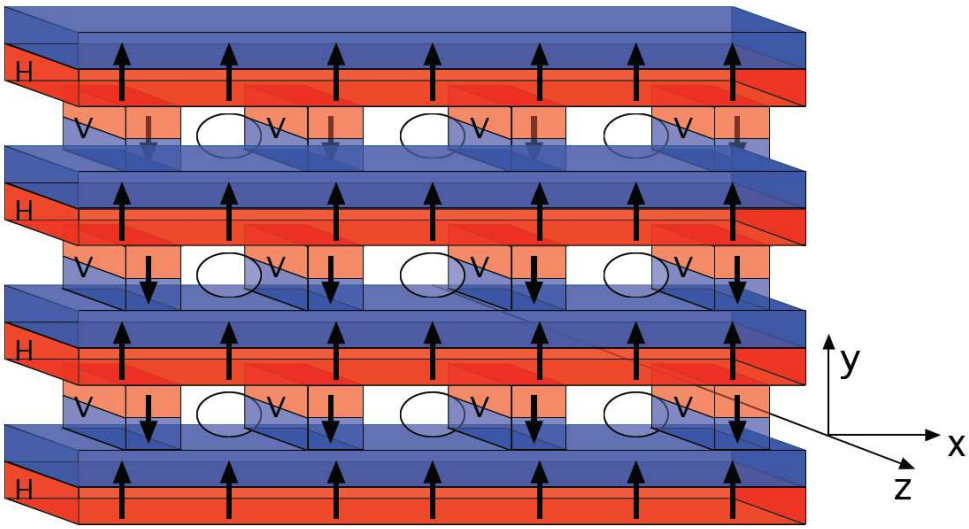

Fig. 38 Combined layout: horizontal and vertical magnet arrays.

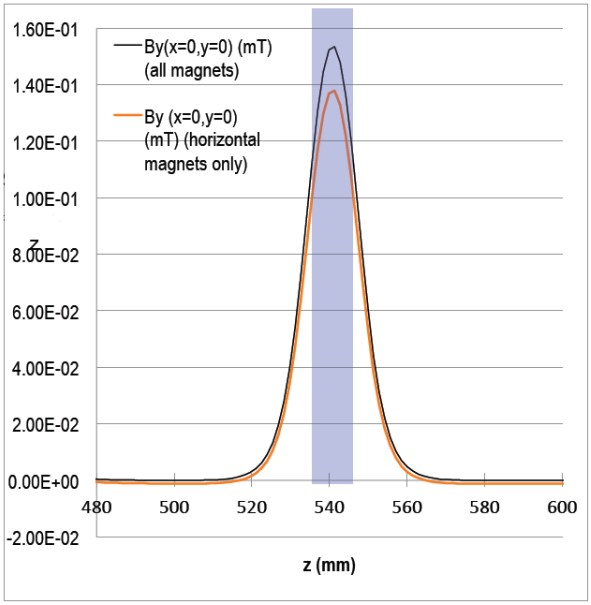

Fig. 39 Magnetic field profile along the central aperture for the combined layout and the horizontal magnet array only.

It can be noticed that the combination of horizontal and vertical magnets further increases By peak and compensates stray field upstream and downstream. Hereafter the GG magnets are called Grounded Grid Steering Magnets (GGSM).

2.2.3. Preliminary evaluation of Grounded Grid Steering Magnets on a single beamlet group

A preliminary evaluation of the chosen magnetic configuration has been performed considering only one beamlet group (5x16 apertures). The geometry is shown in Fig. 40.

The size of the magnets is the following:

- horizontal magnets: 12x4 x120 mm (with vertical magnetization);
- vertical magnets: 12x4x18 mm (with vertical magnetization and opposite direction).

Of course, depending on the beamlet group considered, orientation and strength are to be changed accordingly (left/ right, inner/outer). The magnetic field profile along all the accelerator for this configuration, compared to the one produced by only horizontal magnets is shown in Fig. 41.

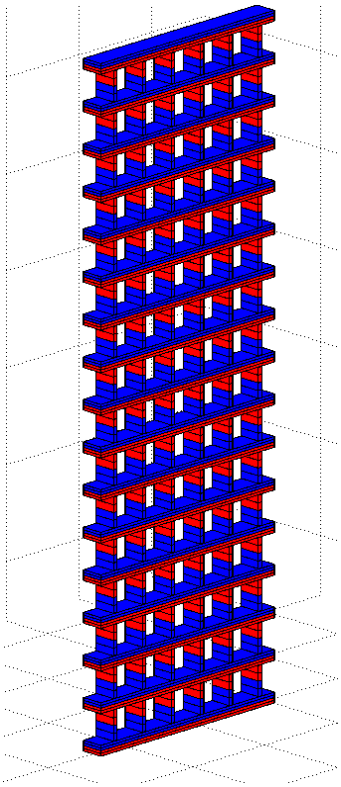

Fig. 40 Grounded Grid Steering Magnets in a beamlet group.

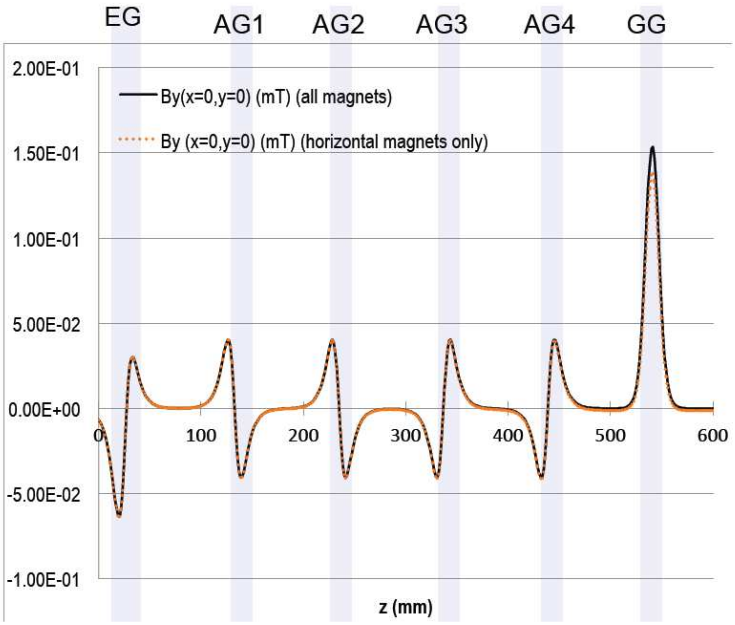

Fig. 41 Magnetic field profile along all the accelerator for the combined layout and the horizontal magnet array only.

Apparently, it seems that the difference is negligible, but if looking at the beamlet deflection profile, Fig. 42, it can be noticed that the effect of the stray field is appreciable and its effect continues also after the accelerator exit.

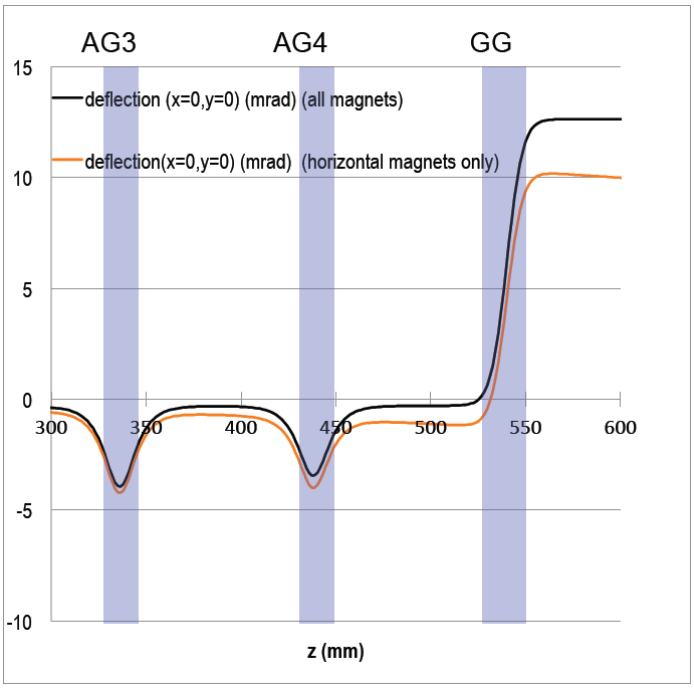

Fig. 42 Deflection profile for the combined layout and the horizontal magnet array only.

When both vertical and horizontal magnets are used, deflection is ~13 mT (better than required). Moreover, as it has already said, using horizontal magnets only, deflection is progressively reversed just upstream and downstream of the GG.

Fig. 43 and Fig. 44 show the magnetic field and the deflection profile including the case of a beamlet of the left side of the GG. In this case, the last field peak is reversed and

consequently the deflection is reversed too, but the last part of the two profiles is symmetrical.

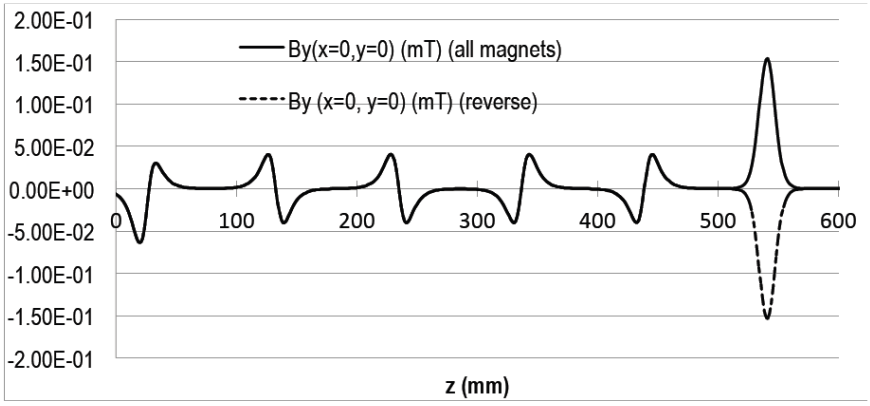

Fig. 43 Magnetic field profile along the accelerator for a left-side and a right-side beamlet.

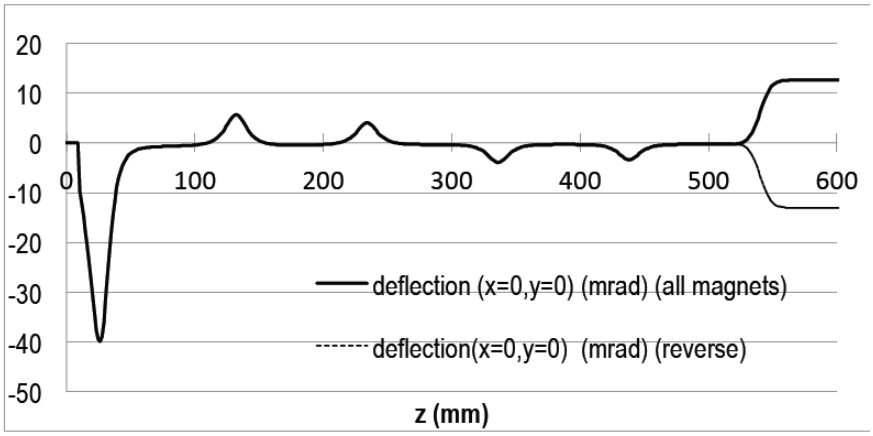

Fig. 44 Deflection profile along the accelerator for a left-side and a right-side beamlet.

The uniformity within an aperture has been evaluated considering 2 additional paths shifted by 4 mm horizontally or by 4 mm vertically. The resulting field profile is shown in Fig. 45, while the resulting deflection is shown in Fig. 46. It can be seen that the deflection uniformity is good (difference is less than 0.6 mrad).

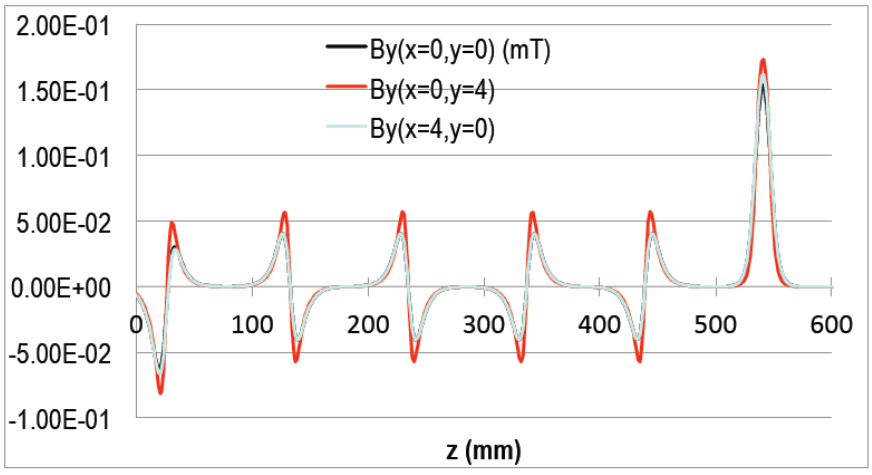

Fig. 45 Field uniformity within an aperture.

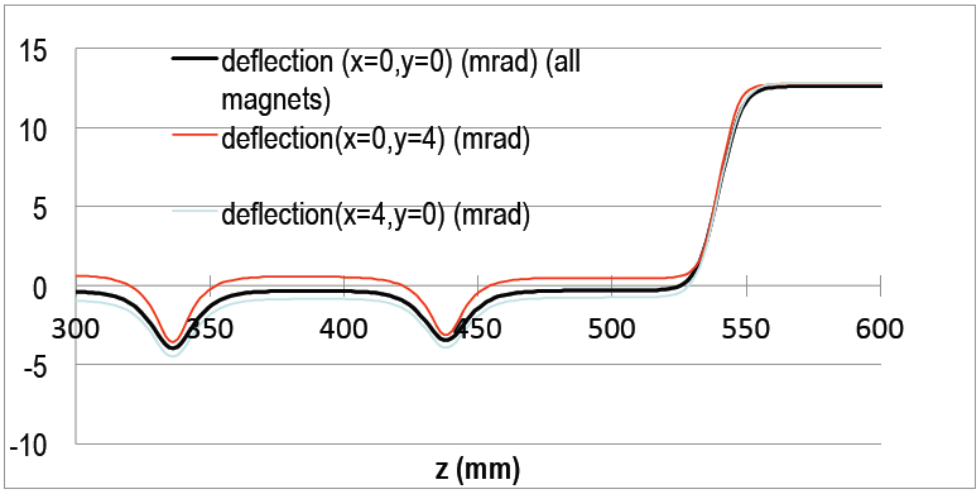

Fig. 46 Deflection uniformity within an aperture.

The size of vertical GGSM here considered is 12x4x18 mm but since the horizontal aperture pitch is 20 mm and the diameter of GG apertures is 16 mm, there is no space for a 4 mm thick magnet. Hereafter vertical GGSM 12x2.5x18 mm will be considered. This fact is expected to decrease the deflection, but hopefully still remaining above 10 mrad.

Moreover, since the GG thickness is 17 mm and can accommodate magnet with maximum thickness of 6.4 mm, it should be brought to 23-24 mm in order to accommodate GGSM with thickness of 12 mm along the beam direction. GG cross-sections are shown in Fig. 47 and Fig. 48.

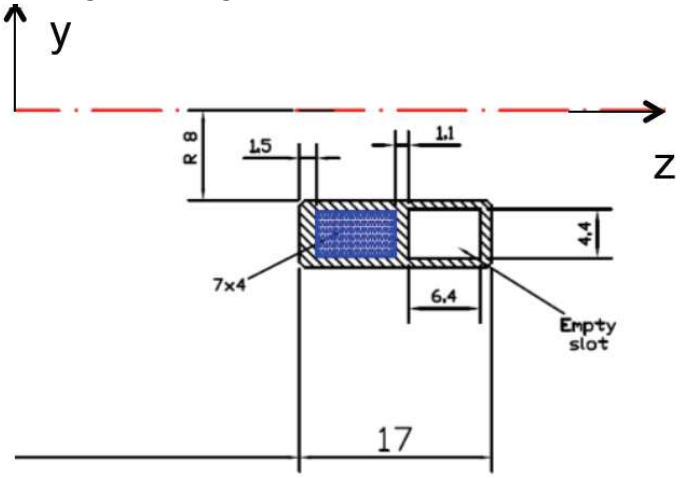

Fig. 47 Grounded Grid horizontal cross-section.

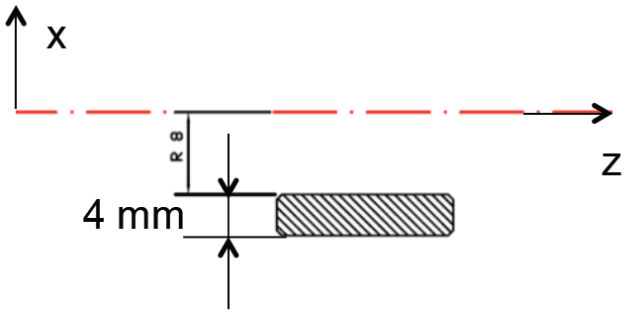

Fig. 48 Grounded Grid vertical cross-section.

2.2.4. Preliminary model of a complete Grounded Grid

A preliminary model of a complete GG has been realized in order to investigate the global uniformity within all the beamlet groups, see Fig. 49. The magnets' size considered is: 12x4x120mm + 12x2.5x18mm (for all groups).

The magnetic field has been evaluated along 21 different apertures distributed within the beamlet groups and thicker near the edges, as can be seen in Fig. 49 and Fig. 50.

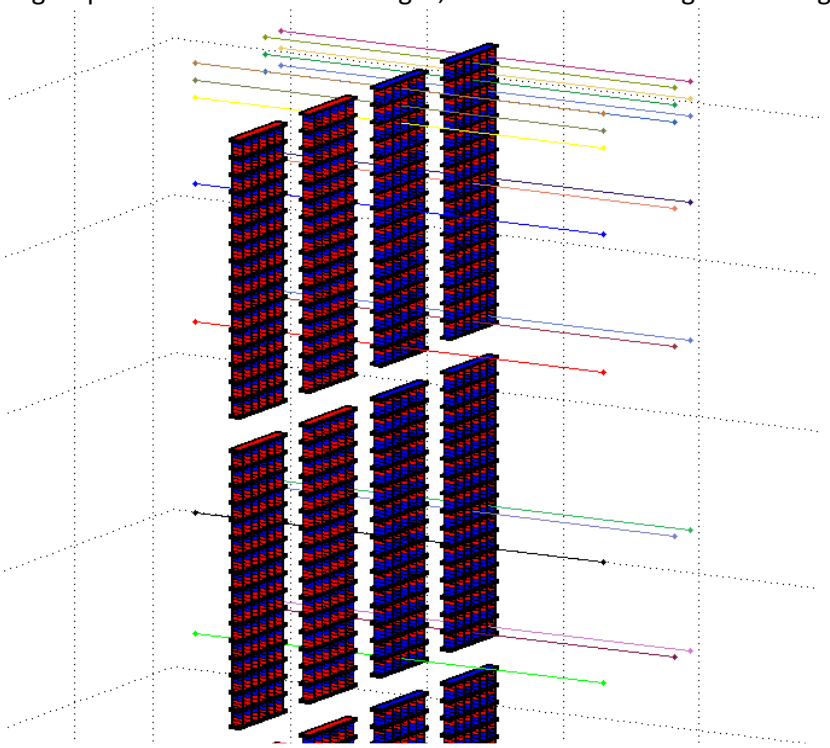

Fig. 49 Model of a complete Grounded Grid.

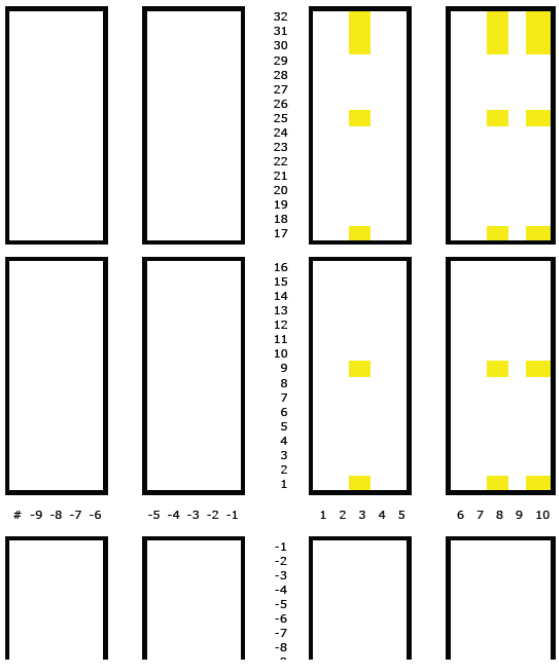

Fig. 50 Aperture considered for the deflection uniformity evaluation.

The results are shown in Fig. 51 and Fig. 52. The maximum deflection is 12.1 mrad in the centre and the minimum is 10.3 mrad, in the upper edge apertures. The difference is less than 2 mrad, so the uniformity is acceptable, although not being optimal.

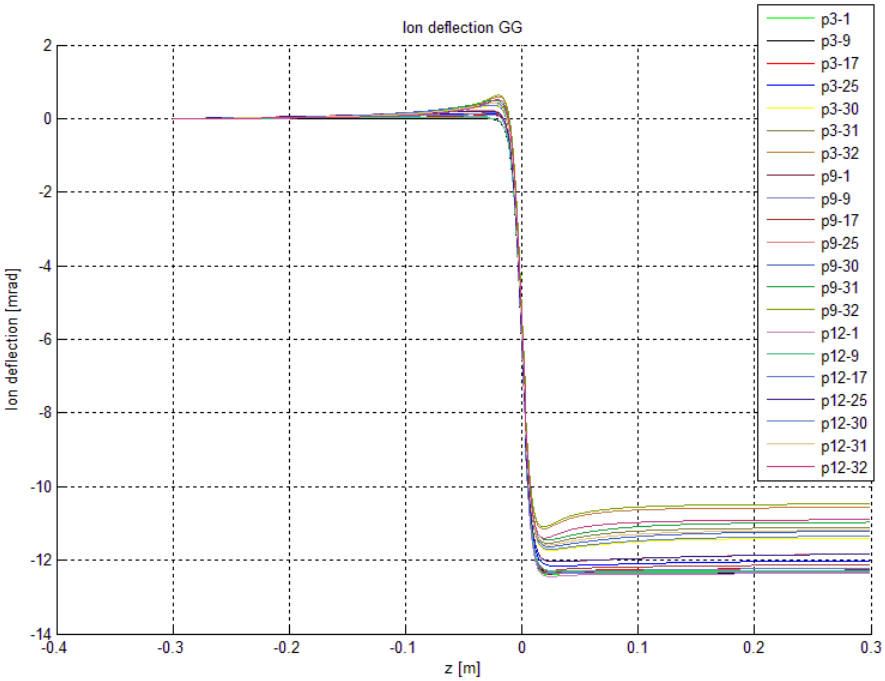

Fig. 51 Deflection uniformity within all the beamlet groups.

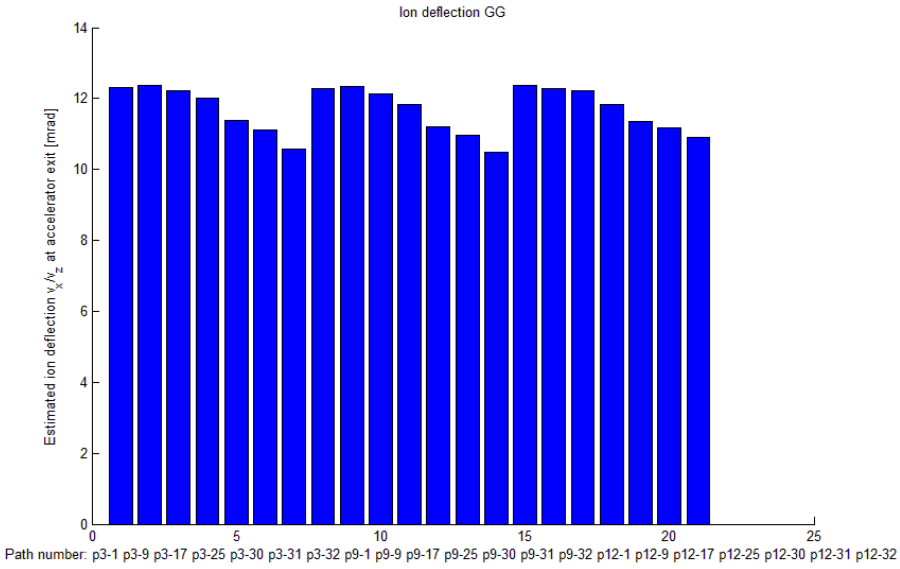

Fig. 52 Deflection uniformity within all the beamlet groups (bar diagram).

If necessary, uniformity could be improved by magnet "grading" and aiming at grid exit (within a beamlet group) might be obtained by the same way.

2.2.5. Alternative layout using ferromagnetic yokes

An alternative layout for avoiding the double array of magnets (that can have some difficulties in the assembling) has been qualitatively evaluated in a simplified model.

In this solution ferromagnetic yokes are present in order to avoid the stray field that can decrease the deflection and have unwanted interactions with other components.
A small model (5x3x2=60 apertures) has been realized with ANSYS for preliminary evaluation and it is shown in Fig. 53. The size of horizontal magnets is 12x4x120 mm and the size of iron yokes is 12x10 mm.

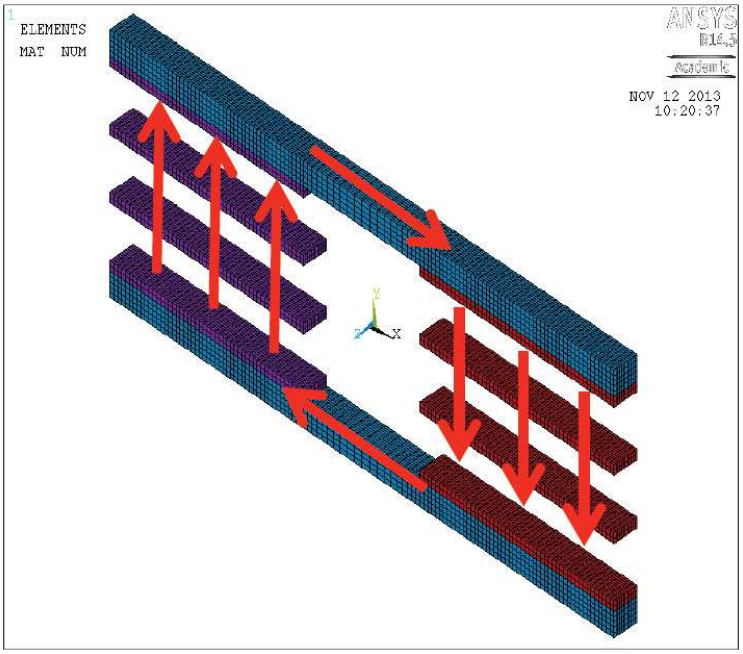

Fig. 53 Alternative layout using ferromagnetic yokes.

The resulting magnetic field profile is shown in Fig. 54 and confirms what expected: the preferential closure path for the magnetic flux produced by opposite beamlet groups leads to a decreasing of stray field and avoids the field reversal upstream and downstream of the GG.

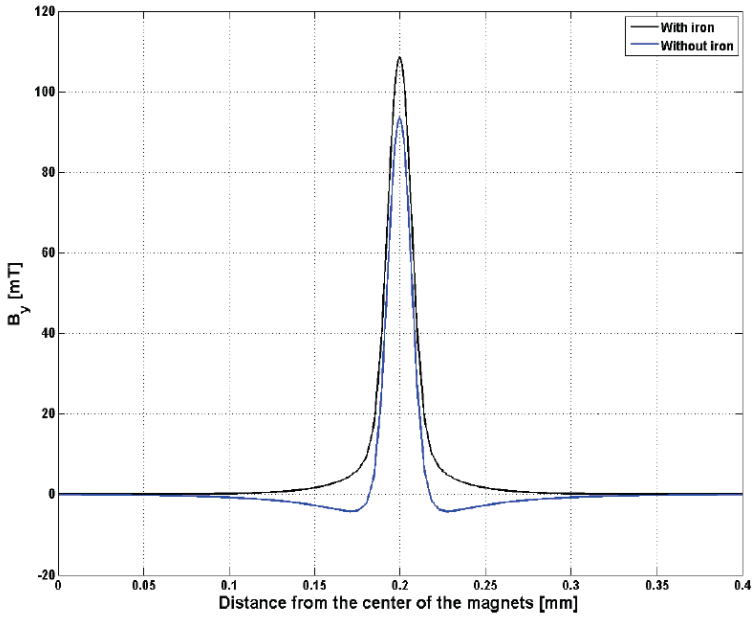

Fig. 54 Magnetic field profile for layouts with and without ferromagnetic yokes.

The absence of field reversal leads to much more effective magnetic deflection as it can be seen in Fig. 55.

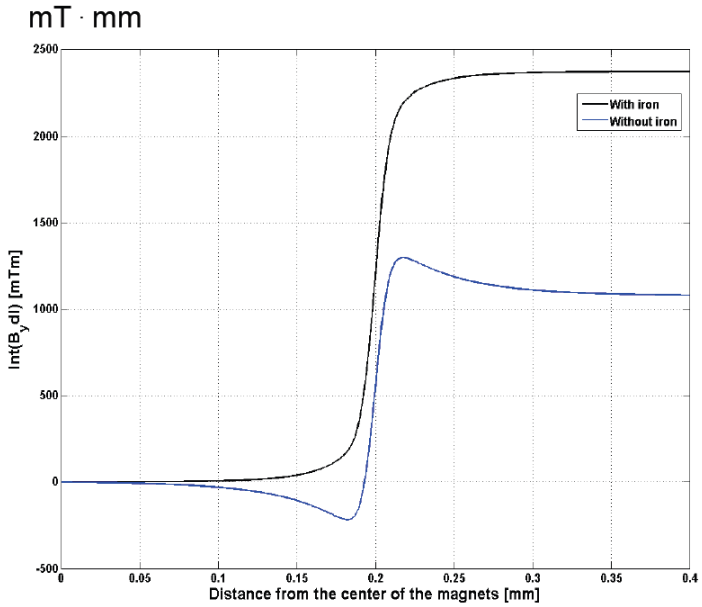

Fig. 55 Deflections profile for layouts with and without ferromagnetic yokes.

Anyway, the deflection uniformity for this configuration has to be evaluated by complete detailed model.

2.2.6. Conclusions

Magnetic aiming at 25.4 m on the GG can be considered a possible backup solution for risk reduction.

Required deflection (~10 mrad) can be obtained by introducing Grounded Grid Steering Magnets (GGSM) and a few modifications of the GG.

Magnet size and deflection uniformity is acceptable only if both vertical and horizontal GGSM are used.

Simpler configuration (no vertical magnets) might be possible using ferromagnetic yokes but uniformity shall be verified by detailed model. Moreover, deflection depends on 1/sqrt(voltage) and does not require replacement of the grids for adjustment. On the other hand, neutrals produced by stripping during acceleration are lost.

2.3. Update of the design of Transverse Magnetic Field Coils (TMFC) for MITICA accelerator

2.3.1. Introduction

As mentioned in Par. 1.8.1. , in MITICA accelerator, a current flowing through the Plasma Grid and a related system of conductors is necessary for generating both the electron suppression long-range magnetic field in the accelerator region, and the filter field in the ion source region, see also [11].

The strength of these two fields had been decided on the basis of the experimental results obtained at IPP on smaller RF-driven negative ion sources, see [33]. However, if a change of the magnetic field configuration is required, in order not to open the vacuum vessel for modifying the bus-bars each time, it seems highly advisable to provide a flexible control of the magnetic field by using a pair of specific coils, called Transverse Magnetic Field Coils (TMFC), located outside the MITICA Beam Source Vessel.

For this reason, in 2013 preliminary design of a pair of TMFC was carried out, see [29].

However, in 2014, after the experimental results obtained at BATMAN, RADI and ELISE sources at IPP, the PG busbars layout for MITICA has been modified [31] in order to accomplish the additional requirement of Bx < 2 mT in the RF driver region (it was observed at IPP that a higher leakage field can compromise the correct operation of the RF drivers). Moreover, the optimal filter field for negative ion extraction was found to be slightly lower than what expected previously. New filter field values are ≈ 2.2 mT for hydrogen and 2.8 - 3.4 mT for deuterium, and this lead to a different nominal PG current, with consequences also in the long-range field strength.

For these reasons, a new design of TMFC was necessary, starting from the previous results of [29]. In this new design, the Simulated Annealing optimization algorithm, already applied with success to the PG busbars optimization, has been used in order to have a better global optimization of the TMFC parameters in a fast and automatic process.

A new thermal analysis was not carried out, since the new optimized geometry has a similar behaviour of the previous geometry described and already verified in [29].

2.3.2. New PG busbar layout PG_24

As mentioned, during 2014, the reference PG busbar layout has changed from the PG_18 to PG_24, for accomplishing new design requirements. The old and new configurations are shown in Fig. 56 and Fig. 57.

In the PG_18 there is only one electric circuit that makes two loops with a nominal flowing current of 4180 A.

In the PG_24 there are two circuits, whose total nominal current is 4200 A, but subdivided into the two as follow: 3500 A in the PG circuit, with red arrows in Fig. 57 and 700 A in the "close conductors" circuit, marked with blue arrows.

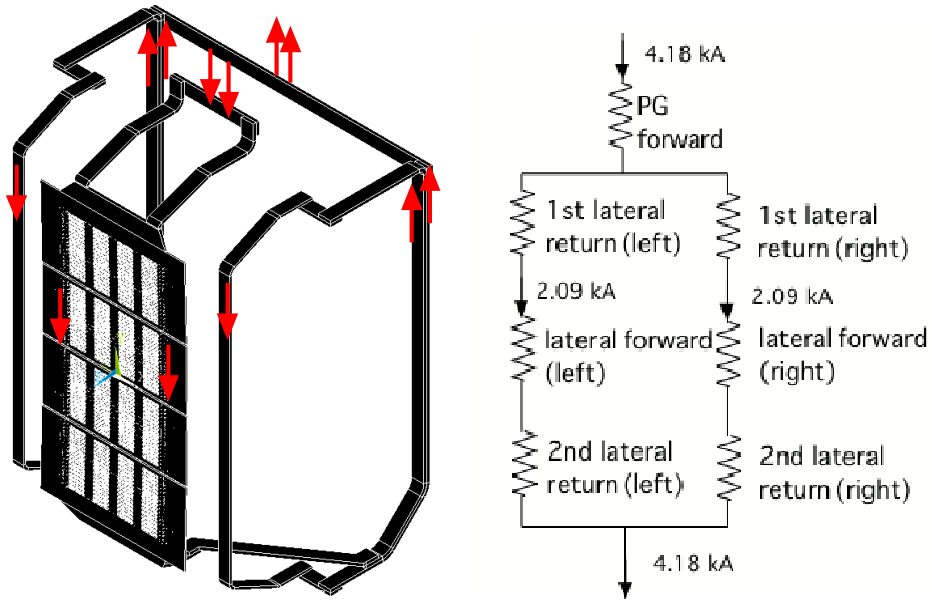

Fig. 56 Layout and electrical scheme of the old PG busbar reference configuration PG_18.

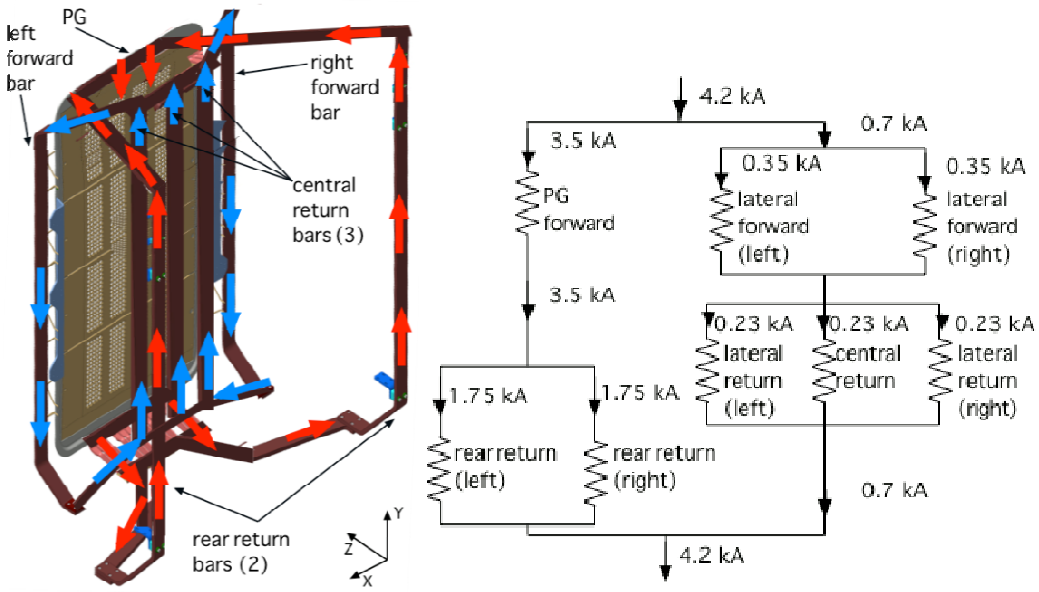

Fig. 57 Layout and electrical scheme of the new PG busbar reference configuration PG_24.

2.3.3. Recall of TMFC design parameters and constraints

Seven parameters are necessary to completely define the geometry of TMFC: coil position along *x*- and *z*-axis (X_{CG} and Z_{CG}), coil size along *y*- and *z*-axis (height and width, indicated with *h* and *w)*, coil length along *x*-axis (length, *l*), coil thickness (*t*) and coil current (I). Coil parameters are illustrated in Fig. 58:

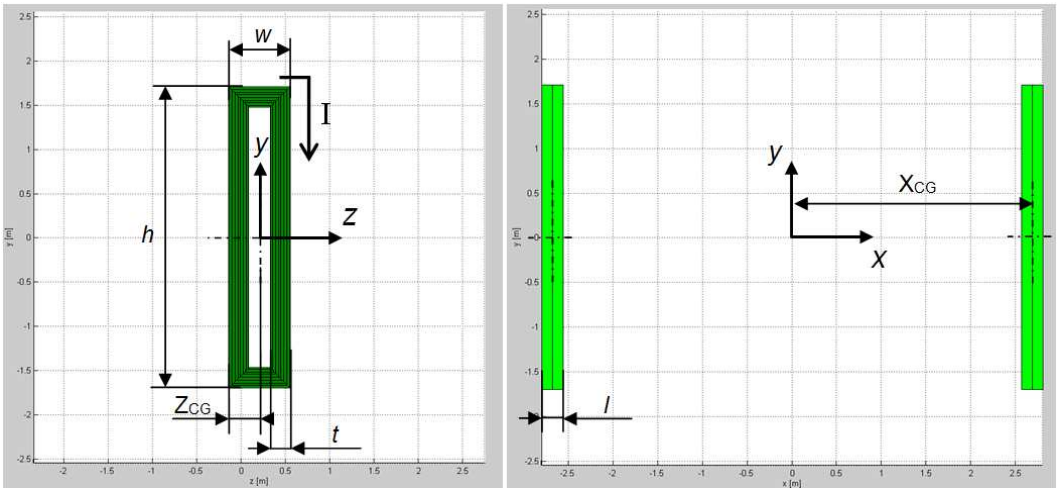

Fig. 58 TMFC design parameters.

Each of the TMFC is geometrically symmetric (up and down symmetry) with respect to the accelerator horizontal midplane (y = 0) and the centres of the two coils are symmetrically located (left and right symmetry) with respect to the accelerator vertical midplane (x = 0).
Fig. 59 represents the NBImag model of all the MITICA magnetic systems, including the TMFC.

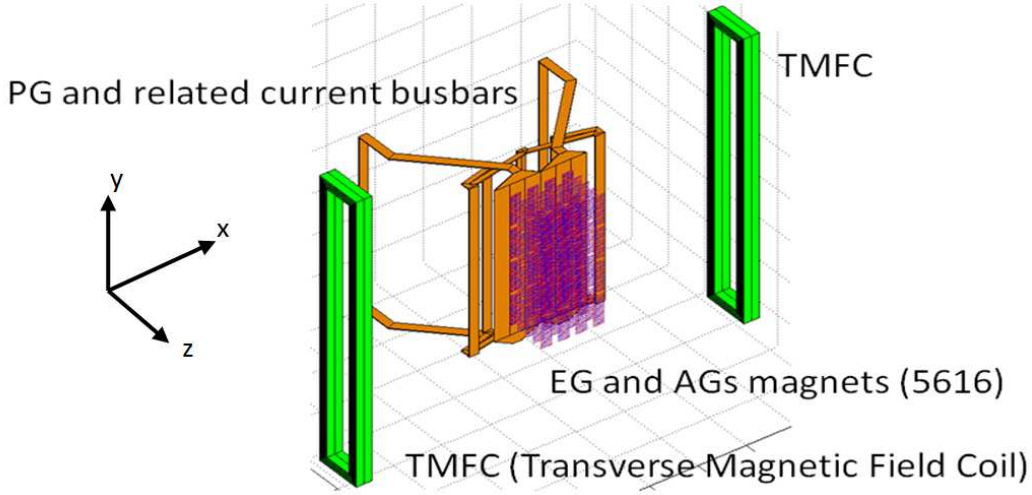

Fig. 59 NBImag model of TMFC, PG busbar system and permanent magnets embedded in the grids.

Coil size along *y*-axis (height) and coil length along *x*-axis were decided in [29] to be respectively 3400 mm and 240 mm. In particular, the coil height (3400 mm) is limited by the beam source vessel. These values are reasonable for guaranteeing an adequate field uniformity along y and an adequate coil cross-section from the thermal point of view.
Once the coil length is fixed to 240 mm, the coil position along x is given by geometrical constraints. The MITICA source vessel is in fact 4960 mm large, and some centimetres must be left for the mechanical connections and holding elements. So, x-position of coil centre of gravity has been chosen to be

$$x = \frac{(4960 + 200 + 240)\ mm}{2} = 2700\ mm$$

For as regards the coil thickness and flowing current, from Chapter 5 of [29], these two parameters appear to be fundamental from the thermal point of view. Of the four optimized solutions of [29] in fact, only one was accepted after the thermal verification

carried out with ANSYS under the thermal conditions of MITICA operation (1 hour long operation, then 3 hours stop, for three cycles).
The acceptable optimized solution of [29] had a coil thickness of 220 mm and current of 30000 A. Given the very small temperature margin (≈ 10 °C) found in the thermal simulations described in [29], these two values have been chosen as lower limit for coil thickness and upper limit for coil current in the new optimization. In this way, a new thermal analysis is not required.
Upper limit for coil thickness has been chosen to be 245 mm, and this gives in turn the lower limit for coil size along z (coil width, two times coil thickness plus some centimetres), chosen to be 500 mm.
The remaining free design parameters are: lower limit of current, upper limit of coil width, and coil position along z. These parameters have been allowed to vary in a broad range, as shown in Tab. 3.

Parameter	Interval
position along x [mm]	2700
position along y [mm]	0
position along z [mm]	(- 300 , 600)
size along x (coil length) [mm]	240
size along y (coil height) [mm]	3400
size along z (coil width) [mm]	(500 , 750)
thickness [mm]	(220 , 245)
current [A turn]	(20000 , 30000)

Tab. 3 Summary of TMFC parameters for the optimization (the reference frame is in the centre of Plasma Grid).

2.3.4. Description of the optimization algorithm

In order to explore all the domain of TMFC parameters, an optimization algorithm based on Simulated Annealing, described in [30], has been used. This algorithm has been already used in [19], for design of PG busbar system.
The algorithm has been adapted for a four-variable optimization (see Tab. 3) and, like in previous cases, it has been coupled with the 3D magnetic code NBImag.
The number of iterations of the algorithm can be adjusted so as to perform a full exploration of the parameter domain, which allows approaching the global minimum (but requires quite a large computation time) or performing a faster exploration which is anyway able to reach an acceptable minimum.
To have an idea, by exploring 1000 different configurations (1000 NBImag runs) an acceptable optimized solutions was found in only 2min total run time. If the number of explored configurations is increased to 30000, an improvement of less than 1% of the performances is obtained at the expense of increasing 30 times the computational burden.
As already discussed in [29], due to the limitation of PG power supply (5000 A maximum), a PG current up to 120% of its nominal value has been considered. Matching the PG current values with appropriate values of TMFC current, it is possible to modify the magnetic field in the accelerator while maintaining it constant in the source, or vice-versa. This is the basic TMFC operational principle and it is shown in Fig. 60.

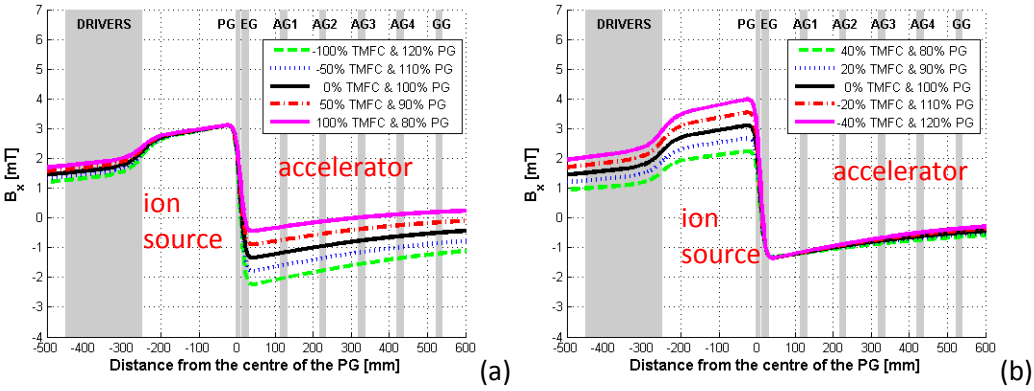

Fig. 60 Independent control of Bx profile by use of TMFC, exploiting different values of PG current and TMFC current. Case (a), B_{SOURCE} kept constant and B_{ACCEL} regulated, case (b) B_{ACCEL} kept constant and B_{SOURCE} regulated.

In order to explore the solutions with constant filter field in the ion source and variable field in the accelerator, the optimization algorithm was defined so as to minimize the variation range of Bx in the ion source (ΔB_{source}) and to maximize the variation range of Bx in the accelerator (ΔB_{ACCEL}) in case (a). On the other hand, case (b) corresponds to a maximum variation range of Bx in the ion source (ΔB_{SOURCE}) and minimum variation range of Bx in the accelerator (ΔB_{ACCEL}).

After few attempts, it was realized that once one variation range ΔB is fixed, the other three variation ranges ΔB cannot be set arbitrarily. For this reason, the only condition for minimizing ΔB_{source} in case (a) has been included in the algorithm objective function. The other conditions have been disregarded.

For this reason, the condition $B_{DRIVER} > 2mT$ is not compatible with this approach and in fact it does not allow to reach useful solutions. Therefore it has been implemented only as a supplementary condition to be considered a-posteriori.

A typical trend for the minimization of the objective function is given in the next figure:

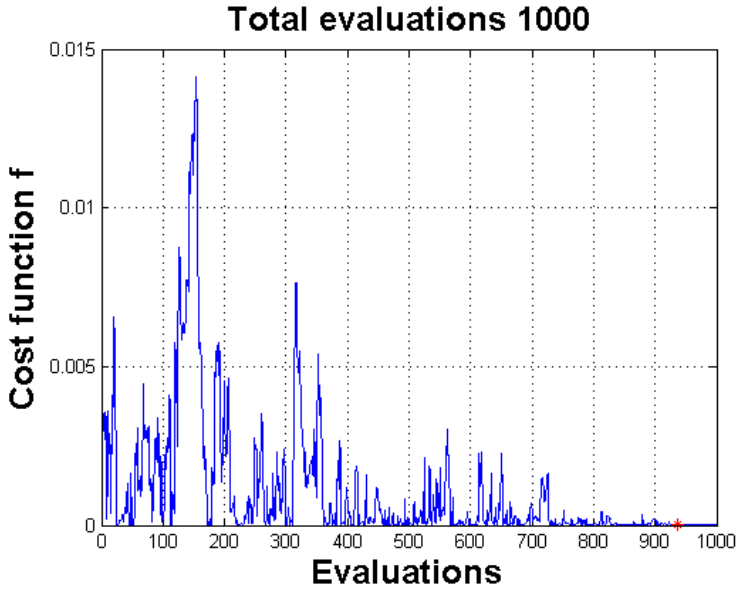

Fig. 61 Typical trend for the minimization of the objective function. 1000 different evaluations have been used in this example.

2.3.5. TMFC optimization results

Before running the optimization algorithm, the design solution obtained in [29] has been checked. The main parameters of this solution are recalled in the next table:

Parameter	Value
current [A turn]	30000
position along z [mm]	200
size along z (coil width) [mm]	625
thickness [mm]	220
size along y (coil height) [mm]	3400
size along x (coil length) [mm]	240

Tab. 4 Optimized TMFC parameters found in TN-239.

The Bx profiles obtained with this TMFC geometry are shown in Fig. 60, in previous section. It can be noticed that, despite the reference Bx profile (black line) is changed from PG_18 to PG_24, the TMFC geometry found in [29] is still acceptable.
A first run of the optimization algorithm (with 1000 iterations) has been made with the parameter domain of Tab. 3. The results are shown in Tab. 5:

Parameter	Value
current [A turn]	24923
position along z [mm]	288
size along z (coil width) [mm]	749
thickness [mm]	228
size along y (coil height) [mm]	3400
size along x (coil length) [mm]	240

Tab. 5 Optimized TMFC parameters obtained after a first run of the optimization algorithm.

The associated Bx profiles are shown in Fig. 62:

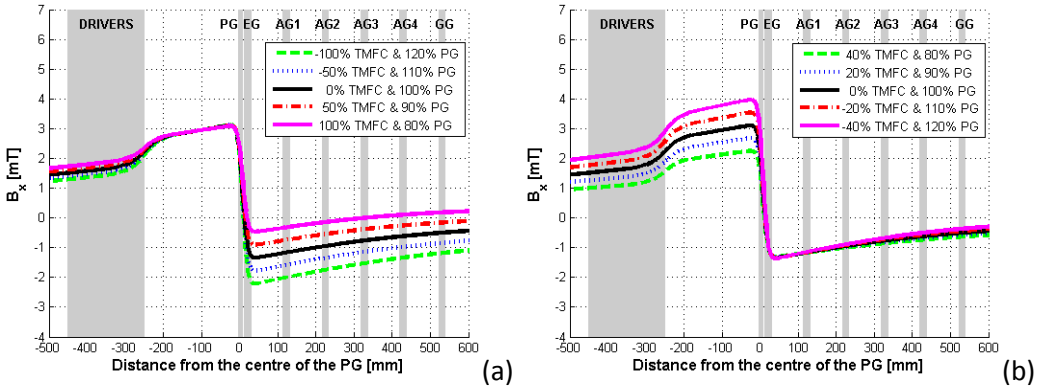

Fig. 62 Bx profiles of the solution obtained with the first run of the optimization algorithm.

The profiles of Fig. 60 and Fig. 62 are very similar, except that Fig. 62 has been obtained with a much lower TMFC current (~ 25000 A instead of 30000 A).
Following the perception that a solution with even lower TMFC current is possible, a second optimization has been carried out with upper limit for TMFC current of 22000 Aturn. The results are shown in Tab. 6 and Fig. 63:

Parameter	Value
current [A turn]	21172
position along z [mm]	-202
size along z (coil width) [mm]	750
thickness [mm]	225
size along y (coil height) [mm]	3400
size along x (coil length) [mm]	240

Tab. 6 Optimized TMFC parameters obtained after a run of the optimization algorithm with upper limit for TMFC current of 22000 A.

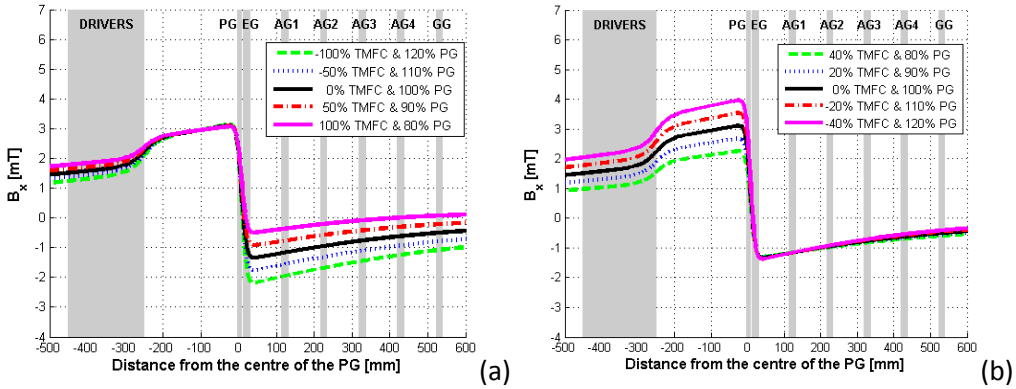

Fig. 63 Bx profiles obtained after a run of the optimization algorithm with upper limit for TMFC current of 22000 A.

Three things can be noticed:

- a solution with TMFC current lower than 22000 Aturn is possible;
- TMFC in this case are positioned much more upstream (z = − 202 mm instead of +288 mm);
- Bx profiles in the accelerator in case (a) are more convergent. In case (b) they are instead more uniform.

Although a solution with lower current in principle is preferable, the smaller Bx variation range in the last acceleration gaps in Fig. 63a, is not desirable. In fact, as shown in Par. 2.3.9. , a reduction of Bx in the last grid gaps corresponds to an increased heat load on the most loaded grid and of the transmitted electrons at exit.
Additional runs of the optimization algorithm with different parameter range confirmed that the solutions with lower current always correspond to a coil position between z = -100 mm and z = -300 mm, and to profiles similar to Fig. 63 (a) and (b).
Moreover, solutions obtained after a higher number of algorithm iterations (up to 30000) show no appreciable difference in terms of performances with the one obtained after 1000 iterations only.
For this reasons, the new reference design solution is chosen to be very close to the one of Tab. 5 and it is summarized in the table below:

Parameter	Value
current [A turn]	25000
position along z [mm]	300
size along z (coil width) [mm]	750
thickness [mm]	220
size along y (coil height) [mm]	3400
size along x (coil length) [mm]	240

Tab. 7 New reference TMFC parameters.

Bx profiles associated to this solution are not distinguishable from Fig. 62, but they are reported for completeness:

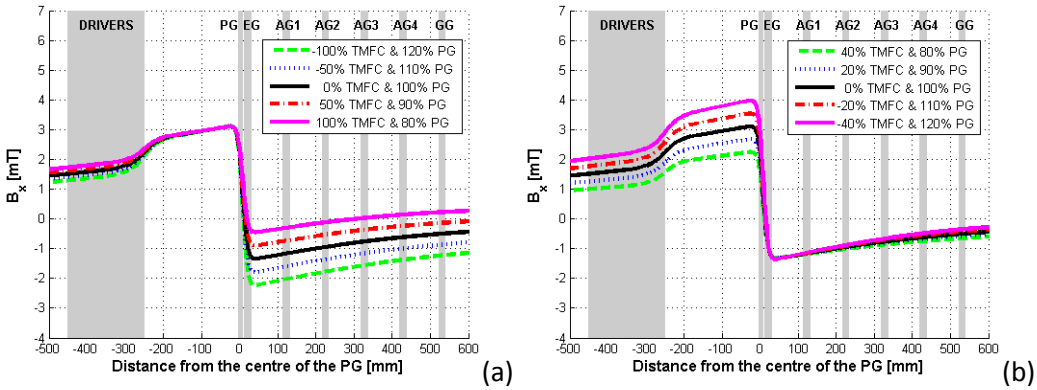

Fig. 64 Bx profiles associated to the new reference TMFC parameters.

2.3.6. Uniformity analysis

A uniformity analysis has been made in order to evaluate the edge effects that modify the Bx profile of the external apertures (especially the lateral ones, closer to the TMFC). Firstly, a uniformity evaluation of MITICA PG busbar system only (without TMFC) is here reported. Bx has been calculated along four different apertures, indicated in Fig. 65. The same picture shows also the result of the calculation:

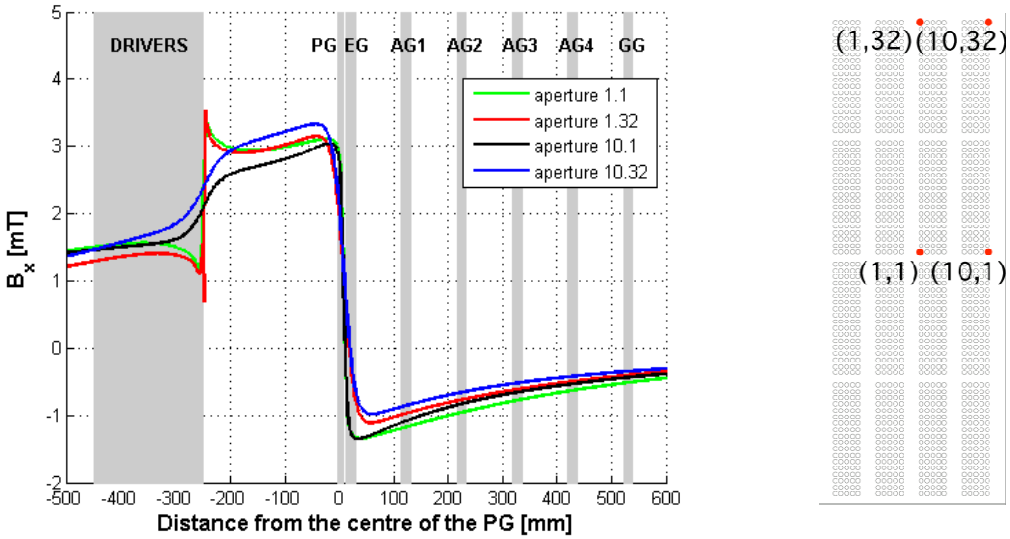

Fig. 65 Uniformity of Bx due to PG busbar system only.

Quantitatively, Bx uniformity inside the source is within 0.4 mT and inside the accelerator within 0.35 mT.

The Bx uniformity of TMFC only, without PG current, is shown in Fig. 66:

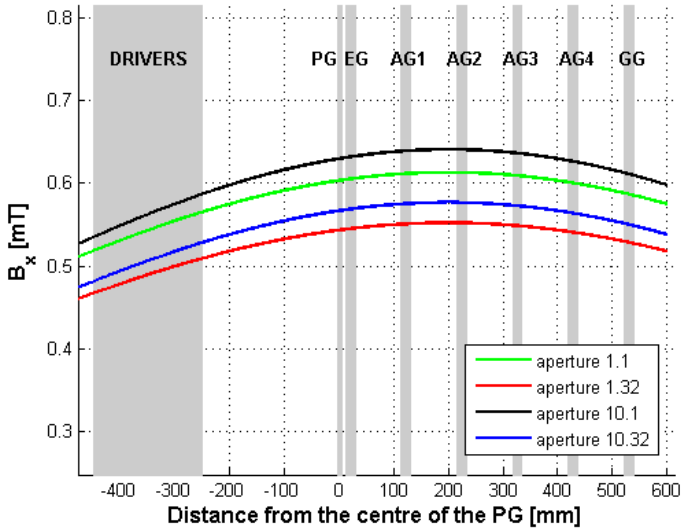

Fig. 66 Uniformity of Bx due to TMFC only.

In this case the uniformity is within 0.1 mT, so much better that the Bx uniformity of PG busbar system.
In the next two figures, Bx uniformity due to PG busbar system and TMFC together is shown:

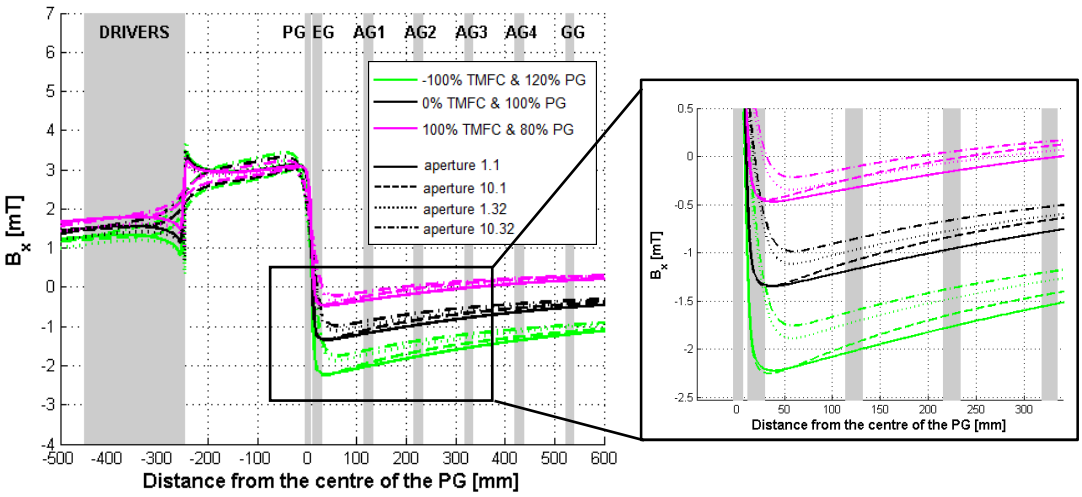

Fig. 67 Uniformity of Bx due to PG busbar system and TMFC, case (a).

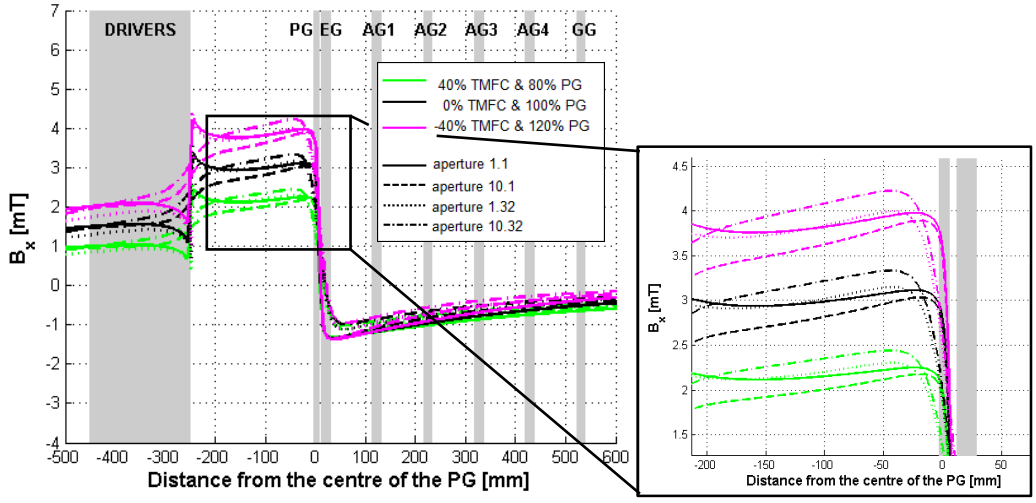

Fig. 68 Uniformity of Bx due to PG busbar system and TMFC, case (b).

It is interesting to note that the effects of PG current and TMFC add or compensate each other, depending on the operating conditions of TMFC.
If for example the TMFC are used to increase Bx inside the accelerator (green line of Fig. 67), Bx uniformity is worse (the two effects add each other). Vice-versa, if the TMFC are used to decrease Bx inside the accelerator (pink line of Fig. 67), TMFC current is reversed and Bx uniformity is better (the two effects compensate each other).
The same trend is true for the case (b). When the TMFC are used to increase Bx in the ion source, the uniformity is slightly worse, while when they are used to reduce Bx in the ion source then the uniformity is better.

2.3.7. Final TMFC Design solution

From now on, all the results and conclusions of Chapters 3, 4, 5 and 6 of [29] are valid. The design concept remains the same; Tab. 6 of [29] is here updated with new TMFC parameters:

current [A turn]	25000
position along z [mm]	300
size along z (coil width) [mm]	750
thickness [mm]	220
size along y (coil height) [mm]	3400
size along x (coil length) [mm]	240
N_x [turns]	12
N_z [turns]	11
N_{turns}	132
Current (2 coils in series) [A]	189.4
Cable length (1 coil) [m]	1095.6
Conductor cross-section [mm^2]	120
Coil resistance (1 coil, Tmax = 80°) [mOhm]	190
Copper weight (1 coil) [kg]	1174
Voltage (2 coils in series) [V]	72
Power (2 coils in series) [W]	13637
Estimated cost [k€]	56

Tab. 8 More detailed design parameters of the chosen TMFC design solution.

Market survey and cable selection made in [29] is still valid, as well as the choice of the water cooling system.

2.3.8. Thermal analysis

As mentioned in Par. 2.3.3. , a new thermal analysis is not required, having optimized the new solution already including the constraints found in the previous thermal analysis ([29], Par. 5). .

In fact, the old and new TMFC solutions have the same coil cross-section, but the new one has a current of 25 kAturn instead of 30 kAturn, so the new one is immediately accepted from the thermal point of view.

2.3.9. Power load scan of TMFC operating point

A series of EAMCC simulations has been made in order to investigate the consequences of the use of TMFC on power loads on the grids and on transmitted electrons.

Only the case (a), i.e. when the TMFC are used to vary Bx in the accelerator, has been considered. The five TMFC operating points simulated with EAMCC correspond to the five profiles of Fig. 64 (a).

Fig. 69 shows the calculated power loads on the grids for the five considered combinations of PG current and TMFC current. The third combination (PG 100% TMFC 0%) correspond to the reference heat loads, i.e. without TMFC.

Fig. 70 shows the highest heat load on a grid and the corresponding grid for each case.

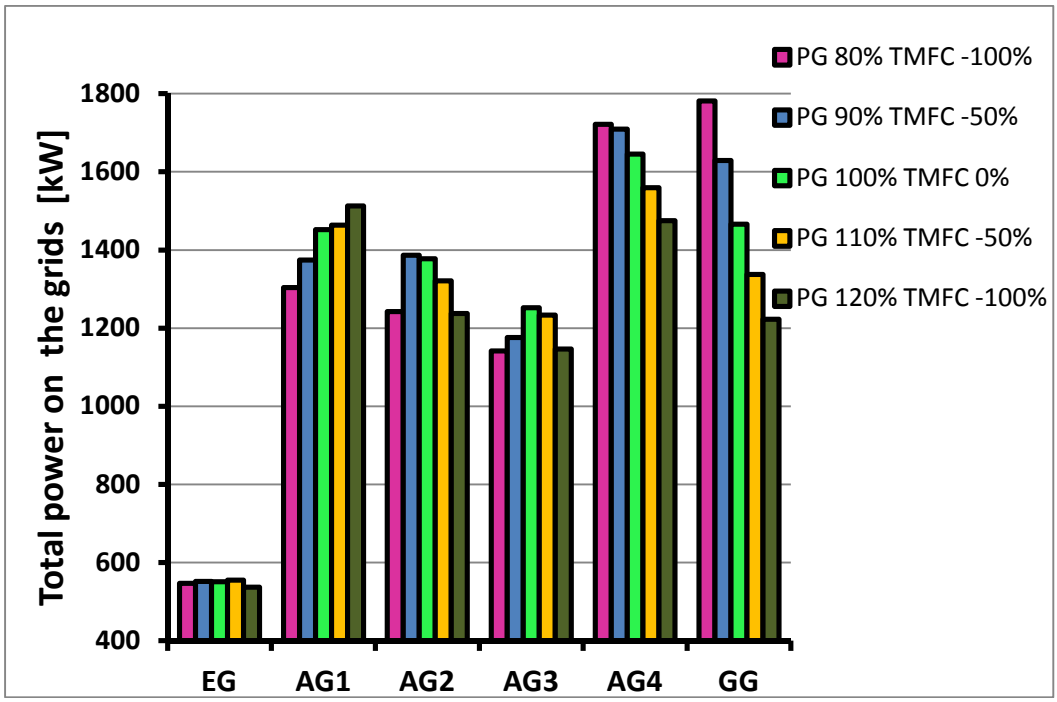

Fig. 69 Power on the grids for various PG current and TMFC current combinations.

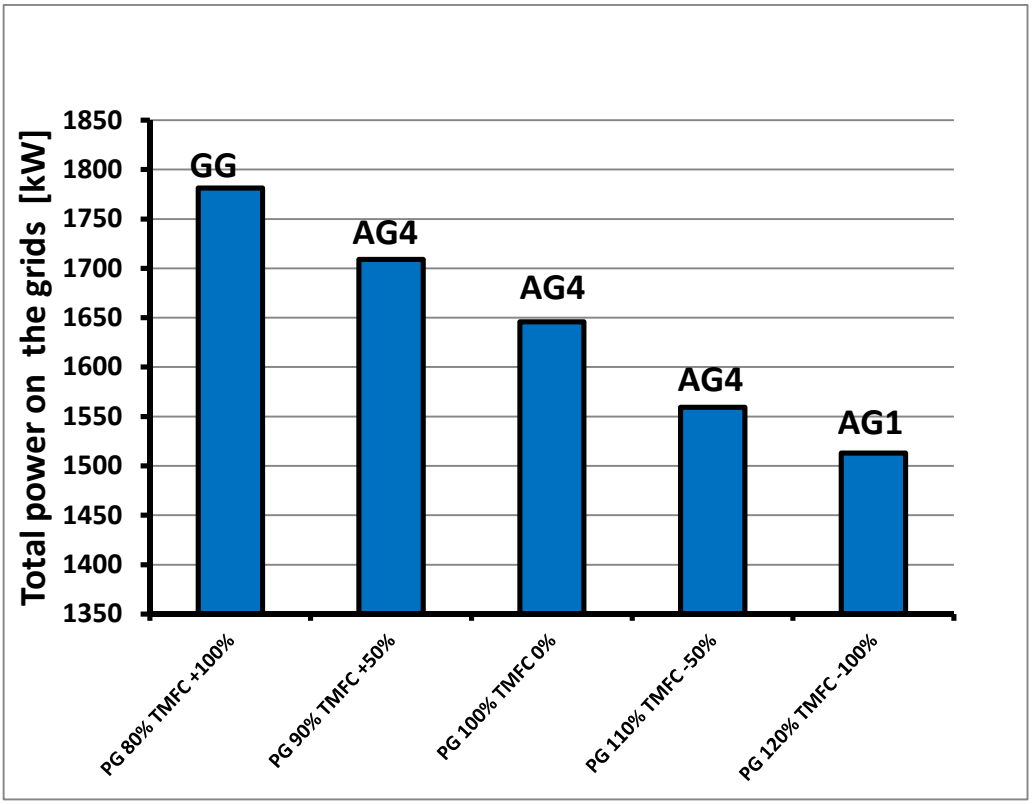

Fig. 70 Maximum heat load on a grid for various PG current and TMFC current combinations. For each case, the most loaded grid is indicated.

From these two pictures, the importance of Bx strength in the last two gaps (AG3-AG4 and AG4-GG) can be clearly understood. The power load on AG4 and GG decreases with the increase of magnetic field strength, so that the best configuration is the one with highest Bx in the accelerator.
The net reduction of maximum heat load on a grid from the reference case (no TMFC) to the best case with TMFC (PG120% TMFC -100%) is of 133 kW, corresponding to the 8% of the nominal heat load.
This combination allows also a considerable reduction of the total heat load on all the grids, as shown in the next Fig.:

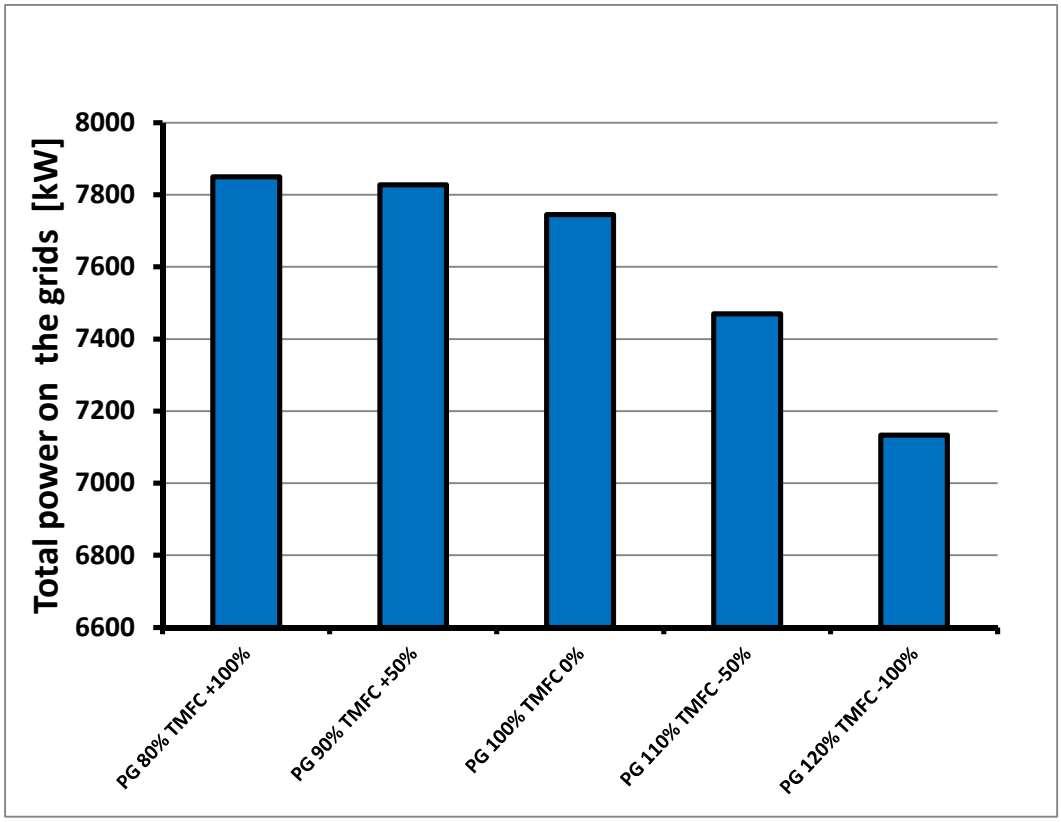

Fig. 71 Total power on all grids for various PG current and TMFC current combinations.

Finally, the calculated transmitted electrons are shown in Fig. 72. By using the TMFC it is possible to substantially reduce the amount of transmitted electrons, in fact, an higher field in the accelerator, and especially in the last gap, leads to a ~ 50% reduction of transmitted electrons, i.e. from 0.90 MW (nominal case, no TMFC) to 0.42 MW (120% PG current and -100% TMFC current).

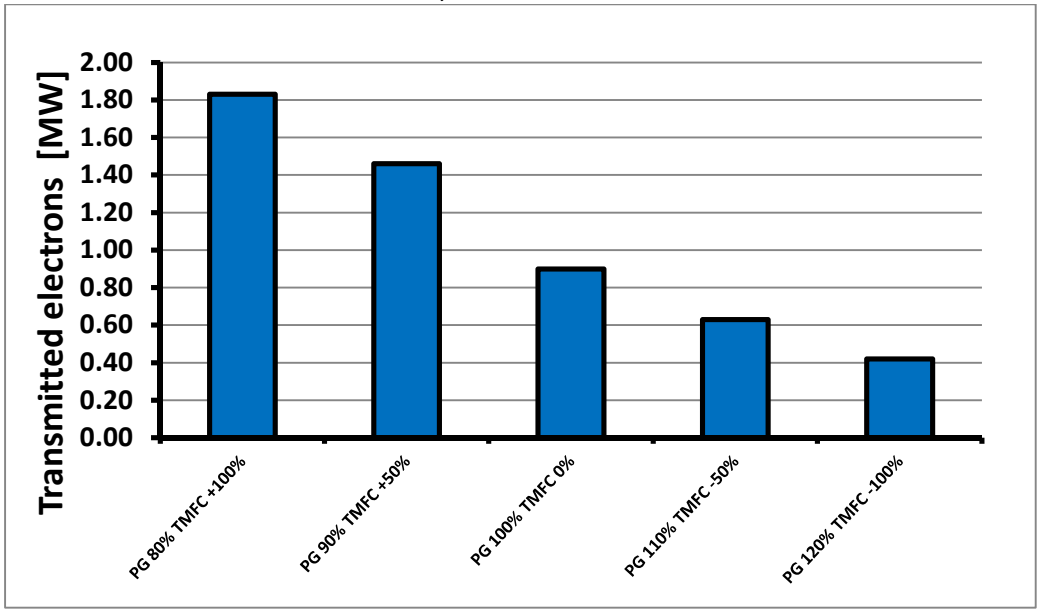

Fig. 72 Transmitted electrons for various PG current and TMFC current combinations.

2.3.10. Conclusions

A new geometry optimization of MITICA TMFC has been carried out, since during 2014 the reference PG busbar system has changed from PG_18 to PG_24.

The new optimization has been performed using an optimization algorithm based on Simulated Annealing, and all the magnetic field calculations have been made with NBImag.

The new solution is similar to the previous one, found in 2013, but has a lower current (25 kAturn instead of 30 kAturn). This is due to the different PG busbar configuration: PG_24 in fact has a lower reference PG current in comparison to PG_18 (3500 A instead of 4180 A). Moreover, the achievable range of variation of magnetic field in the source or in the accelerator with TMFC + PG_24 is slightly lower than the one achievable with TMFC + PG_18, again because the PG current is lower in PG_24.

In the end, variation of about $\pm$ 1 mT in B_{SOURCE} or in B_{ACCEL} can be achieved using the TMFC and this is enough for the achieving the required operational flexibility of the magnetic field configuration of MITICA. In fact, EAMCC simulations have shown that such a variation range is sufficient for reducing the heat load on the most loaded grid by 8% and the transmitted electron power by 50%.

2.4. Magnetic tests on Multi Channel Prototype

A comprehensive set of experimental tests has been carried out at Consorzio RFX regarding the construction of the grids for the ITER Neutral Beam Injectors, in order to validate the proposed manufacturing methodologies, to further develop the details of the engineering design, and to adapt existing production techniques to the specific case. In the framework of this R&D program, two Multi Channel Prototypes (MCPs) have been designed and manufactured. These prototypes feature all the possible manufacturing issues of the SPIDER and MITICA grids. In fact, they reproduce the geometry of the Extraction Grid (EG) for MITICA by having the same thickness, same cooling channels, same distributors, same aperture shape and same slots for the magnets of an EG segment. The differences with respect to the MITICA EG segment regard only the overall dimensions, i.e. reduced width (one fourth) and height (one half).
In this activity the MCP #2 has been used for magnetic mapping of the magnetic configuration foreseen for MITICA EG, developed at RFX, see [20], and already tested on MCP #2 in 2013. A new set of CESM and ADCM has been installed on MCP #2, having a reduced tolerance between the grooves and consequently less positioning errors. Moreover both the new CESM and ADCM have been characterized using a specifically developed tool and selected on the basis of best magnetic uniformity.
Therefore, the magnetic uniformity of the whole MCP is expected to be slightly better than in 2013.

2.4.1. Introduction

Magnetic field of MCP has been mapped using a Sypris DG 6010 gaussmeter with Hall probe and three axis positioning system as shown in Fig. 73:

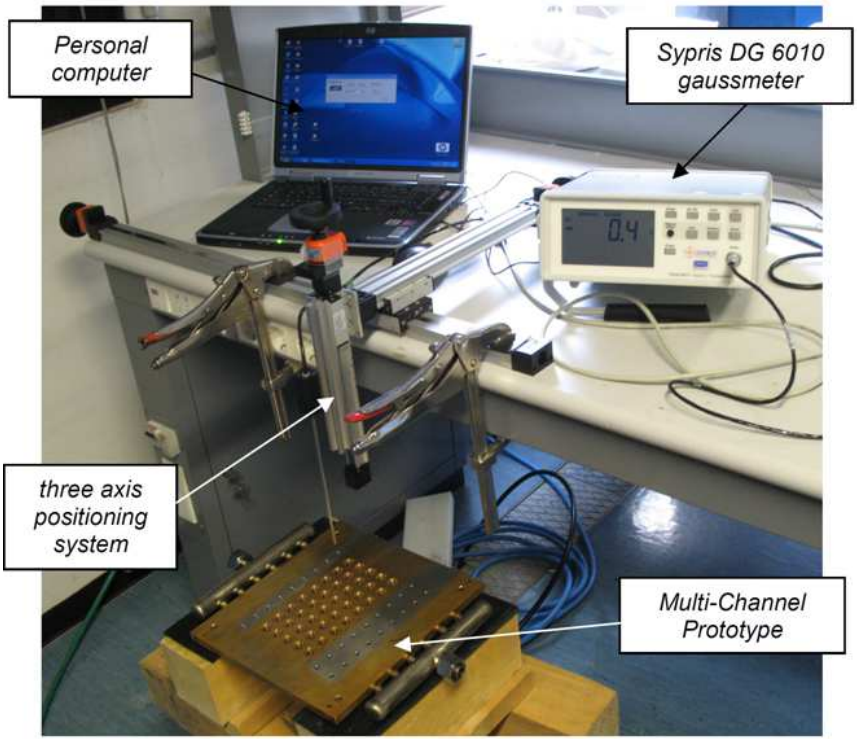

Fig. 73 Experimental equipment for 3D mapping of magnetic field of MCP.

Two magnetic configurations have been analyzed and measured: the first one (configuration #1) includes the standard Co-extracted Electron Suppression Magnets

(CESM) only and the second one (configuration #2) includes both the CESM and the Alternate Deflection Compensation Magnets (ADCM).
The configuration #2 is the reference design for MITICA EG and has been developed at RFX [20] as a new solution for magnetic deflection compensation.
Both configurations have been already implemented and mapped on MCP in the past, see [34] and a certain level of magnetic field non-uniformity was observed. One of the possible causes of non-uniformity was thought to be caused by the mechanical tolerance between the grooves and the inserted magnets these last ones adjusting their position under the effect of the collective magnetic field.
For this reason a new set of CESM and of ADCM have been purchased, having a slightly larger size in order to have smaller tolerance and therefore a better positioning inside the grid grooves. Moreover, the thickness of the previous ADCM had been decided on the base of ion deflection estimated using an analytical formula, [20], while more accurate and comprehensive simulations made with OPERA have shown that the optimal ADCM thickness obtained with the formula is underestimated by approximately a factor of 2. For this reason the new ADCM are thicker, and their hosting grooves had to be enlarged. Tab. 9 summarizes all the dimensions of previous and new magnets and grid grooves. The nominal magnetic remanence of all the permanent magnets in previous and actual configuration is Br = 1.1 T, the maximum achievable for SmCo magnets, this because from the industrial point of view is easier to magnetize permanent magnets at their maximum achievable Br and also because in this way the magnet size is minimum, having the same magnetic strength.

	Previous	**Actual**
CESM size	4.6 mm x 5.6 mm	4.8 mm x 5.8 mm
size of grooves for CESM	5.0 mm x 6.0 mm	5.0 mm x 6.0 mm
ADCM size	0.73 mm x 5.6 mm	1.95 mm x 5.8 mm
size of grooves for ADCM	1.0 mm x 6.0 mm	2.0 mm x 6.0 mm

Tab. 9 Dimensions of grid grooves and magnets of previous and actual MCP configuration.

It can be noticed that the mechanical tolerance between the magnets and the grooves has been reduced from 0.4 mm to 0.2 mm or less in the new configuration.
The layout of magnets arrangement inside the MCP is shown in the next Figure. In the first measurement campaign (configuration #1) only CESM are present.

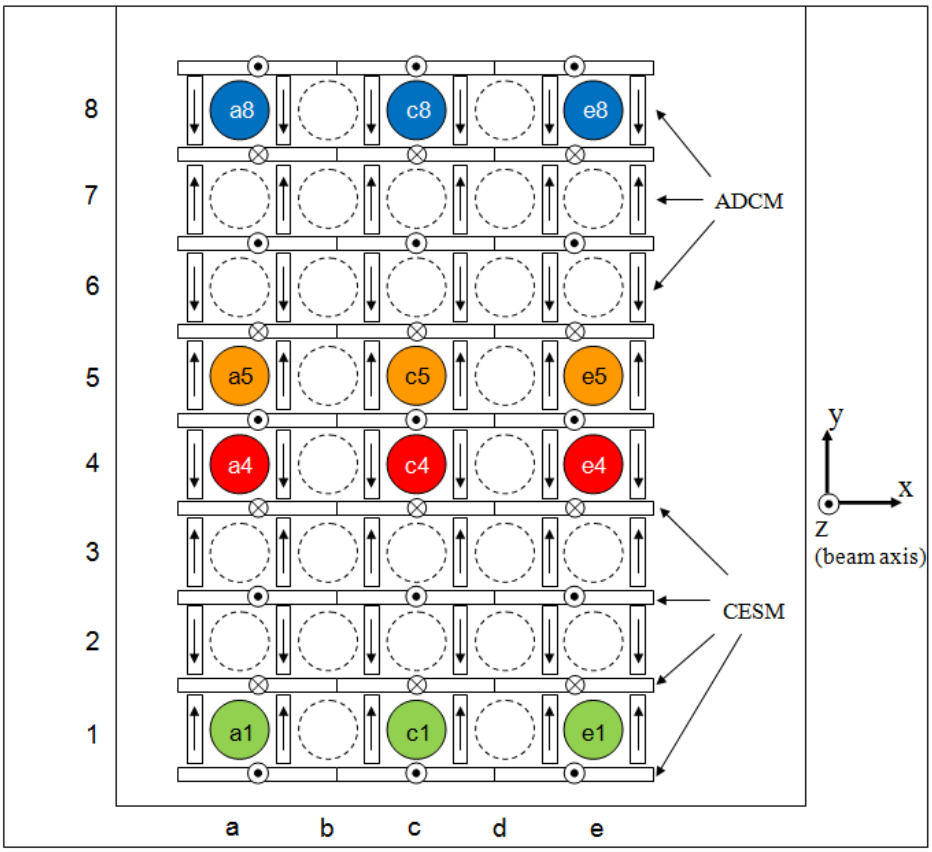

Fig. 74 Layout of CESM and ADCM inside MCP and aperture naming. The colored apertures are the ones used for measurement of magnetic field profile.

2.4.2. MCP configuration #1 - CESM only

Fig. 75 shows the NBImag model of the first considered MCP magnetic configuration, consisting in standard CESM only. The vertical component of magnetic field (By) has been calculated and then measured along the 12 apertures shown in Fig. 74 and Fig. 75.

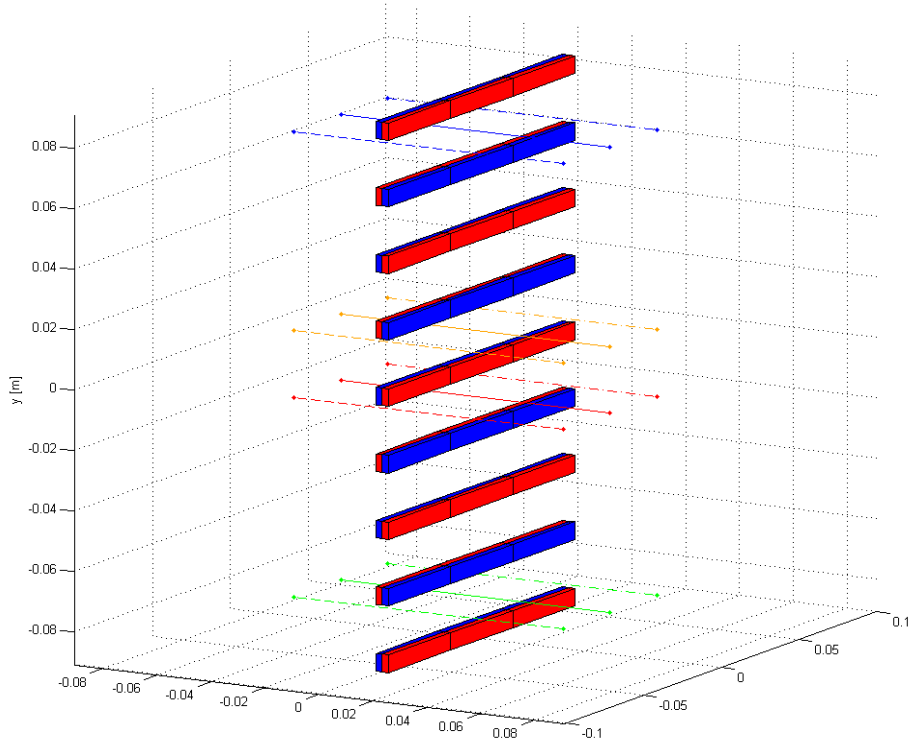

Fig. 75 NBImag model of MCP configuration #1, consisting of CESM only.

The profiles of By measured along the 12 indicated apertures are shown in Fig. 76, while the same profiles calculated with NBImag are shown in Fig. 77. Two facts can be immediately noticed:

- the value of By peaks is slightly higher for the calculated profiles with respect to the measured ones;
- the uniformity of the calculated profiles is higher with respect to the measured ones. All the calculated profiles stay within 5% of relative spread, whereas the measured ones stay within 10%.

The values of upstream and downstream peaks of By relative to the calculated profiles are compared with the real measured ones in the histograms of Fig. 78 and Fig. 79. From these two Figures, the difference between the calculated and the measured peaks appears more clearly. This effect was not observed with the previous set of magnets (see [34]) and it's maybe due to the remanent magnetic field of CESM that is slightly weaker than the nominal one

Moreover, it seems that this difference is more pronounced for the downstream peaks rather than the upstream peaks. This is maybe due to an offset of the gaussmeter measurements.

Since the new set of CESM should reduce the positioning error because of the reduced tolerance between the magnets and the grooves, another explanation for this overall non-uniformity could be the non uniformity of the single magnets themselves.

In order to investigate the uniformity of the single magnets as received from the manufacturer, a tool for magnetic characterization of single magnets has been developed, as described in the next section.

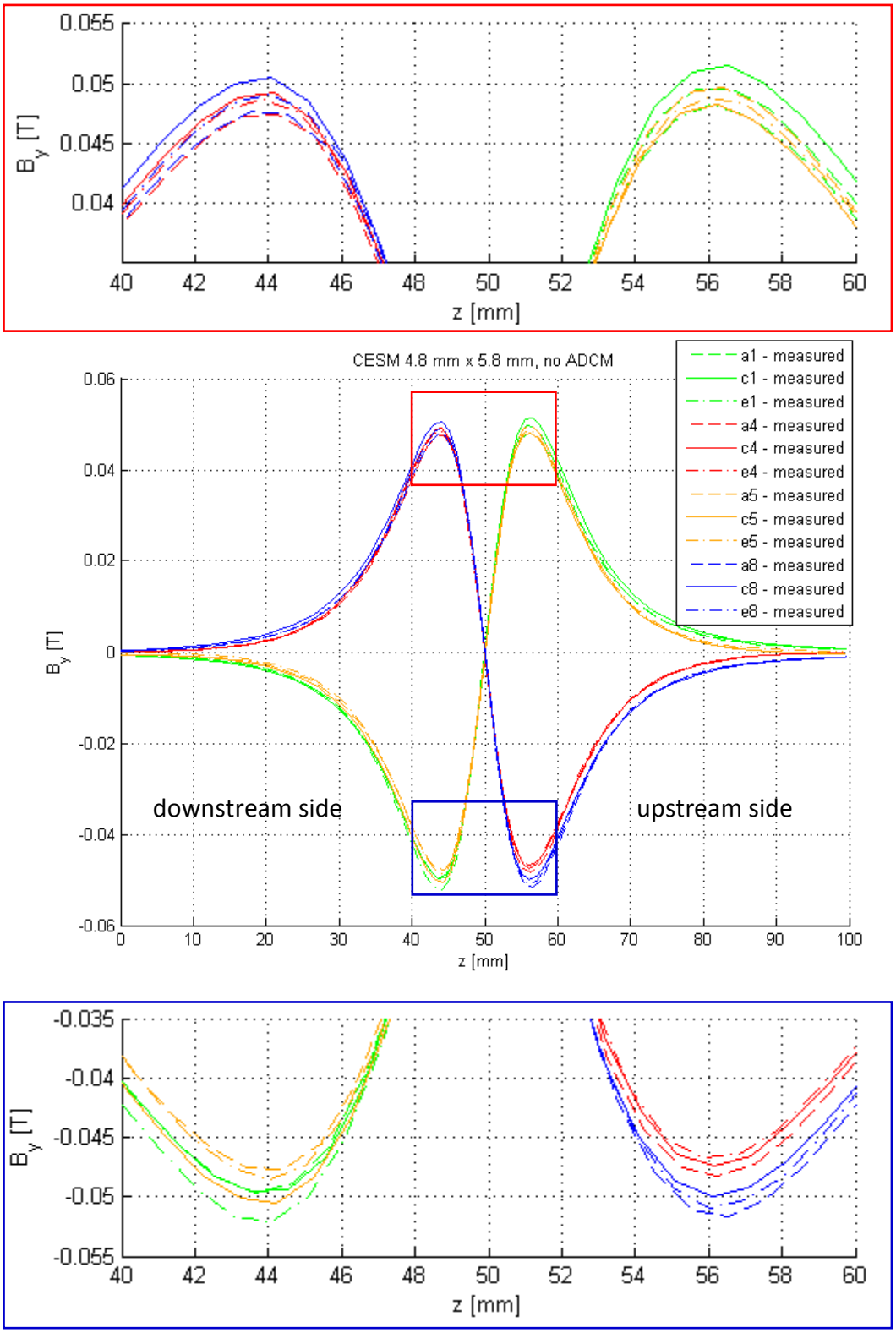

Fig. 76 By profiles measured along 12 MCP apertures in the magnetic configuration #1 (with CESM only).

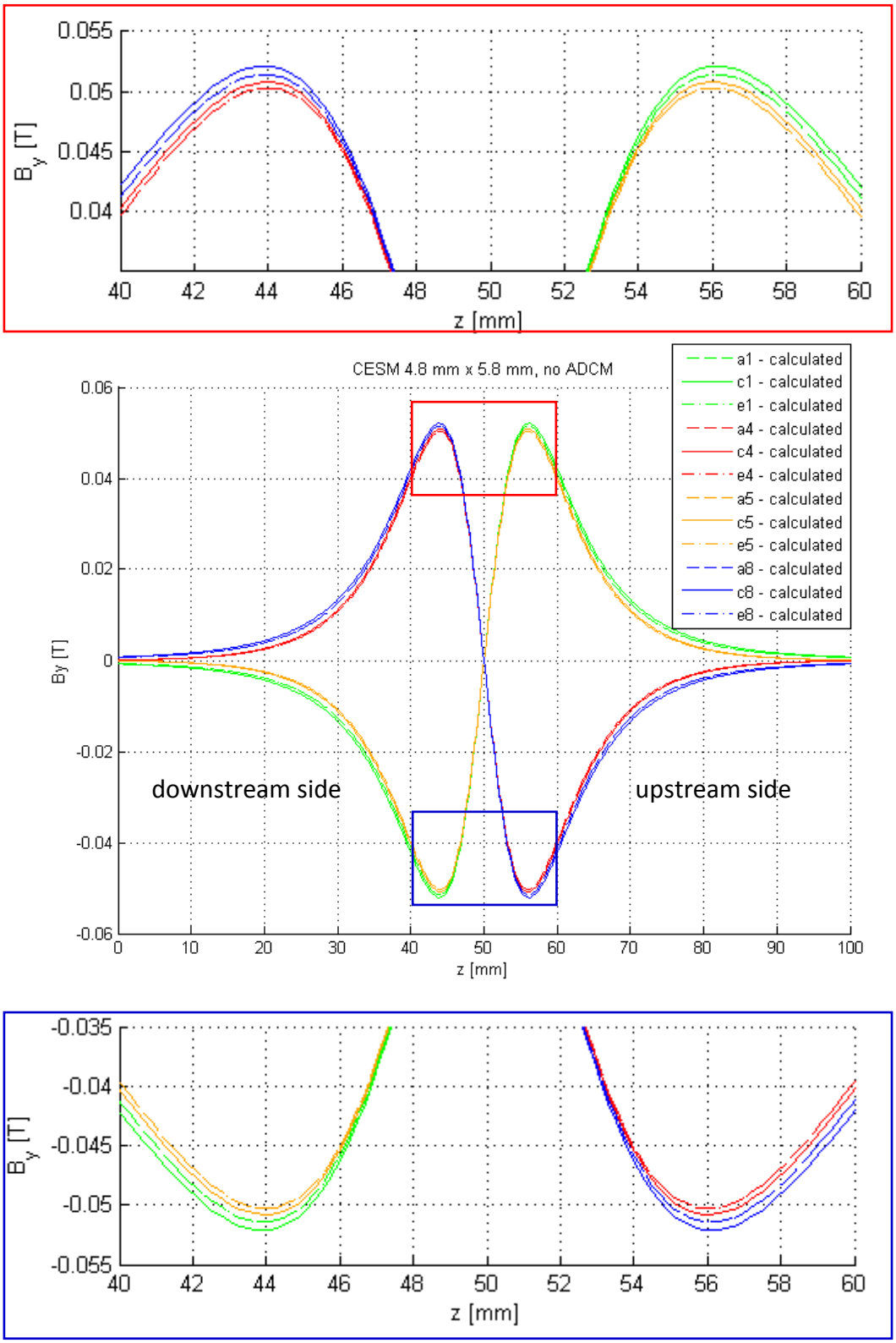

Fig. 77 By profiles calculated along 12 MCP apertures in the magnetic configuration #1 (with CESM only).

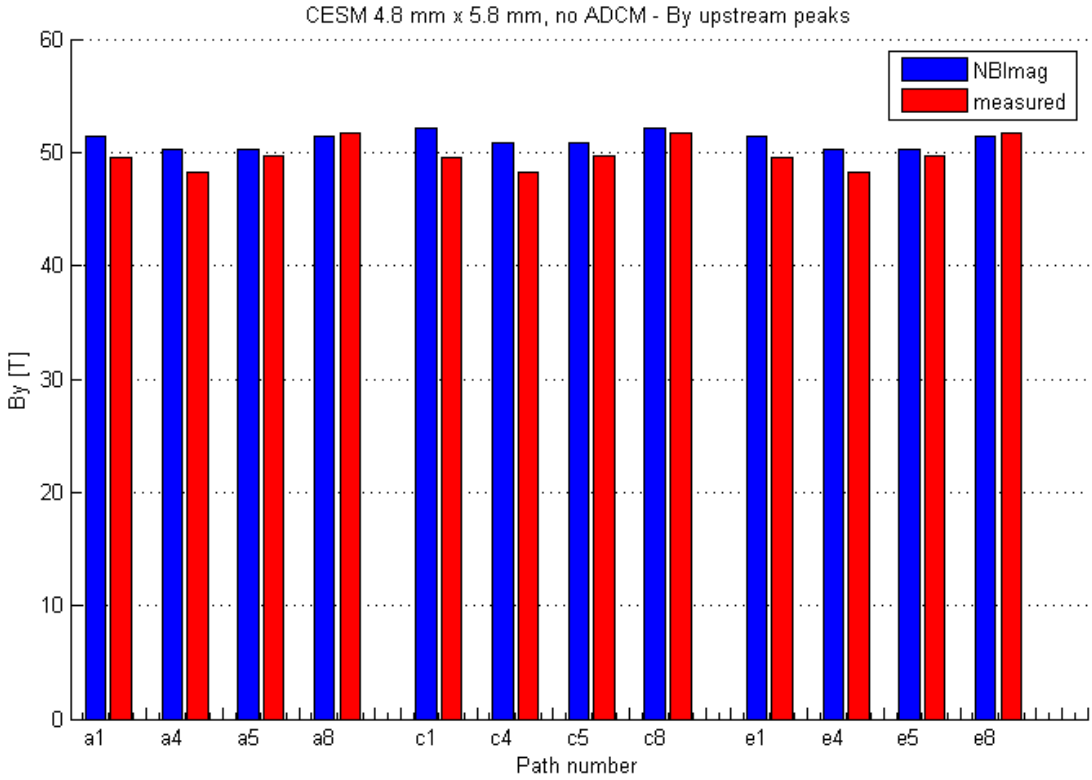

Fig. 78 Upstream peaks of By calculated with NBImag and measured in the magnetic configuration #1 (with CESM only).

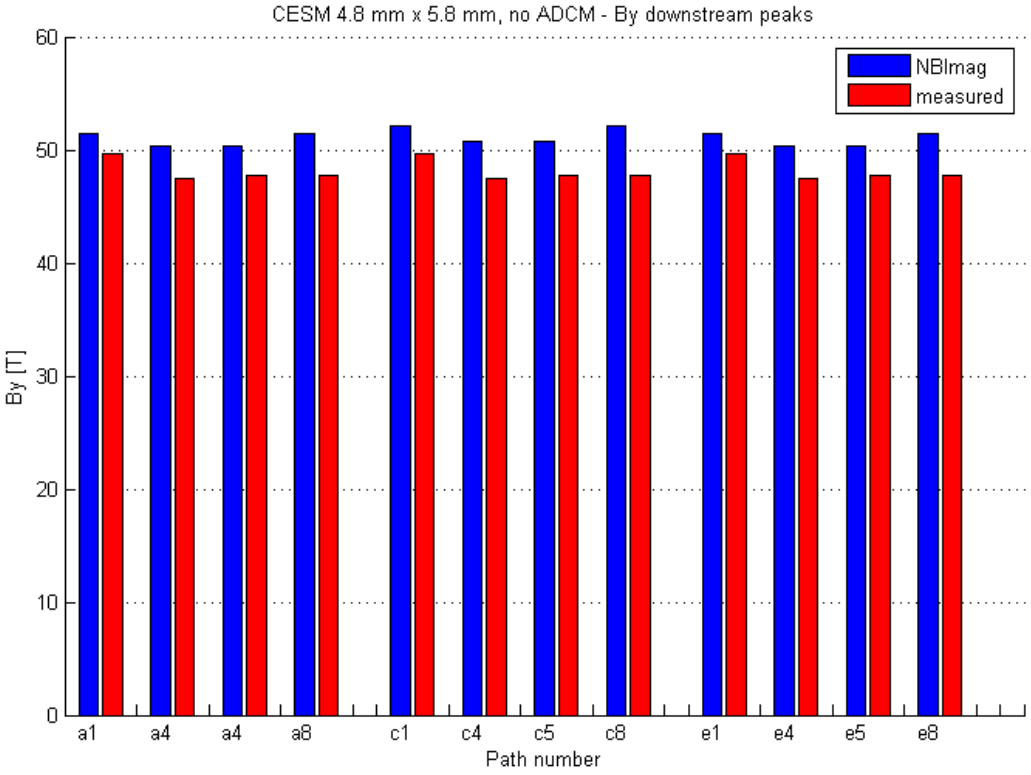

Fig. 79 Downstream peaks of By calculated with NBImag and measured in the magnetic configuration #1 (with CESM only).

2.4.3. Magnetic characterization of single magnets

The manufacturer of the permanent magnets is required to perform a quality control on the single magnets in terms of integrity, absence of defects, dimensional tolerance and magnetic flux. The manufacturer of the permanent magnets used on the MCP during the last measurement campaigns is MPI (Magneti Permanenti Industriali) [35]. In the next two Fig. the results of dimensional and magnetic flux quality control performed by MPI on a subset of the CESM used for the last measurements (4.8x5.8x40 mm^3) are reported.

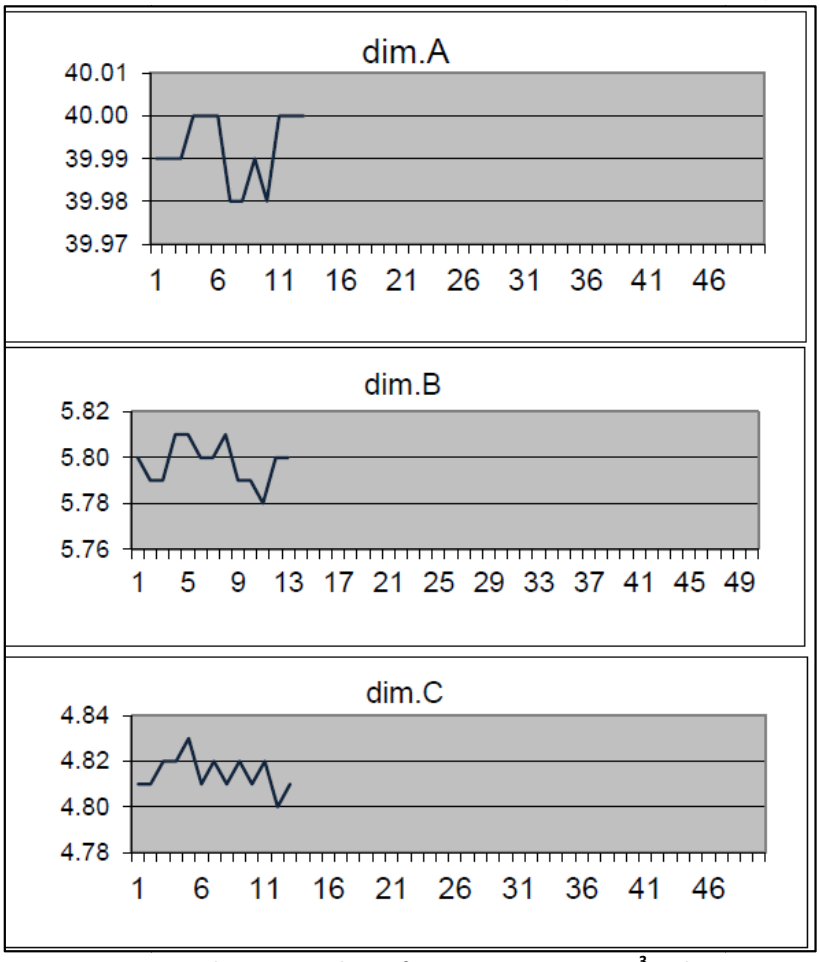

Fig. 80 Dimensional test on a subset of CESM 4.8x 5.8x 40 mm^3 and Br = 1.1 T.

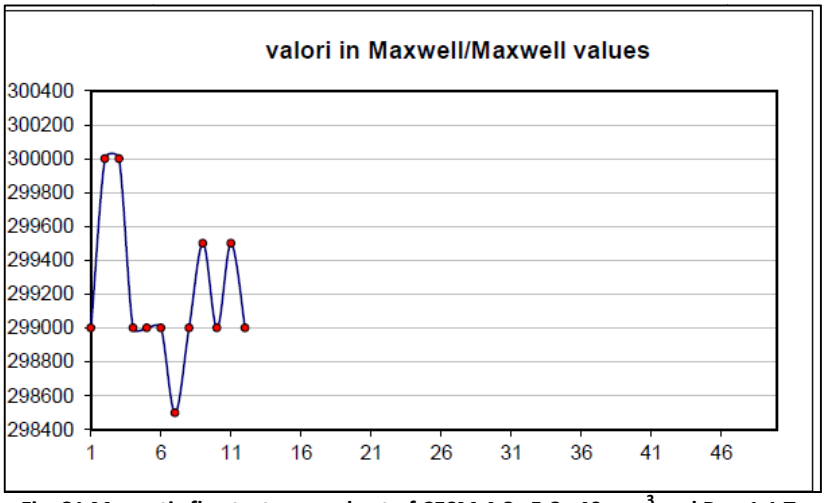

Fig. 81 Magnetic flux test on a subset of CESM 4.8x 5.8x 40 mm^3 and Br = 1.1 T.

From these tests it appears that both the dimensional uniformity and the magnetic flux uniformity of the magnets are very good (maximum non-uniformity ~ 0.5%). Anyway the flux test could be unable to detect local non-uniformity of magnetic field in the proximity of the magnet. For this reason a tool for local magnetic characterization of CESM and ADCM has been designed and realized at Consorzio RFX.
This tool is made by simple aluminum plates mounted together in order to host the magnetic tangential probe of a gaussmeter and with a reference position for placing the permanent magnets as shown in Fig. 82, Fig. 83 and Fig. 84. The measurement point is fixed with respect to the magnet and it's located at a distance of 10 mm.

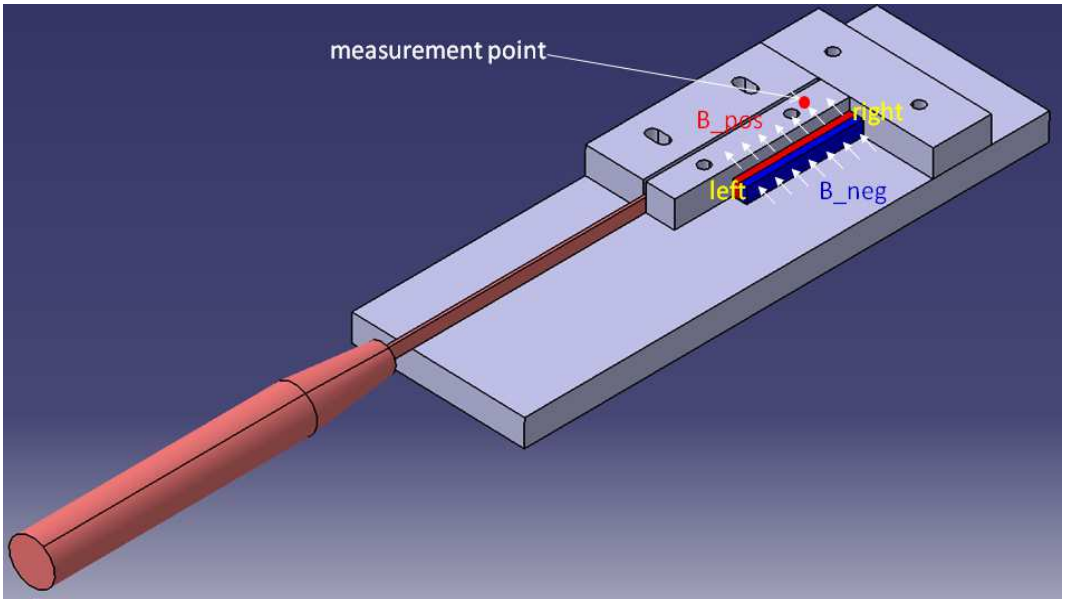

Fig. 82 CAD model of the tool for magnetic uniformity quality control on single permanent magnets. A magnetic probe and a CESM in measurement position are shown.

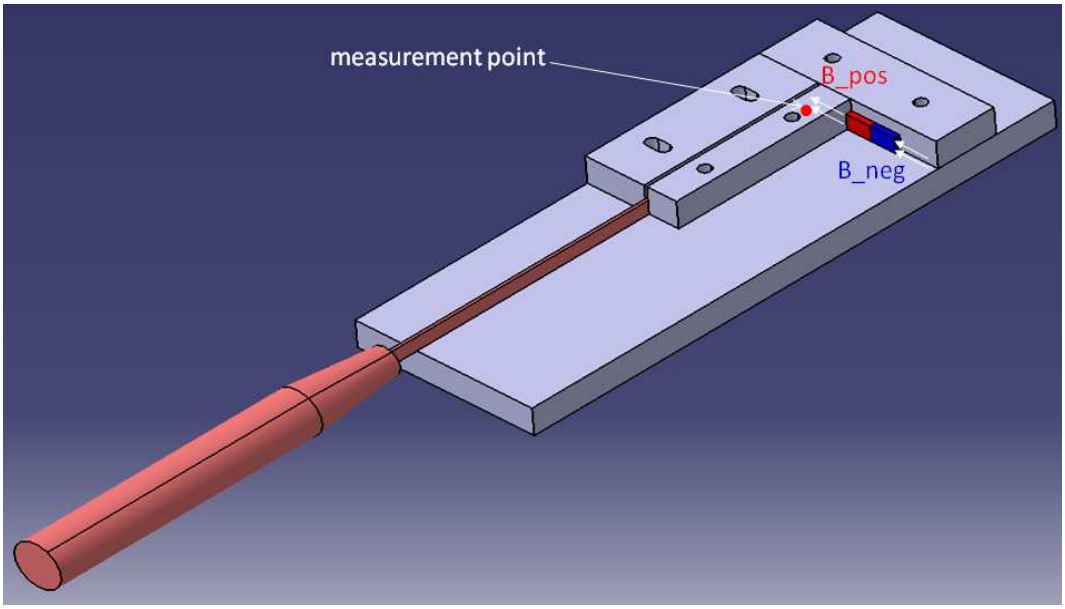

Fig. 83 CAD model of the tool for magnetic uniformity quality control on single permanent magnets. A magnetic probe and an ADCM in measurement position are shown.

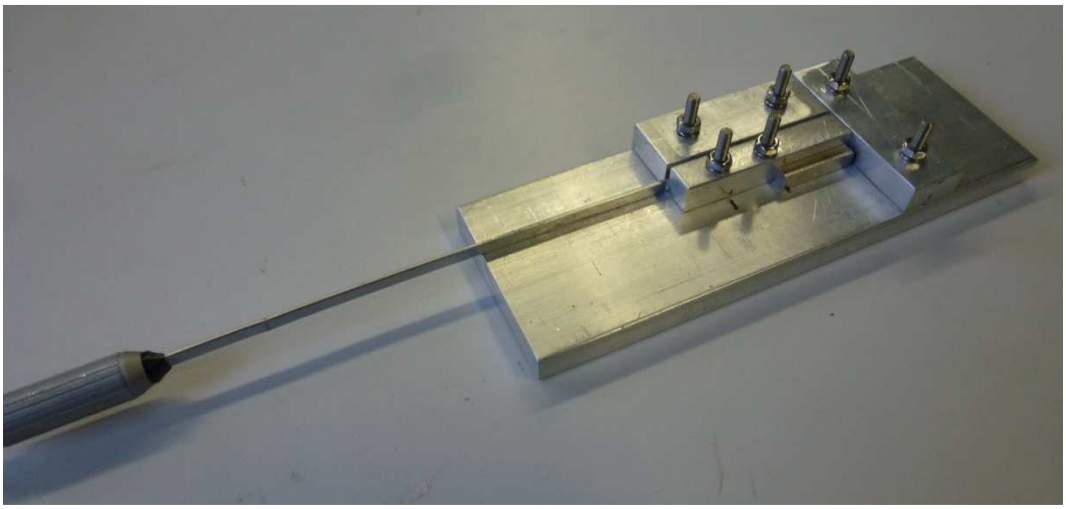

Fig. 84 Assembled tool for magnetic uniformity quality control on single permanent magnets. The magnetic probe of the Sypris DG 610 gaussmeter and a CESM in measurement position are shown.

Using this tool, a campaign of measurement on the single CESM and ADCM has been carried out.

2.4.3.1. Magnetic characterization of CESM

The 40 CESM (27 needed for MCP magnet grid + 13 spare) have been characterized by taking four measurements for each magnet, defined as follow (see also Fig. 82 for better understanding):

B_{pos_l} → first measurement of magnetic field from the positive field side;

B_{pos_r} → measurement of magnetic field from the positive field side after flipping the magnet along the left-right direction, which is along the 40 mm edge for a CESM, see Fig. 82;

B_{neg_l} → first measurement of magnetic field from the negative field side;

B_{neg_r} → measurement of magnetic field from the negative field side after flipping the magnet along the left-right direction, which is along the 40 mm edge for a CESM, see Fig. 82;

Fig. 85 shows the absolute values of all the measurements taken on the 40 CESM:

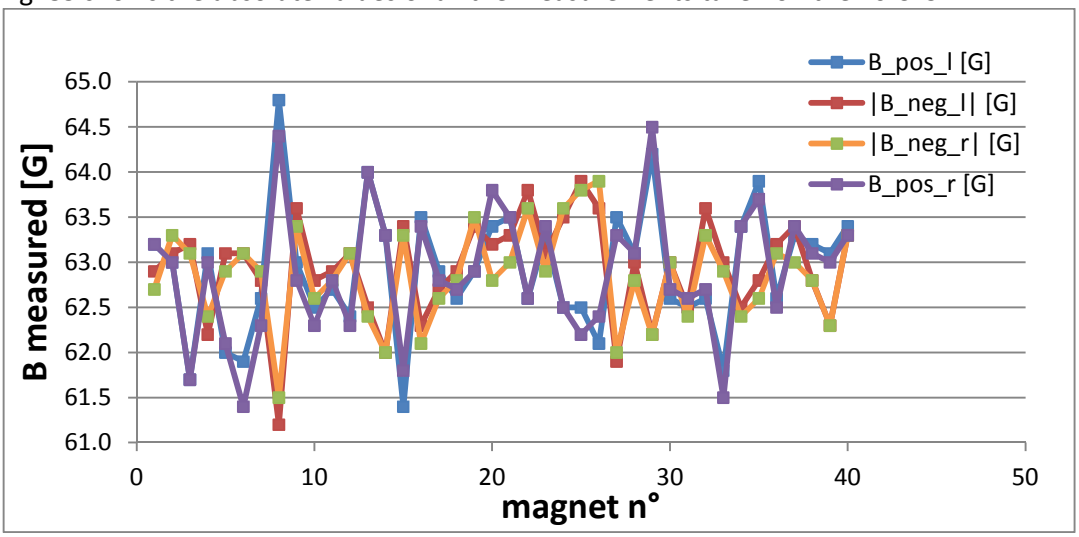

Fig. 85 Absolute values of all measurements taken on the 40 CESM.

For better understanding the magnetic characterization of CESM it's useful to define some average quantities:

$$B_{pos} = \frac{(B_{pos\_l} + B_{pos\_r})}{2}$$

$$B_{neg} = \frac{(|B_{neg\_l}| + |B_{neg\_r}|)}{2}$$

$$B_l = \frac{(B_{pos\_l} + |B_{neg\_l}|)}{2}$$

$$B_r = \frac{(B_{pos\_r} + |B_{neg\_r}|)}{2}$$

$$B_{tot} = \frac{(B_{pos} + |B_{neg}|)}{2}$$

In Fig. 87 B_{pos} and B_{neg} are compared. This plot gives an idea of non-uniformity of the magnets along the N-S direction. This non-uniformity reaches 4% for some magnets and it can be due to an internal remanent magnetic field shaped as a trapezoid, see Fig. 86:

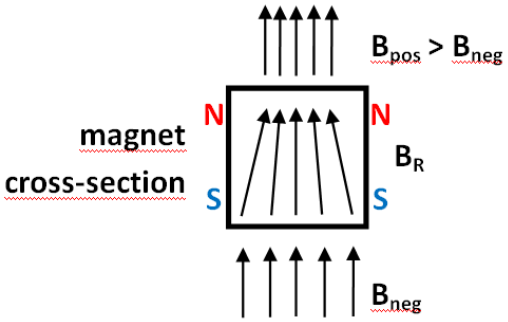

Fig. 86 Non uniform internal magnetization giving rise to a magnetic non-uniformity along N-S direction.

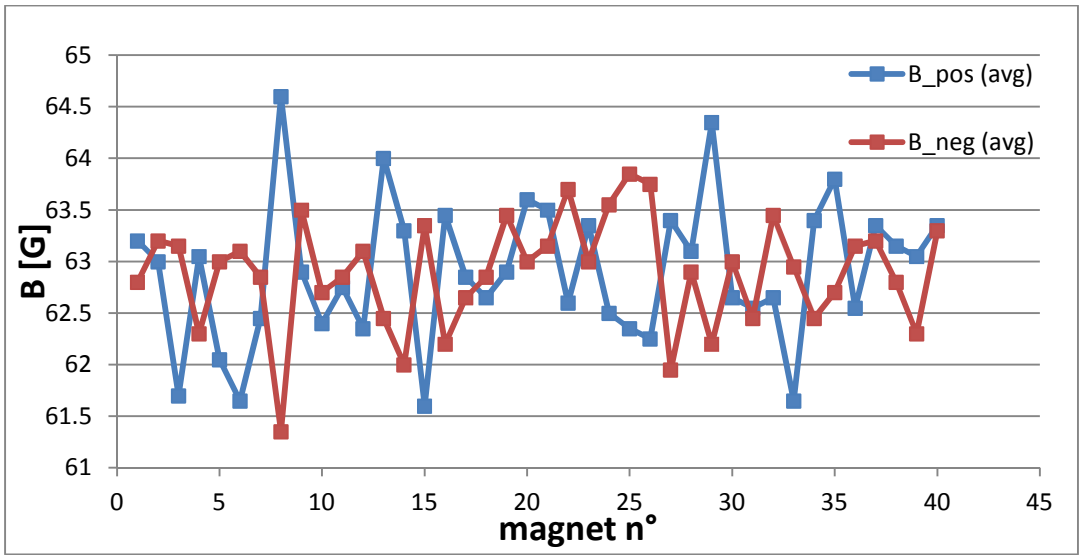

Fig. 87 CESM non-uniformity along N-S direction.

In Fig. 88 B_left and B_right are compared. This plot shows the magnetic non uniformity along the left-right direction, i.e. along the 40 mm edge of CESM. This kind of non-uniformity is due again to a non uniform remanent magnetic field inside the magnet, stronger in one magnet side with respect to the other one.

Anyway, this non-uniformity is much less (within 0.3%) than the N-S non-uniformity (within 4%), as it can be seen also from Fig. 89, that shows the difference in magnetic field along N-S direction and along right-left direction.

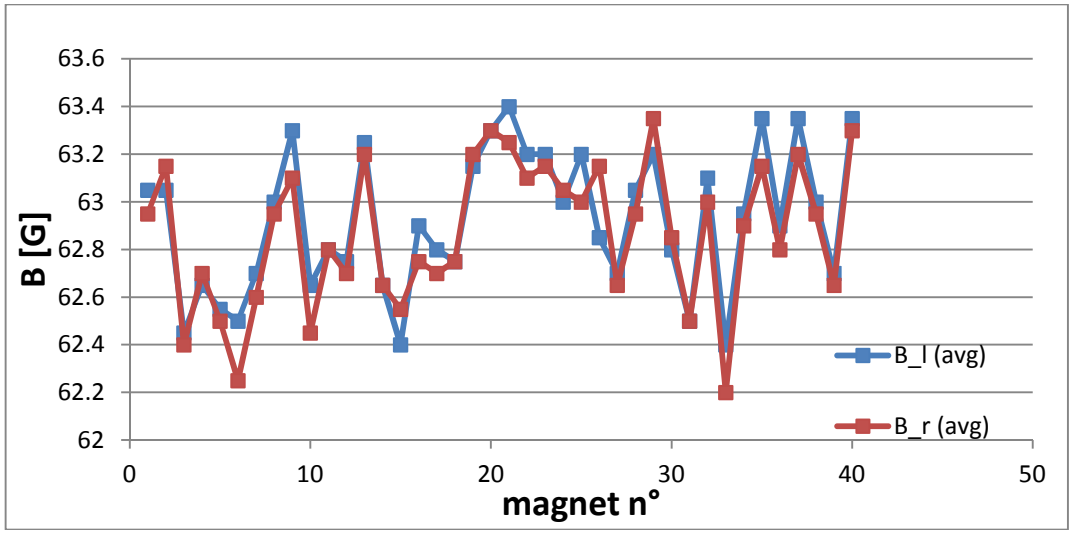

Fig. 88 CESM non-uniformity along left-right direction (or along 40 mm edge).

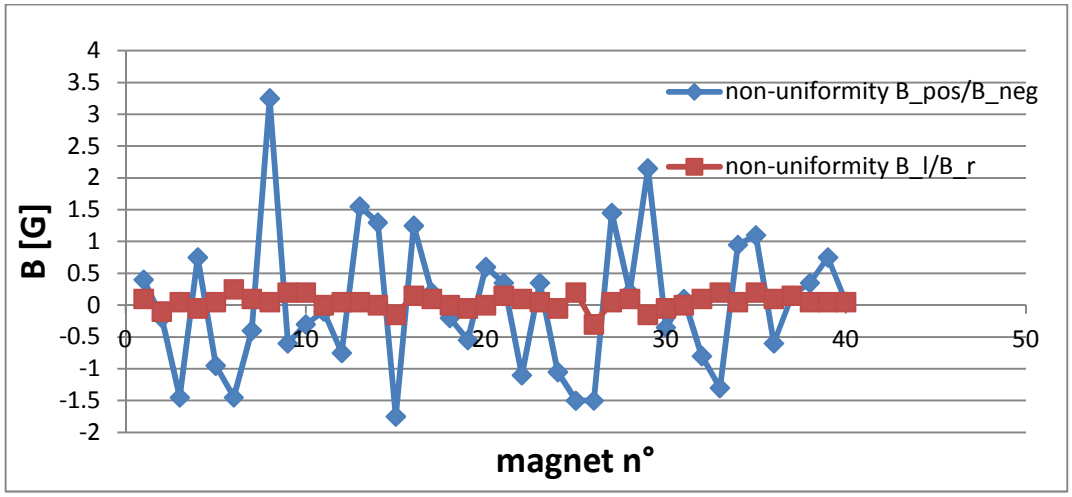

Fig. 89 Comparison between N-S (or B_pos/B_neg) non-uniformity and left-right non-uniformity in terms of difference between the measured fields.

Finally, the average CESM strength B_tot defined above is compared for the 40 CESM, as shown in Fig. 90. The overall CESM non-uniformity considering B_tot is within 2%.
After this measurement campaign, the 13 CESM with worst N-S uniformity have been taken apart and the remaining 27 have been installed again in the MCP.

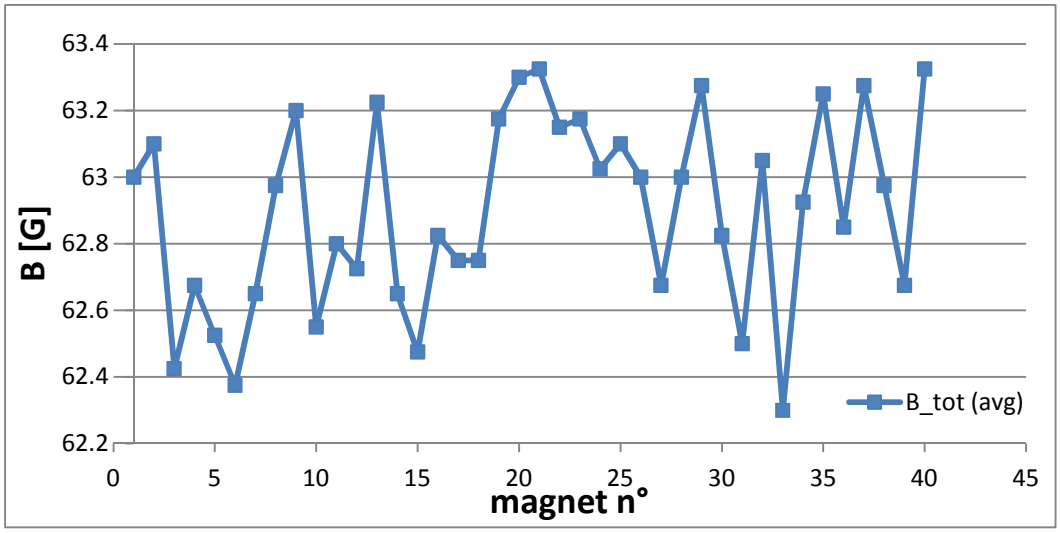

Fig. 90 Comparison of average strength of each CESM.

2.4.3.2. Magnetic characterization of ADCM

For the magnetic characterization of the ADCM, only two measurements have been taken for each magnet, i.e. B_pos and B_neg. In fact, due to ADCM smaller size and different aspect ratio, measuring B_left and B_right has not much sense.

Fig. 91 shows the N-S uniformity of the ADCM in terms of absolute values of measured field and Fig. 92 in terms of difference between them.

In this case the N-S non-uniformity is within 3%, slightly better than the CESM case.

Fig. 93 shows the average strength of each ADCM calculated as average between B_pos and B_neg.

In this case, the overall non-uniformity between the ADCM is within 5.5%, so quite worse than the CESM case.

Even in this case, after the measurement campaign, the 42 best ADCM have been selected among the 48 total for the installation on MCP.

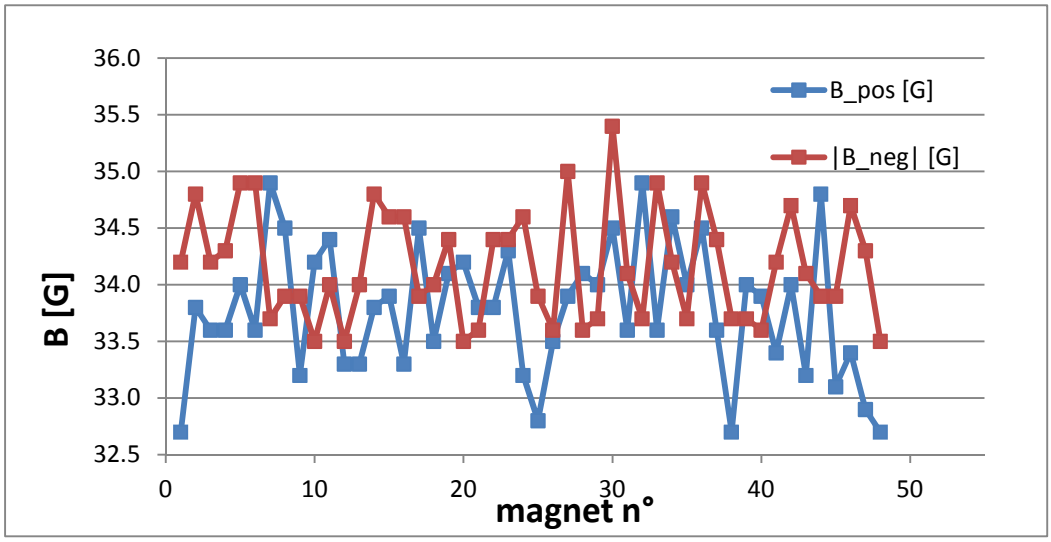

Fig. 91 ADCM non-uniformity along N-S direction.

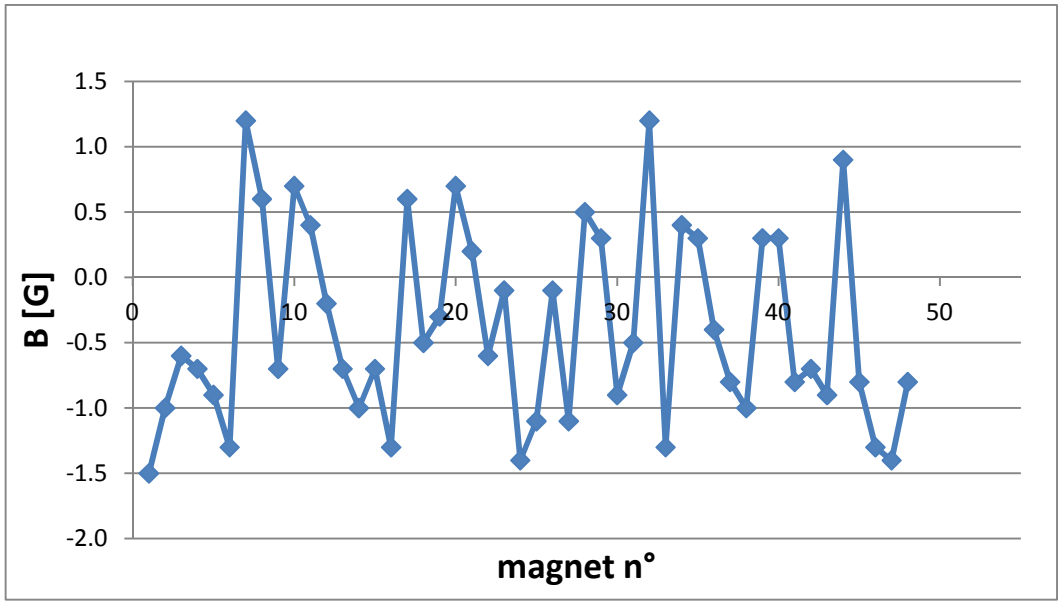

Fig. 92 ADCM non-uniformity along N-S direction in terms of difference between the measured fields.

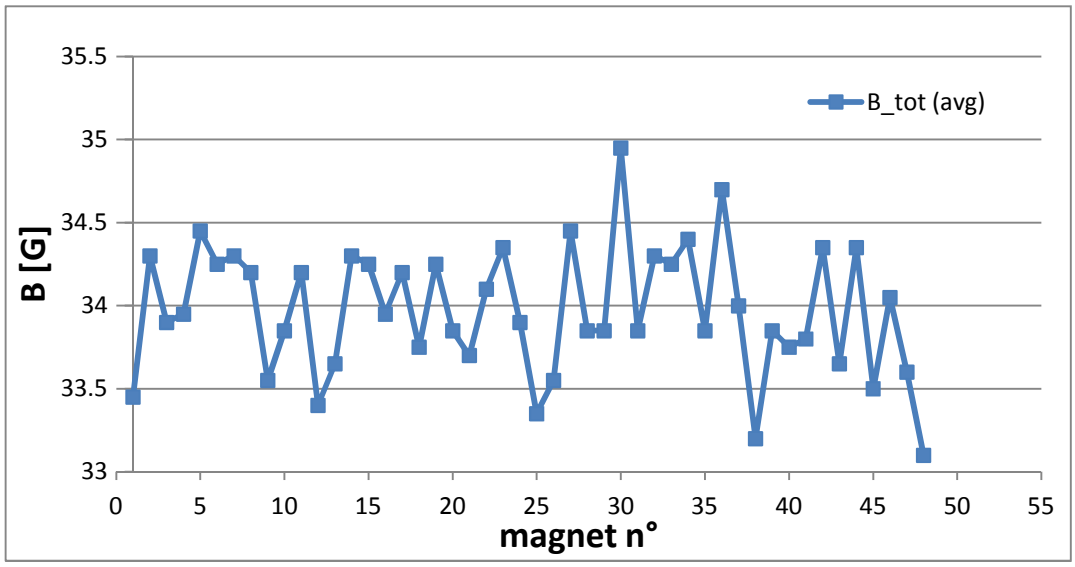

Fig. 93 Comparison of average strength of each ADCM.

2.4.4. MCP configuration #2 - CESM + ADCM

After the selection of the best CESM and ADCM from the magnetic uniformity point of view, the complete configuration CESM + ADCM has been assembled on the MCP. The NBImag model of this configuration is shown in Fig. 94.

Vertical component of magnetic field has been measured along the usual 12 apertures (Fig. 74) and the By measured profiles are shown in Fig. 95.

The By profiles calculated with NBImag are shown in Fig. 96.

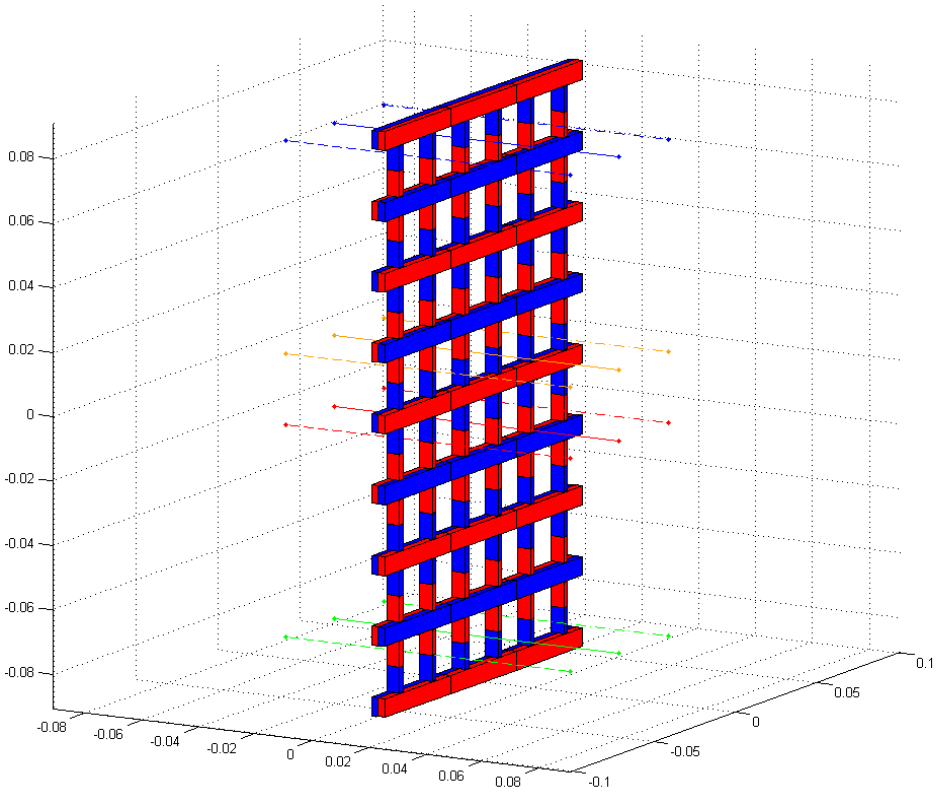

Fig. 94 NBImag model of MCP configuration #2, consisting of CESM + ADCM.

The same observation of the configuration #1 (CESM only) can be drawn in this case:

- the value of By peaks is slightly higher for the calculated profiles with respect to the measured ones;
- the uniformity of the calculated profiles is higher with respect to the measured ones. In this case the calculated profiles stay within 5% of relative spread, while the measured ones stay within 15%.

The value of 15% of non-uniformity in the case of CESM+ADCM with respect to the 10% of the case with CESM only is due to the fact that now the downstream By peak is much smaller, and so the relative difference between the profiles in the downstream part is higher. On the other hand, the upstream peaks seem to be more uniform in the configuration CESM+ADCM. This can be noticed also in Fig. 97 and Fig. 98.

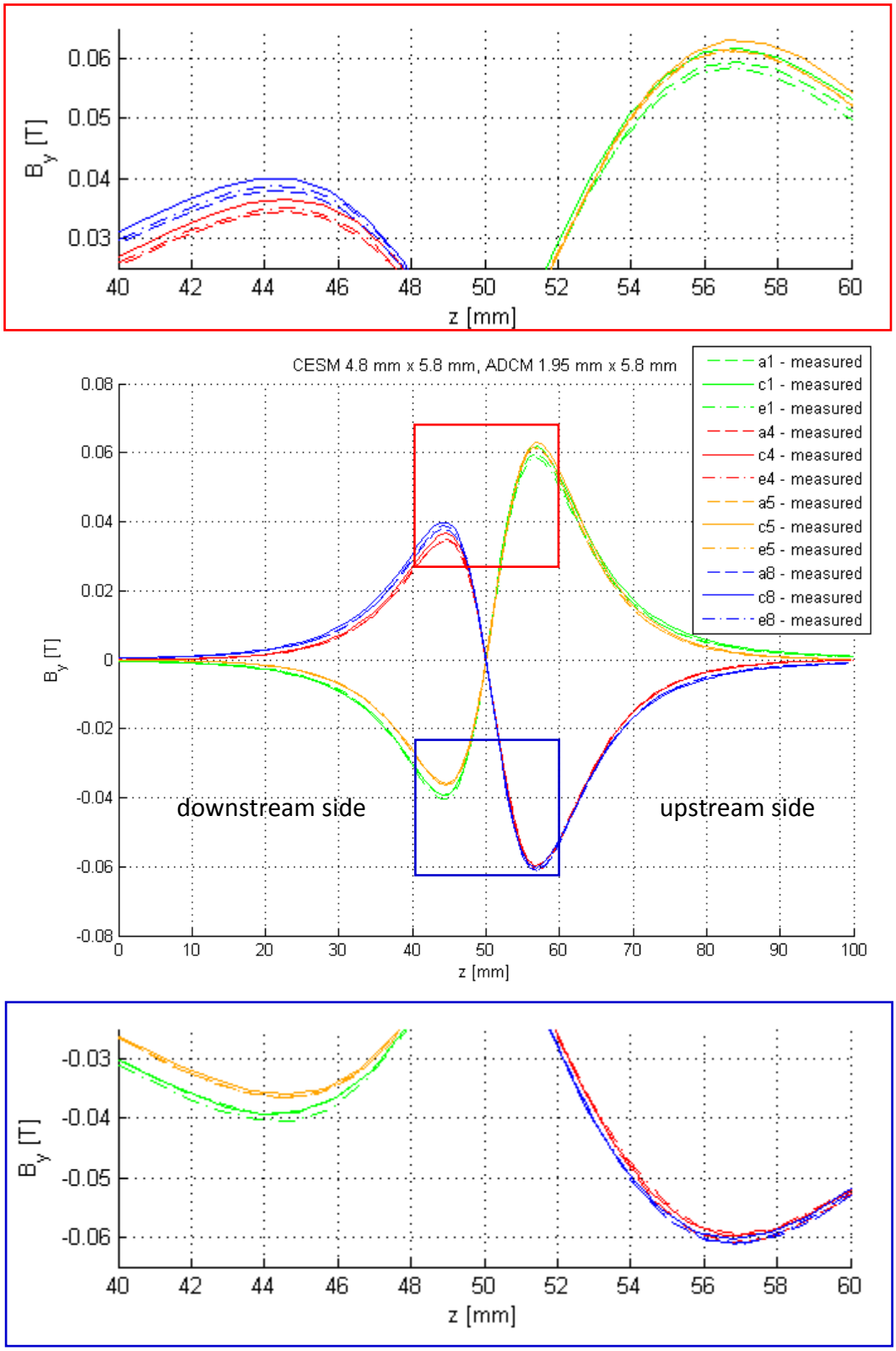

Fig. 95 By profiles measured along 12 MCP apertures in the magnetic configuration #2 (CESM + ADCM).

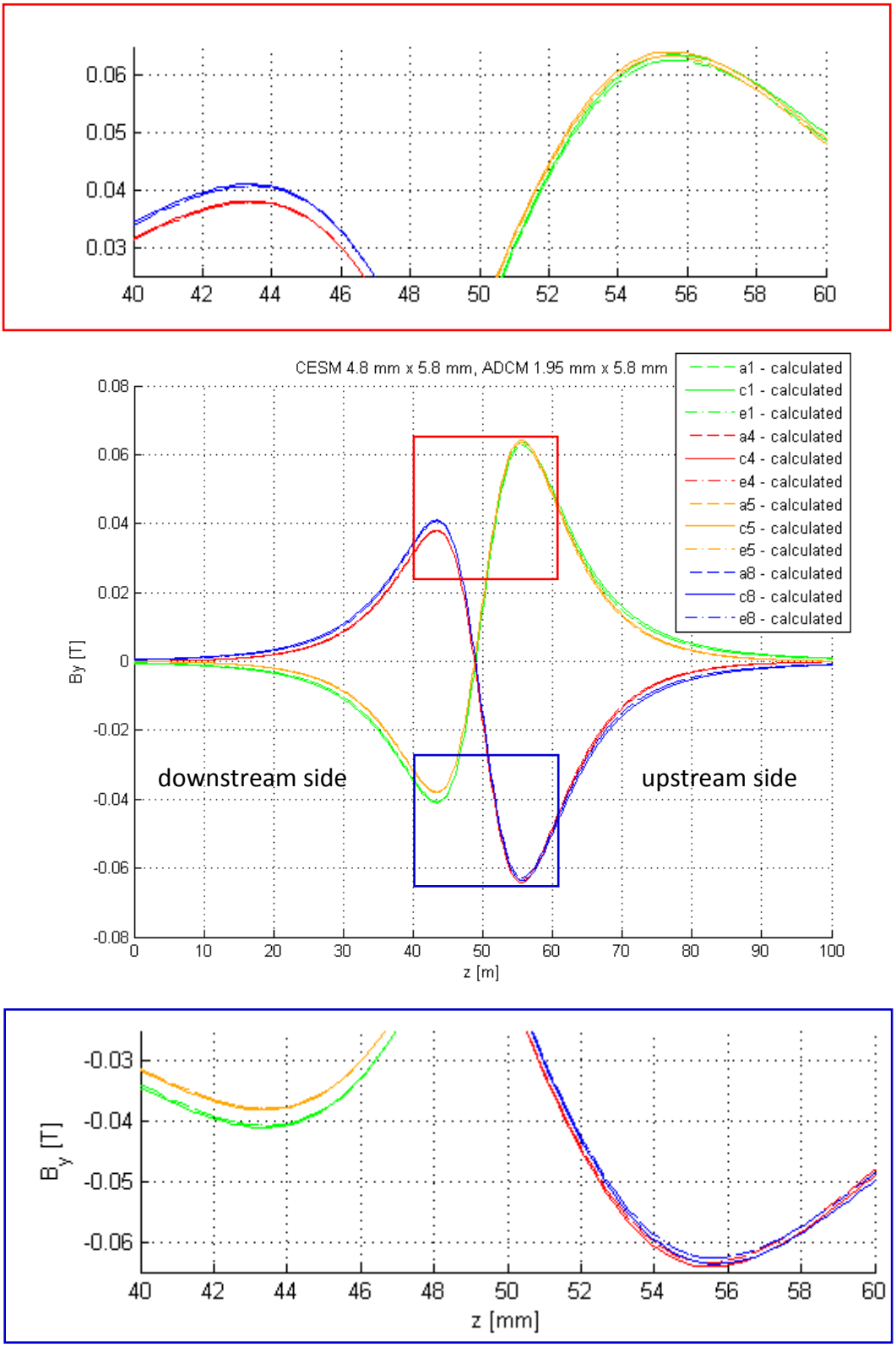

Fig. 96 By profiles calculated along 12 MCP apertures in the magnetic configuration #2 (CESM + ADCM).

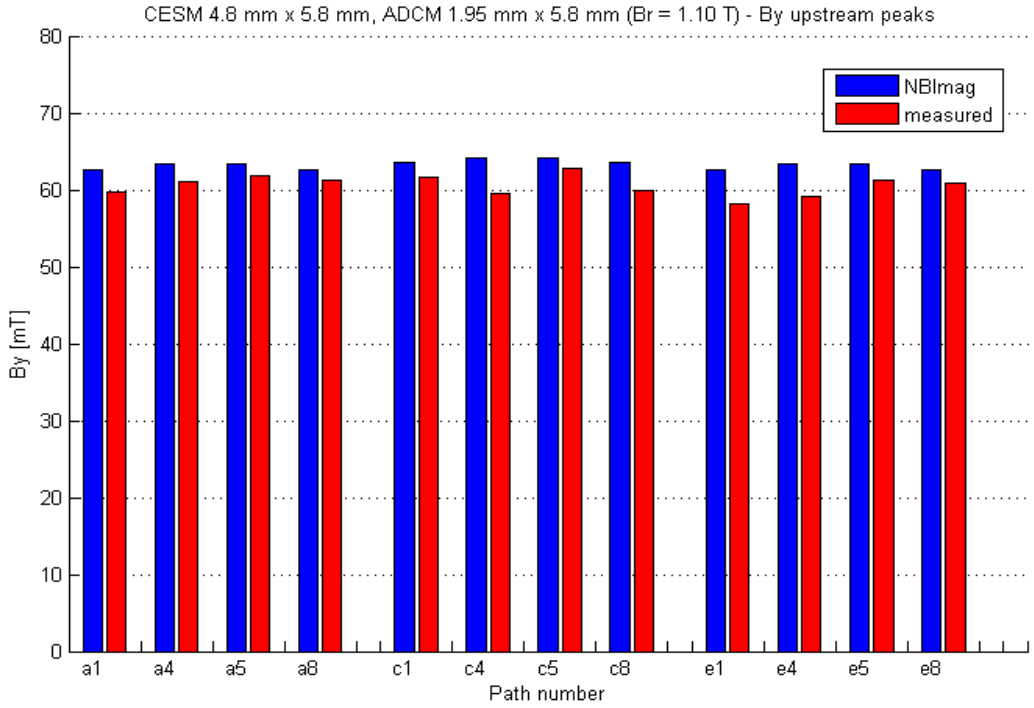

Fig. 97 Upstream peaks of By calculated (Br = 1.1 T) with NBImag and measured in the magnetic configuration #2 (CESM + ADCM).

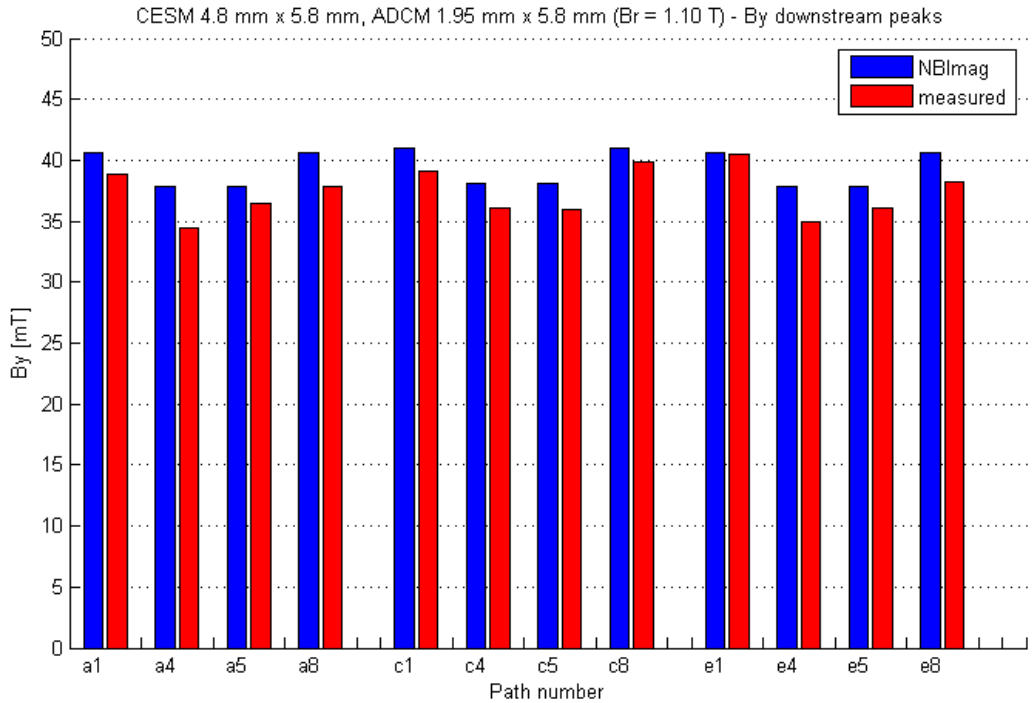

Fig. 98 Downstream peaks of By calculated (Br = 1.1 T) with NBImag and measured in the magnetic configuration #2 (CESM + ADCM).

The difference between the measured and the calculated By peaks is of the order of 5%. This effect was not noted in the measurement campaigns on MCP in the past years, so it can be due to the new set of CESM that are slightly less strong than the requirements.
The next two Fig. show the comparison between the calculated and the measured By peaks in the case that the magnetic remanence is set to Br = 1.05 T instead of the

nominal value of Br = 1.1 T. Using this reduced value of Br the results of the simulation are in much better agreement with the measured values.

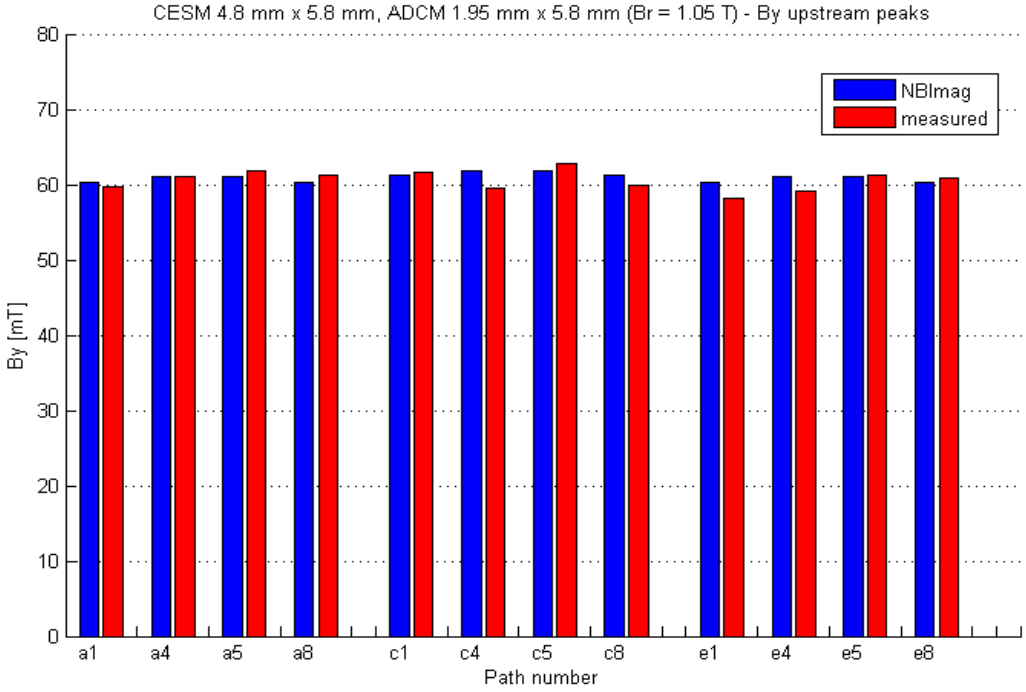

Fig. 99 Upstream peaks of By calculated (Br = 1.05 T) with NBImag and measured in the magnetic configuration #2 (CESM + ADCM).

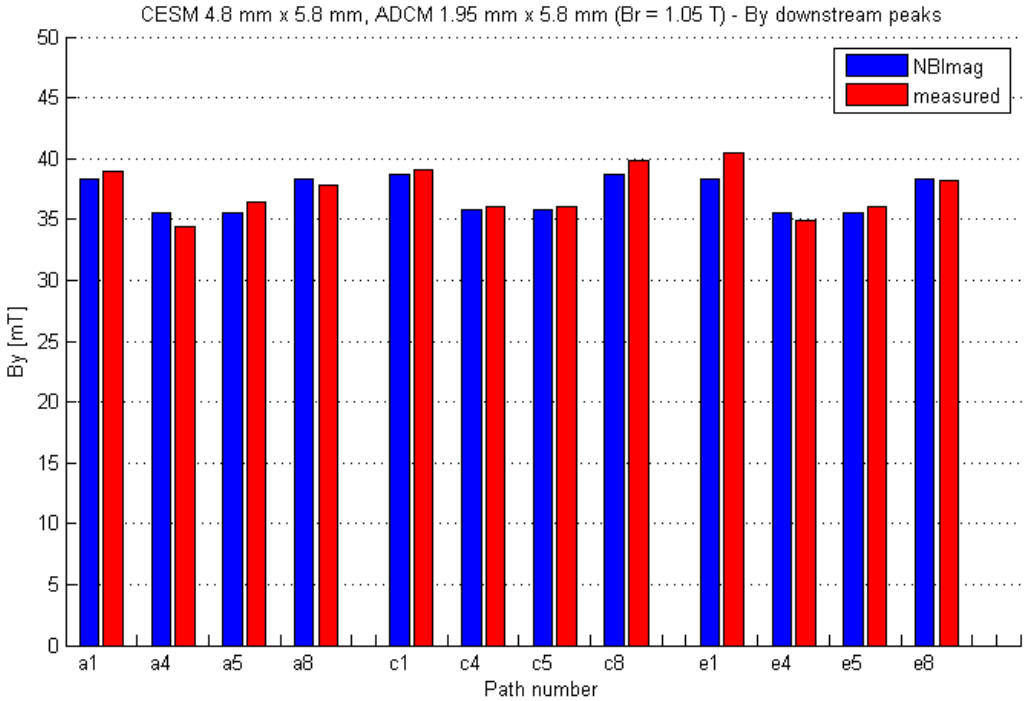

Fig. 100 Downstream peaks of By calculated (Br = 1.05 T) with NBImag and measured in the magnetic configuration #2 (CESM + ADCM).

2.4.5. Conclusions

MCP magnetic field has been mapped in two different magnetic configurations, the first one consisting in CESM only and the second one in CESM+ADCM, as the reference design for MITICA. New set of CESM and ADCM have been used with respect to the past measurements of 2013.

The first configuration (CESM only) showed a non-uniformity of magnetic field profiles taken along 12 different apertures of ± 10%, while simulations made with NBImag predicts a non-uniformity of ± 5% only. This difference can be due to positioning errors or non-uniformity of the single magnets themselves. Positioning errors with the new set of CESM and ADCM should be very low, since the tolerance between the new magnets and the grooves is only 0,2 mm, with respect to the previous value of 0,4 mm.

After the measurements with the first configuration, the single permanent magnets have been investigated: a campaign of magnetic measurements has been carried out on the new set of CESM (4.8x5.8x40 mm^3) and ADCM (1.95x5.8x16.4 mm^3) using a gaussmeter and a holding tool specifically developed.

These measurements allowed the discovery of magnetic non-uniformities along N-S direction (4%) and along left-right direction (0.3%) of CESM, probably due to a non uniform magnetizing field during the manufacturing process. N-S non-uniformity has been measured also in ADCM, despite of a slightly lower level (3%).

On the contrary, the overall uniformity between the average strength of CESM is better (2%) than the one of ADCM (5.5%).

After the measurement campaign, the best magnets were selected for the next mapping of MCP magnetic field.

The relative non-uniformity of the second magnetic configuration (CESM+ADCM), is comparable with the case of CESM only, proving that the ADCM doesn't provide additional non-uniformities to the overall configuration.

A final fact to be noticed is that the new CESM seem to have a magnetization slightly lower (-5%) than the nominal value of 1.1 T.

2.5. Magnetic tests on NIO1

2.5.1. Introduction

NIO1 (Negative Ion Optimization 1) is a 60 kV multi aperture negative ion source operating at RFX, see [36], constituted by a RF source, Plasma Grid (PG), Extraction Grid (EG), Post Acceleration Grid (PA), and calorimeter.

This section reports on a set of measurements of local magnetic fields produced by permanent magnets and by current flowing in the Plasma Grid of NIO1 experiment. The data were collected using a Gaussmeter (F. W. Bell, Model 6010). The purpose of the work was to verify the correct position and orientation permanent magnets in the experiment, and to check the degree of reliability of numerical simulations performed so far.

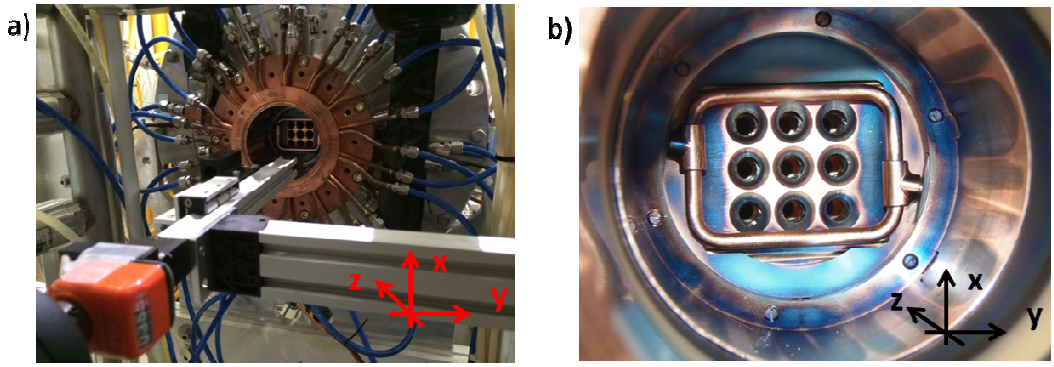

Fig. 101 a) picture of the 3-axis movable support for the Gaussmeter, b) front part of NIO1 chamber, where most of the measurements have been taken. Note the 9 Plasma grid apertures.

2.5.2. Magnetic configuration of NIO1

Several magnets are inserted in the NIO1 chamber. Different groups of magnets or coils can be distinguished depending on their scope:

1) Plasma confinement:

- 3 set of 14 Samarium Cobalt (SmCo) magnets (rear multipole, central multipole, front multipole) plus 5 magnets forming a cross in the rear cover, arranged in a multi cusp configuration, see Fig. 102 a;

2) Filter Field:

- Two couples of ferrite magnets placed in the proximity of the PG entrance (main B field along horizontal y direction), see Fig. 102 b;
- A circuit including the plasma grid (PG) and a return pipe where a current up to 400 A can be flown. The generated magnetic field is mainly horizontal (along the x direction), see Fig. 103;

3) Deflection of co-extracted electrons

- 2 set of 4 SmCo bars placed in the extraction grid (EG) and in the post acceleration (PA, grounded) grid. Main field component along the horizontal y direction, see Fig. 102 c.

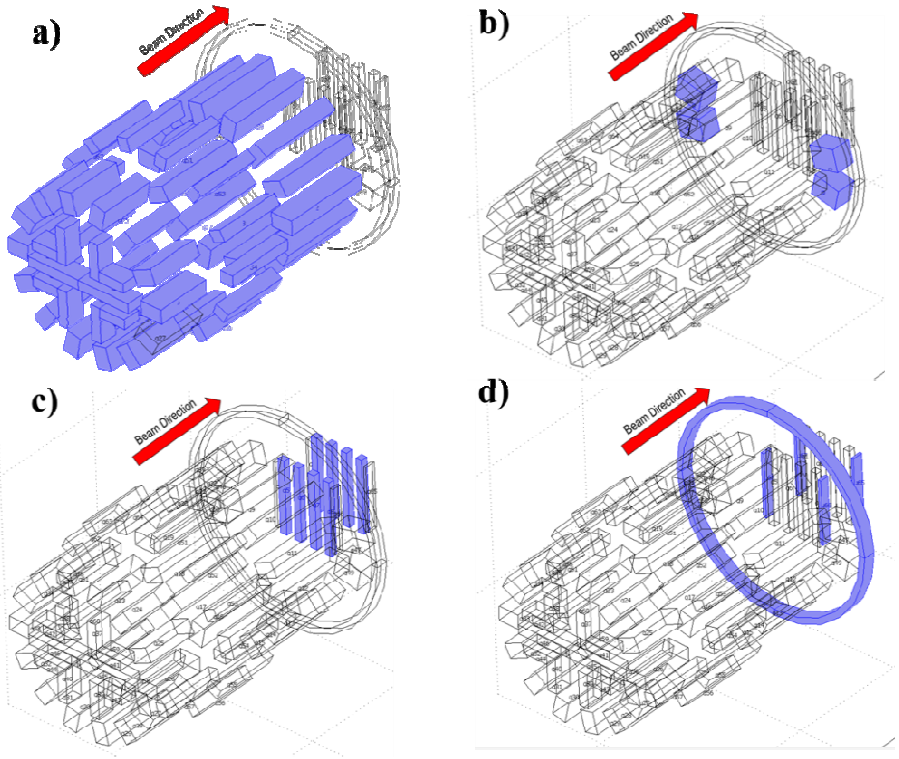

Fig. 102 Schematic of the permanent magnets and soft iron parts included in the NIO experiment. a) the cusp magnets used for plasma confinement, b) two couples ferrite magnets constituting the filter field, c) the magnets embedded in the accelerator grids to deflect the co-extracted electrons, d) the soft iron parts, to equalize field.

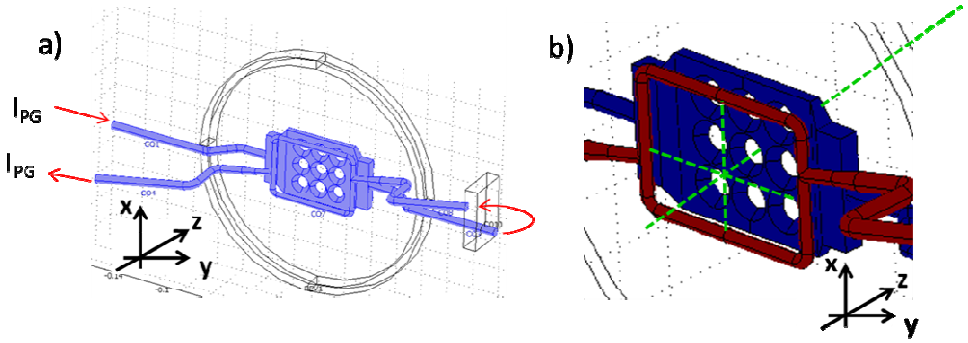

Fig. 103 Schematic of the PG circuit where up to 400 A are used to enhance the filter field.

During the collection of the data, the central and rear multipoles of the source have been removed. The measurements are focused on the cusp field on the front multipole (Bx,By), the axial field across the apertures of the accelerator (By) and the axial and transversal profile of the B field produced by the PG current (Bx).

2.5.3. Axial Profile of By along the accelerator

A series of 4 profiles of By along the beam direction z were taken. The profiles correspond to the center of 5 beamlets (out of the 9 beamlets of NIO1). The beamlets tested with the probe are painted with colors in Fig. 104. The position z=0 corresponds to the knife of the PG.

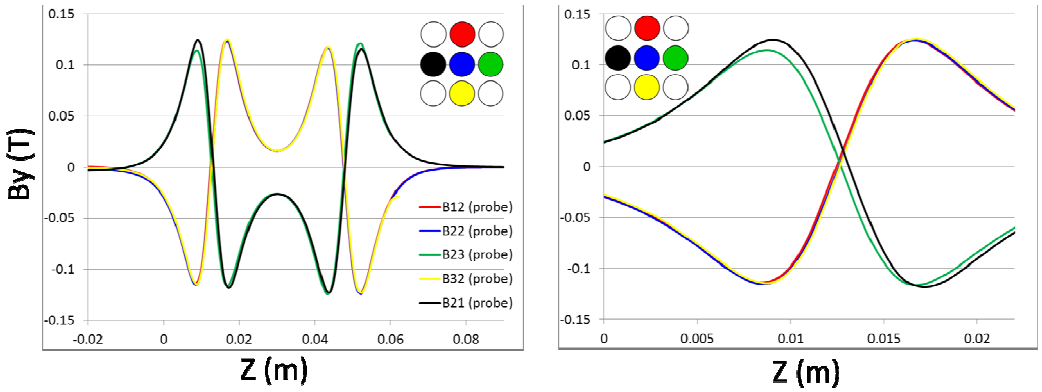

Fig. 104 Plot of the 4 profile of By against z measured with the gaussmeter.

A good uniformity of By was found for all the profiles tested. The measured data were also compared with numerical simulation implemented in COMSOL 3.5 environment. The comparison among measured and numerical values is given in Fig. 105.

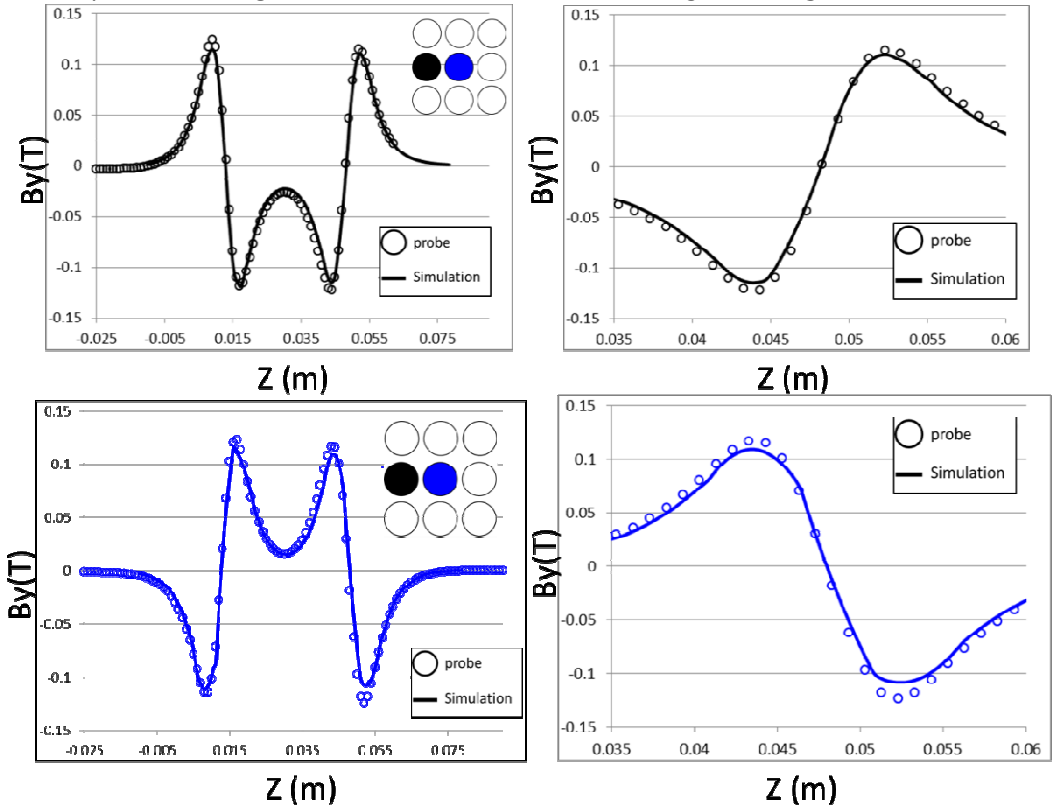

Fig. 105 Plot of the 2 profile of By against z measured with the gaussmeter and compared with the simulations made with COMSOL.

2.5.4. Measurements of Bx and By cusp field

A second set of data was collected at a fixed z position (z=-52 mm), i.e. in around the center of the front multipole, in order to test the cusp field used to confine the plasma. Several points were collected in the (x,y) plane, to cover ¼ of the cylindrical chamber (R=49 mm) with a resolution of one point measured each 4 mm. The resulting map of Bx, By and |B| is reported in Fig. 106.

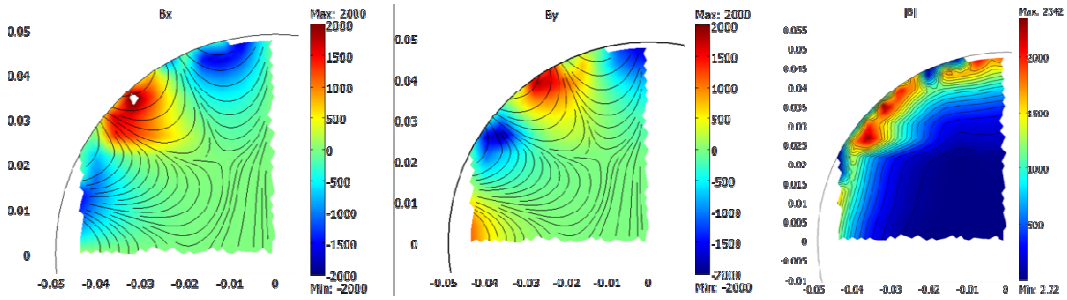

Fig. 106 Surface plot of the measured values of Bx, By and |B| in the ¼ plane tested with the probe. In the first two pictures the streamline of the field are also shown in black. (Black lines in the third picture are just the lines with constant |B|).

The cusp field pattern is well reproduced, and the values are in agreement with the expectations.

In order to check the B field values all around the chamber, the values of Bx and By along two lines at constant radii of R=25mm and R=40 mm have been measured, see Fig. 107 a:

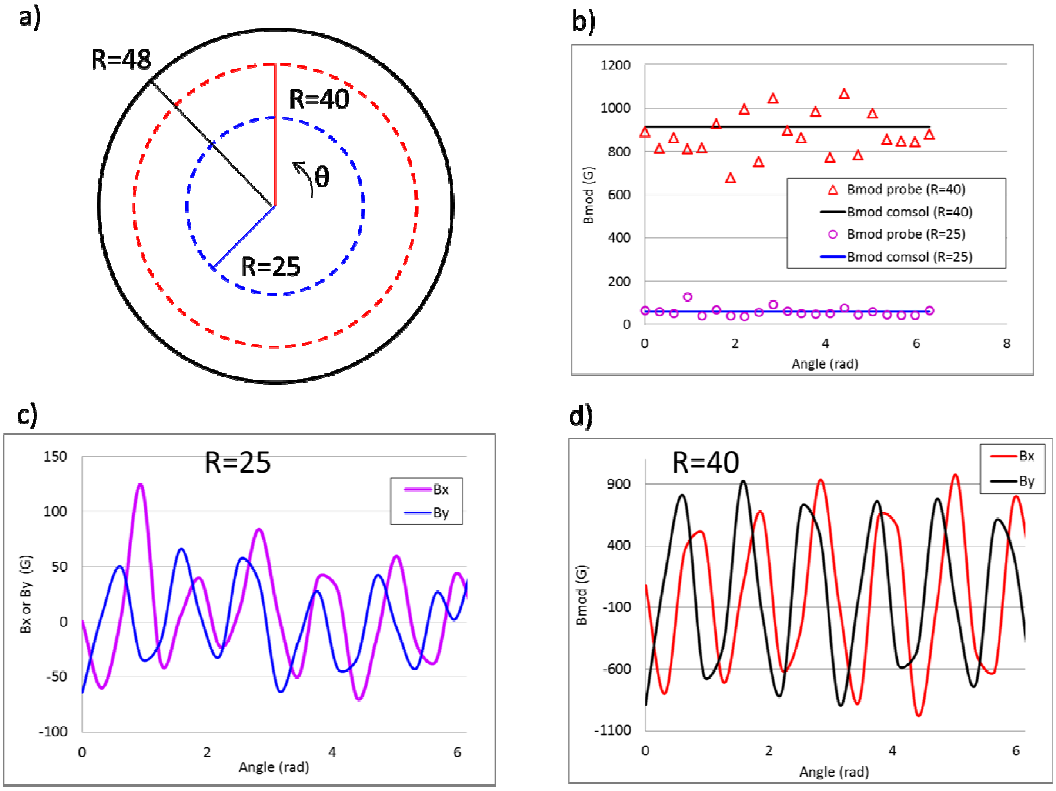

Fig. 107 a) a schematic of the circles where measures are taken, b) the values of the |B|, also compared with the values evaluated numerically with COMSOL, c) and d) the Bx and By components of the field are plotted at R=25mm and R=40mm respectively.

The profiles are quite "noisy" due to the difficulties in positioning the probe around a circular path. Moreover any small angle of the probe around its axis results in the pick-up of a fraction of the transversal field, especially in the vicinity of the cusp, where one component is much greater than the other. In spite of the low quantitative value of this kind of measures, they still prove the correct orientation of magnets in the cusp configuration: see in particular Fig. 107 d, where Bx and By are always anti correlated, as expected. The agreement with the COMSOL results, in terms of |B| (Fig. 107 b) is also satisfying.

2.5.5. Axial profile of Bx along the accelerator

The permanent magnets give no Bx nor Bz component along the source axis x = 0, y = 0. A Bx magnetic field can anyway be created by flowing a current I (up to 400 A) in the PG (see Fig. 103 b). In order to estimate its intensity, the Bx profile along the beam axis z, with I=0, I=50 A and I=100 A has been measured.

At first the Bx profile when I=0 has been measured. In this case no magnetic field was expected, but a small misalignment of the probe (rotation along its axis, or a non perfect alignment of the support structure) caused the By component of magnetic field to influence the Bx measure. In fact, in the profiles of Fig. 108, a profile similar to By profile (see Fig. 104 and Fig. 105) has been found, with peak intensity being just 3% of the By intensity.

Nevertheless, the expected values of Bx generated by the PG current is in the same order of magnitude of this error, hence the results of the numerical simulation have been compared with the difference between the Bx profile measured at I=100 A and the "background" Bx profile taken when I=0 A. The two profiles are reported in Fig. 108 a, and their difference, compared with the numerical expectations is reported in Fig. 108 b.

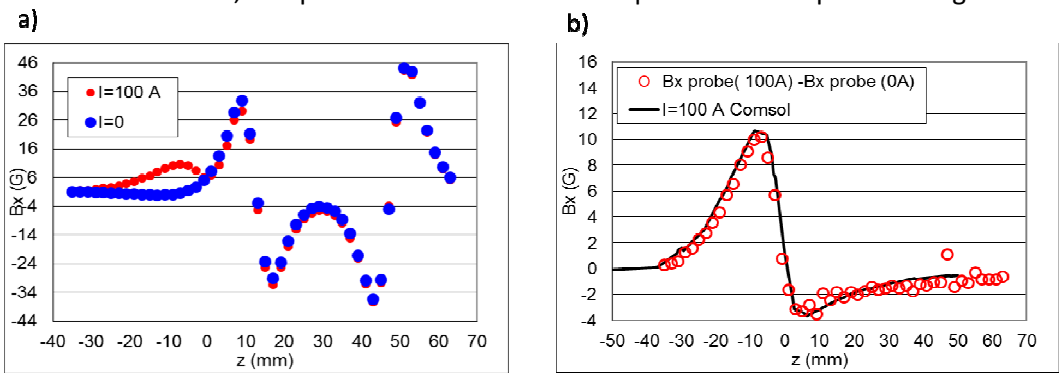

Fig. 108 a) measurement of Bx vs. z, at fixed x,y = (0,0) with I_{PG} = 0 and with I_{PG} = 100, b) difference between the two profiles compared with the COMSOL results.

It has been also verified that the profile taken when I=50A exactly matches ½ of the profile taken when I=100A.

Another set of measures of Bx has been taken at fixed z position (z=-17), along the x and y coordinates, i.e. along the green lines of Fig. 103 b. These data are reported in Fig. 109 and Fig. 110.

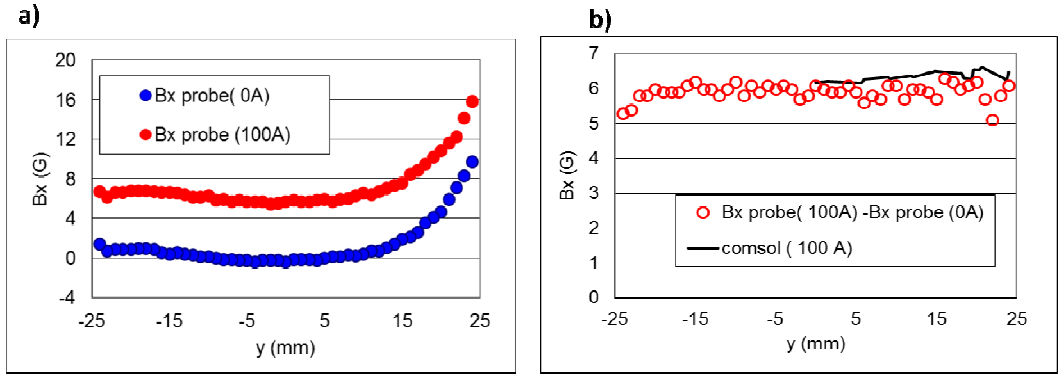

Fig. 109 a) measurement of Bx vs. y, at fixed z = -17 mm, x = 0 with I_{PG} = 0 and with I_{PG} = 100 A, b) difference between the two profiles, compared with the COMSOL results.

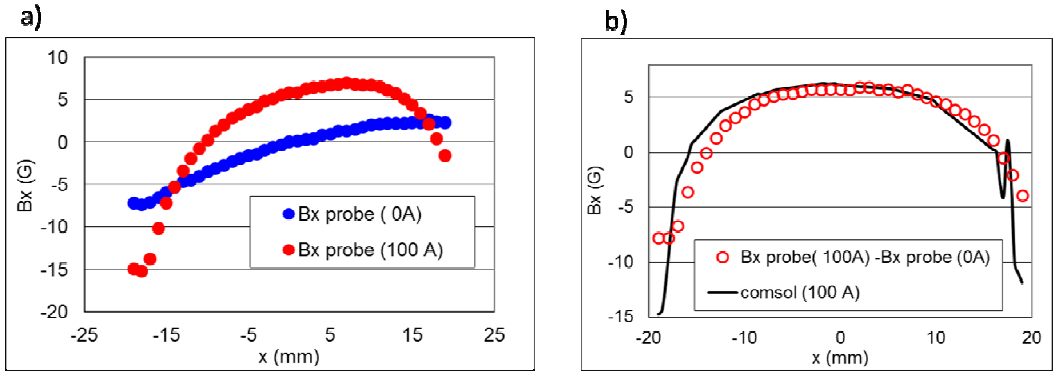

Fig. 110 a) measurement of Bx vs. x, at fixed z = -17 and y = 0 with I_{PG} = 0 and with I_{PG} = 100 A, b) difference between the two profiles, compared with the COMSOL results.

2.5.6. Check on the orientation of rear cover magnets

Finally, a test on the orientation of rear cover magnets has been made using a magnet polarization probe (Model: *Tridelta Magnetsysteme, Magnetpolanzeiger*). This test gives no quantitative measurement of the magnetic fields, but is useful to check the orientation of the permanent magnets. A schematic of magnets positioning is reported in Fig. 111. The magnet position and orientation is consistent with NIO1 drawings.

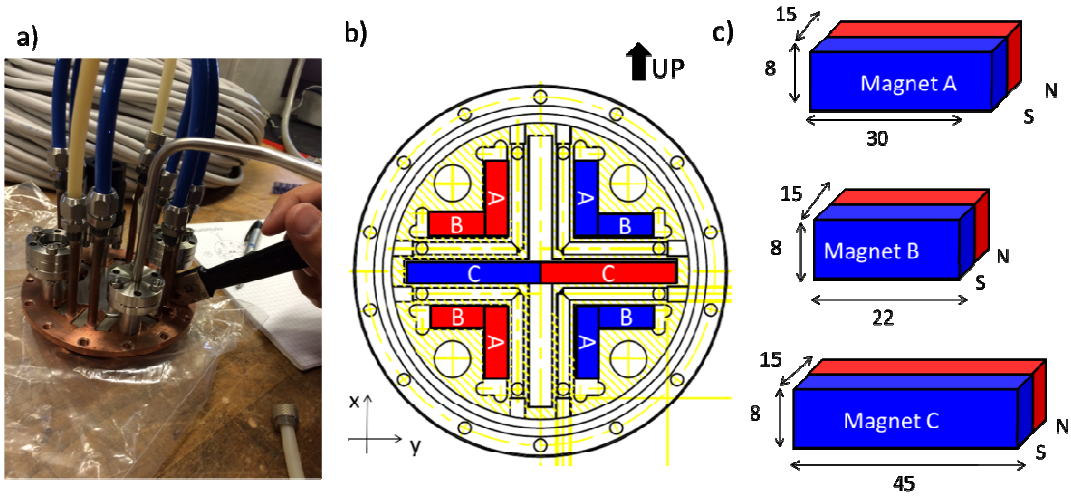

Fig. 111 a) picture of the rear cover of NIO1 and the magnetic direction probe, b) schematic of the magnet orientation (taken from outside the source) as it results from measurement, c) summary of the 3 types of magnets used in the rear cover. Sizes are in mm.

2.5.7. Simulations with NBImag

A model of NIO1 permanent magnets has been realized with the code NBImag, as shown in Fig. 112, in order to have an additional comparison with the results obtained by magnetic measurement and by COMSOL 3.5. The field By has been calculated along the same 5 apertures of Figure 4, reported with the same colors in Fig. 112:

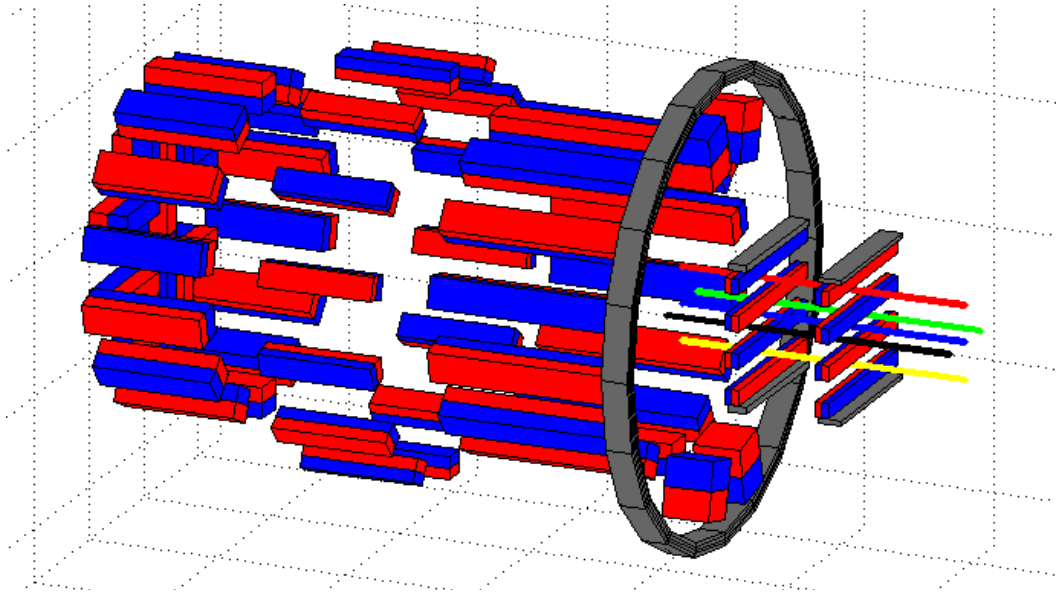

Fig. 112 NBImag model of NIO1 permanent magnets. Ferromagnetic elements are shown, but not calculated with NBImag. The colored lines indicate the 5 apertures along which By field has been calculated.

The results are in good agreement with the measured points and in consequence with COMSOL 3.5 results, as shown in Fig. 113, to be compared also with Fig. 105:

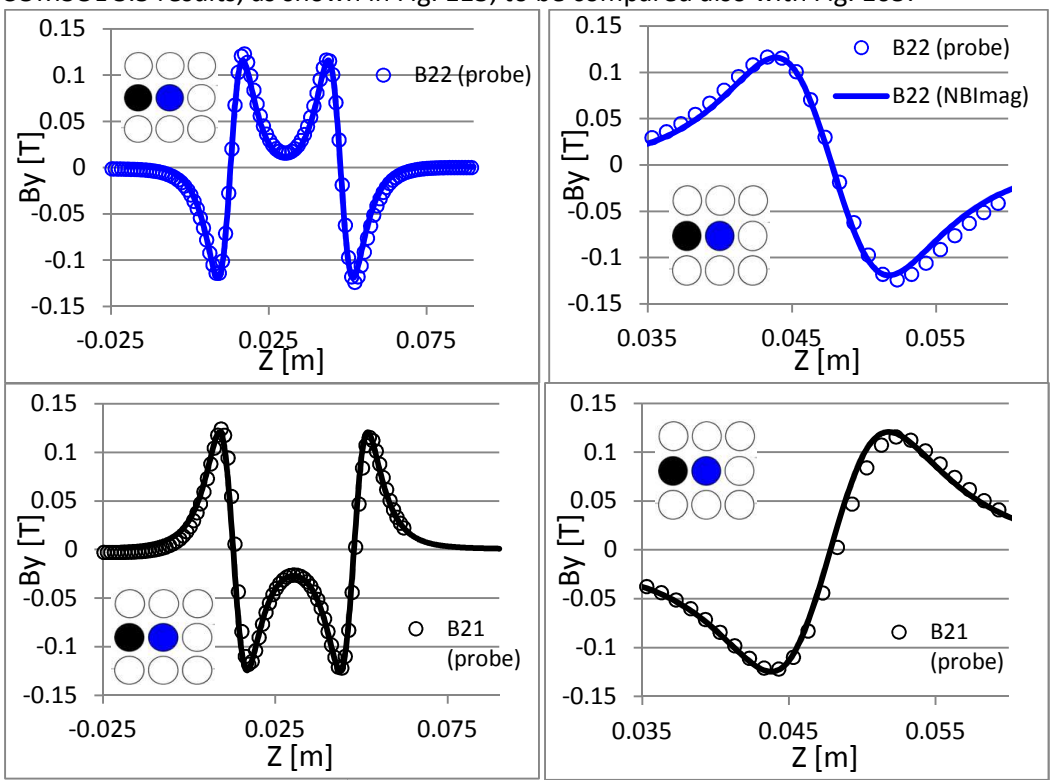

Fig. 113 Plot of the 2 profile of By against z measured with the gaussmeter and compared with the simulations made with NBImag for apertures 1-2 and 2-2 (black and blue respectively).

3. Code improvement activities

In this chapter the main results of the code improvement activities carried out on the magnetic code NBImag, developed at RFX, will be presented. The main of these improvements regard the calculation of magnetic force and inductance.

3.1. Introduction and problem description

A magnetic field calculation code, called NBImag, has been developed as a tool for the design and engineering optimization of MITICA and future Neutral Beam Injectors (NBI), (see sections 1.6. - 1.8.)

As mentioned in Par. 1.8.1. , the local electron-suppression magnetic field in MITICA accelerator is produced by permanent magnets embedded in the Extraction Grid (EG) and in the Acceleration Grids (AGs), each one of them being constituted by 16 Beam Groups (BG).

Each Beam Group contains 351 permanent magnets, for a total of 5616 in the whole accelerator.

Despite reduced models of MITICA accelerator can be realized exploiting symmetries, "collective" effects due to the mutual orientation of large arrays of permanent magnets belonging to different Beam Groups can have an effect on the long-range field, therefore larger models are worth to be studied.

Even considering linear materials and static system, none of the available commercial or freeware code was found suitable for modelling the magnetic field configuration in MITICA accelerator with acceptable detail level and computation time.

Recently, NBImag has been integrated with magnetic force and inductance calculation, extending its applicability to the entire magnetic design of a negative ion accelerator.

Thanks to the capability of efficiently describing a large number of permanent magnets with limited computational effort, NBImag is suitable for the solution of inverse magnetic problems by means of automatic optimization procedures. In fact, NBImag has been successfully used, in combination with various optimization algorithms, for the achievement of the optimal magnetic field inside MITICA, leading to the minimization of electron heat loads on the acceleration grids and to the cancellation of the undesired ion deflection [16].

3.2. Formulation of force and inductance calculation

The force and inductance calculation exploits the already existing architecture of the code for magnetic induction and vector potential calculation, whose accuracy has been validated through benchmarks against other magnetic field codes and experimental measurements on accelerator grid prototypes. The formulation relies on the efficient numerical integration of the Biot-Savart law, considering all the magnetic field sources (coils, busbars and permanent magnets) as composed by solid elements having 8 nodes. The current density distribution inside each element is carefully defined so as to intrinsically satisfy the equation: $\nabla \cdot \boldsymbol{J} = 0$. Hard permanent magnets are modelled using a solid equivalent current sheet having finite thickness, exploiting the Ampére's equivalence principle. No model is required for the surrounding space and no matrix inversion is needed.

Magnetic force is calculated by integrating $\boldsymbol{J} \times \boldsymbol{B}$ over the volume of the active object on which the resulting force is requested. Being Ω the domain of all the field sources and

α one of its subdomains, e. g. a single magnet or coil or busbar, substituting the expression of Biot Savart law, the following equation for the force acting on the subdomain α is obtained:

$$F_\alpha = \int_\alpha \boldsymbol{J}(\boldsymbol{r}) \times \frac{\mu_0}{4\pi} \int_\Omega \frac{\boldsymbol{J}(\boldsymbol{r}') \times (\boldsymbol{r} - \boldsymbol{r}')}{|\boldsymbol{r} - \boldsymbol{r}'|^3} \, d^3\boldsymbol{r}' \, d^3\boldsymbol{r}$$

The integrals are solved using the Gauss quadrature formulae and the integration order in each of the three directions (the number of Gauss points) is chosen between 1 and 24 depending on the geometry of the elements and the distance with respect to the calculation point. The singularity arising when calculating the force produced by an element to itself ($\boldsymbol{r} = \boldsymbol{r}'$ in the denominator) is eliminated by neglecting all the force contribution produced by the whole subdomain α on itself, since these contributions must be self-equilibrated (a single magnet or coil cannot produce a net resulting force on itself), leading to the modified equation:

$$F_\alpha = \int_\alpha \boldsymbol{J}(\boldsymbol{r}) \times \frac{\mu_0}{4\pi} \int_{\Omega-\alpha} \frac{\boldsymbol{J}(\boldsymbol{r}') \times (\boldsymbol{r} - \boldsymbol{r}')}{|\boldsymbol{r} - \boldsymbol{r}'|^3} \, d^3\boldsymbol{r}' \, d^3\boldsymbol{r}$$

Thanks to this position, singularities are eliminated and computational time is further reduced.
The integral expression for the mutual inductance between two coils, identified by the subdomains α and β, is obtained by substituting the expression of magnetic vector potential into the integral of $\boldsymbol{J} \cdot \boldsymbol{A}$:

$$M_{\alpha,\beta} = \int_\alpha \boldsymbol{J}(\boldsymbol{r}) \cdot \frac{\mu_0}{4\pi} \int_\beta \frac{\boldsymbol{J}(\boldsymbol{r}')}{|\boldsymbol{r} - \boldsymbol{r}'|} \, d^3\boldsymbol{r}' \, d^3\boldsymbol{r}$$

This expression is valid also for calculating self-inductance of a coil, but in this case, since $\alpha \equiv \beta$, there is again an arising singularity when an element is acting on itself, so $\boldsymbol{r} = \boldsymbol{r}'$. In this case, these terms cannot be neglected, and the singularity has been eliminated by avoiding the situation in which the Gauss integration order is the same for the element considered as active (first integral) and the element considered as source (second integral). If the orders are different, Gauss points do not coincide and the singularity $\boldsymbol{r} = \boldsymbol{r}'$ is avoided.

3.3. Validation of Force calculation between Permanent Magnets

This validation, along with the following inductance validations, constitutes also an accurate validation of magnetic field calculation in all the domains. In fact, the force and inductance calculation is precise only if **B** and **A** are calculated very precisely everywhere, especially inside the field sources.
The forces calculated between pairs of permanent magnets have been compared and benchmarked against the analytical formula proposed in [37] by Akoun et al. for cuboidal magnets with parallel faces. An example is shown graphically in Fig. 114; the numerical results are reported in Tab. 10:

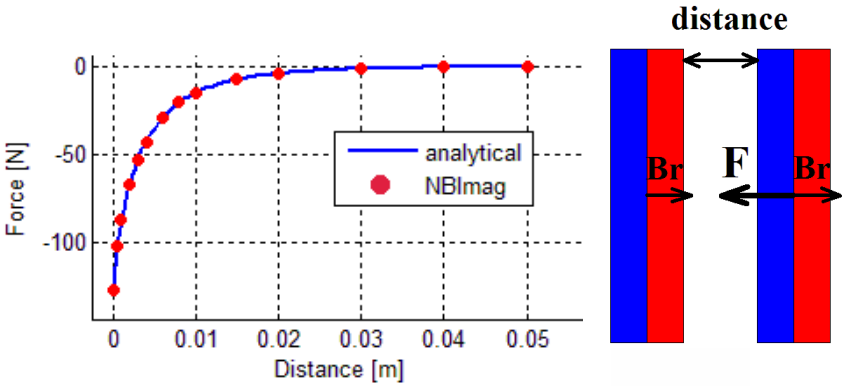

Fig. 114. Force between two parallel magnets having size 10x40x10 *mm* and equal magnetization ($B_r = 1.1\ T$).

d [*m*]	F [*N*] analytical	F[*N*] NBImag	% error
0	127.9198	127.0589	0.6730
0.0005	102.7928	102.7900	0.0027
0.001	87.8612	87.8592	0.0023
0.004	43.1809	43.1790	0.0044
0.010	15.2087	15.2053	0.0224
0.050	0.8112	0.8103	0.1109

Tab. 10 Force between two parallel magnets having size 10x40x10 *mm* and equal magnetization ($B_r = 1.1\ T$).

The analytical formula is very fast in computing the result, and NBImag computational time was slightly longer: $t \sim 2\ s$ in this case. The results are in good numerical agreement.

In order to evaluate the computational efficiency of NBImag with respect to a method that is applicable to realistic magnet geometry (without the limitations of the analytical approach), a comparison has been made with the FEM code ANSYS. In order to have a fair comparison, the geometry considered is still the same of the previous case, with fixed distance $d = 0.010\ m$ between the two magnets. Three ANSYS models have been realized with increasing detail level, the first two considering only 1/8 of the domain and different mesh coarseness, and the last one with full domain and very fine mesh. The results are reported in Tab. 11:

	ANSYS 1/8 domain, coarse mesh	ANSYS 1/8 domain, interm. mesh	ANSYS full domain, fine mesh	NBImag and analytical
F [*N*]	11.60	13.94	14.93	15.21
comp. time	20 *s*	2 m 14 *s*	4 *h*	$\leq 2\ s$

Tab. 11 Force calculation between two permanent magnets having size 10x40x10*mm*, at distance $d = 0.010\ m$, and with equal magnetization ($B_r = 1.1\ T$).

As shown in Tab. 11, the first two models are affected by a numerical error of 9% and 24% respectively. The last model shows an error of 2% only, but its computation time is very high.

A practical application of NBImag is shown in Fig. 115. This is the model of all the magnets (5616) embedded in five of the seven MITICA accelerator grids (see Fig. 12). These grids are actually not planar, but mounted in 16 groups having slightly different orientation for achieving the correct beam aiming on the target. Magnetic field and

force calculation needs to be performed on thousands of magnets without losing the information relative to the overall effect of a large group of alternately oriented magnets, information that is inevitably lost in a reduced model or in a FEM model.

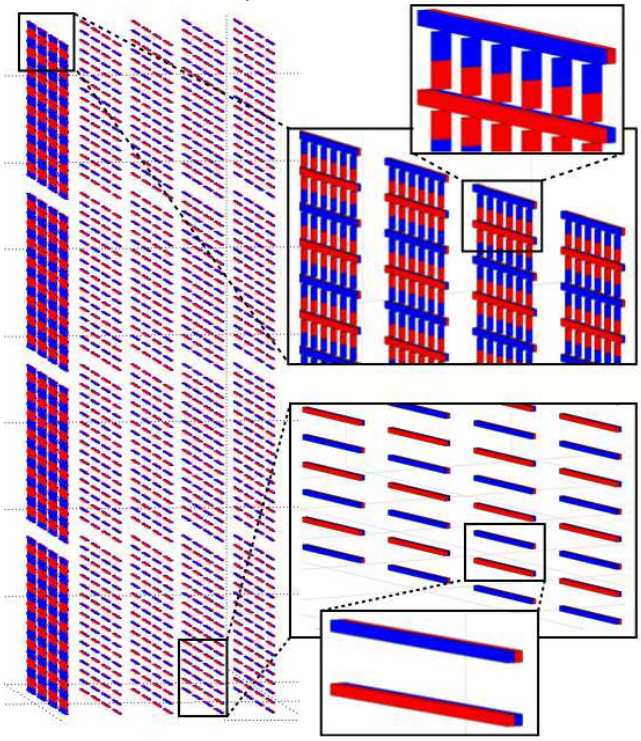

Fig. 115 Model of all the magnets embedded in the Extraction Grid and the four Acceleration Grids of MITICA. There are in total 5616 permanent magnets.

In this very large model, computation time for a force calculation on a single magnet is about 11 minutes.

Force calculation was necessary here for the definition of an appropriate assembly procedure of the magnet array and for the calculation of the overall force acting between two entire grids. One example is shown in Fig. 116, showing the force acting on the magnets during the assembly of the first rows of one of the 16 groups of the Extraction Grid:

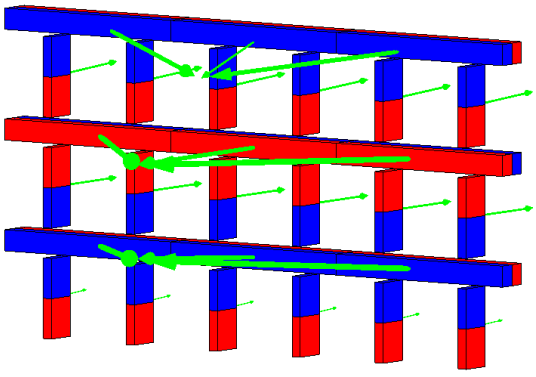

Fig. 116 Forces acting on the magnets during the assembly of the first rows of one of the 16 groups of the Extraction Grid.

3.4. Validation of Force calculation between Coils

Optimization and validation of force calculation between coils has been made against the results obtained by Ravaud et al. in [38] by a semi-analytical method called

Amperian Current Method, which is there compared with the filament method and the FEM code FLUX3D.
Two examples are reported in Tab. 12 and Tab. 13:

d [*m*]	Ravaud (amperian curr.) [*mN*]	Ravaud (filament) [*mN*]	Ravaud (Flux 3D) [*mN*]	NBImag [*mN*]
0.01	128.046	128.172	128	128.026
0.03	73.056	73.139	72	72.959
0.05	46.709	46.773	47	46.633
0.10	18.755	18.793	17	18.712
0.20	4.438	4.451	4	4.412

Tab. 12 Force between two circular coils with same dimension ($R_{ext} = 0.1125\ m$, $R_{int} = 0.0875\ m$, $l = 0.025\ m$, $I = 200\ A$), at distance *d*.

d [*m*]	Ravaud (amperian curr) [*mN*]	Ravaud (filament) [*mN*]	(Ravaud) Flux 3D [*mN*]	NBImag [*mN*]
-0.30	0	0	0	0
-0.15	70.106	70.401	70	70.479
0	76.708	77.003	78	77.068
0.05	66.488	66.731	67	66.778
0.30	22.269	22.279	21	22.269
1.00	1.679	1.672	n. a.	1.666

Tab. 13 Force between two circular coils with different dimension ($R_{1,ext} = 0.2\ m$, $R_{1,int} = 0.1\ m$, $l_1 = 0.2\ m$, $I_1 = 400\ A$, $R_{2,ext} = 0.4\ m$, $R_{2,int} = 0.3\ m$, $l_2 = 0.4\ m$, $I_2 = 800\ A$), at distance *d*.

In these cases, maximum NBImag computation time is about 40 s (when the two coils are very close to each other, $d \leq 0.01\ m$).

3.5. Validation of self-inductance calculation

The optimization and validation of self-inductance calculation has been made mainly against the method proposed by Garrett in [39], which makes use of elliptic integrals. Some results are given in Tab. 14 for single-turn coils of different size.

R_{ext} [*m*]	R_{int} [*m*]	*l* [*m*]	L (Garrett) [*μH*]	L (NBImag) [*μH*]	% error
0.002	0.001	0.001	0.00254	0.00255	-0.3921
0.050	0.045	0.010	0.16318	0.16294	0.1473
0.100	0.060	0.100	0.11346	0.11315	0.2740
0.800	0.600	0.050	2.2840	2.3027	-0.8121
1.4	1.2	0.200	4.5031	4.5095	-0.1419

Tab. 14 Self-inductance of circular coils calculated with Garrett's method and NBImag.

The results are always in a very good agreement. NBImag computation time was typically $t \sim 15\ s$.
Another example has been taken from Conway [40]. Conway's method involves Bessel and Struve functions and computer mathematical packages. The geometry in this case is:
$R_{ext} = 0.044\ m$, $R_{int} = 0.032\ m$, $l = 0.040\ m$, $n = 48$.
The results are again in good agreement:

$$L_{Conway} = 148.0832\ \mu H$$
$$L_{NBImag} = 147.5068\ \mu H$$

3.6. Validation of mutual inductance calculation

Results of mutual inductance of coils have been benchmarked against the results of Ravaud et al. in [38] and Akyel et al. in [41]. A comparison between Ravaud's semi-analytical method and NBImag is shown in Tab. 15:

d [m]	Ravaud et al. [mH]	NBImag [mH]	% error
0	0.77539	0.77384	0.1999
0.005	0.57129	0.57013	0.2030
0.01	0.43483	0.43387	0.2208
0.02	0.26678	0.26590	0.3299
0.03	0.17295	0.17220	0.4337
0.05	0.08232	0.08257	-0.3037

Tab. 15 Mutual inductance between two circular coils with same dimension ($R_{ext} = 0.030\ m$, $R_{int} = 0.025\ m$, $l = 0.025\ m$, number of turns $n = 200$), at distance d.

NBImag maximum computation time was in this case $t \sim 10\ s$ (for $d = 0$).

The next two examples are taken from Akyel et al. [41] and involve coils of particular shape: the thin wall solenoid and the thin disk coil (pancake). These are for showing that NBImag results are still good even when some coil dimensions tend to zero. In the first example, mutual inductance is calculated between two identical thin wall solenoids, with parallel axes and no axial displacement. In this case $R_{ext} \approx R_{int} = 0.025\ m$, $l = 0.050\ m$, distance between axes $= 0.250\ m$, number of turns $n = 125$, and:

$$M_{Akyel} = -0.3826\ \mu H$$
$$M_{NBImag} = -0.3852\ \mu H$$

In the second example mutual inductance is calculated between two single-turn thin disk coils (pancakes) with following geometry: $R_{1,ext} = 1.5\ m$, $R_{1,int} = 1\ m$, $R_{2,ext} = 2\ m$, $R_{2int} = 1.2\ m$, $l_1 = l_2 \approx 0$, distance between axes $= 0.2\ m$, axial displacement $= 0.25\ m$. The results are:

$$M_{Akyel} = 2.2720\ mH$$
$$M_{NBImag} = 2.2687\ mH$$

The results in these two examples are in good agreement. NBImag computation time was $t \sim 3\ s$ in both cases.

3.7. Conclusions

Validation of force calculation between permanent magnets has been made through comparison with the analytical formulae proposed by Akoun et al. in [37]. The results were in very good numerical agreement. A comparison has been made also with the FEM code ANSYS and it showed that for reaching the same precision of NBImag, a FEM code needs a computational effort larger by some orders of magnitude, which in the case of complicate geometry might be impracticable.

Validation of force calculation between circular coils has been made through the results obtained by Ravaud et al. in [38] by a semi-analytical method.

Regarding the validation of self-inductance calculation, NBImag results have been benchmarked against Garrett' method [39], which makes use of elliptic integrals, and

against the results obtained by Conway [40] by a procedure involving Bessel and Struve functions. In every case the results were in very good agreement.
Finally, validation of mutual inductance calculation has been made through benchmark and comparison against the results obtained by Ravaud et al. in [38] and by Akyel et al. in [41], showing again a good numerical agreement between the results in every analyzed geometry.
In this work the formulation and successful validation of the recent improvements to the code NBImag have been presented. The code is daily used for magnetic design of the negative ion accelerators which are under construction in Padua, in which thousands of permanent magnets, in combination with several busbars and coils, are present.

4. Non ideal, off-normal and failure conditions analysis of MITICA accelerator

The actual conditions expected for the MITICA accelerator operation are in many cases different from the ideal conditions considered during the accelerator design. This difference is due primarily to small simplifying assumptions which have been introduced to reduce the complexity of the numerical models used during the design of the MITICA device.
The non-ideal conditions of MITICA concerning the magnetic configuration, the electrostatic configuration, the gas pressure configuration, the grid deformations etc., are here defined. The impact of the combination of these conditions on the injector operation is analysed in detail.
The off-normal operating conditions of the MITICA, i.e. the operating conditions which take place because of the failure or malfunction of one or more components, have also been considered in this section
As these conditions can in principle produce further damages to the device, a series of analyses has been performed in order to assess the consequences and to find possible solutions.

4.1. Introduction

The magnetic configuration of MITICA accelerator has been described in Par. 1.8.1. , and is here recalled.
The transverse magnetic field in the MITICA accelerator has been designed considering two components:

- a "local" component, produced by permanent magnets embedded inside the Extraction Grid (EG) and the four Accelerator Grids (AG1-AG4). This component is vertical has a relatively small range of action in the vicinity of the apertures;
- a "long-range" component, produced by currents flowing in the Plasma Grid (PG) and in the related busbars. This component is horizontal and almost uniform in the accelerator.

These two components have been carefully optimized to minimize the heat loads produced by electrons on the MITICA accelerator grids [16].
The "long-range" component has been calculated considering the full geometry of the PG busbars (see [31]).
On the other hand, the "local" component has been calculated considering only a partial geometrical model of the accelerator grids.
Each grid is composed of 16 separate Beam Groups (BG), arranged as a 4x4 matrix. Each BG is constituted by 5 apertures with 20 mm pitch in the horizontal direction, and by 16 apertures with 22 mm pitch in the vertical direction (see Fig. 117).

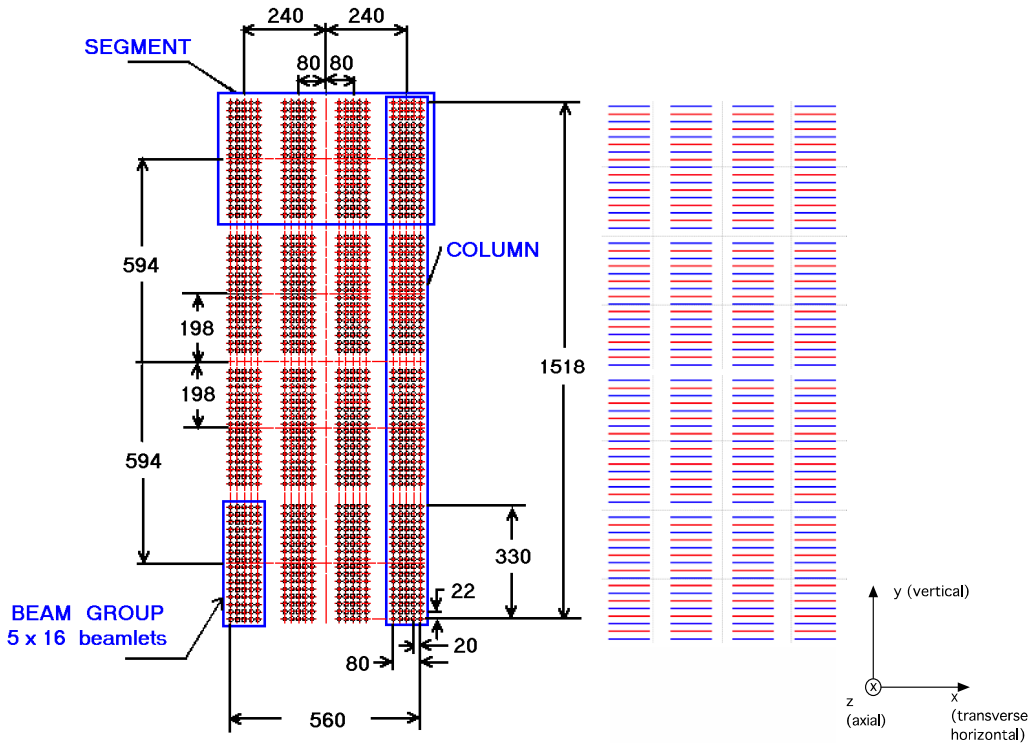

Fig. 117 Front view of a MITICA accelerator grid, showing 4 x 4 Beam Groups (BGs), each constituted by 16x5 apertures (left). Each Beam Group includes 17 magnets located just above and below the apertures. These magnets are magnetized along the axial direction (z) with alternate orientation (right) and produce a vertical magnetic field By across the apertures.

Inside each BG of the Accelerator Grids (AG1-AG4), there are 17 horizontal arrays of "Stripped Electron Suppression Magnets" (SESM) having a section of 6.6x4.2 mm. The 17 SESM arrays are magnetized along the accelerator axis direction (z) and their polarity is alternated row by row.
Inside each BG of the Extraction Grid (EG) there are 17 horizontal arrays of "Co-extracted Electron Suppression Magnets" (CESM), having the same magnetization direction as SESM and section of 6x4 mm. There are also 16 "Asymmetric Deflection Compensation Magnets" (ADCM) having a section of 6.6x1.95 mm.
Adjacent BGs are separated by an edge of 80 mm (corresponding to 4 aperture pitches) in the horizontal direction and of 66 mm (3 aperture pitches) in the vertical direction. In this edge no apertures and no magnets are present.
The calculation and optimization of the "local" field produced by the permanent magnets was carried out considering only one BG, since the magnetic configuration inside each BG is indeed little dependent on the presence of the magnets in the other BGs, whereas the full magnet geometry is very cumbersome.
However, the net magnetic flux across a single BG is non-zero because it is constituted by an odd number (17) of magnet arrays with alternate orientation. When the 16 BGs are assembled together on a single grid, we could expect a "cumulative" effect which depends on the relative orientation of the net magnetic flux produced by adjacent BGs.
In the first part of this section, the "non ideal" operating condition caused by this (previously disregarded) "cumulative" effect is evaluated.
In the same part, also the effects of mechanical tolerances of grid grooves and the effects of real orientation of Beam Groups towards the beam target located at 25.4 m are evaluated.

In the second part, the "off-normal" operating conditions, corresponding to faults such as demagnetization of permanent magnets are considered and their effect evaluated.

4.2. Non ideal operating conditions

4.2.1. Cumulative effects of permanent magnets in the 16 BG grid model

A numerical model of all the magnets (5616) embedded in the MITICA accelerator grids has been implemented using NBImag in order to evaluate possible cumulative effects. Since each Beam Group is composed by an odd number of magnet arrays (17) with alternate orientation, each Beam Group produces a net magnetic field in the beam axis direction (z) that is amplified or reduced depending on the relative orientation of the 16 BG in each grid.

A study of two different layouts, uniform orientation one and "chessboard" orientation, see Fig. 118, has been made in order to evaluate and possibly reduce the afore-mentioned global effect.

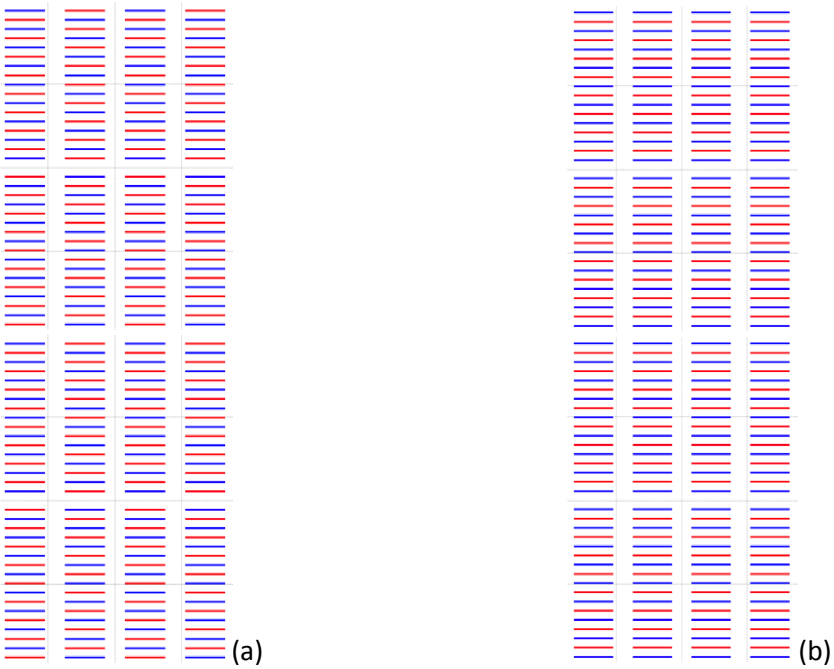

Fig. 118 Two layouts considered for Beam Group orientation inside the accelerator grids: (a) uniform orientation, (b) chessboard orientation.

Magnetic field profiles and ion deflection have been calculated for both configurations along the 21 paths shown in Fig. 119 in order to evaluate the uniformity within the whole grid.

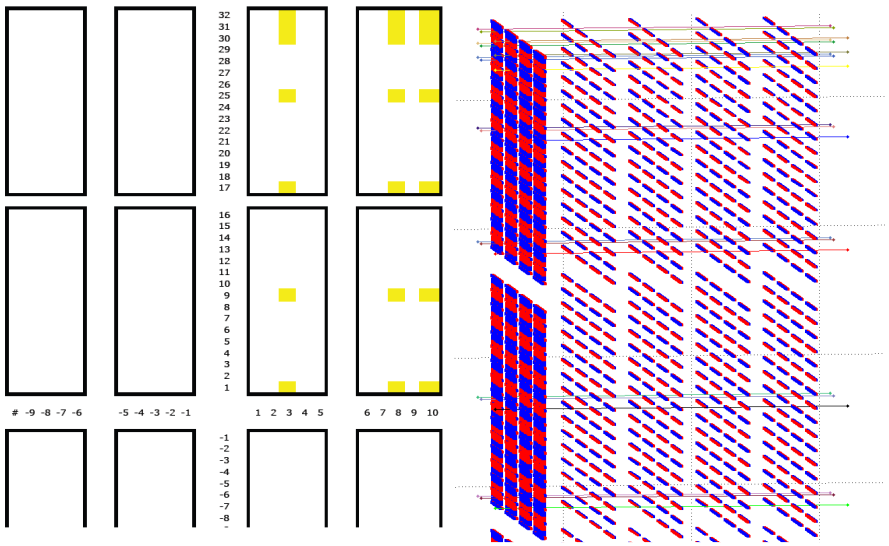

Fig. 119 Path positions considered for magnetic field calculation.

The vertical component of magnetic field (By) along 21 axial paths is shown in the next figures for both layouts (a) and (b):

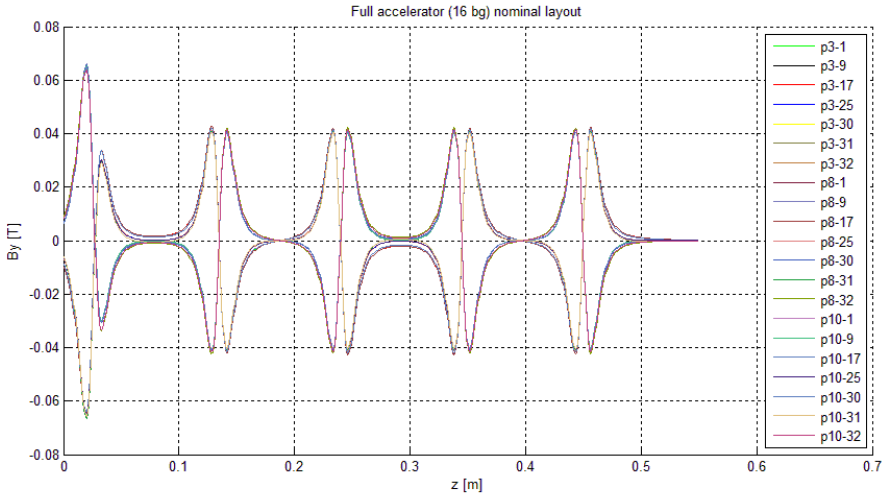

Fig. 120 By profile along 21 paths for layout (a) (uniform orientation).

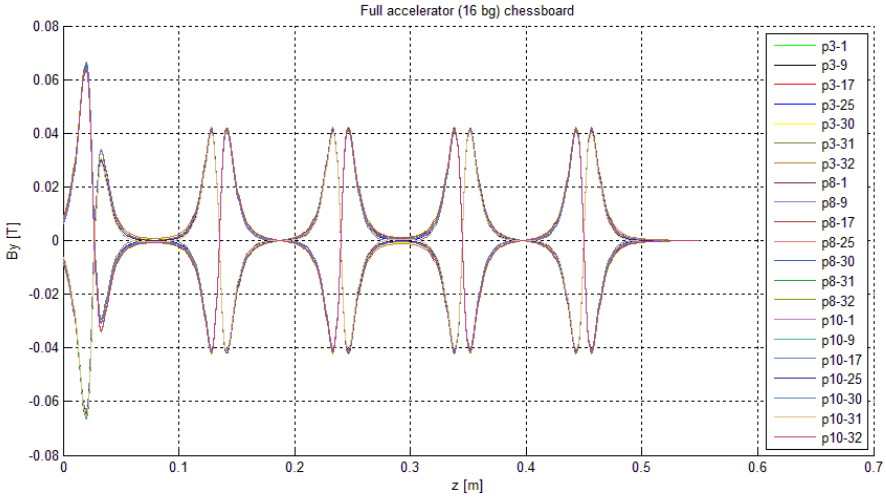

Fig. 121 By profile along 21 paths for layout (b) (chessboard orientation).

The By profiles on all paths in the 16 BG grid model indicate that the edge effects are small despite the size of the whole grid: the profiles are uniform within 2 mT, both with layout (a) and (b).
Only small differences can be noticed between layout (a) and (b). The chessboard layout (b) seems to produce a more uniform profile in some parts. An enlarged view is given in Fig. 122:

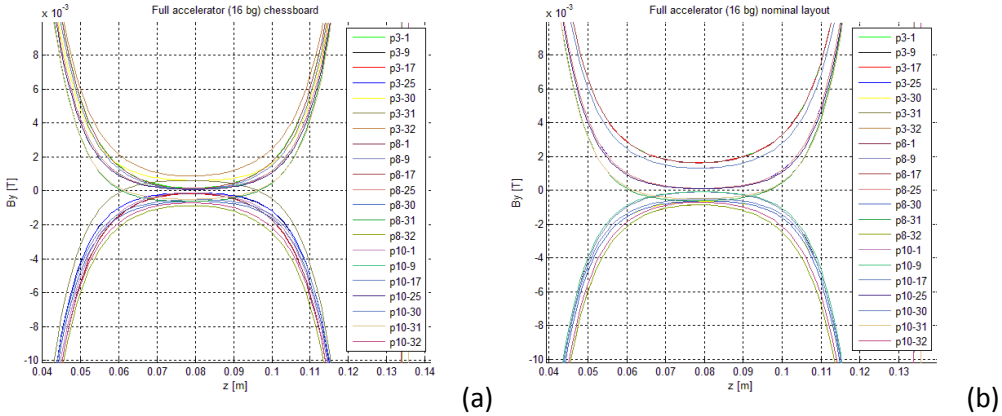

(a) (b)

Fig. 122 By profile uniformity in a zoomed region: (a) uniform orientation, (b) chessboard orientation.

The component of magnetic field along x-direction is shown in Fig. 123 and Fig. 124:

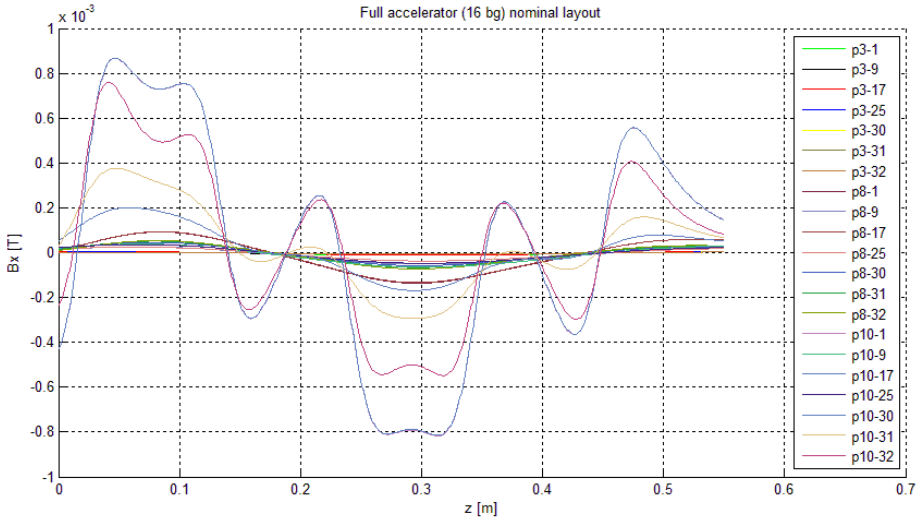

Fig. 123 Bx profile along the 21 considered paths in the layout (a) (uniform orientation).

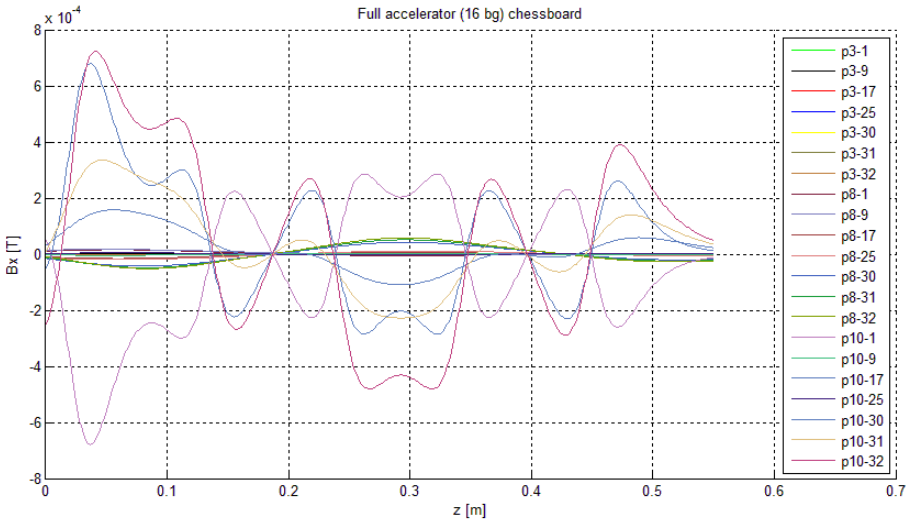

Fig. 124 Bx profile along the 21 considered paths in layout (b) (chessboard orientation).

No peculiar feature can be noticed in the Bx profiles. The profiles are similar for the two different layouts (a part from some reversed profiles), the order of magnitude is the same and in any case smaller by a factor of 100 with respect to By component.
Larger differences are expected from the Bz profile that should show the different global effect of the two configurations. Bz profiles are shown in Fig. 125 and Fig. 126:

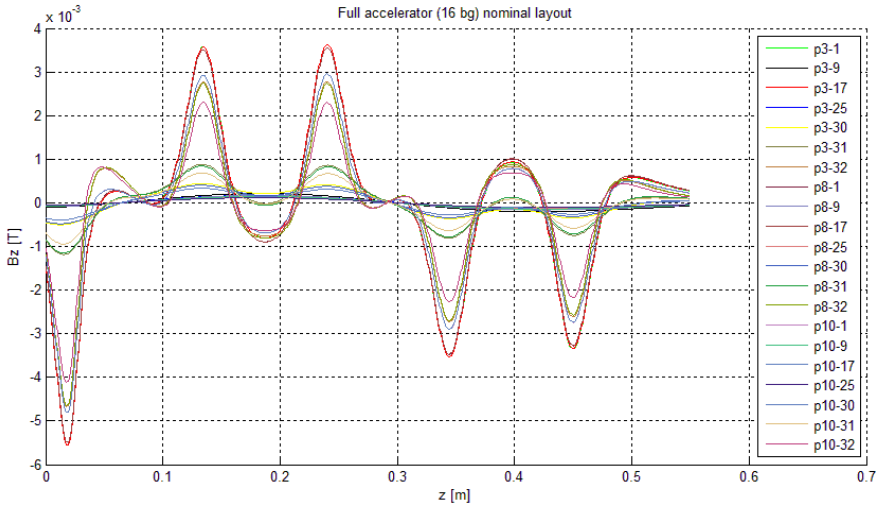

Fig. 125 Bz profile along the 21 considered paths for layout (a) (uniform orientation).

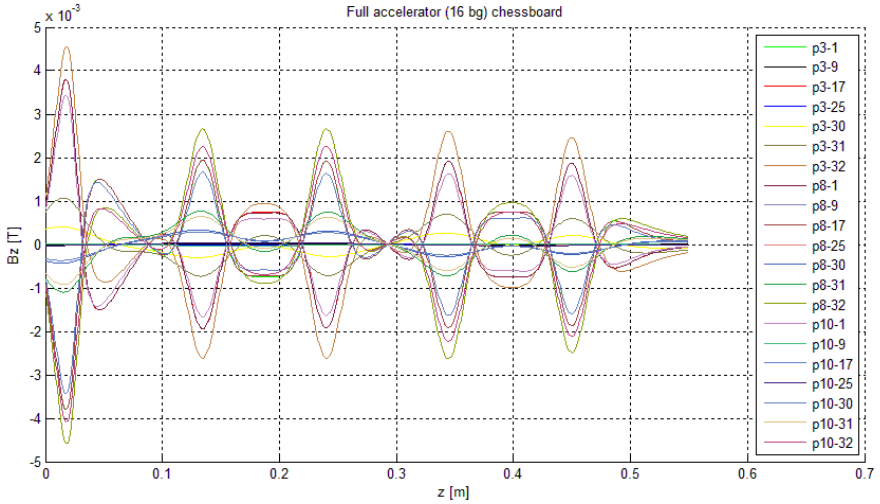

Fig. 126 Bz profile along the 21 considered paths for layout (b) (chessboard orientation).

The last two Fig. show that the axial component of the magnetic field, Bz, is very small ($<2*10^{-4}$ T) in the central apertures of each Beam Group and is about one order of magnitude larger ($4*10^{-3}$ T) in the upper and lower apertures of each Beam Group, showing a clear edge effect.

In order to have a clear evaluation and comparison of global effect in the two layouts, Fig. 127 reports a comparison of the Bz profile for aperture 3-9 only (the central of the most internal Beam Group) calculated considering three cases: 16 BG with uniform BG orientation (nominal layout), 16 BG with chessboard orientation and also single Beam Group.

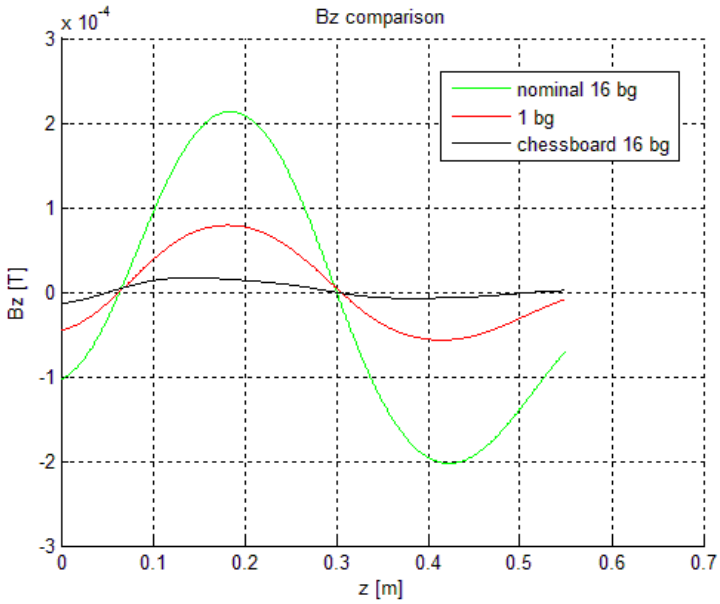

Fig. 127 Comparison of Bz profile calculated along the same aperture in three different models: 16 BG with uniform orientation (nominal), 16 BG with chessboard orientation and single BG.

From this figure it's clear that there is a global effect due to the odd number (17) of magnet arrays in each Beam Group, 8 with an orientation and only 7 with the opposite orientation. A net component of magnetic field along z-direction can be observed already in the single BG model, and then this effect is amplified in the nominal 16 BG model, because all the 16 Beam Groups have the same orientation in this layout (see Fig. 118).

In the chessboard layout instead, the Bz component is much lower, due to the fact that the Beam Groups have alternate orientation and so the number of magnets with opposite orientation is globally the same.

However, there are no appreciable differences in By profile in the three models, as it is shown in Fig. 128:

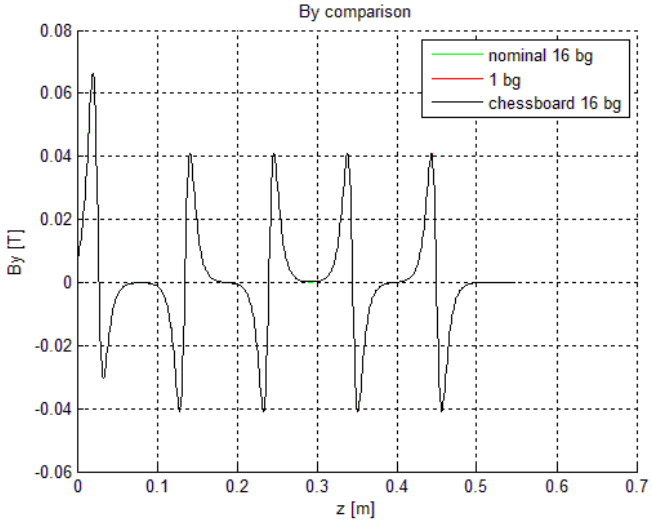

Fig. 128 Comparison of By profile calculated along the same aperture in three different models: 16 BG with uniform orientation (nominal), 16 BG chessboard and single BG.

In order to have quantitative comparison between the two layouts, the ion deflection due to By component has been calculated with the paraxial approximation formula:

$$\delta = \frac{v_{x,exit}}{v_{z,exit}} = \frac{q\int_{z_0}^{z_{exit}} B_y\, dz}{m\, v_{z,exit}} = \sqrt{\frac{q}{m}}\,\frac{\int_{z_0}^{z_{exit}} B_y\, dz}{\sqrt{2\, U_{exit}}}$$

Fig. 129 and Fig. 130 show an overall view of the ion deflection in the two models:

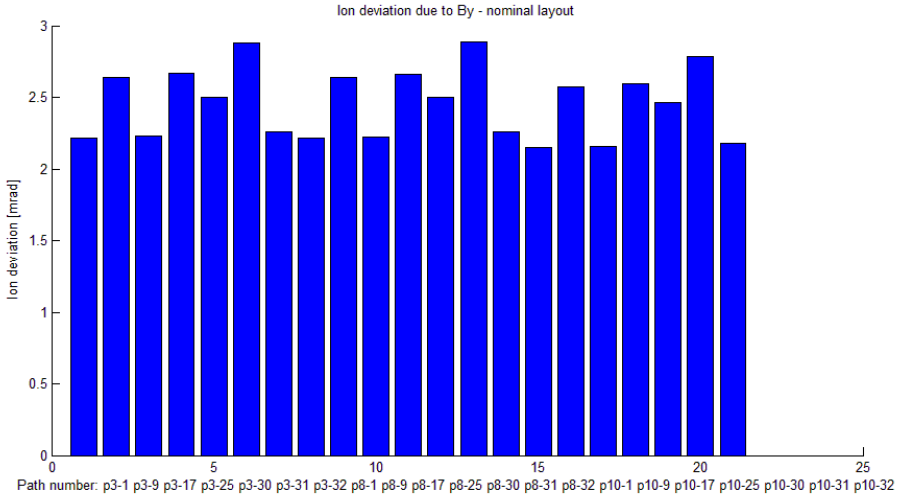

Fig. 129 Ion deflection due to By in the nominal layout.

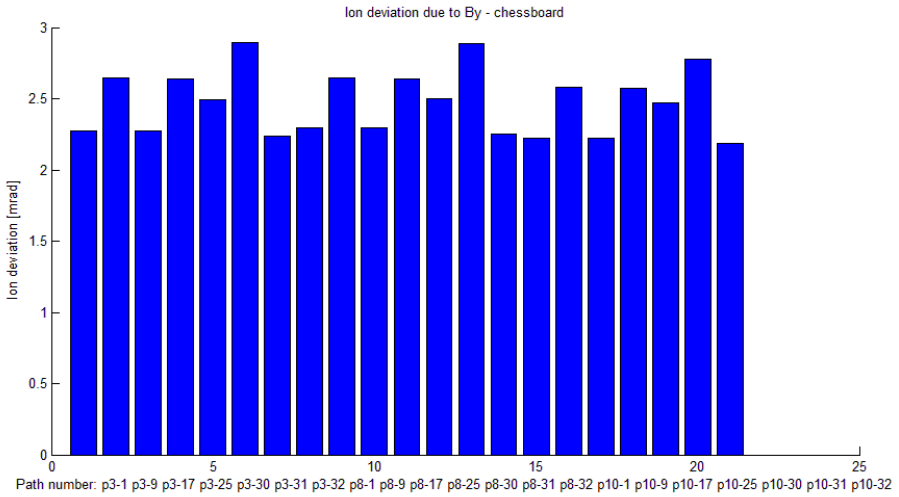

Fig. 130 Ion deflection due to By in the chessboard layout.

The range of ion deflection in the uniform magnetization model is 2.15−2.89 mrad.
The range in the chessboard layout model is almost the same: 2.18−2.90 mrad.
In order to investigate the effects of the chessboard layout in terms of power loads on grids, a simulation with EAMCC has been made for both the models. The results are shown in Fig. 131:

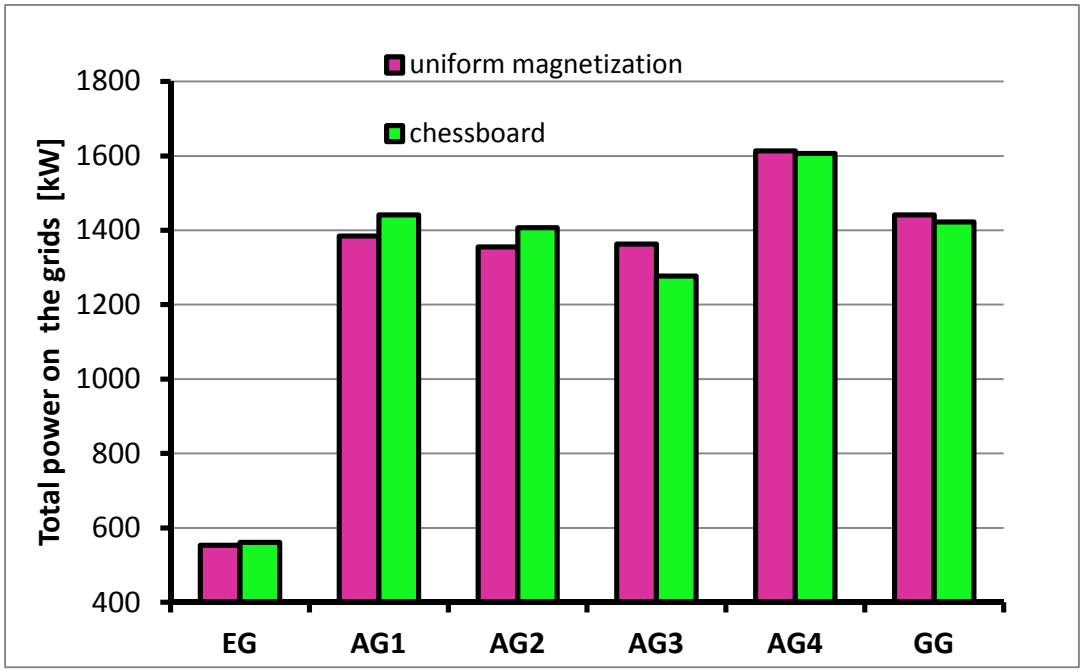

Fig. 131 Power loads on the grids in the 16 BG uniform magnetization model and in the 16 BG chessboard model.

The maximum power on a grid (AG4) is almost the same, as well the total power on all the grids:

	Total power on all the grids
16 BG uniform magnetization	7711 kW
16 BG chessboard	7714 kW

Tab. 16 Total power on all the grids calculated in the 16 BG uniform magnetization model and in the 16 BG chessboard model.

Transmitted electrons, neutrals and power of D^- at exit are shown in the next table:

	Transmitted electrons	**Transmitted neutrals (D_0)**	**Power of D^- at exit**
16 BG uniform magnetization	0.54 MW	2.37 MW	42.16 MW
16 BG chessboard	0.58 MW	2.37 MW	42.21 MW

Tab. 17 Transmitted electrons, neutrals (D_0) and D^- calculated in the 16 BG uniform magnetization model and in the 16 BG chessboard model.

Here an increase of 7% in transmitted electrons is observed in the chessboard model, while transmitted neutrals are the same.
In conclusion, a global effect has been observed in the grid model made of 16 BG with uniform magnetization, but its only consequence is the presence of an axial component of magnetic field in the accelerator (Bz) of order 10^{-4} T (not considering peaks due to edge effects). Axial magnetic field doesn't affect beam optic and its only unwanted consequence could be the presence of a stray magnetic field outside the accelerator, although the magnitude is very small. In the chessboard configurations, where the 16 BG have opposite magnetization, this effect is reduced by a factor of ten (see Fig. 127).
From the point of view of By profile, ion deflection and power loads on grids, the two configurations show the same performances. For as regards transmitted electrons, the chessboard configuration is slightly worse (+ 7% transmitted electrons).

For this reasons there are no strong motivations for substituting the nominal configuration, i.e. with uniform magnetization, with the chessboard one.

4.2.2. Comparison between single Beam Group model and 16 Beam Groups model using EAMCC

A comparison in terms of magnetic field profile, ion deflection, transmitted electrons and power loads on the grids has been carried out using the codes NBImag and EAMCC on the single BG model and the 16 BG model. The purpose of these analyses is to evaluate the uniformity of the results between the complete model of the accelerator (16 BG) and the reduced one used so far in MITICA design optimization (1 BG).

A previous comparison between models of the accelerator considering different number of magnets has been made by H. P. L. de Esch in [private communication]. In this document models with 2, 3, 4, 5, 6, 7, 8, 9 and 17 (1BG) magnets are compared in terms of By profile, transmitted species and power loads on the grids. From this comparison clearly emerges that the results are quite sensitive to the number of magnets included in the calculation, even if the differences in magnetic field are very small.

This effect is observed also in the comparison between the Single BG model (17 magnets) and the 16 BG model (68 x 4 magnets), see Fig. 132, even if on a smaller level.

In Fig. 132 By profile calculated along the central aperture in the Single BG model and along the central aperture of the internal Beam Group in the 16 BG model is compared. Small differences can be noticed in the regions between the grids. Fig. 133 is an enlarged view of By profile, from this figure it can be seen that these differences are smaller than 1 mT. Magnetic field has been calculated using NBImag code.

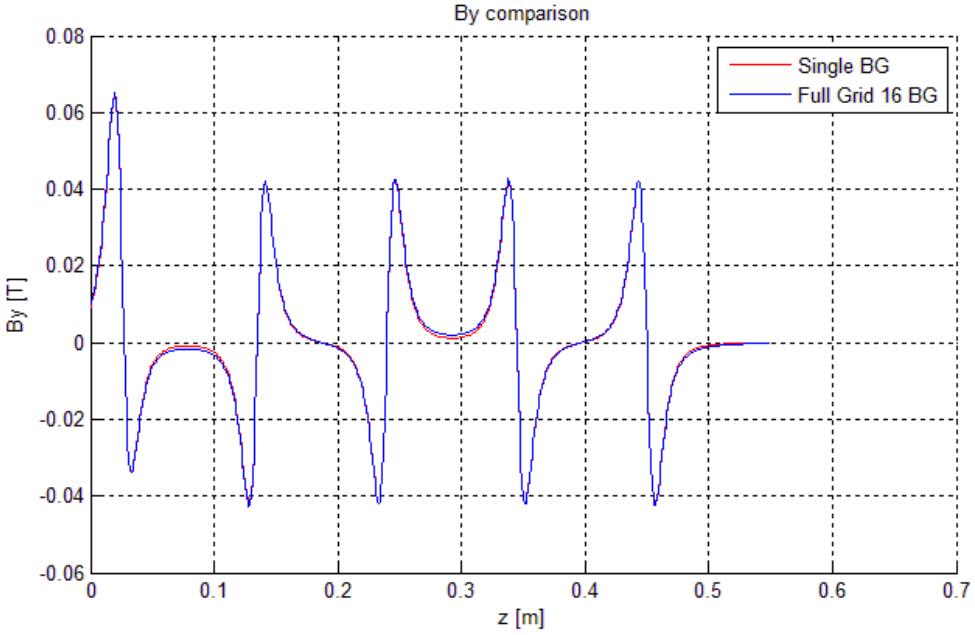

Fig. 132 Comparison of By profile calculated along the same aperture in the Single BG model and in the 16 BG model.

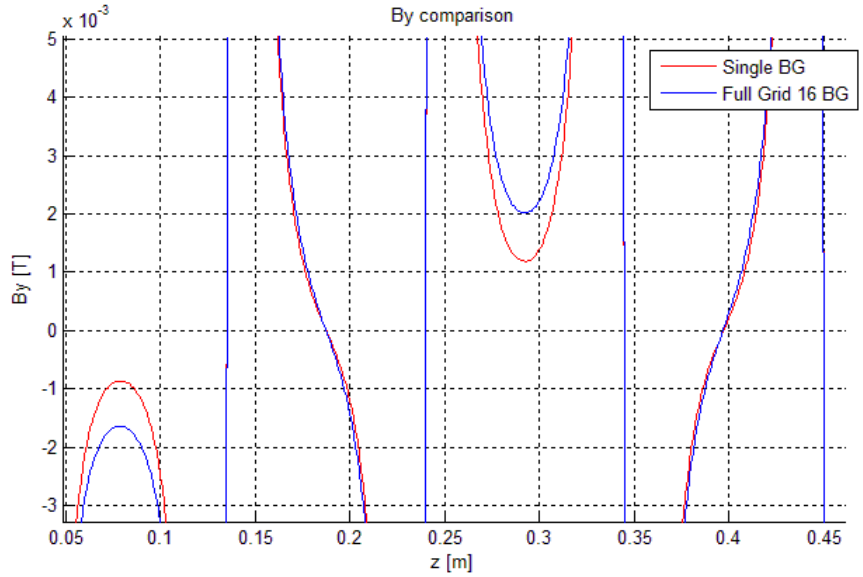

Fig. 133 Comparison of By profile calculated along the same aperture in the Single BG model and in the 16 BG model, enlarged view.

Ion deflection has been calculated with the paraxial approximation formula along the central-central aperture (same of Fig. 133), the central-upper, the lateral-central and the lateral-upper apertures in the Single BG model and in an internal beam group of the 16 BG model. Results differ for only 0.05 mrad in the upper apertures, and are equal for the central apertures, as shown in Fig. 134.

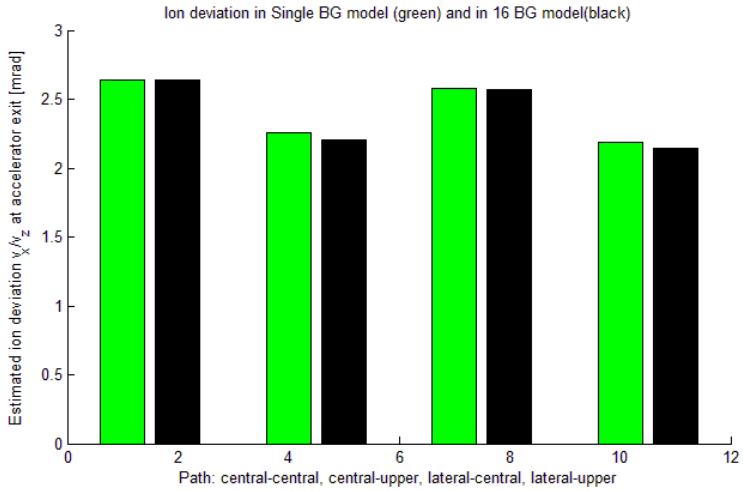

Fig. 134 Ion deflection along four different apertures calculated in the Single BG model (green bar) and in the 16 BG model (black bar).

Using the code EAMCC with the field maps calculated with NBImag, transmitted species and power loads on the grids have been obtained.
Tab. 18 shows the results in terms of transmitted electrons, neutrals (D_0) and D^- calculated in the two models.

	Transmitted electrons	**Transmitted neutrals (D_0)**	**Power of D^- at exit**
Single BG model	0.50 MW	2.37 MW	42.06 MW
16 BG model	0.54 MW	2.38 MW	42.16 MW

Tab. 18 Transmitted electrons, neutrals (D_0) and D^- calculated in the Single BG model and in the 16 BG model.

As it can be seen, there is a difference of 8% between the two models in calculated transmitted electrons.
Next figure shows the power on grids obtained in the two models:

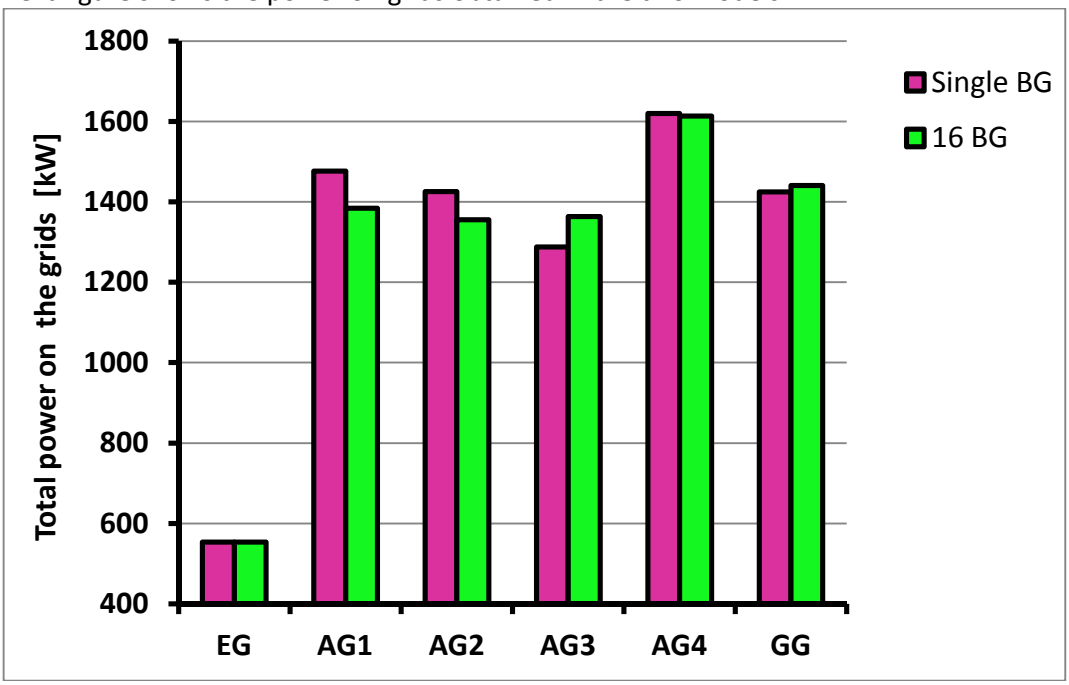

Fig. 135 Power loads on grids calculated in the Single BG model and in the 16 BG model.

From these results, difference of the order of 4-6% appears in power load on AG1, AG2 and AG3. Maximum power is on AG4 and is almost the same in the two models. Total power on all the grids is also very similar, as reported in Tab. 19:

	Total power on all the grids
Single BG model	7759 kW
16 BG model	7711kW

Tab. 19 Total power on all the grids calculated in the Single BG model and in the 16 BG model.

In conclusion, very little difference has been observed in By profile between the Single BG and the 16 BG models, but this difference is able to produce a variation of 8% in transmitted electrons and of 4-6% in power loads on AG1, AG2, and AG3.
However the maximum power load (on AG4) is almost the same in the two models as well as the total power on all the grids, so the sensitivity to the size of the model in this specific case doesn't seem large enough to invalidate previous calculations and design optimization based on the Single BG model.

4.2.3. Effect of mechanical tolerance of grid grooves

Two simulations have been carried out with NBImag with the purpose of evaluating the effect of mechanical tolerances of grid grooves on permanent magnets position and thus on magnetic field profile.

First simulation is a calculation of magnetic force acting on all the magnets of a Beam Group. This simulation could be interesting also out of this context and its purpose is the determination of the spontaneous repositioning of magnets inside the grooves. Once the new positions, most likely corresponding to the real positions, are obtained, a second simulation has been carried out for magnetic field calculation and comparison with the ideal case.

Fig. 136 shows graphically the results of the first simulation, the force evaluation on all the magnets of Beam Group. Since the plot is to scale, only the major actions appear and these are the repulsive forces between CESMs and ADCMs. The actions on the magnets of AG1, AG2, AG3 and AG4 are some orders of magnitude smaller. The numerical results of force calculation on EG magnets are reported in Tab. 20 while in Tab.21 are reported the forces acting on AG1 magnets. Force pattern on AG2, AG3, and AG4 is very similar to the one of AG1, so it's not reported here for simplicity.

Groups of three CESMs or SESMs in the same row have been modelled as a single magnet in order to reduce the computational cost.

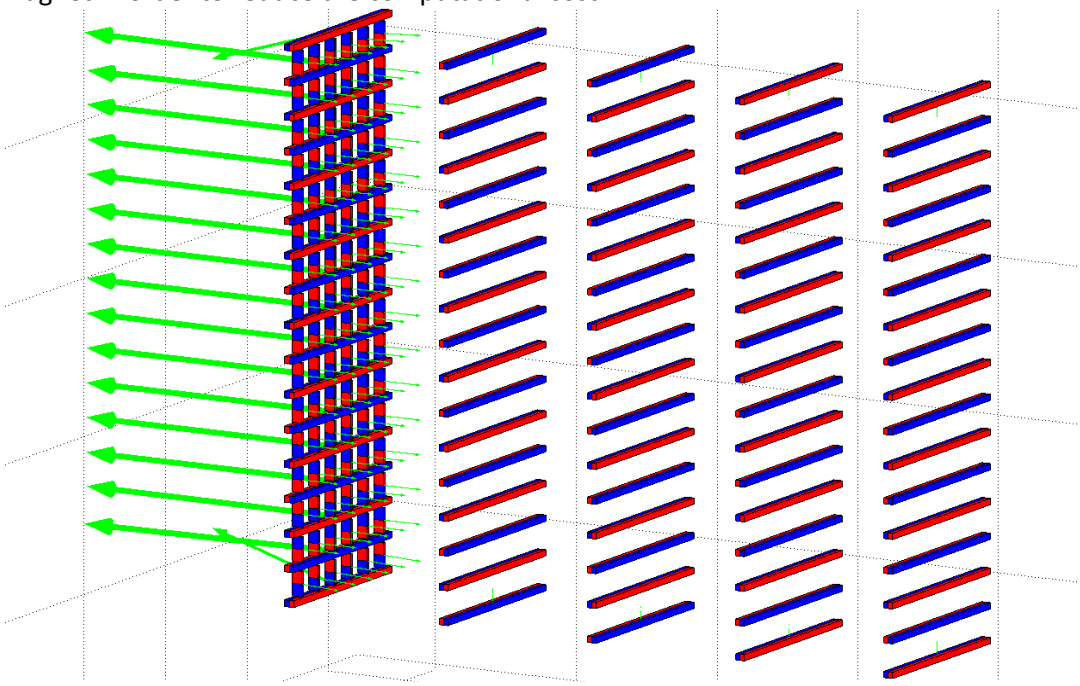

Fig. 136 Plot to scale of forces acting on all the permanent magnets of a Beam Group.

EG - Magnets	Fx [N]	Fy [N]	Fz [N]
ADCM - upper and lowest row (average)	$< 4*10^{-2}$	-0.21 (upper) 0.21 (lowest)	4.5
ADCM - all the others (avg)	$< 4*10^{-2}$	$< 7.7*10^{-3}$	4.5
CESM "-8"(lowest)	0	4.13	-13.38
CESM "-7"	0	-0.23	-26.98
CESM "-6"	0	$5.87*10^{-2}$	-26.71

CESM "-5"	0	$-2.25*10^{-2}$	-26.76
CESM "-4"	0	$1.04*10^{-2}$	-26.74
CESM "-3"	0	$-5.24*10^{-3}$	-26.75
CESM "-2"	0	$2.64*10^{-3}$	-26.75
CESM "-1"	0	$-1.11*10^{-3}$	-26.75
CESM "0" (central)	0	0	-26.75
CESM "1"	0	$1.11*10^{-3}$	-26.75
CESM "2"	0	$-2.64*10^{-3}$	-26.75
CESM "3"	0	$5.24*10^{-3}$	-26.75
CESM "4"	0	$-1.04*10^{-2}$	-26.74
CESM "5"	0	$2.25*10^{-2}$	-26.76
CESM "6"	0	$-5.87*10^{-2}$	-26.71
CESM "7"	0	0.23	-26.98
CESM "8" (upper)	0	-4.13	-13.38

Tab. 20 Forces on EG permanent magnets.

AG1 - Magnets	**Fx [N]**	**Fy [N]**	**Fz [N]**
SESM "-8"(lowest)	0	1.56	$1.59*10^{-2}$
SESM "-7"	0	-0.16	$-1.08*10^{-2}$
SESM "-6"	0	$3.96*10^{-2}$	$4.69*10^{-3}$
SESM "-5"	0	$-1.49*10^{-2}$	$-6.90*10^{-4}$
SESM "-4"	0	$7.16*10^{-3}$	$-1.00*10^{-3}$
SESM "-3"	0	$-3.86*10^{-3}$	$1.55*10^{-3}$
SESM "-2"	0	$2.09*10^{-3}$	$-1.52*10^{-3}$
SESM "-1"	0	$-9.25*10^{-4}$	$1.47*10^{-3}$
SESM "0" (central)	0	0	$-1.38*10^{-3}$
SESM "1"	0	$9.25*10^{-4}$	$1.47*10^{-3}$
SESM "2"	0	$-2.09*10^{-3}$	$-1.52*10^{-3}$
SESM "3"	0	$3.86*10^{-3}$	$1.55*10^{-3}$
SESM "4"	0	$-7.16*10^{-3}$	$-1.00*10^{-3}$
SESM "5"	0	$1.49*10^{-2}$	$-6.90*10^{-4}$
SESM "6"	0	$-3.96*10^{-2}$	$4.69*10^{-3}$
SESM "7"	0	0.16	$-1.08*10^{-2}$
SESM "8" (upper)	0	-1.56	$1.59*10^{-2}$

Tab.21 Forces on AG1 permanent magnets.

The results of this simulation are interesting for two reasons: they allow the evaluation of mechanical loads on the grids due the presence of the magnets, and they allow the

determination of the real position of the magnets due to a self-adjusting inside the grooves, that are realized with a certain mechanical tolerance.
For example, summing up all the forces acting on EG magnets, a global resulting force of:

$$\boldsymbol{R_{EG}} = \begin{cases} R_{EGx} = 0 \\ R_{EGy} = 0 \\ R_{EGz} = 0.10\ N \end{cases}$$

is obtained. For as regards the other grids, the magnitude of global resulting force is even smaller.
This means that the actions exchanged between the grids, at least in nominal working position, are very small, practically negligible.
Internal forces within AG1, AG2, AG3 and AG4 are also very small, as it can be seen from Tab.21, so absolutely not worrying from the mechanical point of view.
The only worthwhile actions are the repulsive forces between CESMs and ADCM. They globally cancel each other, but they produce a net force on one side of the grid grooves equal to:

$$\boldsymbol{R_{EGz\ -one\ side}} = 428\ N$$

Compared to the mechanical loads due to thermal stresses on EG, this force is probably negligible, but it could be a problem in case of the presence of a closure lid instead of embedded grooves (like for example in the Multi Channel Prototype or in possible other future prototypes). In this eventuality, the lid should be adequately designed.
For as regards the determination of final position of the magnets inside the grooves, the knowledge of the resulting force only is not sufficient but also the torque is needed. NBImag calculates the polar torque of the force distribution acting within each magnet with respect to the origin, i.e. the point (0,0,0). What is really needed is the polar torque with respect to the centre of gravity of the magnet, and this can be simply obtained from:

$$\boldsymbol{M_{CG}} = \boldsymbol{M_O} + \boldsymbol{R} \times \overrightarrow{O\ CG}$$

being $\boldsymbol{R}$ the resulting force acting on the magnet, $\boldsymbol{M_O}$ the polar torque of force distribution within the magnet with respect to (0,0,0) and $\overrightarrow{O\ CG}$ the vector going from (0,0,0) to the centre of gravity, simply the coordinates of CG.
This calculation has been carried out for all the magnets of the Beam Group. Concerning the EG magnets, the polar torque is negligible for all the magnets but the upper (CESM "8") and the lowest (CESM "-8") CESMs. These two magnets have a non negligible x-component of $\boldsymbol{M_{CG}}$:

$$\boldsymbol{M_{CESM"-8"}} = (-0.045, 0, 0)Nm$$
$$\boldsymbol{M_{CESM"8"}} = (0.045, 0, 0)Nm$$

this means that they will tend to rotate inside the groove, as shown in Fig. 137. Equilibrium will be reached because of groove reaction, but not necessarily as in Fig. 137. If the torque produced by F_z and R_{gz} (approximately equal to $F_z\ {}^{h_m}/_2$) is greater than M_x, then $R_{gy} = 0$ and the magnet will almost completely lean to the left wall of the groove

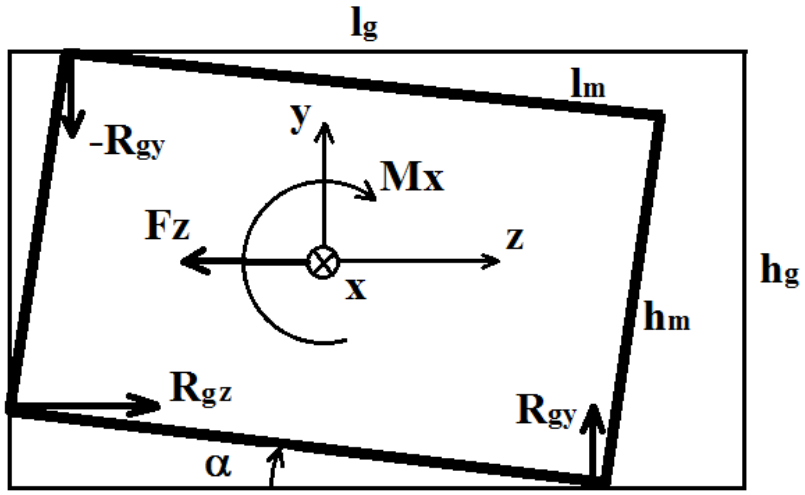

Fig. 137 Magnet real position inside the groove under the effect of magnetic force and torque.

For a CESM:

$$\begin{cases} l_m = 6.6\ mm \\ h_m = 4.2\ mm \\ l_g = 7.0\ mm \\ h_g = 4.6\ mm \end{cases}$$

For CESM "8" and "-8": $F_z\,{}^{h_m}/_2 = 0.028\ Nm < 0.045\ Nm = M_x$

so the magnet is actually rotated, as in Fig. 137. Rotation angle can be obtained from geometrical considerations:

$$\begin{cases} l_m \sin\alpha \le h_g - h_m \\ h_m \sin\alpha \le l_g - l_m \end{cases} \quad \rightarrow \quad \alpha \le \arcsin\left(\frac{h_g - h_m}{l_m}\right)$$

So, for CESM or SESM:

$\alpha_{\text{CESM}} = 0.060\ \text{rad} = 3.47^\circ$

$\alpha_{\text{SESM}} = 0.067\ \text{rad} = 3.82^\circ$

Polar torques with respect to centre of gravity of magnets of AG1 are reported in Tab. 22:

AG1 - Magnets	Mx [Nm]	My [Nm]	Mz [Nm]
SESM "-8"(lowest)	0.030	0	0
SESM "-7"	-0.218	0	0
SESM "-6"	0.291	0	0
SESM "-5"	-0.275	0	0
SESM "-4"	0.219	0	0
SESM "-3"	-0.155	0	0
SESM "-2"	0.097	0	0
SESM "-1"	-0.046	0	0
SESM "0" (central)	0	0	0

SESM "1"	0.046	0	0
SESM "2"	-0.097	0	0
SESM "3"	0.155	0	0
SESM "4"	-0.219	0	0
SESM "5"	0.275	0	0
SESM "6"	-0.291	0	0
SESM "7"	0.218	0	0
SESM "8" (upper)	-0.030	0	0

Tab. 22 Torques with respect to centre of gravity of AG1 magnets.

In none of these magnets F_z is great enough to counterbalance M_x, so the magnets are rotated like Fig. 137, coherently with the sign plus or minus of M_x.
The situation of AG2, AG3 and AG4 is similar to the one of AG1 (for this reason the relative torque table won't be reported), but with one difference: the signs in AG2 and AG3 are reversed and consequently the rotations are opposite.
So, in the final geometry CESMs and ADCMs are moved inside the grooves to maximize the distance between each other (CESMs toward PG), CESM "8" and "-8" are rotated, and all the SESM, but the central ones, are rotated accordingly to Tab. 22 for AG1 and AG4 and oppositely for AG2 and AG3. The final NBImag model is shown in Fig. 138 and Fig. 139.
The stability of equilibrium in the final geometry has been verified with an additional simulation, a force and torque calculation in this geometry, in order to verify that the sign plus or minus of forces and polar torques is still the same of previous simulation. The results show that forces and torques are coherent, verifying the stability, and that the torques on SESM are much smaller, meaning that the final geometry is reasonably a consequence of magnet position self-adjustment.

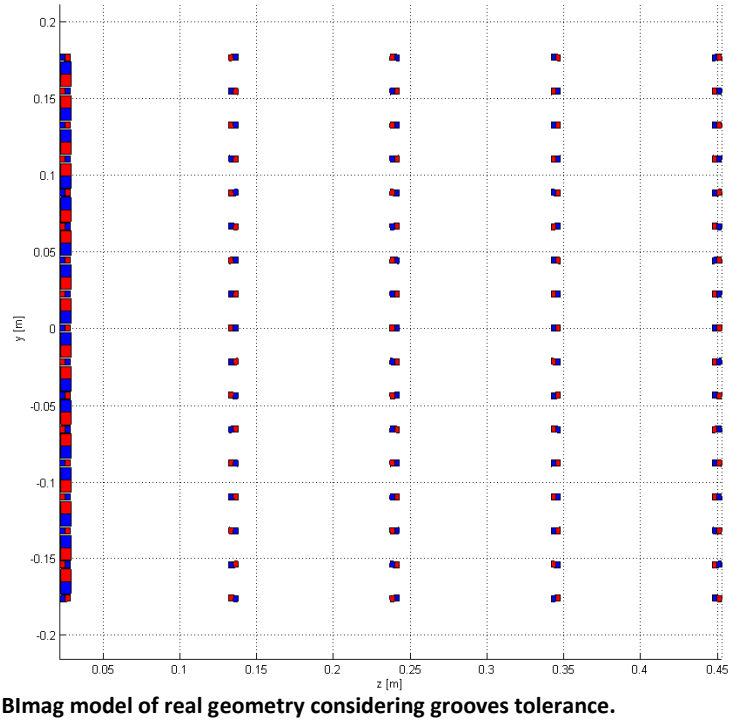

Fig. 138 NBImag model of real geometry considering grooves tolerance.

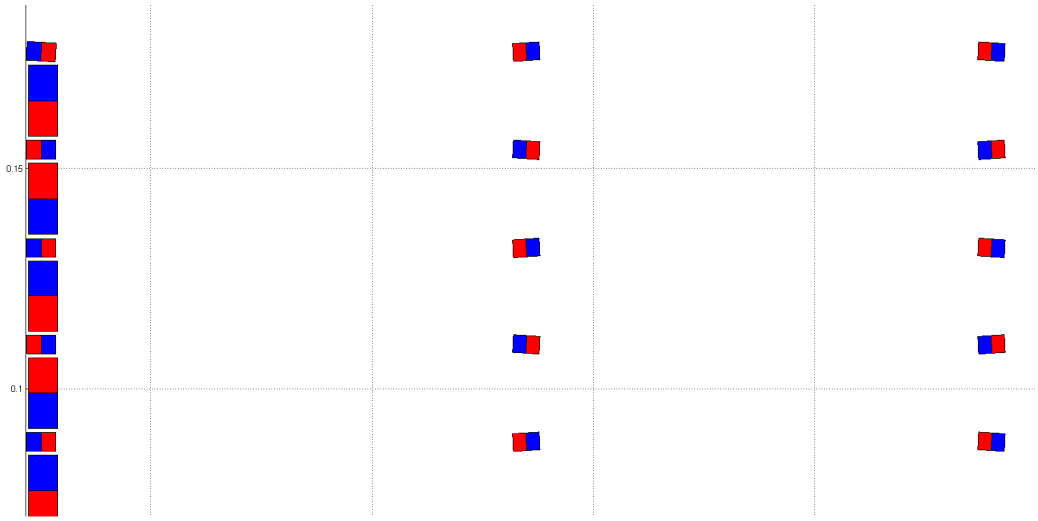

Fig. 139 NBImag model of real geometry considering grooves tolerance (enlarged view).

Magnetic field has been calculated along the four usual paths, shown in Fig. 140, and compared with the nominal geometry. Results of By comparison are shown in Fig. 141, Fig. 142, Fig. 143 and Fig. 144.

The only differences between the profiles in nominal and real case are related to the field peaks, which in fact are shifted downward or upward for a given grid in real case with respect to nominal one. These differences are very little (≈2.5%) for the central apertures and just a bit more pronounced (≈5%) for the upper apertures. Comparison in terms of ion deflection, calculated with the usual analytical formula, is shown in Fig. 145. There is almost no difference on ion deflection along central apertures and a difference of 0.07mrad (≈3%) for upper apertures.

In conclusion, the groove tolerance has a visible effect on magnets position but a little effect on field profile or ion deflection.

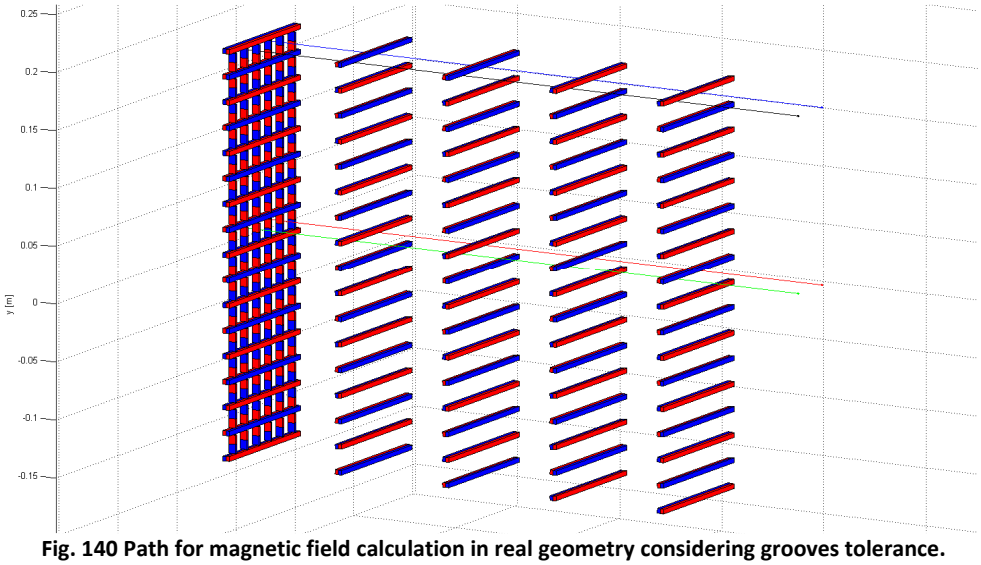

Fig. 140 Path for magnetic field calculation in real geometry considering grooves tolerance.

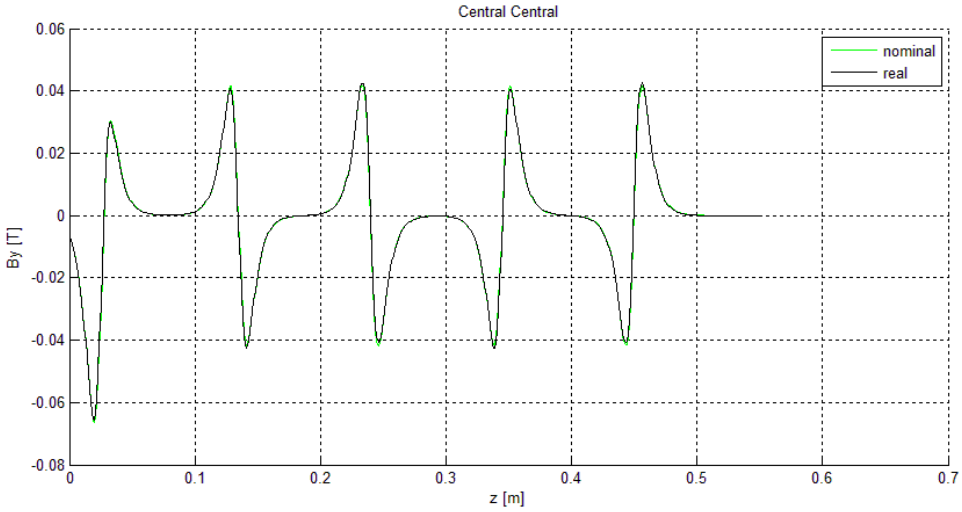

Fig. 141 By field comparison between nominal geometry and real considering grooves tolerance, aperture central-central.

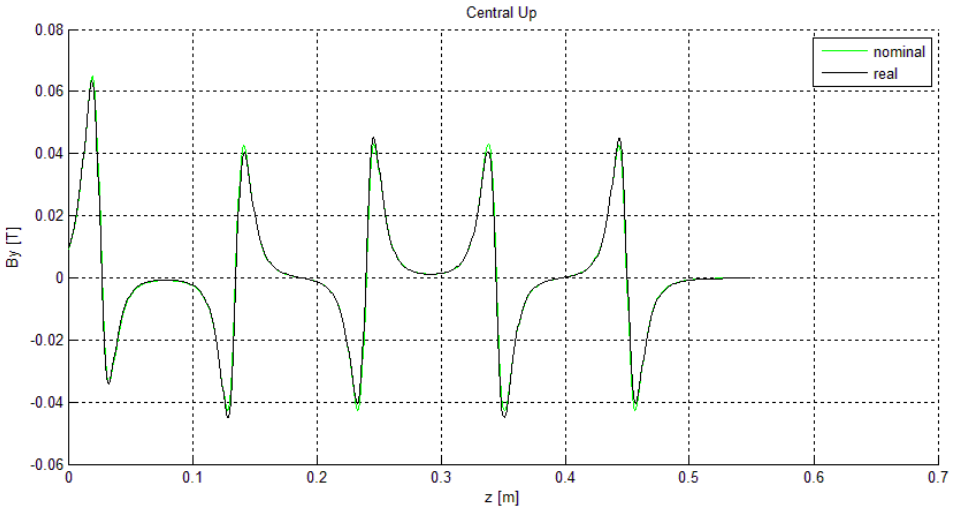

Fig. 142 By field comparison between nominal geometry and real considering grooves tolerance, aperture central-up.

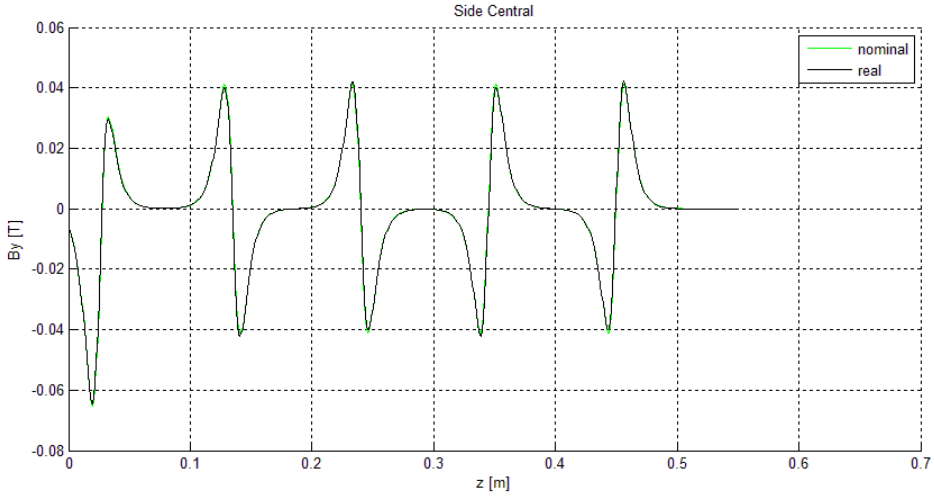

Fig. 143 By field comparison between nominal geometry and real considering grooves tolerance, aperture side-central.

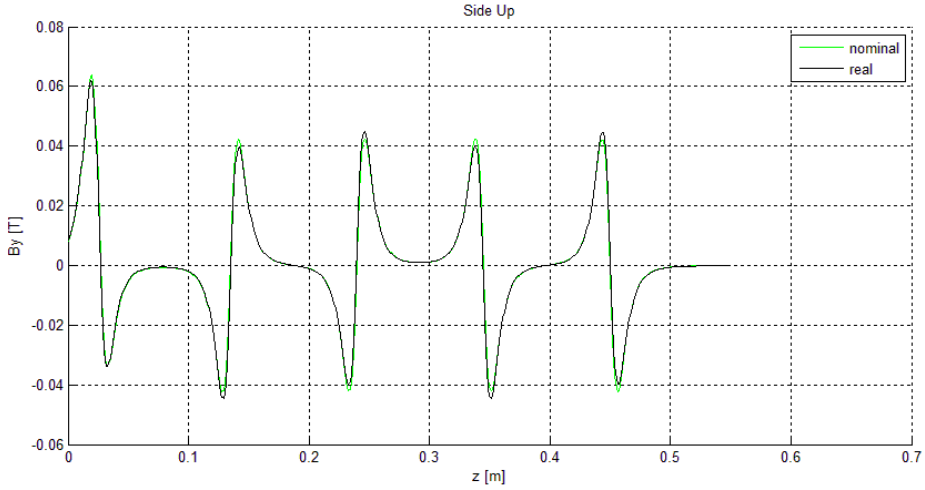

Fig. 144 By field comparison between nominal geometry and real considering grooves tolerance, aperture side-up.

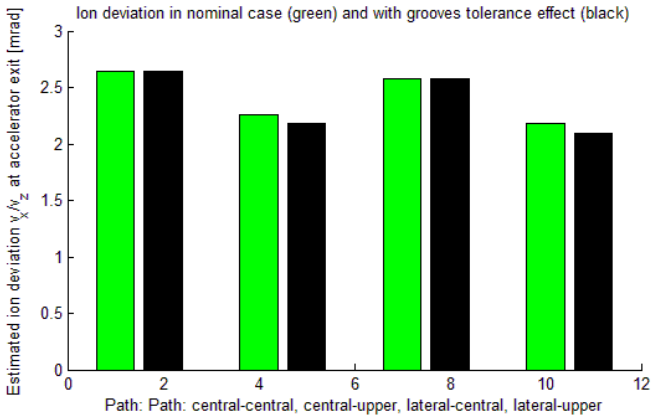

Fig. 145 Ion deflection comparison between nominal geometry and real considering grooves tolerance.

4.2.4. Effect of real orientation of Beam Groups

A considerable effort has been put in the realization of an NBImag model of the accelerator considering the Beam Groups in the real position, i.e. oriented with the correct aiming angles of the hyperlens.

A code has been written for the generation of the input file for NBImag of a "hyperlens" accelerator constituted by individually-oriented Beam Groups, in which it is possible to specify the orientation angles of the Beam Groups in a segment (for achieving horizontal aiming) and the mounting angles of the segment (for achieving the vertical aiming).

The code reads an NBImag input file of the approximated geometry used till now for all the calculations, where the grids are flat, and applies to each magnet a proper translation and a proper rotation in order to determine the final centre of gravity and orientation angles, depending on the given aiming angles, the grid and Beam Group whom the magnet belongs to, the type of magnet (CESM-SESM or ADCM) and its previous position and orientation.

The total rotation is just the composition of two elementary rotations, the first about the y-axis (segment curvature, angle α_1 or α_2) and the second about the x-axis (rotated mounting of the segment, angle β_1 or β_2). By applying the matrix representing the total rotation, to the direction cosines of the axes of the magnet's reference frame it's possible to directly obtain the new direction cosines. Angles α_1 and α_2 are visualized in Fig. 146 and their value is:

α_1 = 0.18°

α_2 = 0.54°

Angles β_1 and $\beta_2$are visualized in Fig. 147 and their value can be obtained looking at Fig. 148:

β_1 = arctan(198/25479) = 0.007771 rad = 0.445°

β_2 = arctan(594/25479) = 0.023313 rad = 1.336°

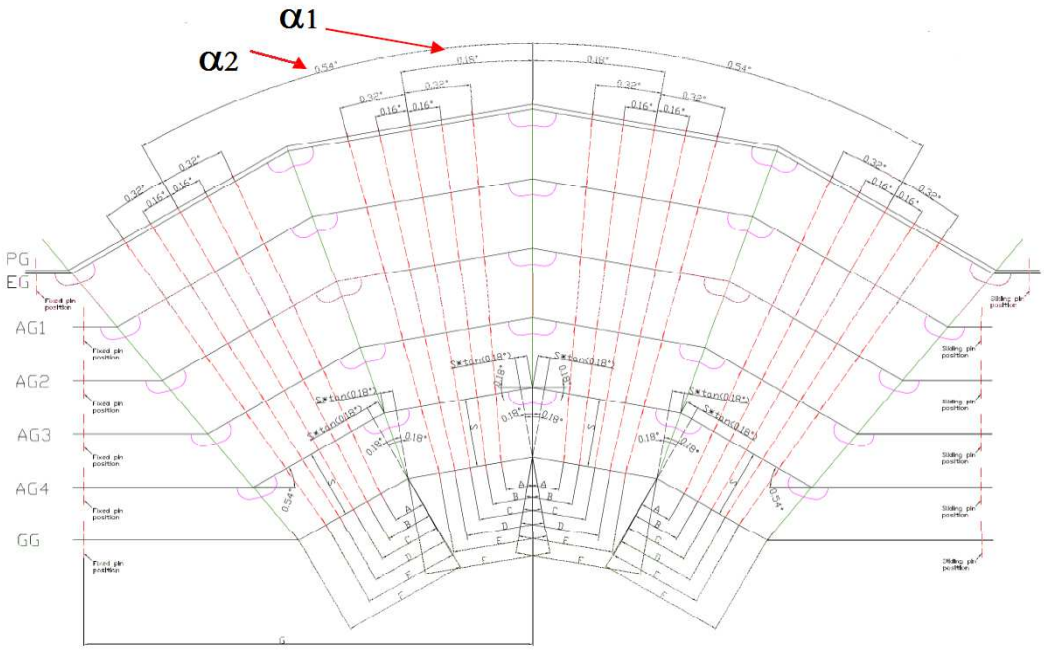

Fig. 146 Horizontal aiming strategy.

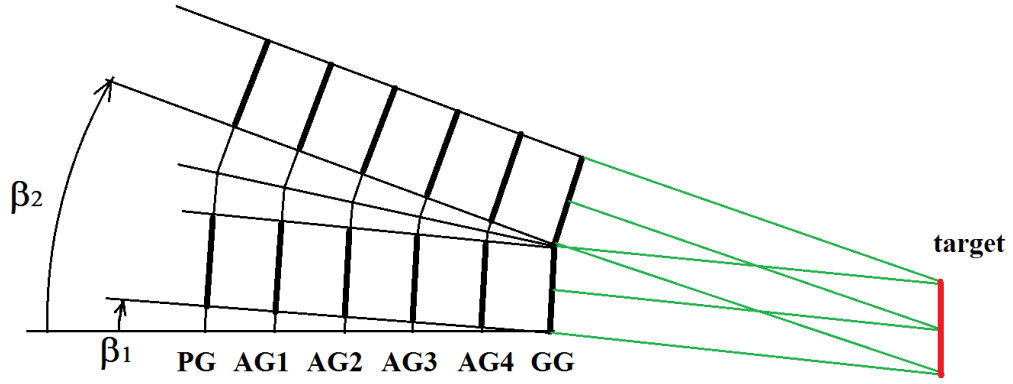

Fig. 147 Vertical aiming strategy (scheme).

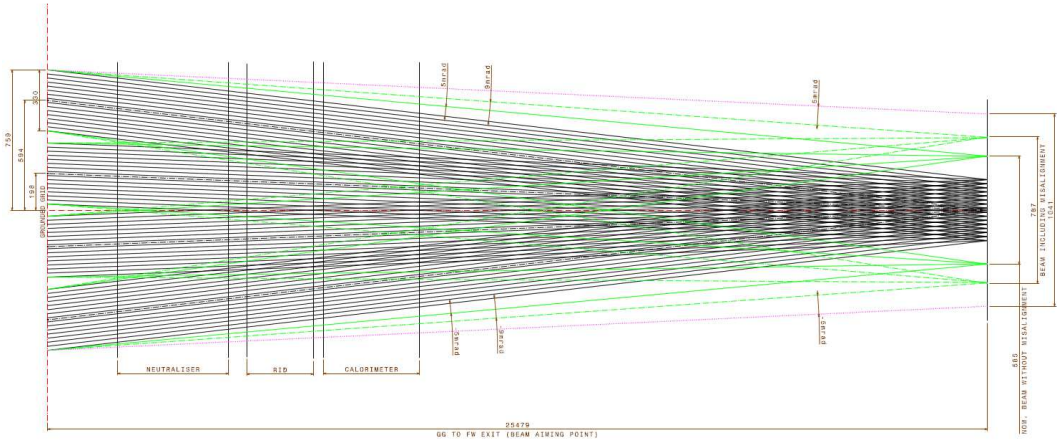

Fig. 148 Vertical aiming strategy (detailed).

The rotation matrix is:

$$\bar{\bar{\boldsymbol{R}}} = \bar{\bar{\boldsymbol{R}}}_2\bar{\bar{\boldsymbol{R}}}_1 = Rot(\boldsymbol{k},\beta)\,Rot(\boldsymbol{j},\alpha) = \begin{pmatrix} 1 & 0 & 0 \\ 0 & \cos\beta & -\sin\beta \\ 0 & \sin\beta & \cos\beta \end{pmatrix}\begin{pmatrix} \cos\alpha & 0 & \sin\alpha \\ 0 & 1 & 0 \\ -\sin\alpha & 0 & \cos\alpha \end{pmatrix}$$

$$= \begin{pmatrix} \cos\alpha & 0 & \sin\alpha \\ \sin\alpha\sin\beta & \cos\beta & -\cos\alpha\sin\beta \\ -\sin\alpha\cos\beta & \sin\beta & \cos\alpha\cos\beta \end{pmatrix}$$

where $\alpha = \pm\alpha_1$ or $\alpha = \pm\alpha_2$ and $\beta = \pm\beta_1$ or $\beta = \pm\beta_2$ depending on the Beam Group.

If $\boldsymbol{a} = \begin{pmatrix} a_1 \\ a_2 \\ a_3 \end{pmatrix}$ is a vector in space before rotation, for example one of the axes of magnet's reference frame, then the vector $\boldsymbol{a}'$ after rotation is simply given by

$$\boldsymbol{a}' = \bar{\bar{\boldsymbol{R}}} \cdot \boldsymbol{a}$$

Determining the translation vector and thus the final position of magnets centres of gravity it's more difficult and requires a bit of care.

Imagining to start from the flat grid, first step is finding the magnet's translation due the first rotation (grid curvature) and this is easy, it's just a variation in z-coordinate, as shown in Fig. 149 (the variation of x-coordinate is negligible in the small angles hypothesis)

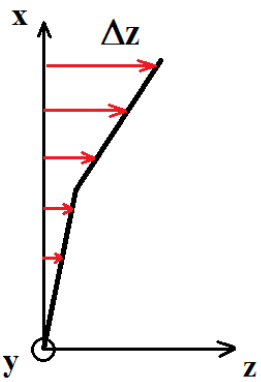

Fig. 149 Translation due to the first rotation (top view).

Second step is determining the translation due to the second rotation, and now there is a variation in both z and y-coordinates, as shown in Fig. 150. Variation in y-coordinate is not negligible anymore in this case because of the effects of previous rotation.

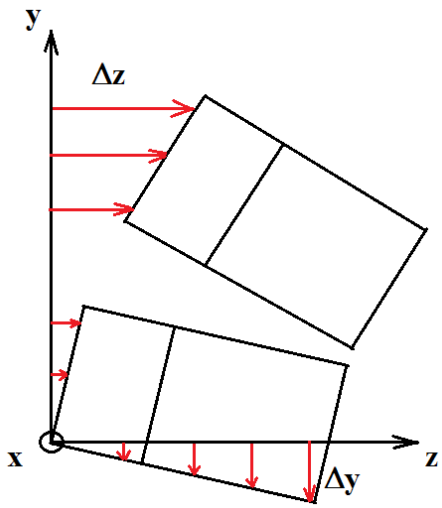

Fig. 150 Translation due to the second rotation (lateral view).

Last step is adding a correction translation in order to take into account the fact that axis of the second rotation is changing from grid to grid and not corresponding anymore to the corner of the segment, as in Fig. 150. Correction translation is applied to all the magnets of a certain grid and Beam Group. In Fig. 151 the correction translation is shown for AG3 and AG4. The figure can be intended as a lateral or a top view of the grid. This last translation involves all the three coordinates even if the variation of z-coordinate can be neglected in the small angle hypothesis.

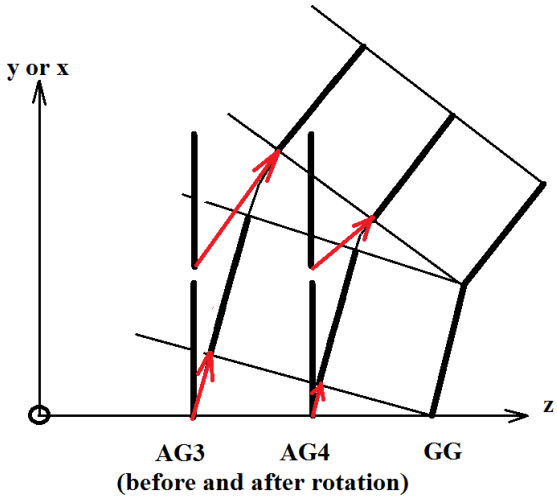

Fig. 151 Correction translation for AG3 and AG4 (lateral or top view).

Summing up all these contributions, the final translation vector is obtained for every magnet, and it depends on the grid and Beam Group whom the magnet belongs to, its previous position and the given aiming angles.

The final result is checked graphically with NBImag. Fig. 152 shows the result with exaggerated aiming angles:

$$\alpha_1 = \beta_1 = 0.08 \text{ rad}$$

$$\alpha_2 = \beta_2 = 0.24 \text{ rad.}$$

Fig. 153 and Fig. 154 show the model with real aiming angles and real paths for magnetic field calculation.

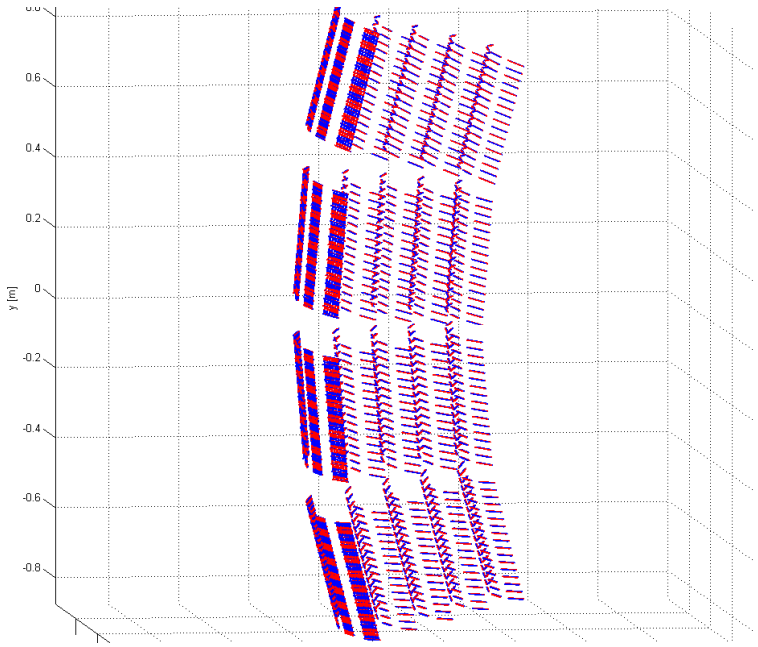

Fig. 152 NBImag model of MITICA accelerator with exaggerated curvature.

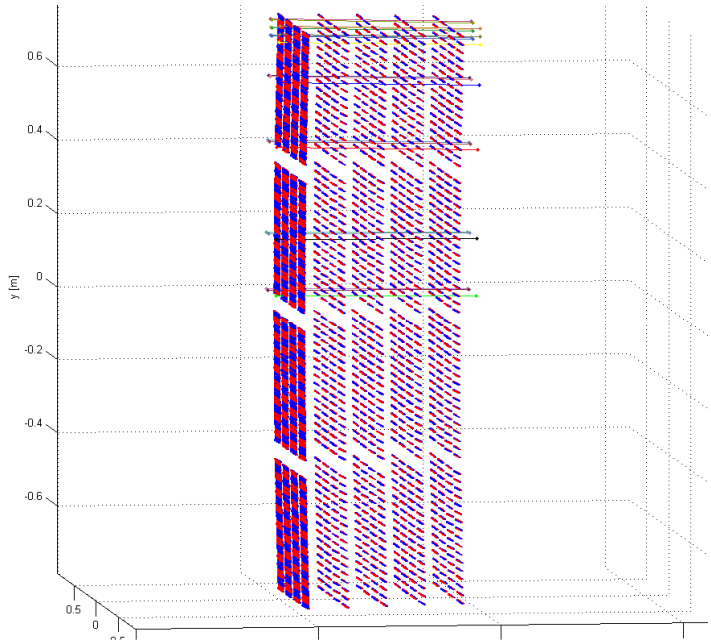

Fig. 153 NBImag model of MITICA accelerator with real curvature.

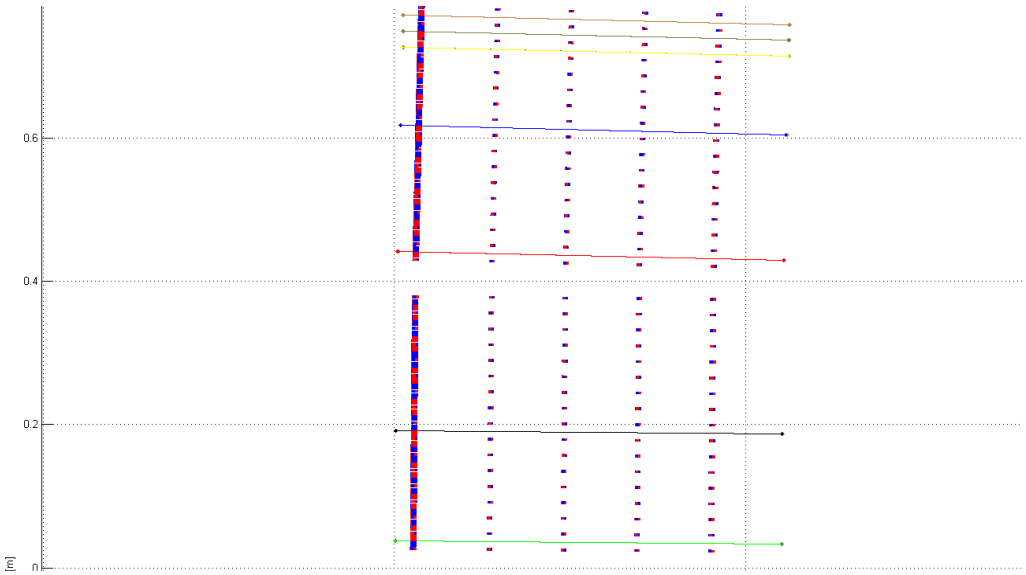

Fig. 154 Enlarged lateral view of NBImag model of MITICA grids with real curvature.

From Fig. 153 the curvature is hardly visible, because the real aiming angles are very little, but it can be noticed from the enlarged view of Fig. 154.
The paths for magnetic field calculation in the real geometry have been obtained by applying the same translation vector discussed above to the central points of the required apertures and then calculating the straight line passing through them and with the same extension as in the NBImag model with flat grids.
Once obtained the NBImag model of the accelerator with the real curvature, magnetic field has been calculated in the usual apertures pattern, like in Fig. 119.
Profile of By-component of magnetic field is plotted in Fig. 155:

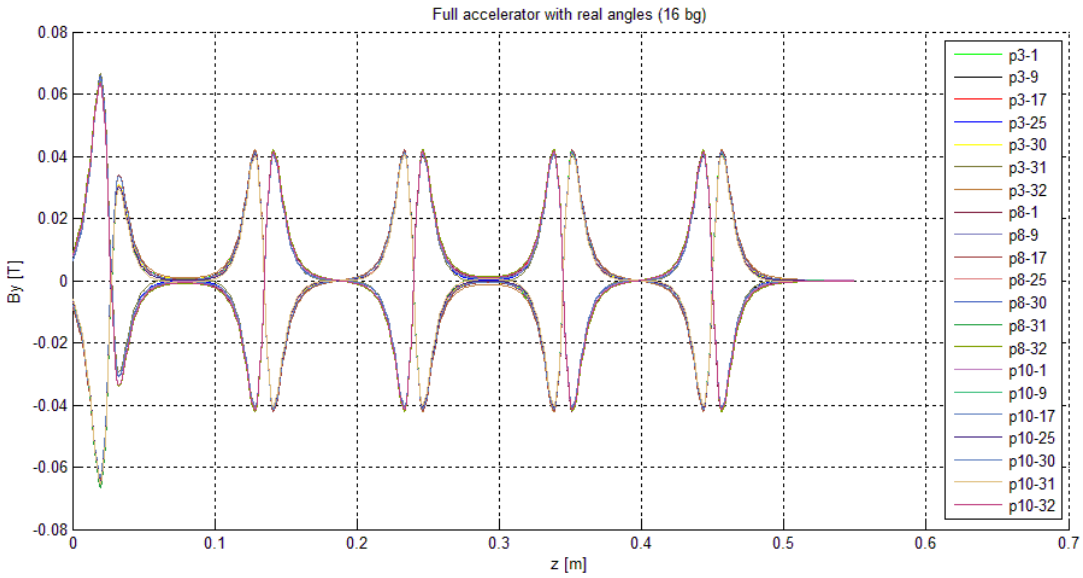

Fig. 155 By profile along the usual paths in the real curvature model.

This plot has to be compared with Fig. 121, its correspondent but obtained in the flat grid model.

A careful inspection of these profile reveals that the differences between the flat grid model and the real curvature model in By profile are very little, practically negligible. The next three figures show the By profile along a single aperture in the two model. The green and the black lines are perfectly superposed.

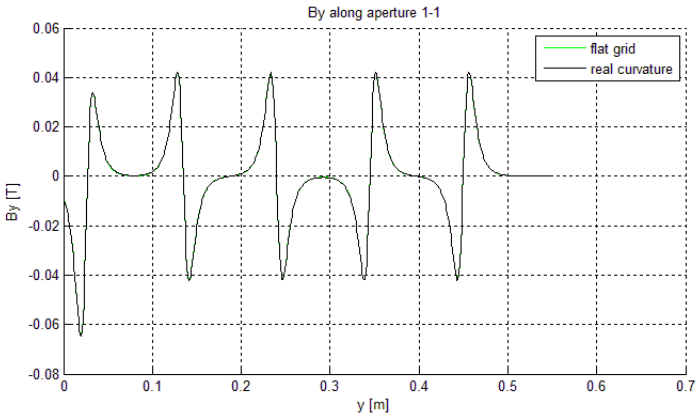

Fig. 156 By profile along aperture 1-1 in the models "flat grid" and "real curvature grid".

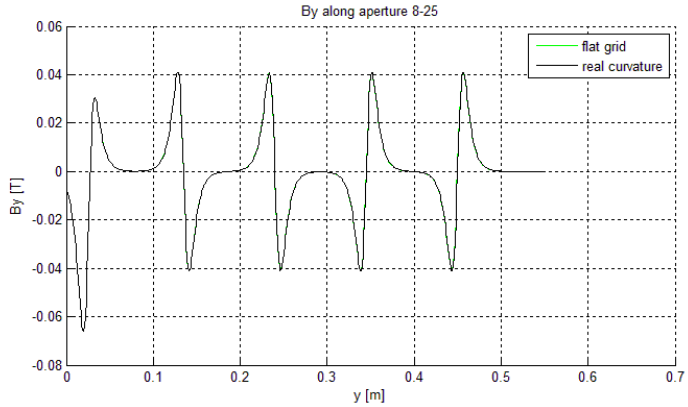

Fig. 157 By profile along aperture 8-25 in the models "flat grid" and "real curvature grid".

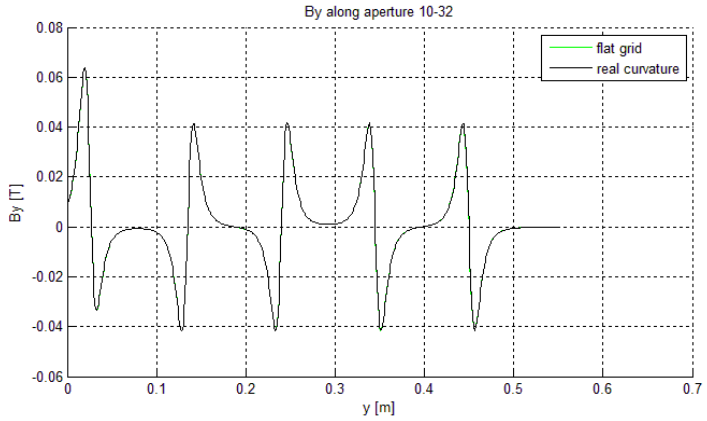

Fig. 158 By profile along aperture 10-32 in the models "flat grid" and "real curvature grid".

Deflections due to By field component are also identical between the two models. For sake of completeness, in Fig. 159 the plot of ion deflection due to By is reported. This plot is practically identical to Fig. 130.

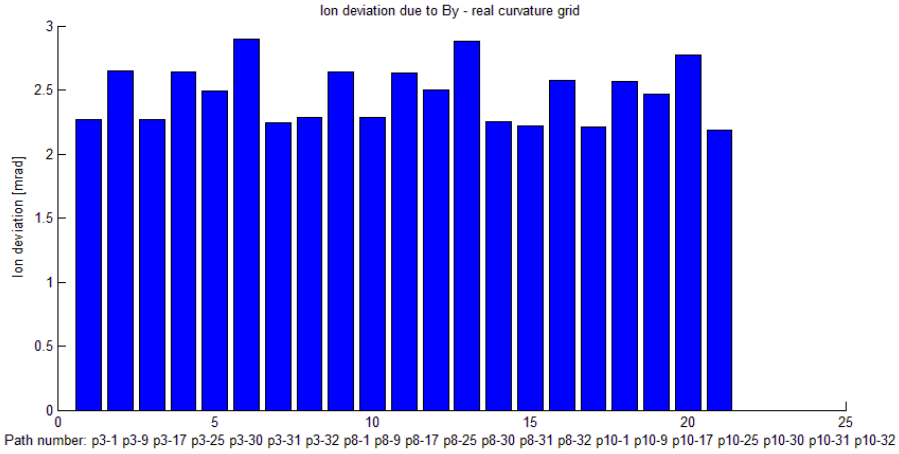

Fig. 159 Ion deflection due to By in the real curvature model.

Concerning the Bx component of magnetic field, the situation is more or less the same, there are some differences but very small, practically negligible. Moreover this component is two orders of magnitudes smaller with respect to By component. The plot of Bx profile is not reported because it's not interesting.

On Bz instead there are some visible differences, but still nothing practically relevant. In Fig. 160 Bz profile is reported while in Fig. 161 is shown the integral of Bz along the usual paths. These two plots are noticeably different from the corresponding Fig. 126 and Fig. 129 but the maximum Bz field intensity is still one order of magnitude smaller than By.

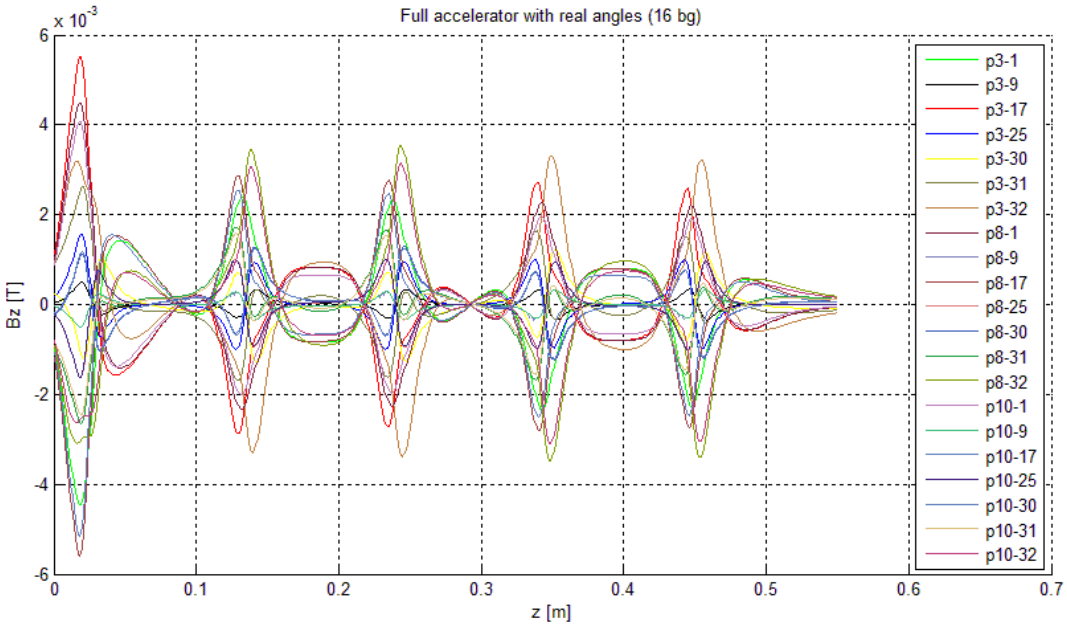

Fig. 160 Bz profile in real curvature grid model.

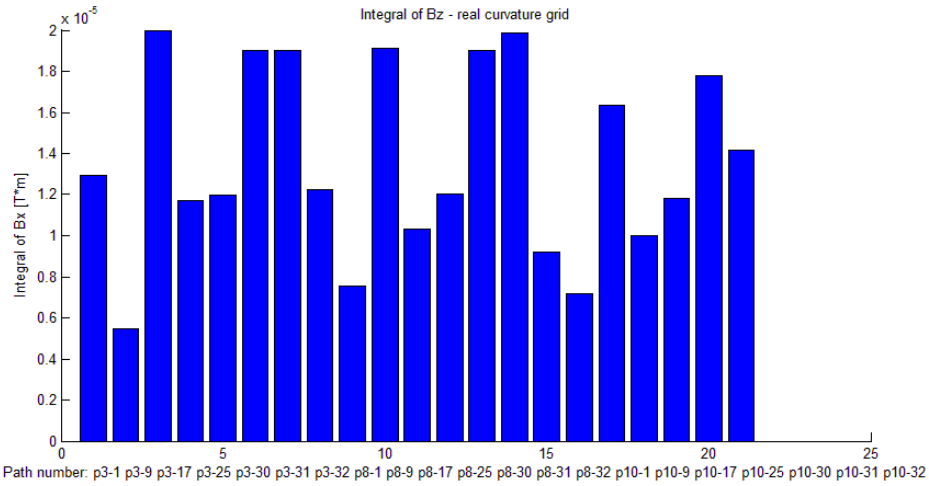

Fig. 161 Integral of Bz in the real curvature grid model.

In conclusion, the flat grid model till now adopted for all the magnetic calculations on MITICA grids is a very good approximation of the real geometry of the hyperlens grid, and so the validity of all the results obtained so far is preserved.

4.3. Off-normal operating conditions

4.3.1. Effect of demagnetization of permanent magnets

Demagnetization of permanent magnets inside the grids could happen as a consequence of localized overheating beyond the operational temperature of SmCo magnets, typically 250 °C.

In this section the consequences of demagnetization of the permanent magnets is analyzed in terms of increase of heat load on the grids and transmitted electrons.

In order to simulate the demagnetization, the magnetic remanence of the permanent magnets has been reduced from Br = 1.1 T to Br = 0.5 T and all the magnets surrounding a beamlet have been considered.

The next picture shows the position of the demagnetized magnets, and the six apertures used in the magnetic field simulations. The vertical component of magnetic field, By, calculated with NBImag along these profiles and compared to the nominal case is shown in Fig. 163.

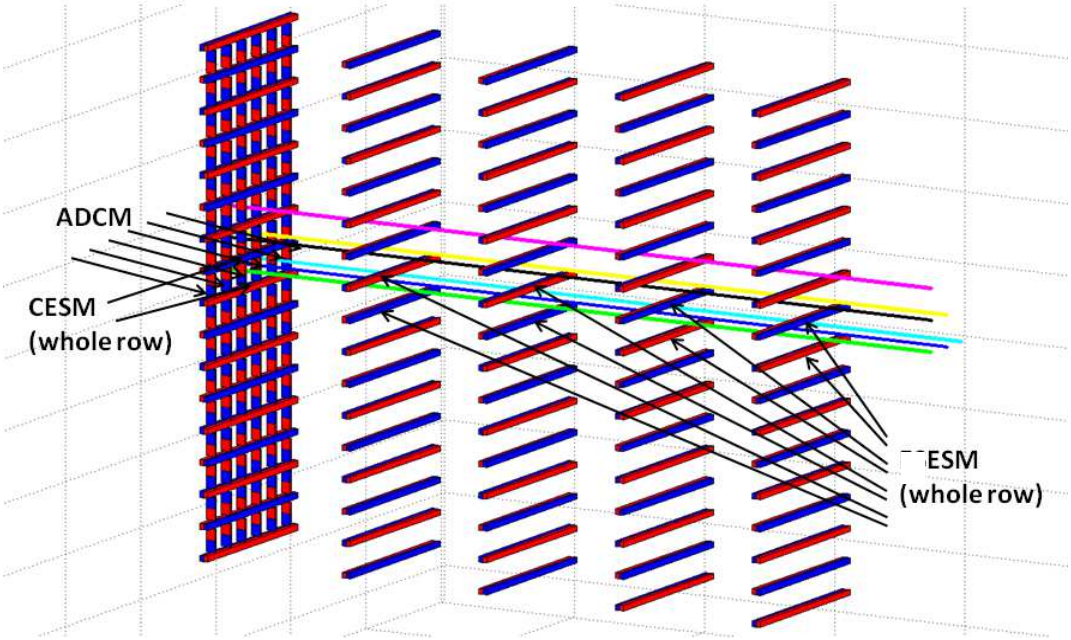

Fig. 162 Hypothetically demagnetized magnets and apertures considered in magnetic field simulations.

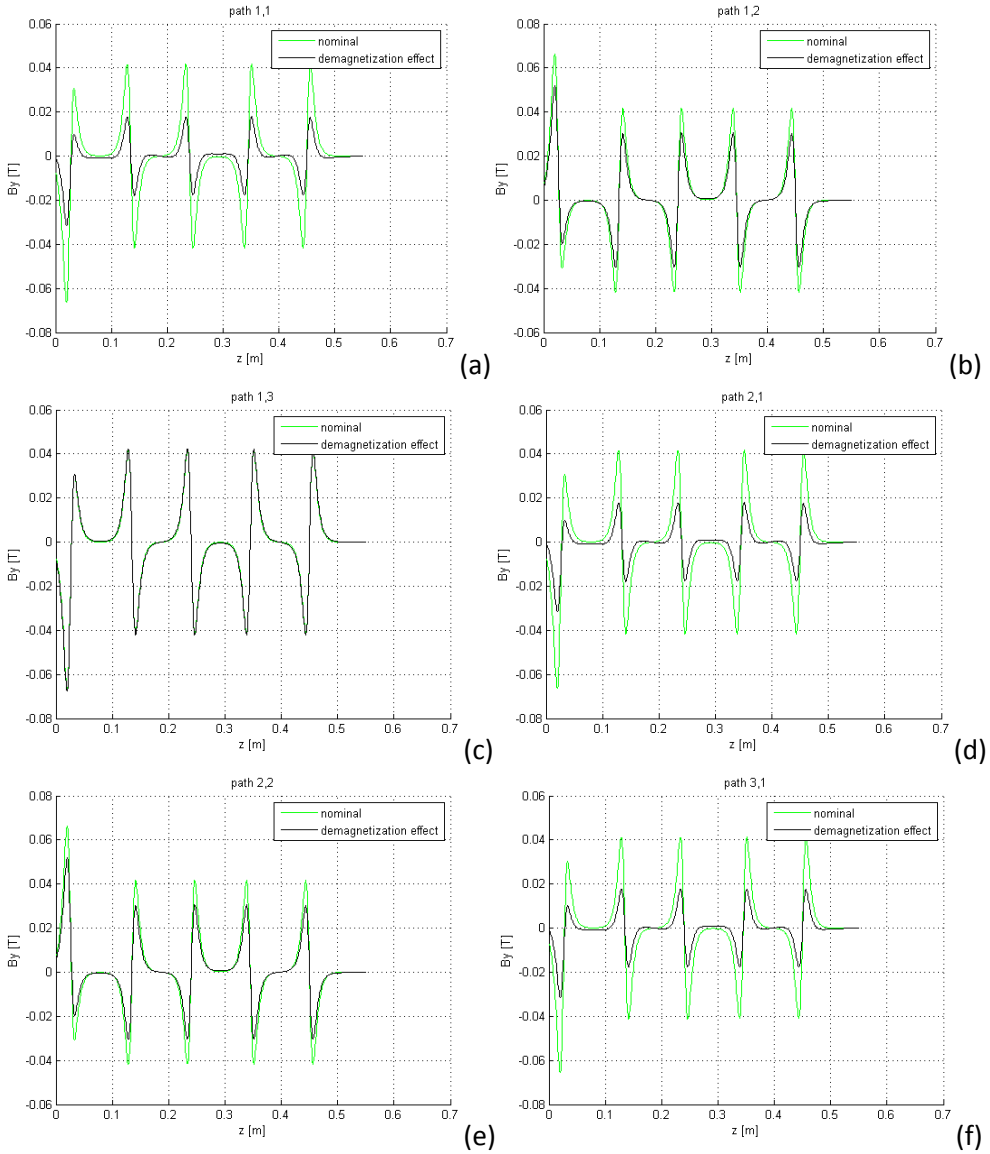

Fig. 163 By profile along six different aperture around a demagnetized group of magnets: (a) Central aperture = 1-1, (b) aperture 1-2 (adjacent vertically), (c) aperture 1-3, (d) aperture 2-1 (adjacent horizontally), (e) aperture 2-2, (f) aperture 3-1.

It can be noticed that By is strongly reduced in consequence of magnets demagnetization. The power load deposited on the grids by a beamlet undergoing this reduced magnetic field has been calculated with EAMCC and compared to the nominal case in Fig. 164. The increase of heat load on AG1 and AG2 is about 250%.

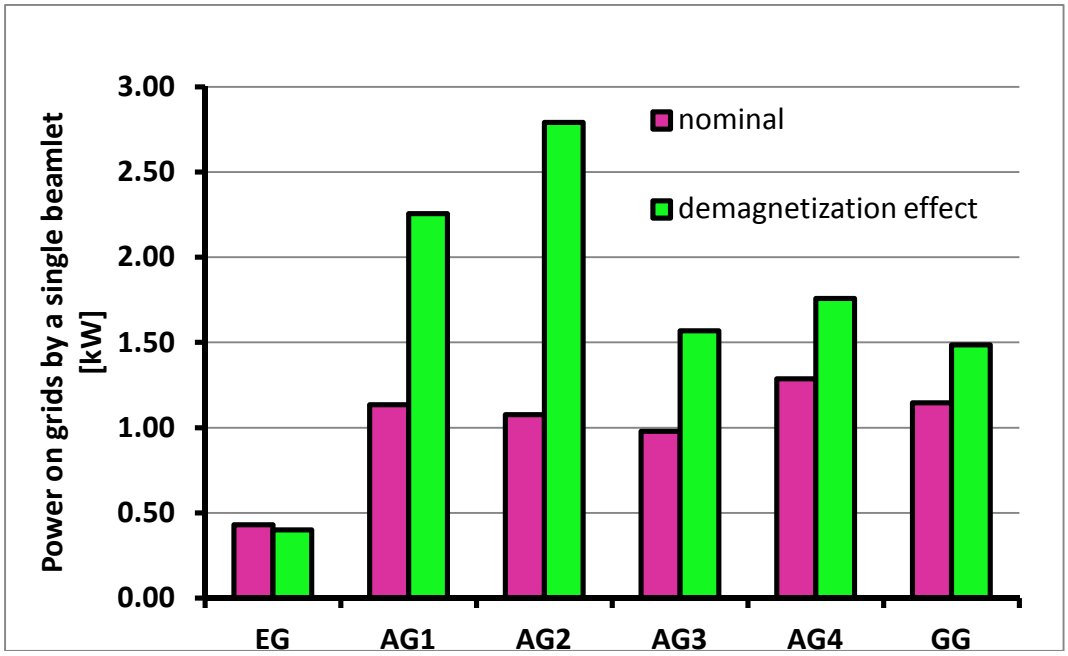

Fig. 164 Power on grids delivered by a single beamlet calculated in the nominal model and with demagnetization effect.

Transmitted electrons in the case of demagnetizations are reduced with respect to the nominal case, as shown in Tab. 23, because most of the electrons are stopped by the grids due to a reduced electron-suppression magnetic field.

	Transmitted electrons [MW]
Nominal	0.90
With demagnetization	0.72

Tab. 23 Transmitted electrons calculated with EAMCC in nominal case and with demagnetization effect.

4.3.2. Effect of wrong PG current value

In this section the effects of a wrong PG current value or a total PG current fault have been analyzed.

Three cases have been studied: the first with no PG current at all, the second with PG current at 75% of its nominal value and the third with a PG current at 125%.

Heat loads on the grids and transmitted electrons have been calculated with EAMCC and are shown in the next two figures:

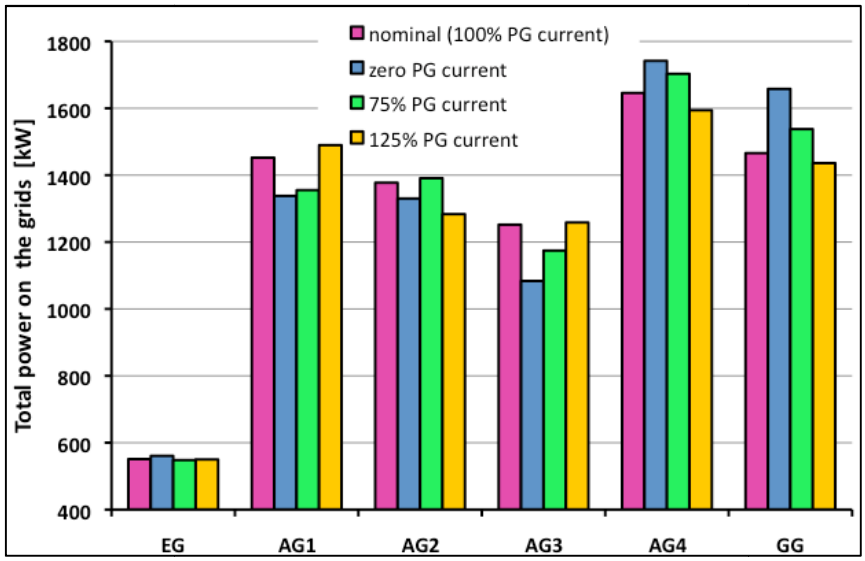

Fig. 165 Heat loads on the grids for various PG current levels.

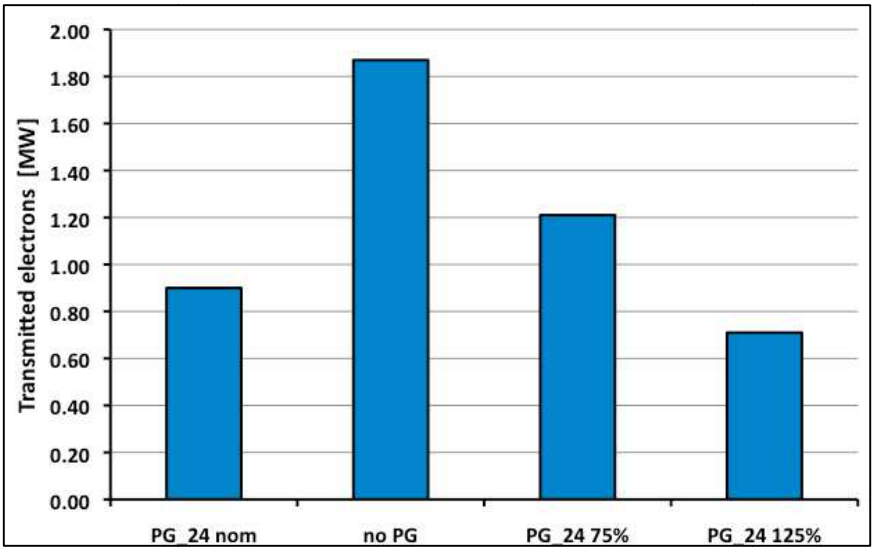

Fig. 166 Transmitted electrons for various PG current levels.

The effect of PG current variation in terms of power deposition on all the grids is not substantial, but the effect on the AG4, that is the grid with the maximum heat load, can be considerable.
The increase of AG4 power deposition for various PG current levels is summarized in the next table:

Case	Power load on AG4 [W]	% variation
Nominal PG current (3500 A)	1646	0%
no PG current	1742	+ 5.8%
PG current 75%	1703	+ 3.5%
PG current 125%	1594	- 3.2%

Tab. 24 Power load on AG for various PG current levels.

An increase of 5.8% on the maximum power load is considerable, but this situation can be prevented. In fact, a total fault of the PG current can be rapidly detected and a

protection protocol suddenly activated, so that the extra heat load would be very limited in time, without damaging the grid.
The effect on transmitted electrons is much higher, as shown in the next table:

Case	Transmitted electrons [MW]	% variation
Nominal PG current (3500 A)	0.90	0%
no PG current	1.87	+ 107.8%
PG current 75%	1.21	+ 34.4%
PG current 125%	0.71	- 21.1%

Tab. 25 Transmitted electrons for various PG current levels.

Also in this case, the regime with extra transmitted electrons would last for a limited time only, but in any case these results have been brought to the attention of the Beam Line Components (especially the neutralizer) designers. It emerged that the Neutralizer is still able to withstand a power load of transmitted electrons up to 2 MW, so, no damages should be caused to the BLC by this off-normal condition.

4.3.3. Clarification on transmitted electrons calculation

Before the analysis carried out in section 4.3. , the reference nominal value of transmitted electrons for the single BG model was 0.50 MW, while in the above section a value of 0.90 MW is shown.
This difference is due to three different reasons. The first one is that meanwhile these non ideal and off-normal analyses were performed, the reference PG busbar layout has changed from PG_18 to PG_24, in order to accomplish new design requirements. The results of Par. 4.2.2. are obtained with the PG_18 configuration, whereas the results of Par. 4.3.2. with the PG_24.
A second reason is that the long-range field in Par. 4.2.2. has been calculated using an Ansys model of plasma grid with detailed geometry of a grid slice, but with symmetry conditions along vertical direction. This model is certainly accurate in near-PG magnetic field calculation, but less accurate in far-PG field calculation. Unfortunately, as it can be intuitively expected and as it will be shown later, the leading parameter for the transmitted electrons is the magnetic field in the last gap of the accelerator, that is between the AG4 and the GG. For this reason, concerning the transmitted electrons calculation, an NBImag model, that is fully 3D, has been considered to be more meaningful in magnetic field calculation in the region far from the PG with respect to the above described Ansys model.
So, the calculations of Par. 4.3.2. are made using the long-range magnetic field calculated with NBImag.
The third reason is that in Par. 4.2.2. the magnetic field map has been calculated along the aperture 1.1 (see Fig. 119), while in Par. 4.3.2. along the aperture 3.8. This last difference has only a little impact on the result.
The increase from nominal level of transmitted electrons of 0.50 MW to the new one of 0.90 MW due the above mentioned three reasons is shown in the next figure:

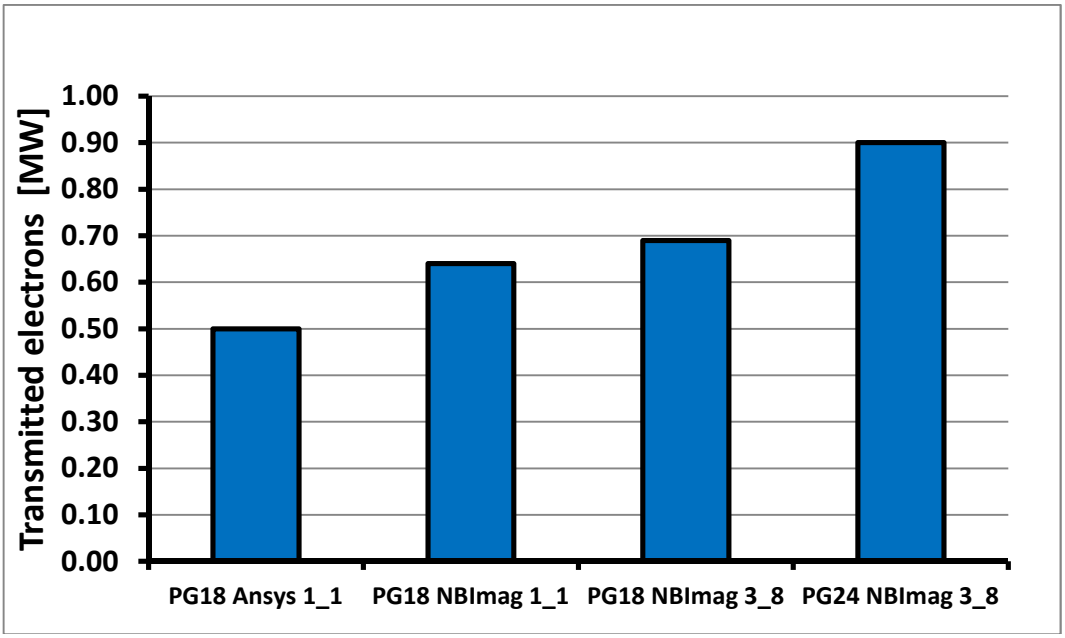

Fig. 167 Transmitted electrons for PG_18 calculated with Ansys or NBImag model of PG and PG_24 with NBImag model of PG.

Quantitatively, the increase in transmitted electrons for each different model is reported in the table below:

Step	transmitted electrons	% variation
PG_18 Ansys ---> PG_18 NBImag (aperture 1.1)	0.50 MW ---> 0.64 MW	+ 28.0%
PG_18 NBImag ap. 1.1 ---> PG_18 NBImag ap. 3.8	0.64 MW ---> 0.69 MW	+ 7.8%
PG_18 NBImag ---> PG_24 NBImag (aperture 3.8)	0.69 MW ---> 0.90 MW	+ 30.4%

Tab. 26 Increase of transmitted electrons due to different PG models and different reference PG busbar layouts.

Tab. 26 can be better understood if looking at Fig. 168, where the Bx profiles for the above considered PG models are shown. It's clear that the amount of transmitted electrons strongly depends on the intensity of the long-range magnetic field in the gap between AG4 and GG.

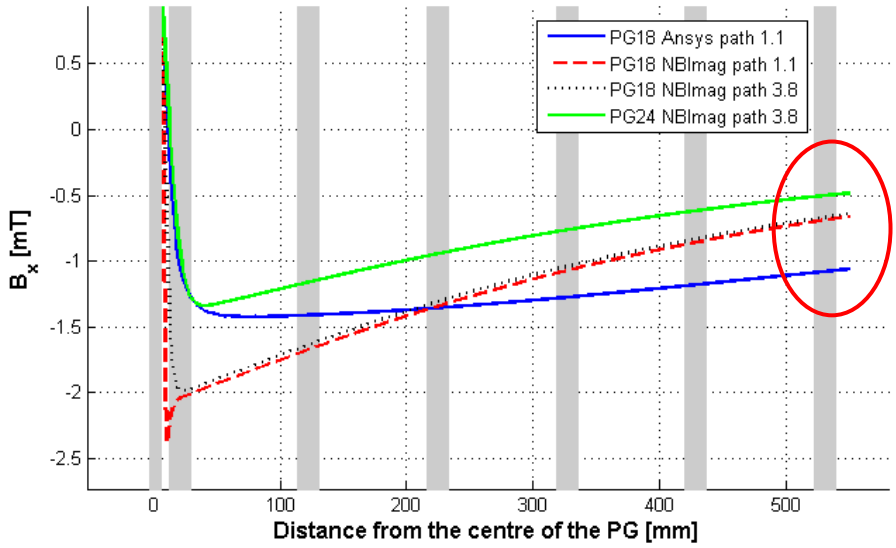

Fig. 168 Bx profiles for various different PG models.

4.3.4. Non uniform gas density and extracted current

A possible off-normal condition is related to non-uniform extraction of negative ions along the Plasma Grid surface, which has been sometimes observed in large ion sources and can be caused by non uniform distribution of cesium and/or by plasma drift within the ion source.

Numerical simulations with SLACCAD indicate that non-uniform extracted current leads to a degradation of the divergence of the affected beamlets of at least 1 mrad for -20% extracted current and of 3 mrad for -30% extracted current. An increase of the AG4 heat load in also expected, as shown in Fig. 169. The heat load on the last grids, however, is probably underestimated due to lack of a reliable model of the beam halo region.

Variations of the background gas density profiles are also considered off-normal conditions. Fig. 169 also shows the effect of density variations of ± 20% in the accelerator.

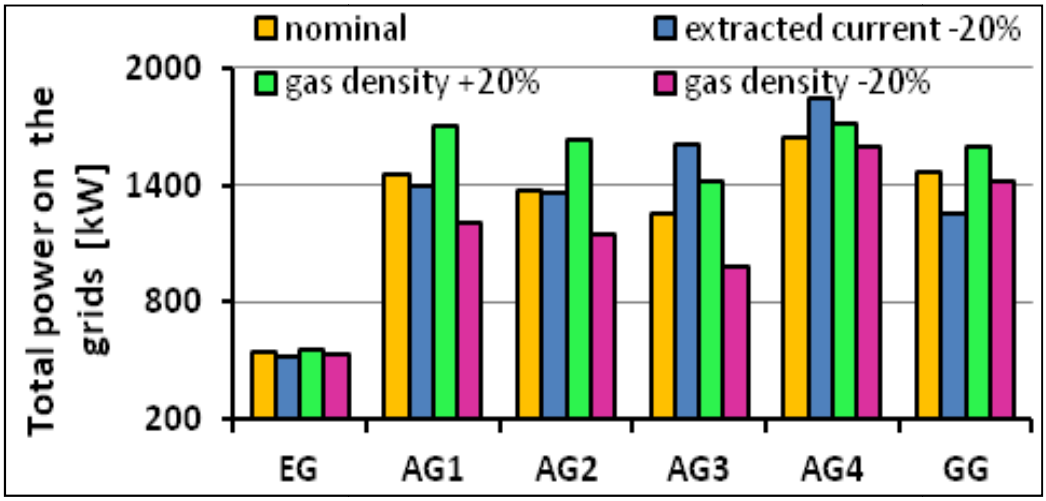

Fig. 169 Thermal loads on the grids calculated in case of reduced extracted current (-20%) and in case of different gas density profiles (±20%).

4.3.5. Effect of breakdowns between grids

The failure of one of the Acceleration Grid Power Supplies (AGPS) and/or an electrical breakdown between two consecutive grids also constitute off-normal operating conditions. These conditions were modeled considering zero voltage across one of the acceleration gaps (AG1-AG2, AG2-AG3, AG3-AG4 or AG4-GG), whereas the voltage on the other gaps remains unchanged.

The simulation results show that the divergence of the beamlets is increased with respect to the nominal case (+ 1.6 mrad in the worst case, see Fig. 170), but is still within the requirements. The thermal loads on the grids are in all cases lower with respect to the nominal case, as shown in Fig. 170.

(a)

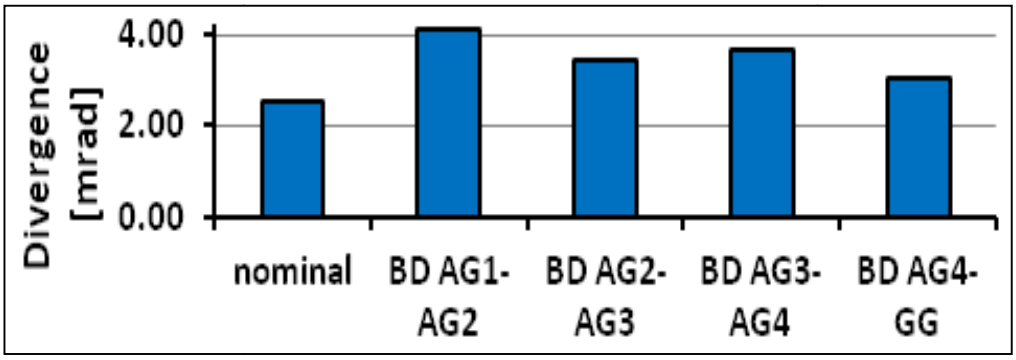

(b)

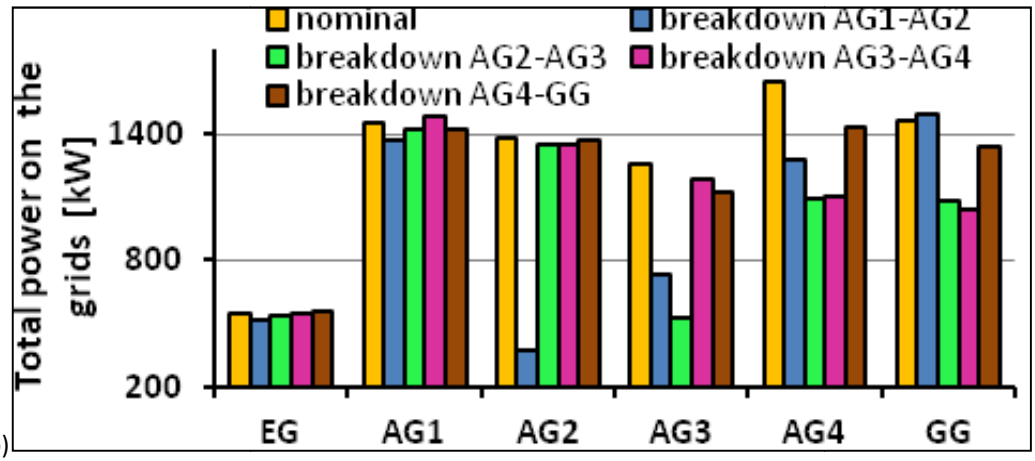

Fig. 170 Beamlet divergence (a) and thermal load on each grids (b), in case of breakdown between two grids or power supply fault.

Breakdowns between PG and EG, or between EG and AG1 have not been considered, as accelerator operation will be stopped immediately by an automatic protection to avoid high risk of damage to the accelerator due to unacceptable beam optics.

4.3.6. Off normal operating conditions of thermo-mechanical nature

Due to the high heat loads, out-of-plane deformations of the grids are foreseen during the operations of the accelerator, as shown in Fig. 171a for the EG. As a consequence, the gaps between the grids are modified with respect to the nominal geometry.

The effect of a variation of the extraction gap between 5 and 7 mm has been investigated, keeping the acceleration gaps at the nominal value. As shown in Fig. 171b, variations of the beam divergence of about ± 0.5 mrad have been obtained, which are considered acceptable for the MITICA accelerator.

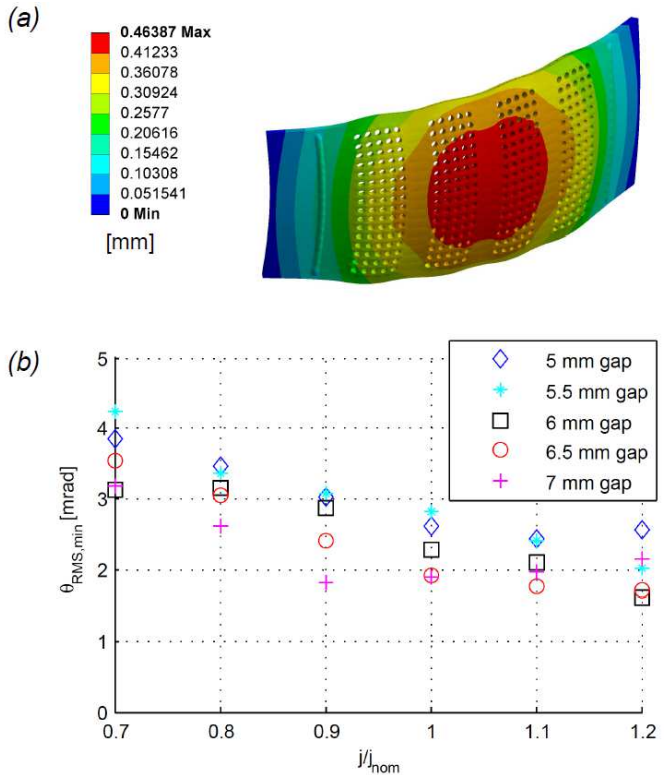

Fig. 171 Effect of out-of-plane deformation on beam optics: (a) typical deformation of the EG under nominal heat load; (b) beam divergence as a function of extracted current and extraction gap length.

The effects of grid misplacement and deformations due to wrong mechanical tolerances and over-constrained thermal expansion have also been analyzed. Tab. 27 reports a summary of the possible sources of beamlet deflections.

Cause of Beamlet deflection	**deflection (mrad)**
Grid offset in plane (±50% Power Load)	[-0.15, 0.25]
Grid offset in plane (mechanical Positioning tolerance)	±0.7
Grid offset out of plane (Thermal deformation)	+0.3
Grid offset out of plane (±50% Power Load)	±0.1
Grid offset out of plane (Positioning tolerance)	[-0.5, +0.6]
Magnetic non uniformity	±0.35
Tolerance on magnet positions	±0.1
Total Beamlet Deflection (range)	[-1.6, 2.4]

Tab. 27 Summary of beamlet deflection effects in the accelerator.

The most important effect is from in-plane grid positioning offset, caused by thermal expansion and positioning tolerance: the presence of an offset δ between the beamlet axis and the aperture centre tends to deflect the beamlet according to the well-established formula of Davisson and Callbick: $\phi=\delta(E_1-E_2)/4V$. (φ is the deflection that the beamlet receives after crossing the grid, E_1 and E_2 are the values of the electric field before and after the grid respectively, V is the beam energy when crossing the aperture). From the direct summation of the effects it is obtained that the worst-case

maximum total beamlet deflection at the exit of the accelerator is in the range [-1.6, 2.4] mrad, which is slightly larger than the requirement on beamlet alignment (±2mrad).

4.3.7. Detection and protection strategies

Detecting off-normal operating conditions is easy only in the case of faults having purely electric nature (power supply fault and electrical breakdown). In the other cases, detection can rely on temperature measurement on the cooling water of the accelerator grids and beam line components, in synergy with different diagnostics, such as:

- Beam Emission Spectroscopy (BES) which provides integrated information on 20 beamlets (horizontally) or 64 beamlets (vertically) downstream of the accelerator;
- Beam Tomography, also located downstream of the accelerator;
- Secondary Emission Imaging on the calorimeter.

Cross-checking experimental data and comparison with simulations will also be necessary. This can be a tricky and time-consuming procedure, particularly in case of local effects such as demagnetization of permanent magnets and non-uniform extracted current.

4.4. Conclusions

Several non-ideal magnetic field effects and off-normal operating conditions have been analyzed in this section and are here briefly summarized.
Analyzed non ideal effects:

- Cumulative effects of permanent magnets in the 16 BG grid model;
- Effect of mechanical tolerances of grid grooves;
- Effect of real orientation of Beam Groups.

Conclusions on non-ideal effects:
The considered effects have negligible consequences from the point of view of heat loads on the grids, and only limited consequences on magnetic field uniformity and ion deflection. The approximations used so far in modelling of MITICA accelerator (single Beamlet Group model, flat grid, magnets in nominal position) are all valid.

Off-normal operating conditions:

- Effect of demagnetization of permanent magnets;
- Effect of wrong PG current;
- Clarification on transmitted electrons calculation;
- Non uniform gas density and extracted current;
- Effect of breakdowns between grids;
- Off normal operating conditions of thermo-mechanical nature;
- Detection and protection strategies.

Conclusions on off-normal operating conditions:
Demagnetization of a large number of permanent magnets is a severe accident and leads to a high increase (up to 250% of nominal value) of power load locally deposited on the grids.
Failure of PG current power supply increases the transmitted electrons by a factor of two, putting into risk the neutralizer.
The other considered effects are not worrying from the point of view of heat loads on the grids, but can, in the worst case, lead to a total beamlet deflection slightly out of specification (+2.4 mrad, having ±2mrad maximum deflection as requirement).

Finally, failure detection can require complex procedures, which are to be based on processing and cross-checking data from different diagnostic systems.

5. Development of a flux-gate magnetic sensor

A magnetic sensor of the type flux-gate has been studied and developed at Consorzio RFX in order to comply with the particular requirements for magnetic measurements inside HNB and MITICA vessel, described in the ITER document [50].

5.1. Introduction

ITER Neutral Beam Injectors will operate in an environment characterized by a relatively strong stray magnetic field coming from the Poloidal Field Coils of ITER, capable to deflect the beam, and for this reason each injector will be provided with a Passive Magnetic Shield (PMS) all around.

Despite the PMS, it's still necessary to adopt active compensation systems, and for this reason six large Active Correction and Compensation Coils (ACCC) will be installed on each injector to compensate for the residual magnetic field, mainly vertical, inside the vessel.

The ACCC will operate in feedback control and will need as input the measure of magnetic field inside the vessel, i.e. in an environment subjected to the neutron flux coming from the tokamak.

For these reasons a magnetic sensor that is robust, radiation hard, and remotely controllable has to be designed. This sensor has then to be tested on MITICA and finally installed on the ITER HNB.

Magnetic sensors of the type "flux-gate" could possibly satisfy all the above-mentioned requirements, but there are no commercial models working in the required magnetic field range.

For this reason a prototype of a new flux-gate capable to measure magnetic field in the required range has been realized and tested at Consorzio RFX. In parallel, a numerical simulation tool has been developed in order to predict the results of the prototype and of future flux-gate sensors, which shall comply with the particular requirements for magnetic measurements inside HNB and MITICA vessel, described in the ITER document [50]. This document describes the requirements for the sensors to be installed on HNB, the range of magnetic field to measure, the sensitivity, the speed and the accuracy, the signal-to-noise ratio and the required radiation hardness.

In Tab. 28 the main sensor requirements are summarized, for a complete description, refer to [50].

Range of magnetic field	0 – 2 mT
Sensitivity	0.01 mT for ITER HNB and 0.001 mT for MITICA
Absolute accuracy	<0.02 mT
Time derivative of magnetic field	>5.8 mT/s
Neutron flux to withstand	Estimated neutron flux near calorimeter $\approx 10^9$ n/cm^2/s for a total burn time of $2x10^7$ seconds

Tab. 28 Summary of main sensor requirements.

Considering these requirements, a flux-gate type magnetometer seems to be a possible solution for the following reasons:

- the ferromagnetic iron core is intrinsically radiation hard to a very high level (possible effects of radiation on the magnetic properties have to be evaluated, but they could be compensated rather easily);
- the driving coil and the pick-up coil can be made of copper conductor with radiation-hard insulation, such as metal-oxide insulated cables (MIC) or fiberglass insulated cables (POZh), which have already been considered for in-vessel magnetic sensors for ITER;
- it's intrinsically robust and its range and sensitivity can comply with the requirements of Tab. 28.

Many models of flux-gate magnetometers are commercially available, (some companies are Burtington, Stefan Mayer, Applied Physics Systems, Speake & Co), but they are mainly used as magnetic compass or to measure magnetic field anomalies due to ferromagnetic objects, so they are designed for measuring magnetic field in the order of Earth magnetic field, i.e. 0.05 mT. Their measurement range is therefore not larger than 0.1 mT, but their resolution and accuracy can be very good, smaller than 0.001 mT
The main purpose of this work is to analyze the feasibility of a flux-gate sensor having an extended measurement range, up to ~ 10 mT.
For an exhaustive review of magnetic sensor, see Chapter 1 of [51].

5.2. Flux-gate operating principle

A flux-gate sensor is a type of magnetic field sensor typically capable of measuring DC or low frequency AC fields in the range 10^{-10} – 10^{-4} T. Its basic configuration is constituted by a cylindrical core made of soft magnetic material periodically saturated by an excitation field induced by an excitation coil. The component of external magnetic field parallel to the core is channeled trough the core and changes its permeability, modulating the induced voltage measured by a sense coil or pick-up coil placed around the core. The second harmonic of the induced voltage is proportional to the external field, as shown in Fig. 172, taken from [52].

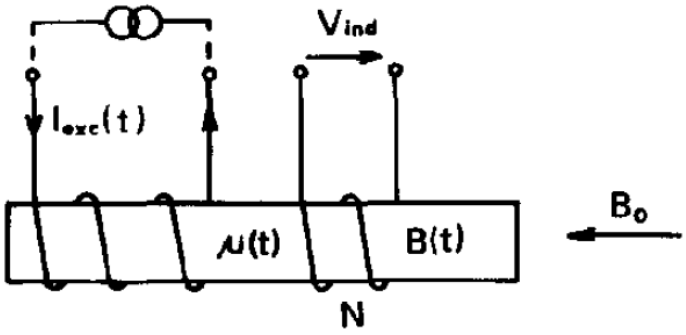

Fig. 172 Basic sensor configuration. The core is excited by an AC current I_{EXC} and μ(t) is modulated with twice the excitation frequency. The signal induced in the sense coil, V_{IND}, at the second harmonic of I_{EXC} is proportional to the external field $B_{0.}$ (picture taken from [52]).

Since in the basic sensor configuration the sense coil picks up also the excitation frequency, at a high level, removing this signal for having the second harmonic only can be problematic. For this reason a double core configuration is usually adopted, in this way the induced excitation voltages in the two cores cancel each other and the sense coil picks up the second harmonic only, ideally.

Fig. 173 is taken from [53] and shows two possible layouts for the double-rod core configuration: the Forster type and the Vacquier type. The difference is only in the pick-up coil configuration.
The flux-gate prototype realized at Consorzio RFX and discussed in the next sections is of the Forster type in order to minimize the noise picked-up by the sense coil.

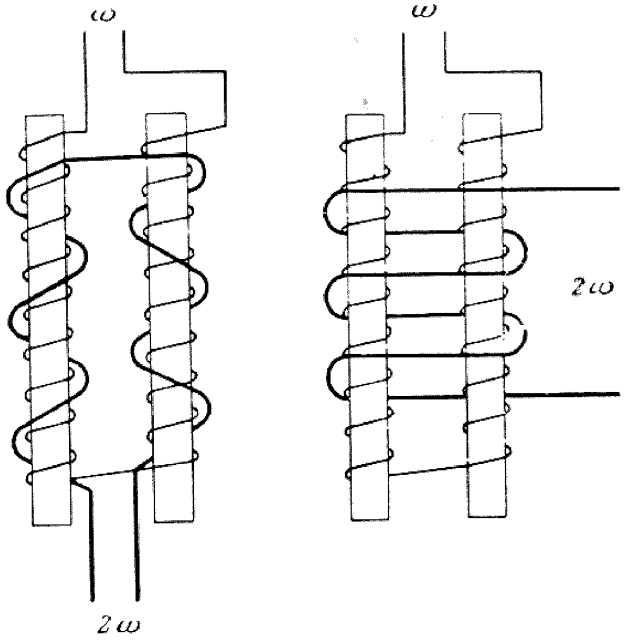

Fig. 173 Double-rod core configurations: left Forster type, right, Vacquier type (picture taken from [53]).

Another possibility is to join the two rod cores in a single core, ring shaped, as shown in Fig. 174, also taken from [53]. This layout is the evolution of the Vacquier type flux-gate and by placing two ring cores and three sense coils it's possible to build a three axes magnetic sensor.

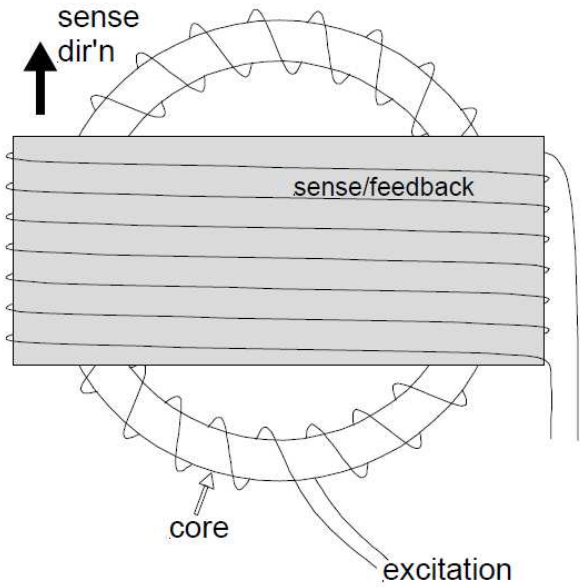

Fig. 174 Ring core type flux-gate (picture taken from [53]).

For a deeper knowledge on flux-gate magnetic sensors, refers to [51], [52], [53] and [54].

5.3. Description of numerical model

The model of the flux-gate sensor consists of two parts:

- a numerical approximate model describing the hysteresis phenomena in a ferromagnetic material;
- an analytical model of the electromagnetic behavior of magnetic core of the flux-gate including air gaps.

The numerical model of the hysteresis phenomena is parametric, so that it can be adjusted to describe common ferromagnetic materials, both soft magnetic materials, such as iron, carbon steel, silicon steel for magnetic applications, and hard magnetic materials, such as NdFeB and SmCo permanent magnets.
The main parameters of the model are:
B_r = remanence = residual magnetic induction (or flux density) B in the material when the applied external magnetic field H is zero (Tesla);
H_c = coercivity = external magnetic field H which produces zero magnetic induction B=0 in the material (Ampere/m);
B_s = magnetic induction (or flux density) B in the material at saturation (Tesla);
alfa = exponent describing the sharpness of transition from $-B_s$ to $+B_s$ in the hysteresis loop.
The hysteresis model describes the new value of the induction field B(t) as a function of the new value of the external magnetic field H(t) and of the previous values of the induction B(t-1) and external magnetic field H(t-1).
The new value of the induction field B(t) is calculated using a sigmoid function for describing the transition between the previous (H(t-1), B(t-1)) values and the new (H(t), B(t)) values.

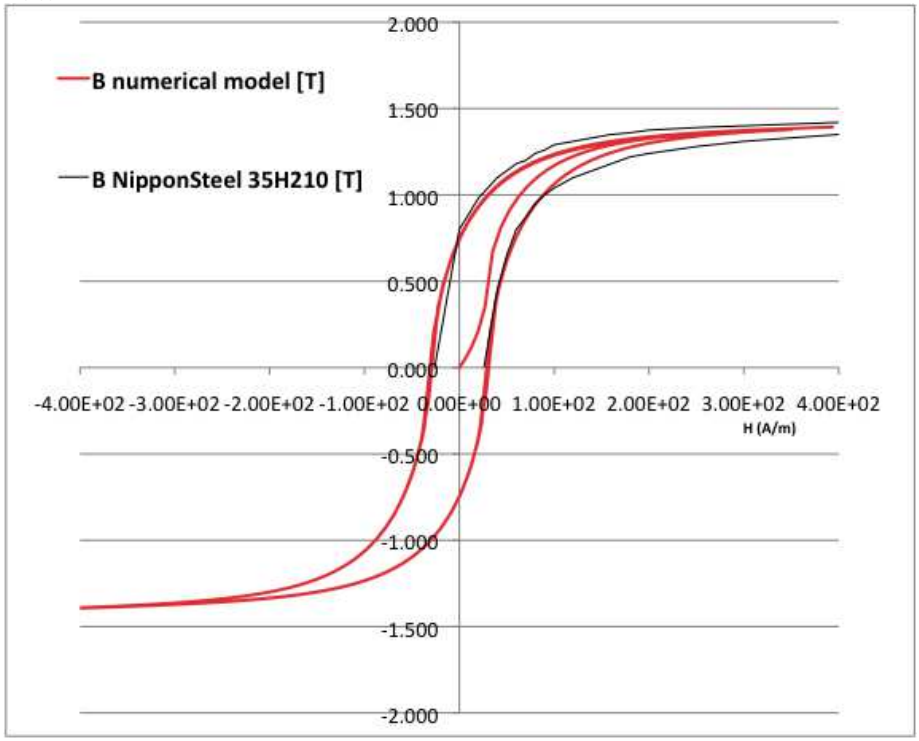

Fig. 175 Hysteresis loop B=B(H) of a commercial non-oriented electrical steel 35H210 produced by Nippon Steel and used for electrical motors and alternators (black line). The red line shows the first magnetization curve and the hysteresis loop B=B(H) obtained from the numerical model of the core of the flux-gate sensor. The hysteresis model parameters are: Hc=30 A/m, Br= 0.8 T , Bs=1.35 T, alfa=0.6. The model reproduces with sufficient accuracy the behavior of the commercial steel.

The analytical model of the electromagnetic behavior of the flux-gate is based on the usual magnetic-circuit approximation (including the air gap) and allows to estimate the magnetic flux in the core $\Phi(t)$ as a function of the externally applied magnetic field B_{ext} (t) and of the sinusoidal current in the "excitation coil" I_{exc} (t). However, the analytical model is continuously updated using the results of the above described B=B(H) hysteresis model, in place of the constant-permeability model normally used in the magnetic-circuit approximation.
The induced voltage in the "sense coil" $v_{sense}(t)$ is thus calculated by determining the time-derivative of the magnetic flux in the core $\Phi(t)$. However, $v_{sense}(t)$ typically has a fundamental component at the same frequency as the excitation current I_{exc} (t), which is not related to the magnetic field to be measured. Instead, the second harmonic, produced by the non-linear hysteretic behavior of the ferromagnetic core is related to the externally applied magnetic field H_{ext} (t).
It is therefore necessary to filter the output signal $v_{sense}(t)$ in order to extract the useful component.

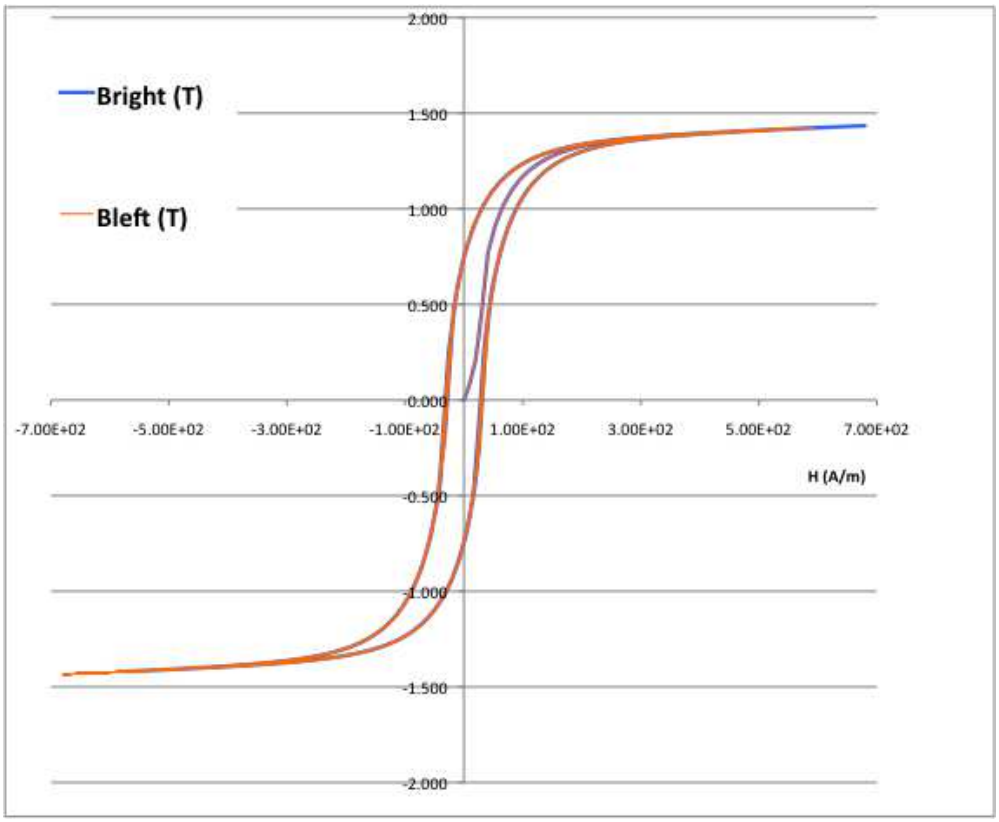

Fig. 176 Simulation of the hysteresis loop of a flux-gate sensor having the same magnetic properties as in Fig. 175 with no gap (gap = 0.0 mm), Iexc=0.3 A (sinusoidal), Nturns=100, subjected to an external induction field Bext= 0.1 mT. The blue curve represents the behavior of the right part of the core, whereas the red curve represents the left part of the core. The two curves are overlapped for most of the loop, except in the lower left part (red curve only) and upper right part (blue line only).

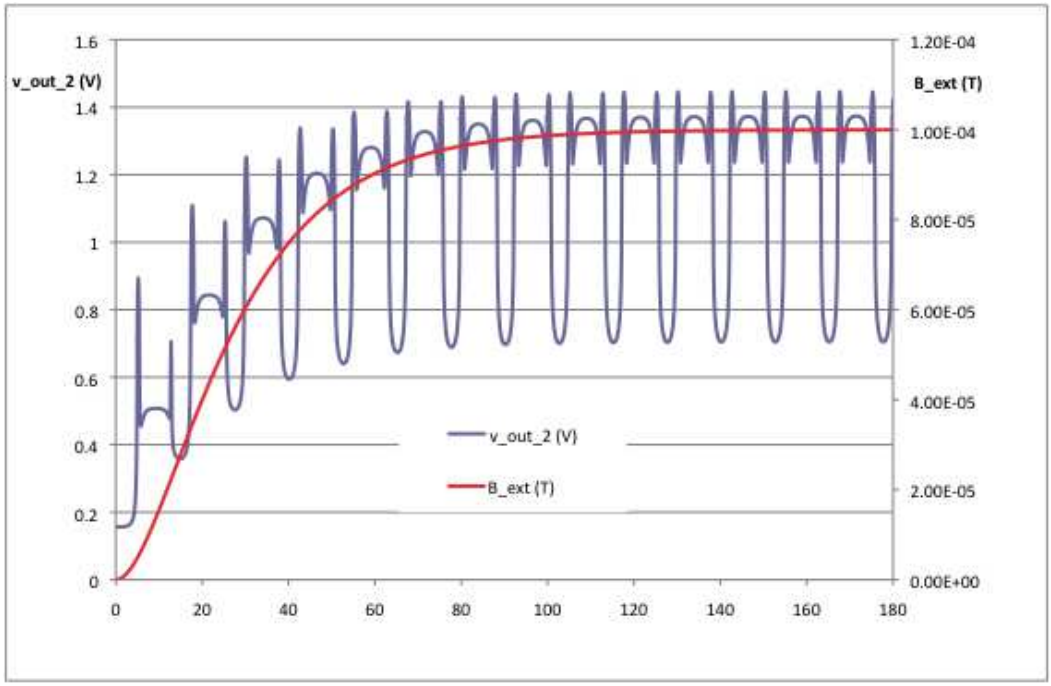

Fig. 177 Waveform of the external magnetic field $B_{ext}(t)$ (red curve, Bmax= 0.1 mT) and corresponding time behavior of the 2nd harmonic of the output voltage of a flux-gate sensor (parameters as described in Fig. 176).

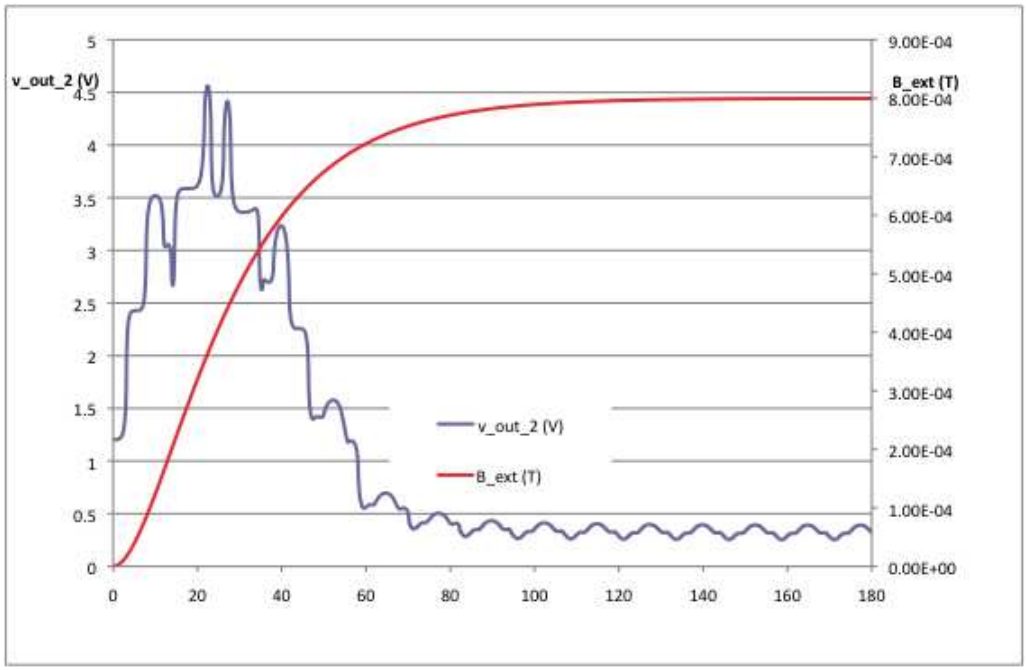

Fig. 178 Waveform of the external magnetic field $B_{ext}(t)$ (red curve, Bmax= 0.6 mT)) and corresponding time behavior of the 2nd harmonic of the output voltage of a flux-gate sensor (parameters as described in Fig. 177). The saturation of the output voltage is evident.

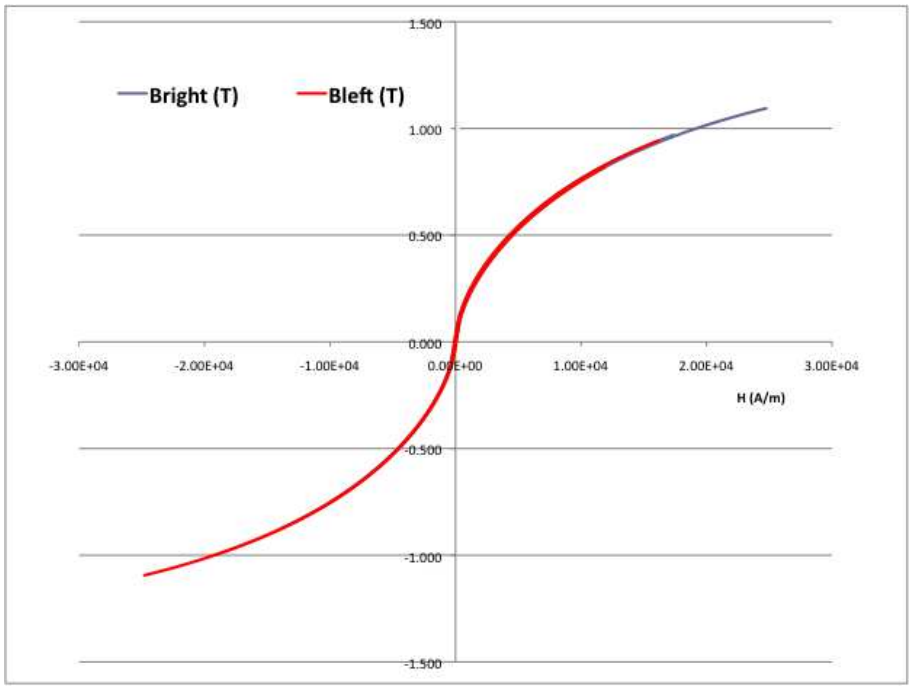

Fig. 179 Simulation of the hysteresis loop of a flux-gate sensor having the same magnetic properties as in Fig. 175 however with 1.0 mm gap, Bext=10.0 mT, Iexc=8 A (sinusoidal), Nturns=100, subjected to an external induction field of 0.1 mT. The blue curve represents the behavior of the right part of the core, whereas the red curve represents the left part of the core. The two curves are overlapped for most of the loop, except in the lower left part (red curve only) and upper right part (blue line only).

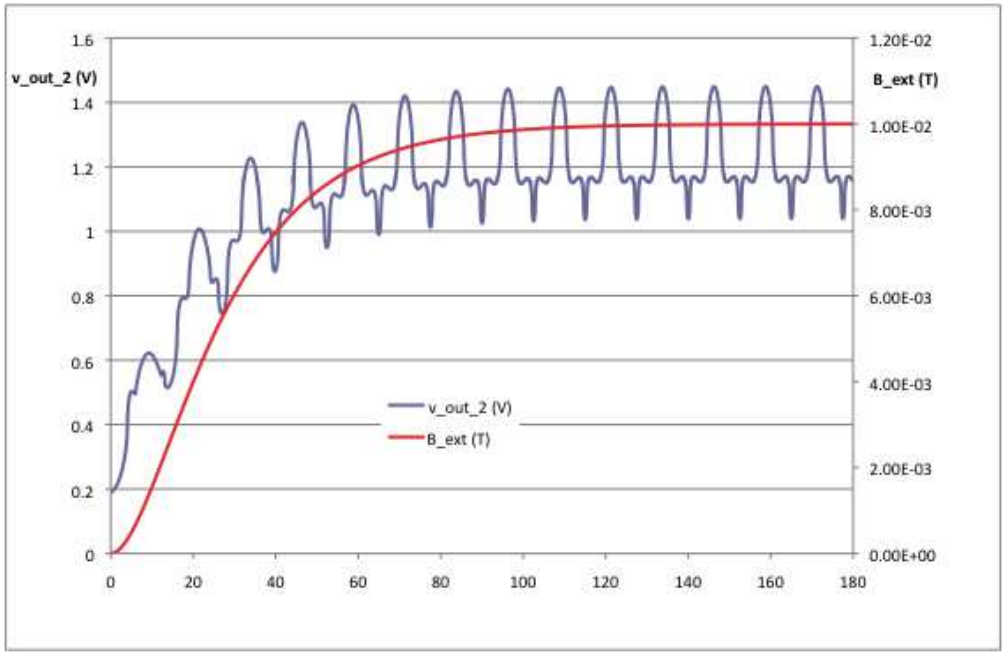

Fig. 180 Waveform of the external magnetic field $B_{ext}(t)$ (red curve, Bmax= 0.1 mT)) and corresponding time behavior of the 2nd harmonic of the output voltage of a flux-gate sensor (parameters as described in Fig. 179).

From the simulations it is possible to see that the output signal of the flux-gate sensor saturates when the external field

$Hext(t) \approx Bext(t)/\mu_0$

combined with the field produced by the excitation current

Hexc(t)=Nexc * Iexc(t)/lcore
causes both cores to work in a region where the slope of the hysteresis loop is the same (or the hysteresis loops become symmetrical). This can happen when one or more of the following conditions are verified:

- the sinusoidal excitation field Hexc(t) or excitation current Iexc(t) is too large;
- the sinusoidal excitation field Hexc(t) or excitation current Iexc(t) is too small;
- the external field Hext(t)≈Bext(t)/μ_0 is too large;
- the coercivity of the ferromagnetic core (Hc) is too large;
- the average permeability of the ferromagnetic core (≈Br/Hc) is too large.

For these reasons, the high-sensitivity flux-gate sensors commercially available are normally made of highly permeable magnetic cores (such as permalloy and amorphous magnetic materials, such as ferrites), have a very good resolution (~1 μT) but have a limited measurement range (0.1 mT).
For the MITICA HNB sensors, lower permeability material such as standard low-loss electric steel in combination with a small air gap can be used to achieve the required range of 10 mT.

5.4. Description of FEMM model

A magnetic model of the flux-gate sensor has been realized with the 2D software FEMM and it is shown in Fig. 181. By varying the excitation current and thus H in the model, a magnetization curve of the whole sensor has been obtained. In Fig. 182 this curve is shown together with the magnetization curve of the pure core material (m36-steel for transformer cores).
It can be noticed that the whole magnetic permeability of the sensor is lower than the one of the pure material, as well as the saturation limit.

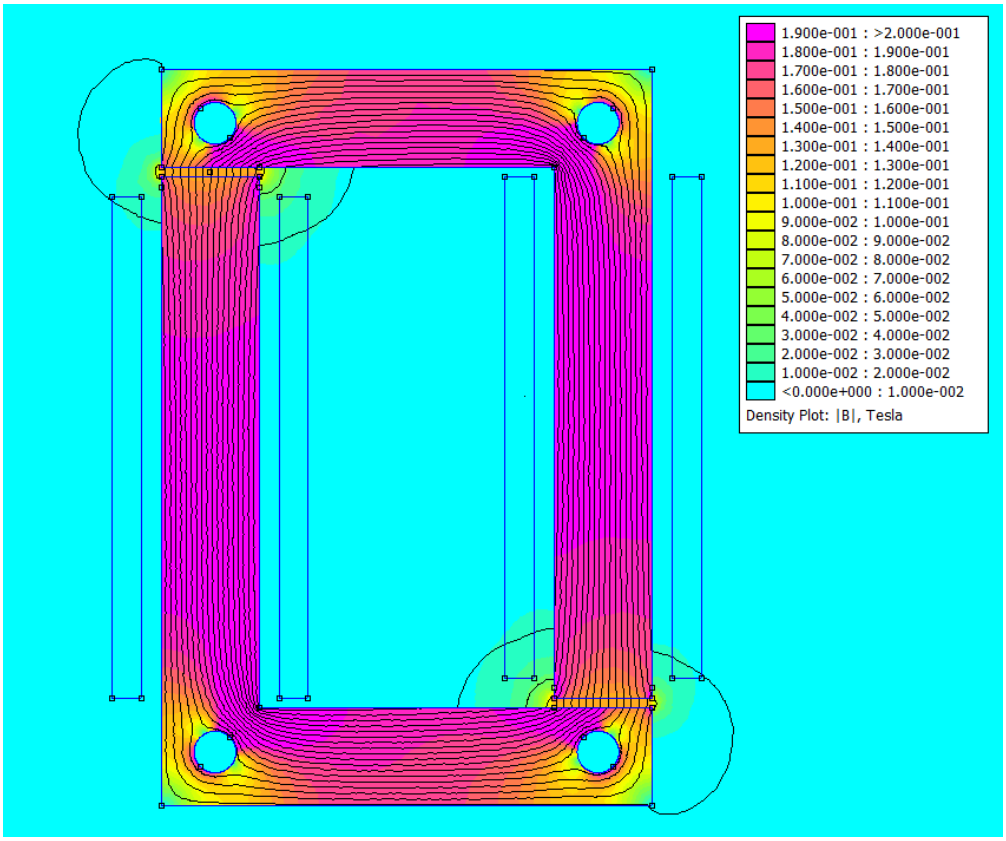

Fig. 181 2D FEMM model of the flux-gate sensor. In this example the excitation current is 200 Aturn in each of the two parts of the ferromagnetic core.

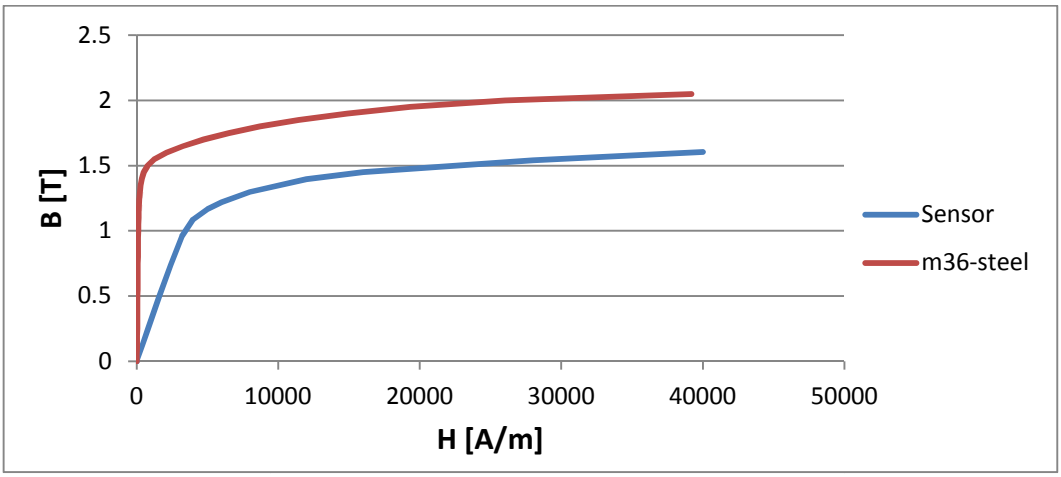

Fig. 182 Magnetization curve of the core material compared with magnetization curve of the whole sensor, obtained by varying H in the FEMM model.

5.5. Construction of the prototype

The flux-gate prototype has been realized at Consorzio RFX using steel sheets taken from a transformer to make the ferromagnetic core. The core has been realized in two L-shaped parts in order to allow the insertion of the excitation coils. The two parts have been mounted on a support leaving two air gaps between them. The gaps have the purpose of avoiding the magnetic saturation of the core, which would invalidate the flux-gate operation.

The excitation coils have been realized on two spools Φ15mm x 45 mm (3 radial turns), the electric wire has been selected in order to keep the dissipated power below 5 W, having a maximum current flowing in the wire of 3 A. In Tab. 29 the various parameters depending on wire diameter are reported. The selected wire diameter is highlighted in light blue:

d [mm]	Resistance [mΩ/m]	n axial turns	wire length [mm]	Total resistance [Ω]	n total turns	total coil current [A]	dissipated power [W]
1.00	22.92	38	6618	0.152	114	342	0.68
0.95	25.39	40	6901	0.175	120	360	0.79
0.90	28.29	43	7348	0.208	129	387	0.94
0.85	31.72	45	7616	0.242	135	405	1.09
0.80	35.81	48	8045	0.288	144	432	1.30
0.75	40.74	51	8464	0.345	153	459	1.55
0.70	46.77	55	9038	0.423	165	495	1.90
0.65	54.24	59	9599	0.521	177	531	2.34
0.60	63.66	64	10307	0.656	192	576	2.95
0.55	75.76	70	11159	0.845	210	630	3.80
0.50	91.67	77	12148	1.114	231	693	5.01
0.45	113.18	86	13427	1.520	258	774	6.84
0.40	143.24	96	14831	2.124	288	864	9.56
0.35	187.09	110	16814	3.146	330	990	14.16
0.30	254.65	129	19506	4.967	387	1161	22.35
0.25	366.69	155	23184	8.501	465	1395	38.26
0.20	572.96	193	28551	16.358	579	1737	73.61
0.15	1018.59	258	37743	38.445	774	2322	173.00
0.10	2291.83	387	55980	128.297	1161	3483	577.34
0.05	9167.32	775	110834	1016.051	2325	6975	4572.23

Tab. 29 Selection of wire for the excitation coils. The final choice is highlighted in light blue.

A picture of the prototype, without the pick-up coil, is shown in the next Fig.:

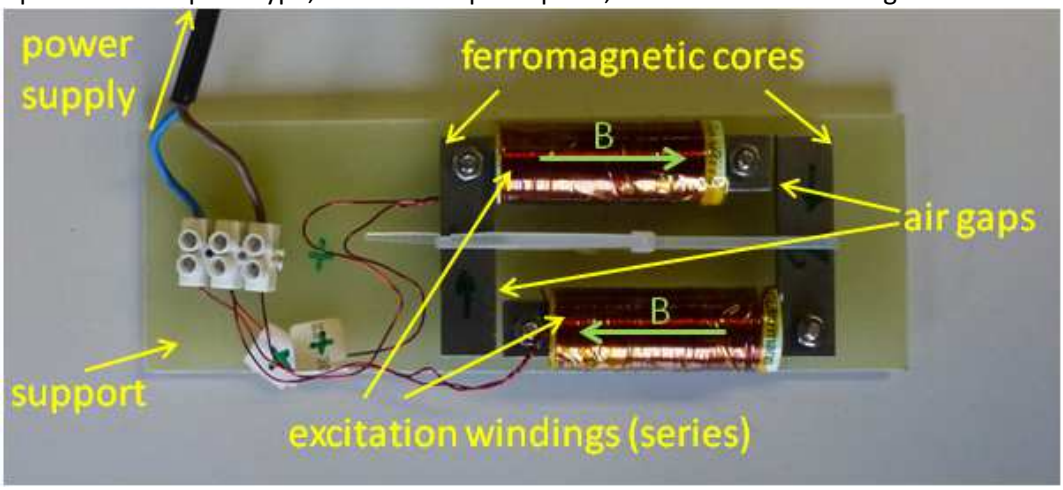

Fig. 183 Flux-gate prototype (without pick-up coil).

The pick-up coil (460 turns) has been winded on top of the excitation coils, but oriented in such a way to measure magnetic flux variations along the same oriented direction. In

Fig. 184 the prototype completed with the pick-up coil and inserted in the solenoid for generating the external field is shown:

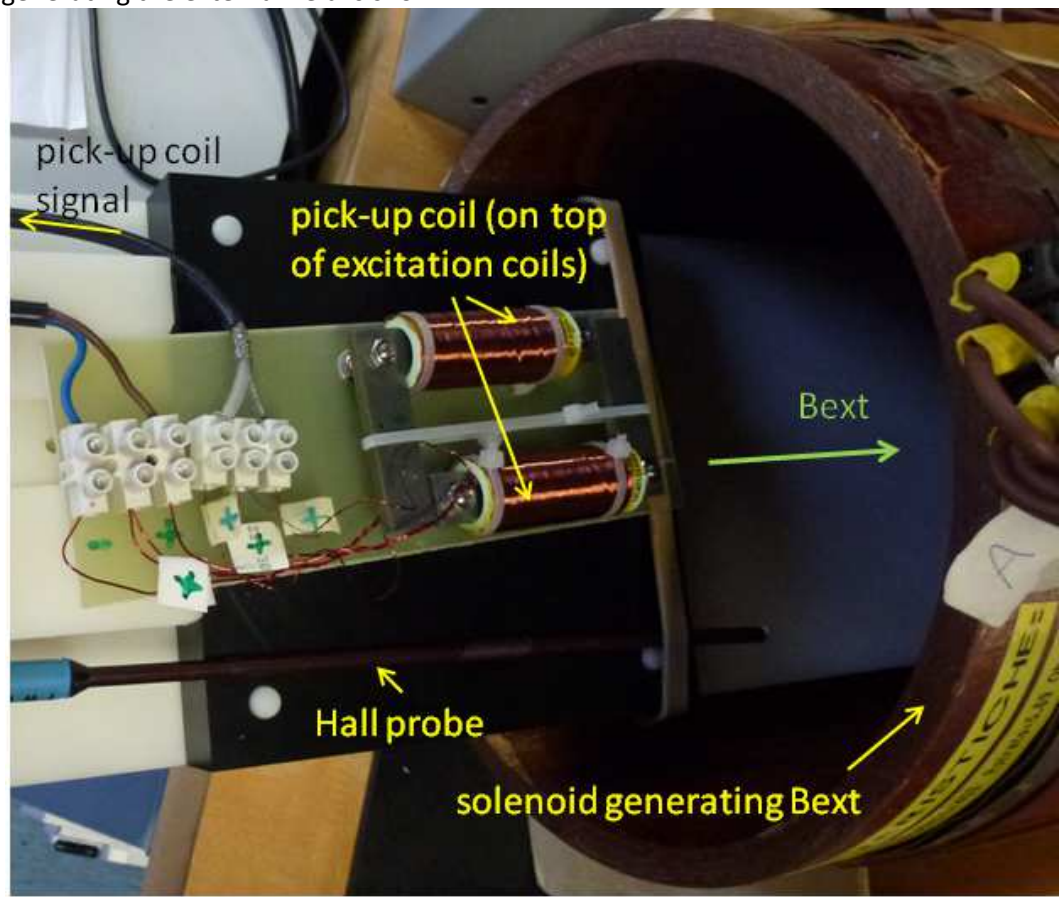

Fig. 184 Flux-gate prototype completed with pick-up coil. In the picture are visible also the solenoid generating the external field and the axial Hall probe for measuring it and benchmarking the flux-gate sensor.

5.6. Experimental set-up

The experimental setup is shown in Fig. 185 and Fig. 186. It consists on the following devices:

1. HPxxxx Wave generator: it generates the waveform for the excitation coil of the flux-gate sensor;
2. Kepco Amplifier: it amplifies the waveform generated by the wave generator and send it to the excitation coils of the flux-gate sensor;
3. DC Power supply for the solenoid: it feeds the solenoid generating Bext;
4. HPxxxx Multimeter: it controls the output of the power supply;
5. Solenoid: it generates Bext;
6. Flux-gate sensor: it's inside the solenoid and it indirectly measures Bext;
7. FW Bell 6010 Gaussmeter: it directly measures Bext;
8. Stanford Research Instruments SR510 Lock-in amplifier: it receives the pilot frequency from the wave generator and the signal from the pick-up coil of the flux-gate sensor, and extracts the amplitude of the second harmonic, that is directly proportional to Bext;
9. LeCroy Wavesurfer Oscilloscope: it shows the waveforms of the excitation current, the waveform of the pick-up coil signal and the amplitude of the second harmonic from the lock-in amplifier. It saves all the data in text files.

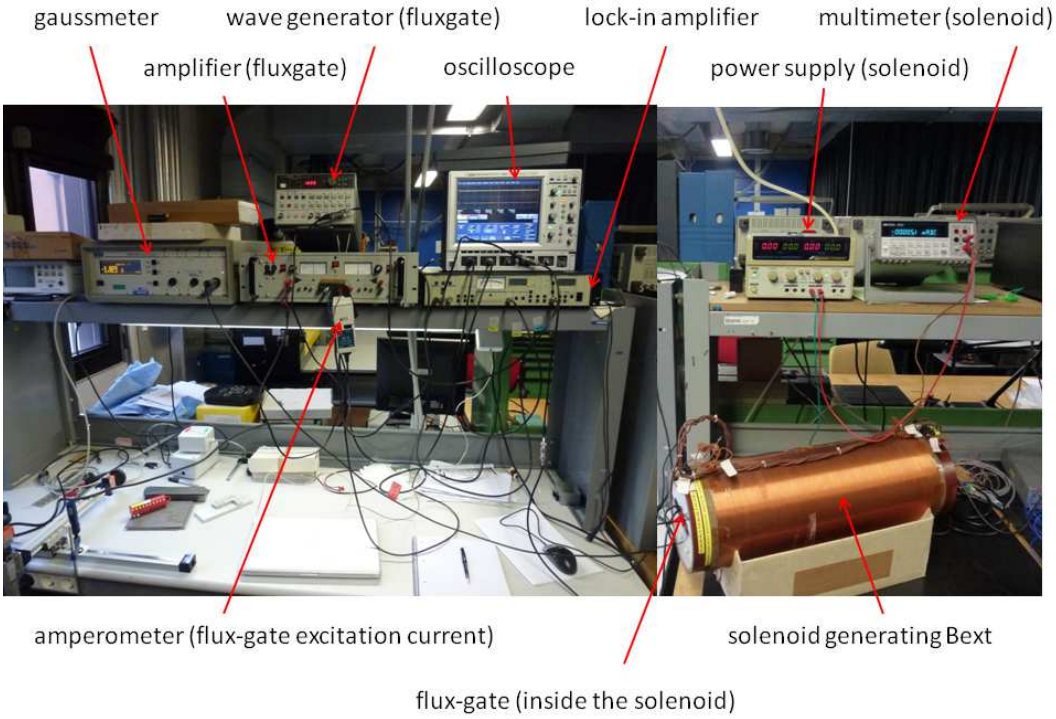

Fig. 185 Experimental set-up for testing the flux-gate sensor.

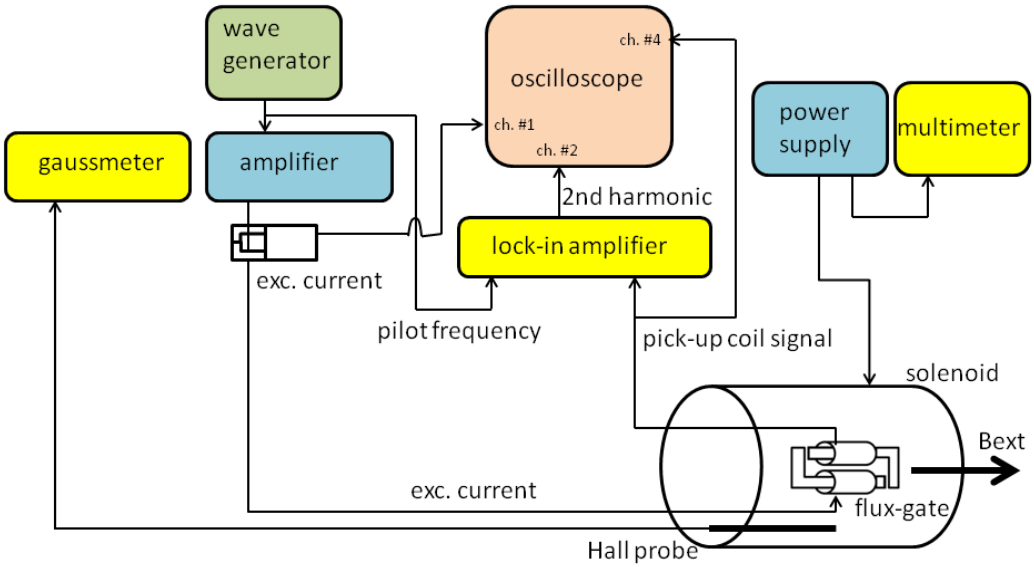

Fig. 186 Experimental set-up for testing the flux-gate sensor (scheme).

5.7. Experimental results

A preliminary set of measurements have been carried out on the flux-gate sensor without the big solenoid for the generation of Bext. In this way it has been possible to obtain the hysteresis cycle of the sensor by placing a tangential Hall probe in one of the sensor air gaps. This measurement is not possible anymore once the sensor is placed inside the solenoid because of lack of space for the tangential Hall probe.

In this case the external field has been generated by placing a permanent magnet in the proximity of the sensor. The results are purely qualitative; anyway they confirmed the operating principle of the flux-gate sensor and were useful for the experimental set-up optimization.
In Fig. 187 the hysteresis cycle has been obtained by plotting the excitation current against the magnetic field measured in one of the air gaps of the ferromagnetic core. It can be noticed how the cycle is perfectly symmetrical in the absence of external magnetic field (a), while it's translated and twisted in the presence of an external magnetic field.

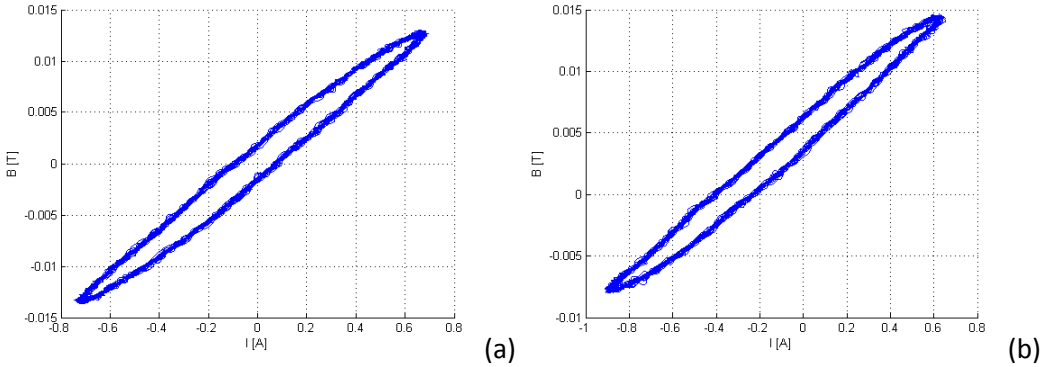

Fig. 187 Flux-gate excitation current plotted against magnetic field measured in the gap between the two parts of the ferromagnetic core: (a) without external field, (b) with external field.

The magnetic flux variation in the ferromagnetic core is gathered by the pick-up coil. In the absence of external magnetic field this signal is almost a pure sinusoid, see Fig. 188 (a) and Fig. 189 (a), while in the presence of an external magnetic field the second harmonic starts to be more and more predominant, see Fig. 188 (b) and Fig. 189 (b).
The amplitude of the second harmonic should be directly proportional to the external magnetic field in the direction of the flux-gate.

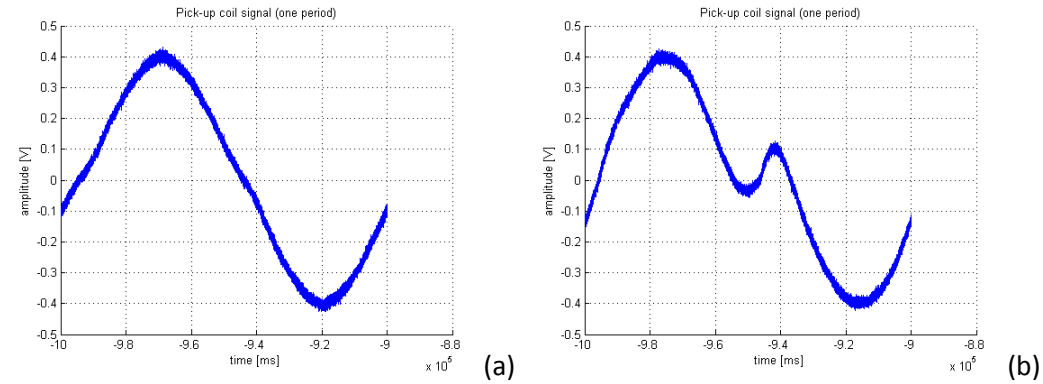

Fig. 188 A single period of the pick-up coil signal: (a) without external field, (b) with external field.

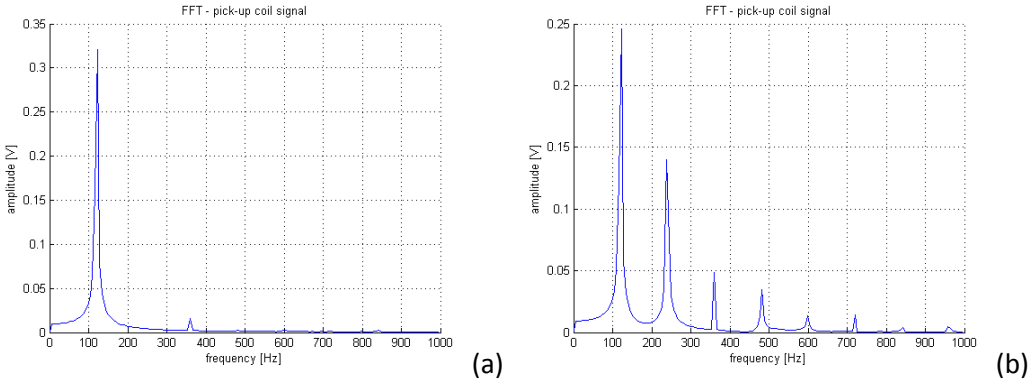

Fig. 189 FFT of the pick-up coil signal: (a) without external field, (b) with external field.

A second measurement campaign has been carried out using the complete experimental setup as shown in Fig. 185. In this case the external magnetic field has been generated by the solenoid connected to its power supply and cross checked using an axial Hall probe connected to a gaussmeter (see also Fig. 184).
Unfortunately, during the measurements, the lock-in amplifier has stopped working, due to a still unknown failure. For this reason, the amplitude of the second harmonic of the pick-up coil signal has been calculated after the measurements, similarly to what has made during the preliminary measurements (like in Fig. 189).
The external field has been varied between [0, 1, 2, 4, 6, 8] mT, the excitation frequency and voltage have been kept constant and equal to 120 Hz and 1.0 V respectively.
The next Fig. shows the quite linear relation between the applied external magnetic field and the amplitude of the second harmonic of the pick-up coil signal, at least until an external field of 8 mT, which is fully complying with the requirement of 2 mT.

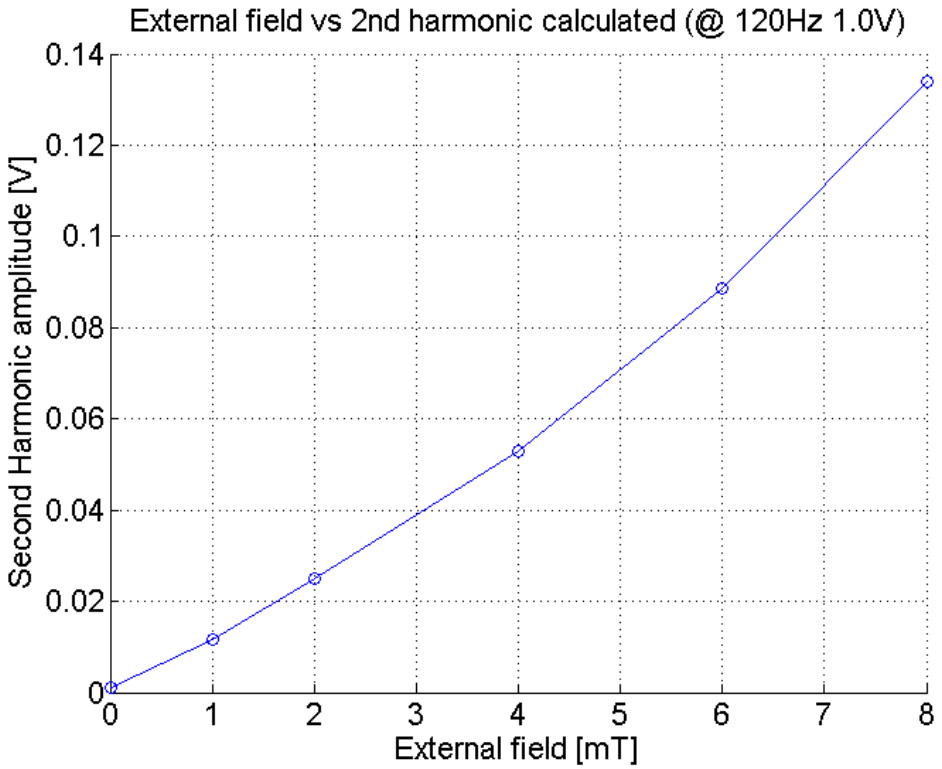

Fig. 190 Linearity between applied external magnetic field and amplitude of second harmonic.

Activities on the flux-gate prototype are still ongoing. The next step is to complete the characterization of the flux-fate sensor at small and high magnetic field, and then compare the results with the numerical model presented in section 5.3. , in order to be predictive in view of application to MITICA and ITER HNB.

5.8. Conclusions

A magnetic sensor of the type flux-gate has been studied and developed at Consorzio RFX in order to comply with the requirements for magnetic measurements inside MITICA and ITER HNB vessel, in order to operate the Active Control and Compensation Coils in closed loop with feedback control.

A numerical model has been developed and a 2D femm model has been realized.

A prototype of flux-gate sensor has been constructed and tested, proving its operating principle and the possibility of extending its typical operating range until magnetic fields of the order of 10 mT and more.

Complete characterization of the prototype as well as the comparison with the numerical model is still ongoing.

6. Design of an Extraction Grid to be tested on Negative Ion Test Stand (NITS)

In this chapter some of the design activities on an Extraction Grid featuring the magnetic solution described in 2.1. will be presented. This grid has been already constructed and will be tested on NITS accelerator at JAEA Naka during February 2016.

6.1. Introduction

On October 2015 a scientific cooperation agreement has been signed between JAEA Naka Fusion Institute and Consorzio RFX, with a series of common objectives:

- benchmarking of NBI numerical simulation codes used in the two labs for injector design and for interpretation of experimental results;
- preparation and execution of Joint Experiments on the accelerators NITS (Negative Ion Test Stand, see [55]) and MTF (Megavolt Test Facility, see [56]) at JAEA;
- improvement of personnel expertise and NBI diagnostic tools;
- validation and optimization of ITER HNB / MITICA design.

The first Joint Experimental campaign will be done on February 2016 and will consist on the demonstration of the new solution developed at Consorzio RFX for beamlet deflection compensation, described in Par. 2.1. This solution includes a series of new permanent magnets called Asymmetric Deflection Compensation Magnets (ADCM) to be embedded in the Extraction Grid with the purpose of minimizing the ion deflection that arises because of the presence of the standard Co-extracted Electrons Suppression Magnets (CESM).
This new solution has been accepted as a reference design for MITICA and HNB accelerator, and will be tested experimentally for the first time on the accelerator NITS at JAEA during the first Joint Experimental campaign.

6.2. Description of NITS accelerator

NITS is a negative ion source and accelerator composed by a Kamaboko arc source, an extraction stage and a single acceleration stage (see [55]), followed by a long beam line, allowing the installation of multiple diagnostics. Acceleration potential is up to 60 kV, with the limit of 30 kV for stable operation. The number of apertures is 49 (7x7). A general layout of the device is given in Fig. 191:

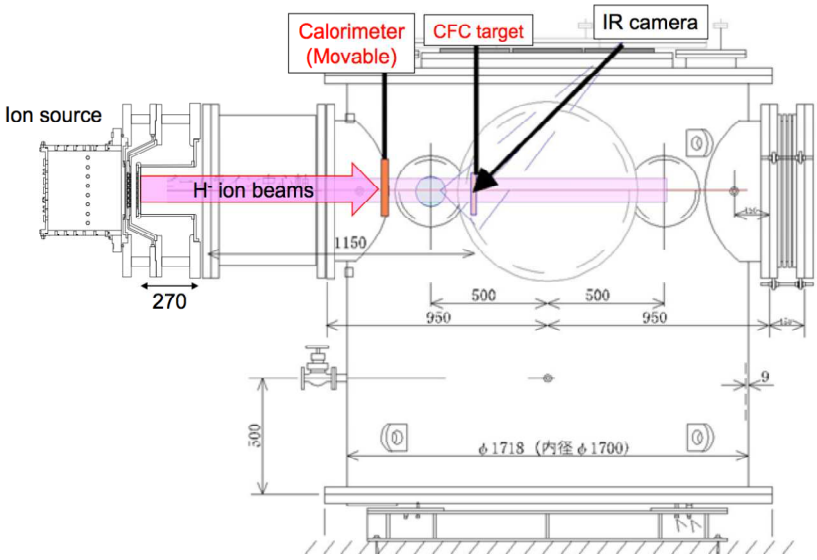

Fig. 191 General layout of NITS device and calorimetric diagnostics position.

Fig. 192 shows a picture of the NITS source and accelerator and beam line. The Kamaboko arc source is on the left, then the three stages (PG, EG and GG) are visible. The name "Kamaboko" comes from the name of a fish-cake, whose shape is similar to the cross-section of this particular arc source (a half cylinder). The beam line is much extended and many diagnostics can be installed on it.

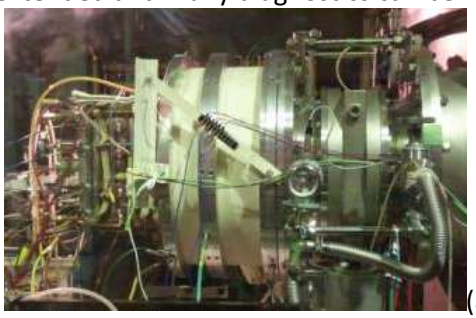
(a)

(b)

Fig. 192 Pictures of the NITS experiments: (a) source and accelerator, (b) beam line.

6.3. Experimental setup of first Joint Experiments

The first Joint Experiments have the purpose of validating the beamlet deflection compensation capability by the use of Asymmetric Deflection Compensation Magnets (ADCM), described in Par. 2.1. For this reason, a new Extraction Grid (EG) has to be designed, realized and installed on NITS accelerator. In order to have a direct comparison of the effect of ADCM on the beamlets, a layout has been proposed for the new EG in which the beamlets of the upper half will be compensated by the effect of the ADCM and the beamlets of the lower half will be left uncompensated, as shown in Fig. 193. For symmetry reason, it can be noticed that not all the 49 apertures can be used for the experiments, but only 15 in the upper half and 15 in the lower half.

Fig. 193 Apertures layout of the new EG to be installed on NITS for the first Joint Experiments.

The effect of the ADCM in terms of beamlet deflection will be investigated by calorimetric diagnostic on a CFC target, as shown in Fig. 191 and in Fig. 194, and for this reason the beam has to be well focused in order to distinguish the footprints of the single beamlets on the CFC target. Fig. 194 shows the proposed experimental setup for these experiments and the maximum allowable voltage that can be provided by the PG power supply and the EG power supply:

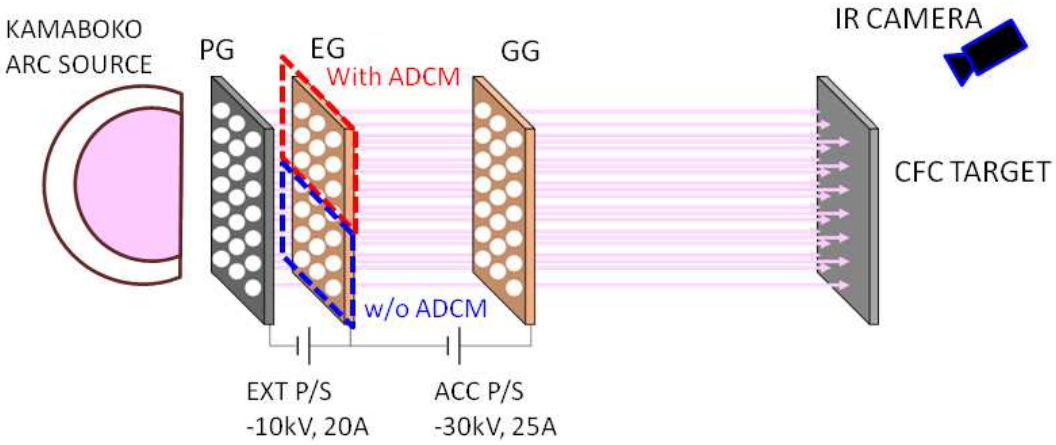

Fig. 194 Experimental setup proposed for the first Joint Experimental campaign.

The new EG will be designed and realized by Consorzio RFX, while JAEA will realize a new EG support and will prepare the experimental setup including the CFC target and the IR camera.

6.4. Magnetic analysis of new EG

A magnetic model of the new EG has been realized with NBImag and it is shown in Fig. 195. The purpose of this simulation is to check the uniformity of By in the two grid regions with the different magnetic layout (with and without ADCM), in fact, being only 3 rows of apertures in each region, the edge effects could be non negligible. Moreover, in order to minimize this edge effect, two rows of “short ADCM” (with half the length of a standard ADCM) have been included in the upper part of the grid, as shown in Fig. 195.

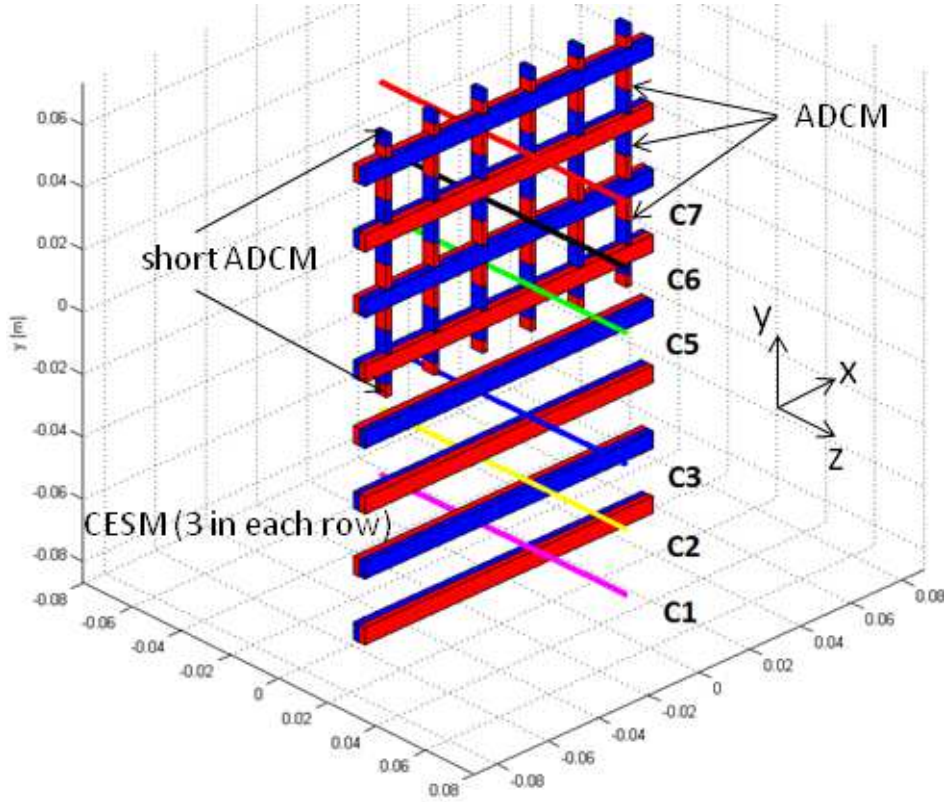

Fig. 195 NBImag model of the new EG for NITS.

For this first simulation the size and magnetic remanence (Br) of CESM and ADCM has been chosen as similar as possible to MITICA, as summarized in Tab. 30. The ADCM strength (combination of thickness and remanence) will be then optimized in order to minimize the beamlet magnetic deflection, as shown in section 6.8.

	CESM size [mm^3]	CESM Br [T]	ADCM size [mm^3]	ADCM Br [T]
MITICA	4.2x6.6x40 (3 in a row)	1.1	1.95x6.6x17.4	1.1
NITS (first estimation)	4.2x6.6x28.5 (4 in a row)	1.1	1.95x6.6x16.4	1.1

Tab. 30 CESM and ADCM size in MITICA and NITS.

The difference comes from the fact that the vertical and horizontal aperture pitch is slightly different from MITICA and NITS, as shown in Tab. 31:

	Aperture vertical pitch [mm]	Aperture horizontal pitch [mm]
MITICA	22	20
NITS	21	19

Tab. 31 Aperture vertical and horizontal pitch in MITICA and NITS.

Magnetic field has been calculated along the six apertures shown in Fig. 195 (indicated as C1-C7), and the result is shown in Fig. 196:

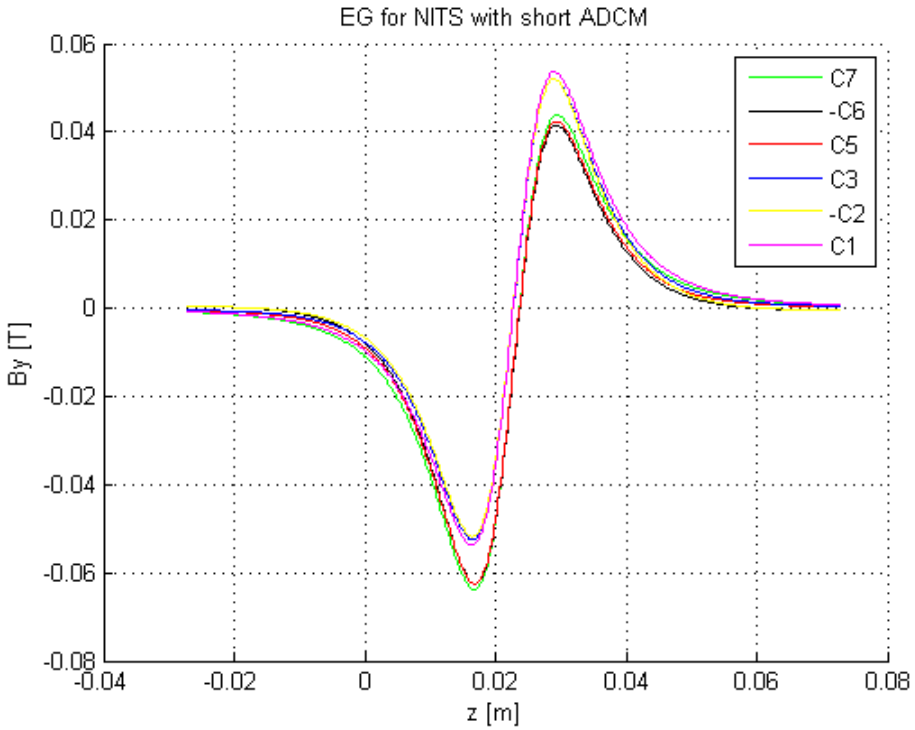

Fig. 196 By uniformity in EG for NITS with short ADCM.

In Fig. 197 is shown an enlarged view of the downstream peaks, while in Fig. 198 the same peaks calculated in a model without the short ADCM are shown. From this two figures the beneficial effect of the short ADCM in terms of By uniformity in the upper region (apertures C5, C6, C7) can be noticed. Quantitatively, it passes from ~9%, in the case without short ADCM, to ~5% in the case with short ADCM, a considerable increase. The situation is similar if looking at the upstream peaks.
For as regards By uniformity in the lower region (without any ADCM), it is similar in the two cases, about 3-4%.

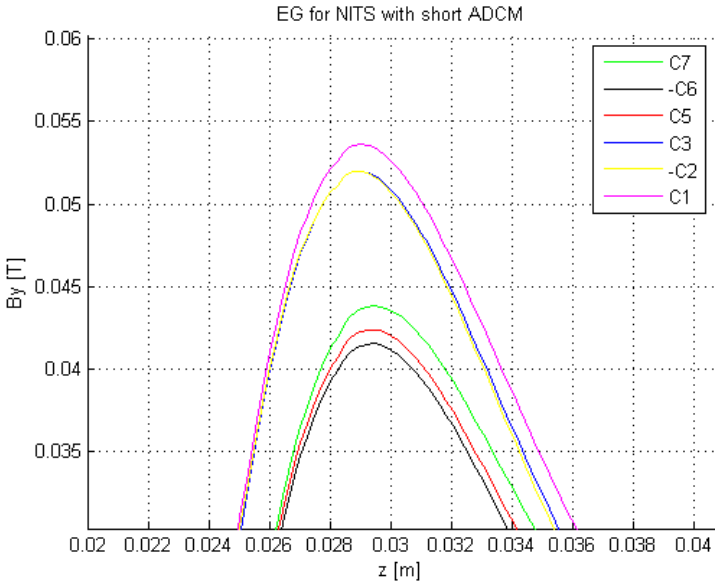

Fig. 197 By uniformity in EG for NITS with short ADCM, enlarged view of downstream peaks.

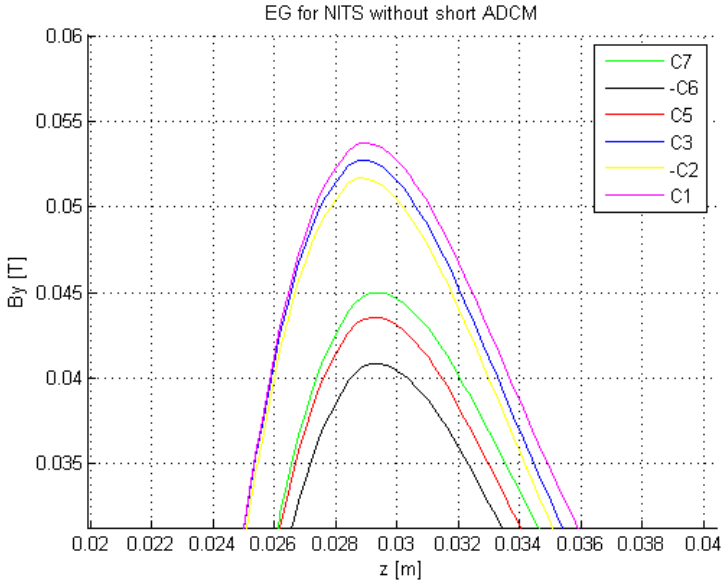

Fig. 198 By uniformity in EG for NITS without short ADCM, enlarged view of downstream peaks.

In conclusion, despite the limited number of apertures in vertical direction in NITS (only 3 for each layout), there is an acceptable By uniformity (≤ 5%) in both grid regions (upper with ADCM and lower without ADCM), in the case that short ADCM are used to minimize the edge effect.
By uniformity in horizontal direction has not been taken into account since the number of apertures in a row is the same for NITS and MITICA (5 apertures).

6.5. Electrostatic analyses and optics optimization of new EG

A series of electrostatic analyses has been carried out using the code SLACCAD in order to evaluate the beamlet divergence and to optimize the accelerator geometry in order to have the best beamlet optic during the first Joint Experiments. Having a well focused beamlet is crucial for this Joint Experiments, since the beamlet deflection will be evaluated by looking at the correspondent footprint on the CFC target, which is placed at about 1m from the Grounded Grid. If the beamlets are not well focused, their footprints on the target will be overlapped, making impossible to measure their deflection.
Tab. 32 summarizes the main constraints of NITS accelerator to be taken into account in the electrostatic analyses of the new EG:

Constraints for Joint Experiments on NITS		
gas type	Hydrogen	
max extraction voltage: Vext	10	kV
max acceleration voltage: Vacc	30	kV
max arc power: Parc	50	kW
max extracted ion current density: Jext	300	A/m2
extraction gap (PG-EG) length	6	mm
acceleration gap (EG-GG) length	12 or 23	mm

Tab. 32 Assumption and constraints for Joint Experiments on NITS.

It can be noticed that the Extraction gap is fixed (6 mm, the same MITICA), while the acceleration gap can be set at 12 mm or 23 mm. This is a first important constraint, but the main limitation is on the maximum acceleration voltage, 30 kV.
The geometry of the EG apertures has been kept the same of MITICA, in order to have experimental results obtained in conditions that are as far as possible similar to MITICA and HNB. The geometry of NITS accelerator with the new EG is shown in the next Fig.:

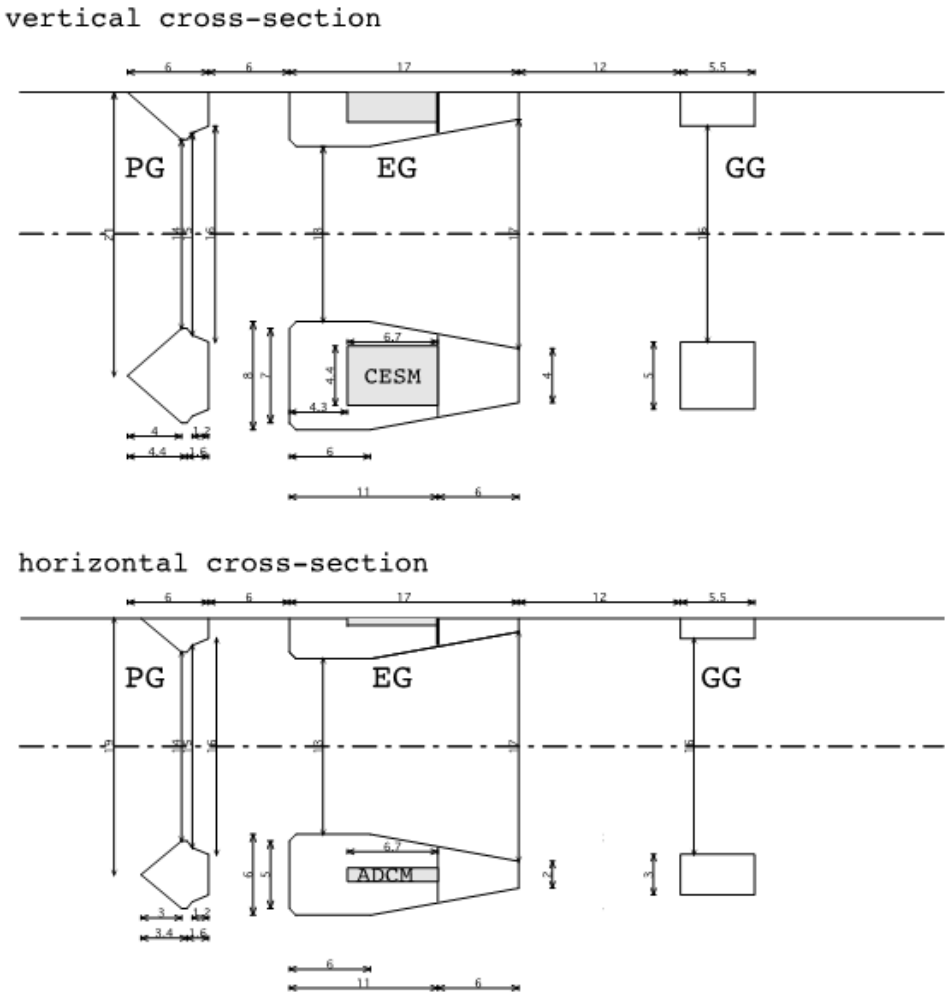

Fig. 199 Geometry of NITS accelerator with the new EG, whose aperture geometry is the same of MITICA EG. Acceleration gap can be either 12mm or 23mm.

Initially, the gap length of 23 mm has been considered. A scan of beamlet divergence has been performed with SLACCAD using the parameters summarized in Tab. 33:

Parameter	**Variation interval**	
extraction gap	6	mm
acceleration gap	23	mm
acceleration voltage	30 or 20	kV
extraction voltage	[2.4 - 6.0]	kV
extracted current density	80, 100, 135, 170	A/m^2

Tab. 33 Parameters used in the divergence scan carried out with SLACCAD with acceleration gap of 23 mm.

Fig. 200 shows the results of beamlet divergence calculated for Vacc = 30 kV. Fig. 201 is an enlarged view of the same results including also the beamlet trajectories relative to

the points of minimum divergence. From this picture important information can be obtained: under the constraints of Vacc = 30 kV and acc. gap = 23 mm it's not possible to achieve a focused beam at high extracted current. For example, the red curve, obtained at Jext = 135 A/m^2 shows a minimum of divergence angle at Vext = 4 kV. In this condition, the clearance between the beamlet and the EG is insufficient, as it can be seen in Fig. 201. In fact, if Vext is slightly reduced the divergence passes from 5 mrad to 75 mrad, a clear evidence of the fact that the beamlet is touching the EG.
Whenever in this kind of plot a situation like the red or the magenta curve of Fig. 200 is obtained, with the relative minimum preceded by a sharp increase of the divergence, it means that beam is touching the EG, and so that minimum is not really acceptable from the operational point of view.

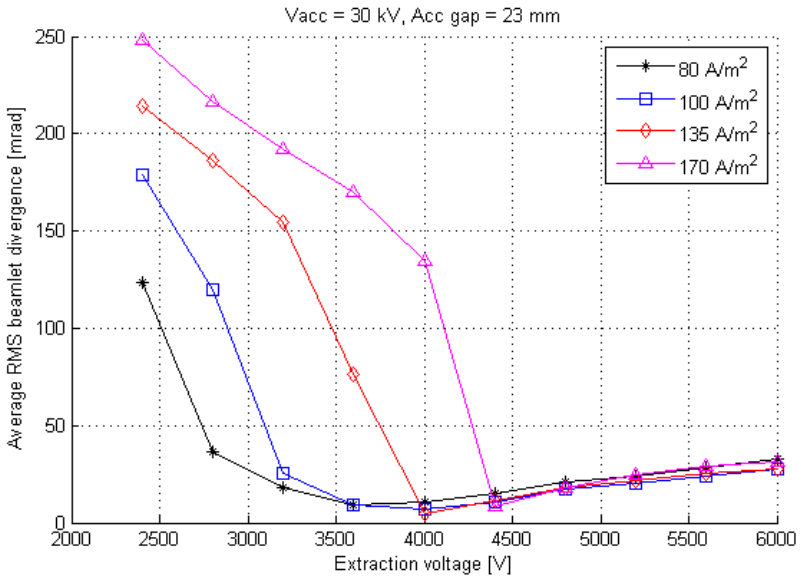

Fig. 200 Beamlet divergence calculated for acceleration gap = 23 mm and Vacc = 30 kV.

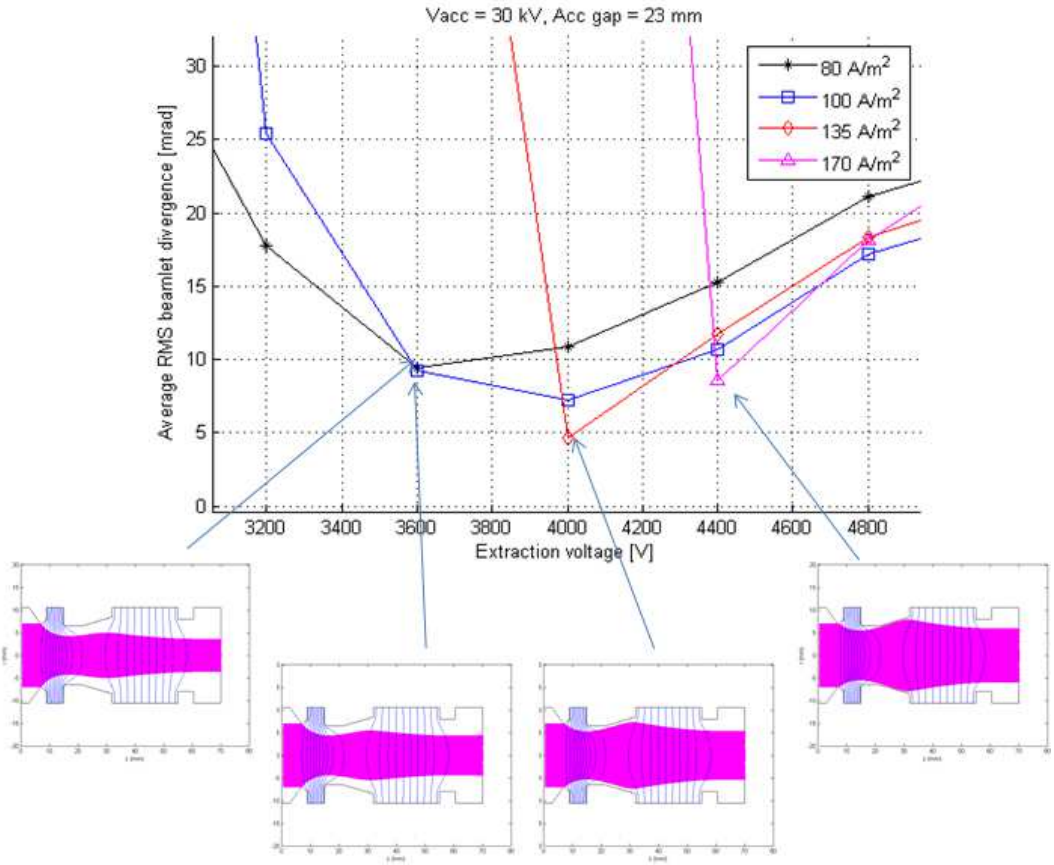

Fig. 201 Beamlet divergence calculated for acceleration gap = 23 mm and Vacc = 30 kV. Enlarged view with beamlet trajectories.

If looking at the divergence calculated for Vacc = 20 kV it immediately appears that there are no acceptable points of minimum divergence for the considered extracted current densities. This means that Jext should be further reduced, going towards conditions that are very far from the ITER-like condition of Jext $\simeq$ 300 A/m^2. For this reason, this configuration won't be further investigated.

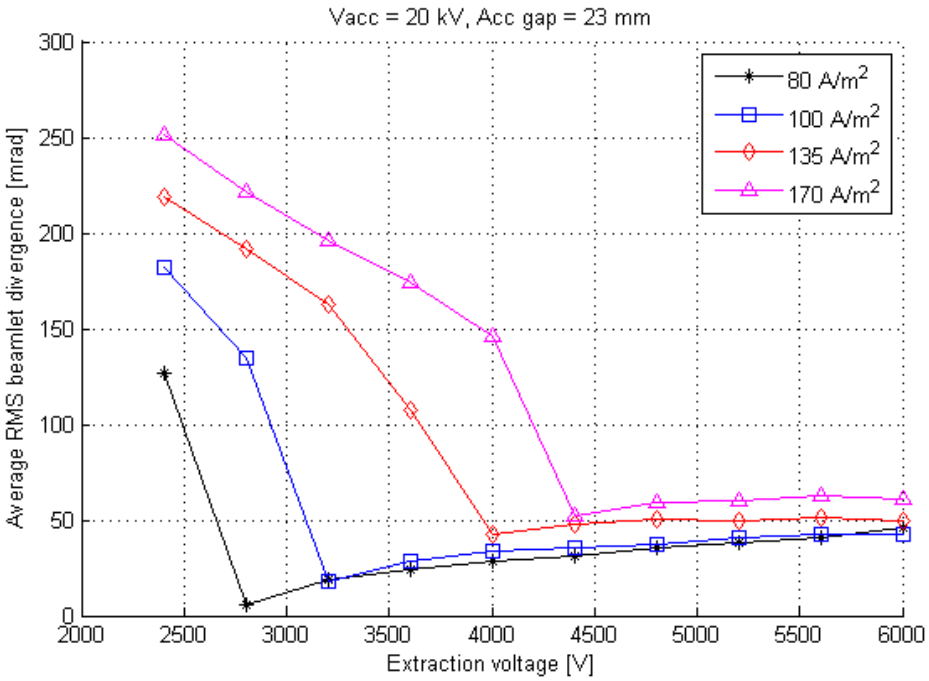

Fig. 202 Beamlet divergence calculated for acceleration gap = 23 mm and Vacc = 20 kV.

The situation in the case of a smaller acceleration gap, 12 mm, and higher acceleration voltage, 30 kV, is much better. In this case higher current density can be extracted still having a quite well focused beamlet. The parameters used for these simulations are reported in Tab. 34:

Parameter	**Variation interval**	
extraction gap	6	mm
acceleration gap	12	mm
acceleration voltage	30 or 20	kV
extraction voltage	[2.4 - 8.0]	kV
extracted current density	80, 100, 135, 170,200,220,240,260,280	A/m^2

Tab. 34 Parameters used in the divergence scan carried out with SLACCAD with acceleration gap of 12 mm.

The full results are shown in Fig. 203, while Fig. 204 shows an enlarged view of the minimum divergence points with the relative beamlet trajectory.

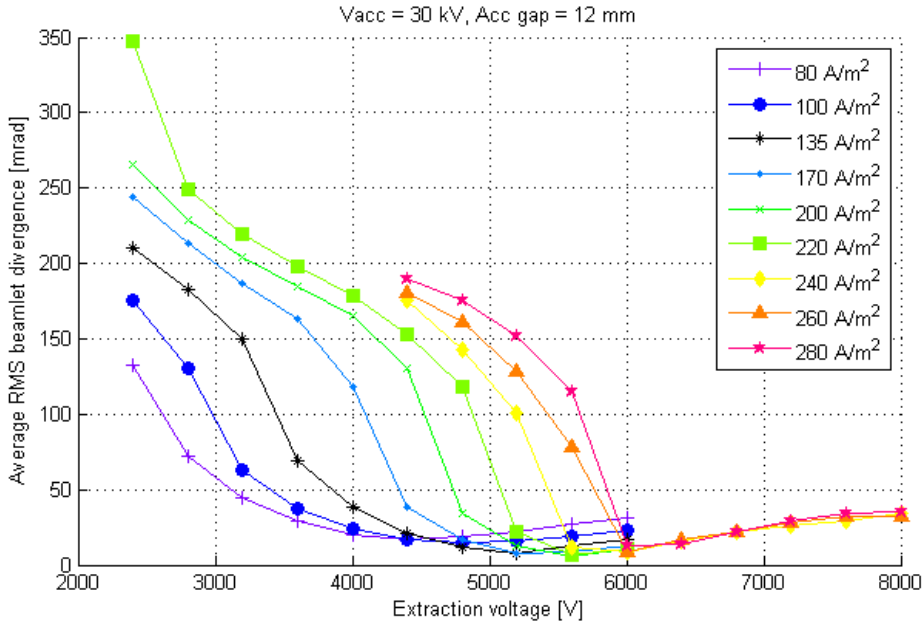

Fig. 203 Beamlet divergence calculated for acceleration gap = 12 mm and Vacc = 30 kV.

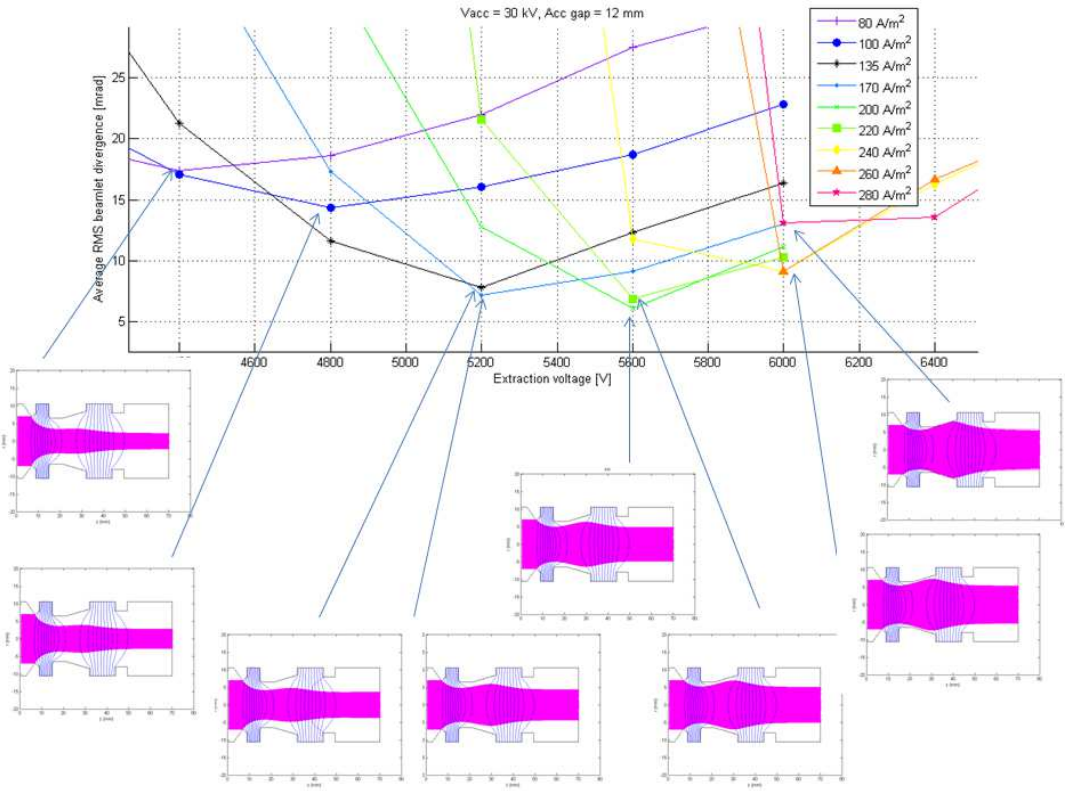

Fig. 204 Beamlet divergence calculated for acceleration gap = 12 mm and Vacc = 30 kV. Enlarged view with beamlet trajectories.

From this last figure it can be concluded that the maximum extracted current density that still allows a quite well focused beamlet with acceptable clearance between the beamlet and the EG is about 200 A/m^2. In this case the minimum divergence is about 6.5 mrad, which is also the absolute minimum of all the curves. At 220 A/m^2 the clearance starts to be too small for allowing a stable accelerator operation around this point.

Unfortunately, the value of 200 A/m^2 is still quite far from ITER like conditions (300 A/m^2). This value could be increased by increasing the Acceleration Voltage, but this is not possible due to the limitations of NITS power supplies.
For the sake of completeness, in the next figure the divergence calculated for Vacc = 20 kV is reported. Similarly to the case of acc. gap = 23 mm, it appears that if Vacc is decreased to 20 kV then the optic related to higher extracted current density is not acceptable anymore. In this case the limit is at about 100 A/M^2.

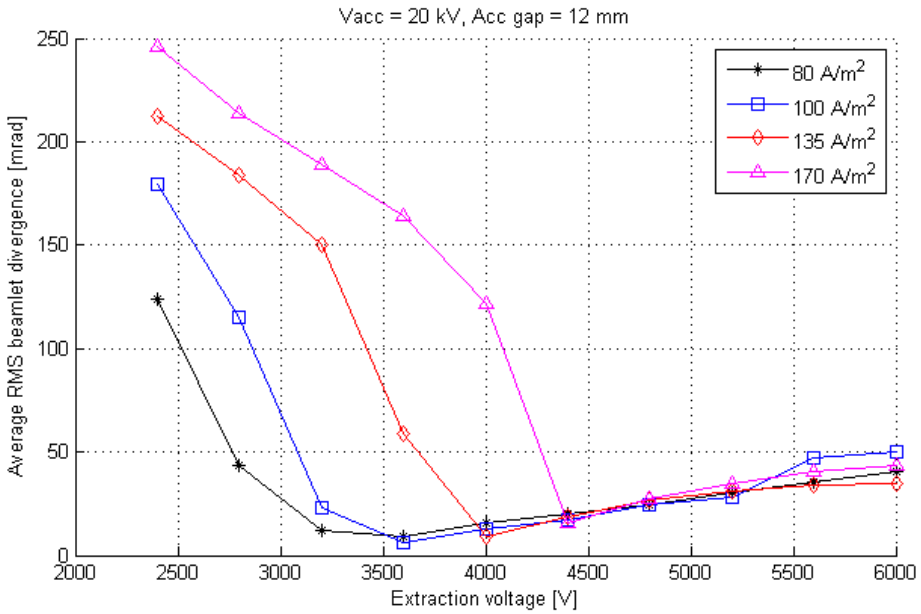

Fig. 205 Beamlet divergence calculated for acceleration gap = 12 mm and Vacc = 20 kV.

In conclusion, given the NITS accelerator geometry and operating constraints, the minimum beamlet divergence together with the maximum extracted current density can only be achieved with the acceleration gap of 12 mm, Vacc = 30 kV and Vext about 5.6 kV. In this case the divergence calculated with SLACCAD is about 6.5 mrad with an extracted current density Jext of ~ 200 A/m^2. The final geometry of NITS with the new EG is shown in Fig. 199.

6.6. Electrostatic analyses of original EG of NITS

Similarly to what has done for the new EG for NITS, a series of electrostatic analyses has been carried out on the original NITS EG and accelerator configuration, whose geometry is shown in Fig. 206. The parameters used in the SLACCAD simulation are summarized in Tab. 35.
These analyses have been carried out in order to compare the results of SLACCAD with the code BEAMORBIT, used at JAEA. This comparison is shown in the next section.

Parameter	**Variation interval**	
extraction gap	4.7	mm
acceleration gap	12	mm
acceleration voltage	20	kV
extraction voltage	[3.0 - 4.9]	kV
extracted current density	60, 80, 100, 135, 170	A/m^2

Tab. 35 Parameters used in the divergence scan carried out with SLACCAD on the original NITS geometry.

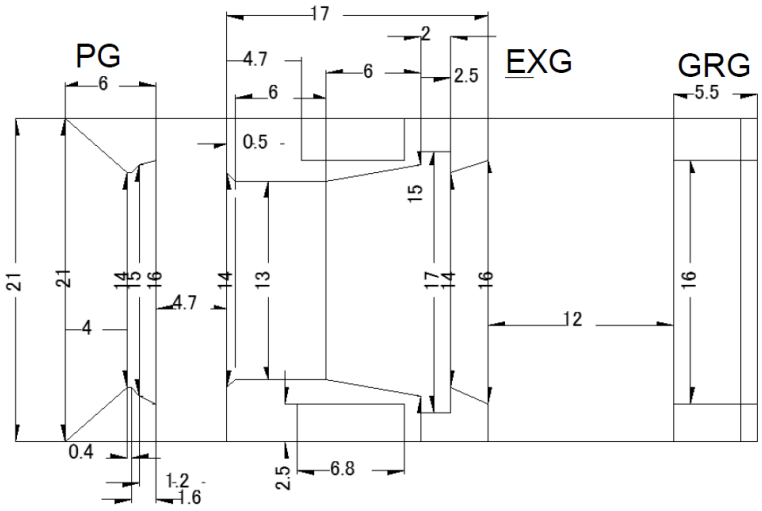

Fig. 206 Original NITS accelerator geometry.

The results of the simulations are shown in Fig. 207. From this Fig. it can be noticed that the minimum beamlet divergence is about 8 mrad, corresponding to an extracted current density of 135 A/m^2.

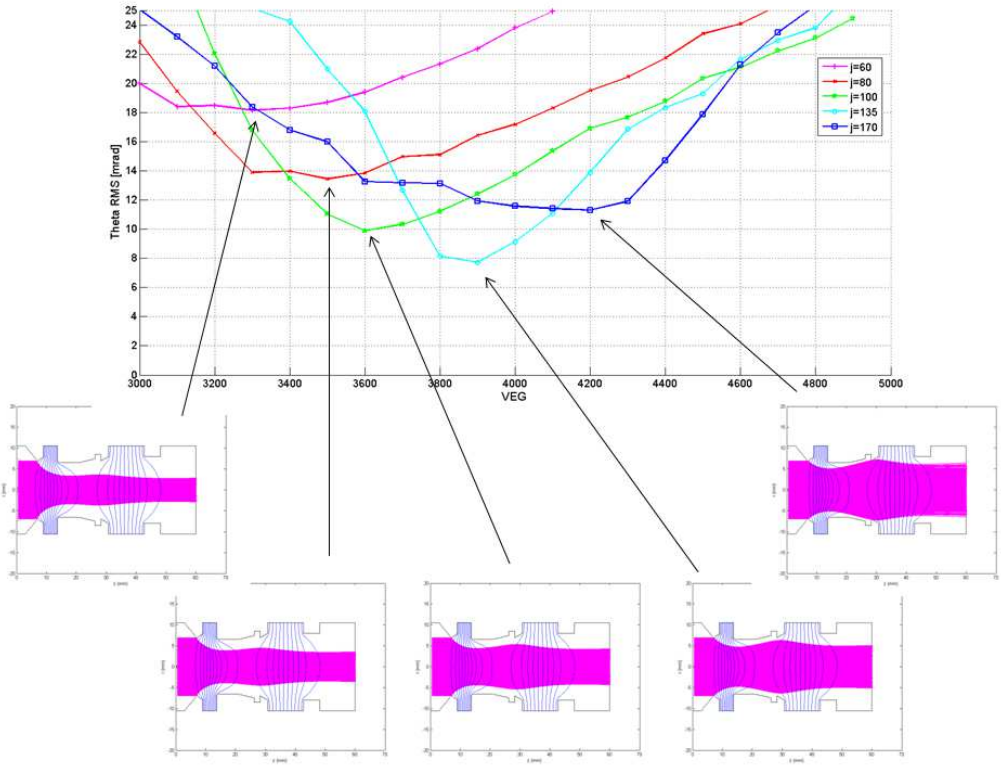

Fig. 207 Beamlet divergence calculated with SLACCAD on original NITS geometry. Enlarged view with beamlet trajectories.

6.7. Comparison between SLACCAD and BEAMORBIT

The results of the SLACCAD simulation carried out on the original NITS geometry and on the new NITS geometry, presented in the previous two sections, have been compared with the results obtained at JAEA with the code BEAMORBIT on the same geometries.
Fig. 208 shows the results of BEAMORBIT simulations (carried out at JAEA) of the original NITS geometry, to be compared with Fig. 207.

The curves obtained with SLACCAD (Fig. 207) and BEAMORBIT (Fig. 208), are compared together in Fig. 209. From this Fig. it can be noticed that the two codes are not in a perfect agreements. In particular:

1. The calculated divergence of SLACCAD is lower with respect to the one calculated with BEAMORBIT;
2. The optimal extraction voltage for obtaining the minimal beamlet divergence having the same extracted current density is lower for SLACCAD with respect to BEAMORBIT.

The optimal extraction voltages, corresponding to the minima of the curves of Fig. 209 are better compared in Fig. 210. The difference from the two codes can be due to several reasons, for example the modeling of the meniscus region of the plasma grid, different between the two codes.

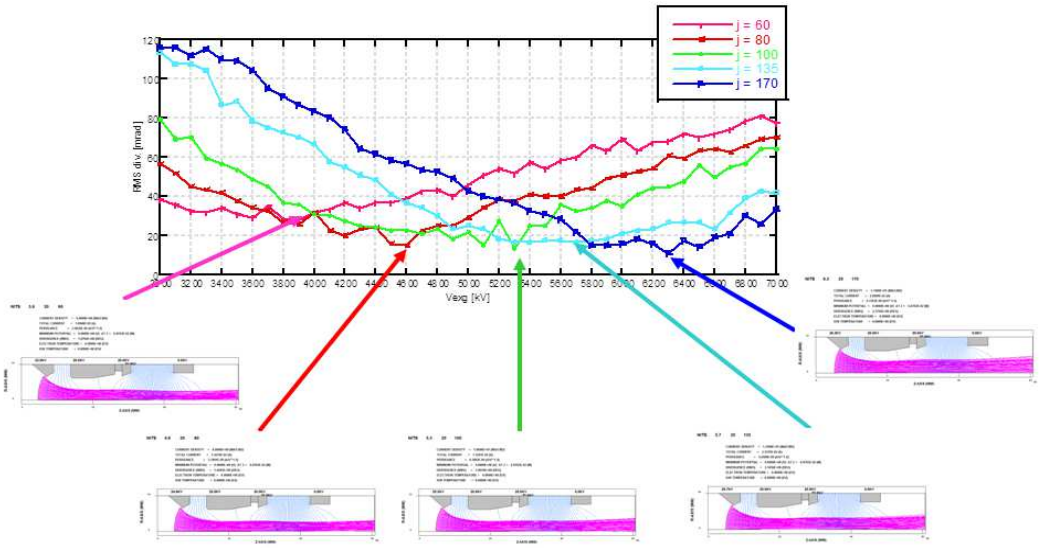

Fig. 208 Beamlet divergence calculated with BEAMORBIT on original NITS geometry. Enlarged view with beamlet trajectories.

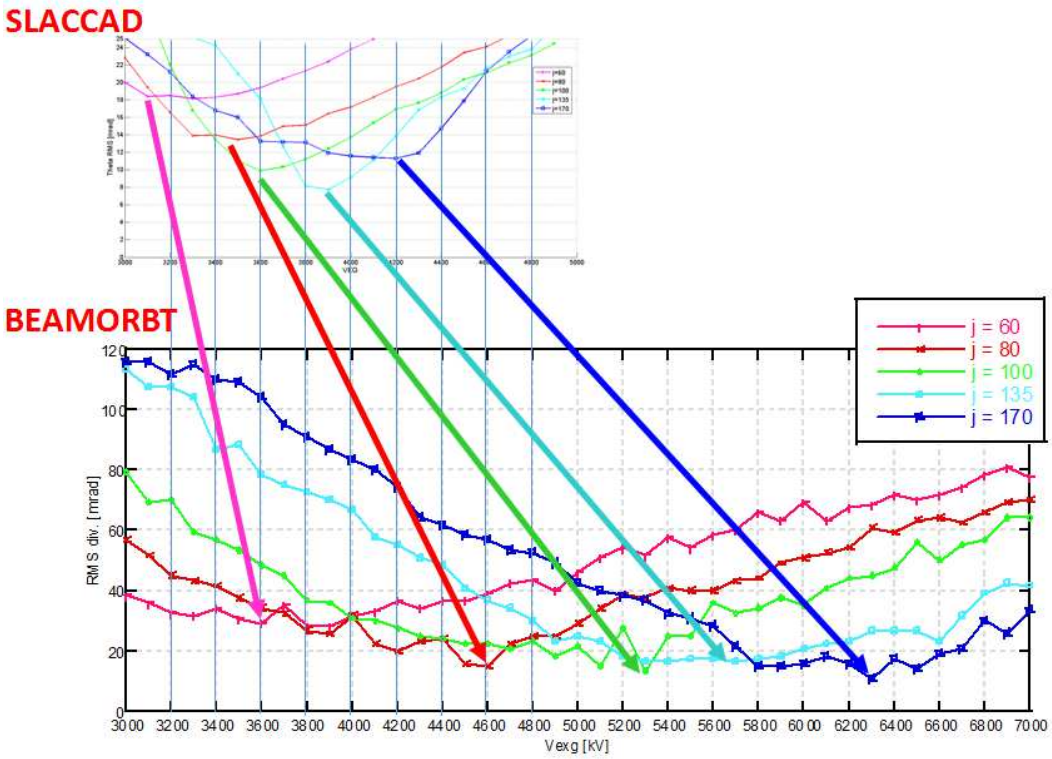

Fig. 209 Comparison between SLACCAD and BEAMORBIT on original NITS geometry.

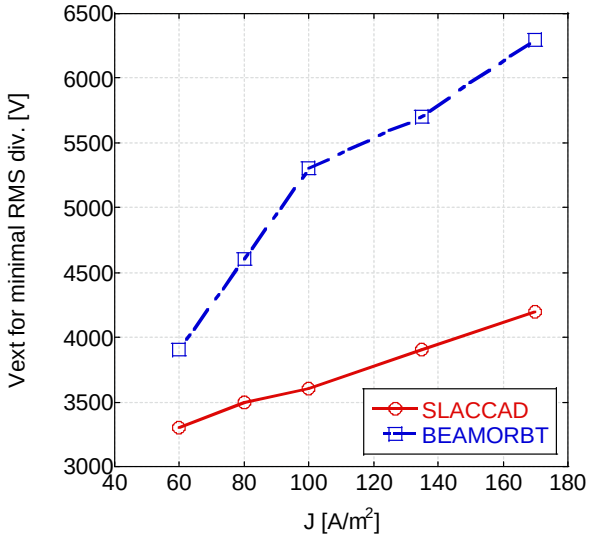

Fig. 210 Comparison between points with minimum divergence of SLACCAD and BEAMORBIT (original NITS geometry).

The same comparison has been made for the new NITS geometry. For this geometry there is a better agreement between SLACCAD and BEAMORBIT.
The BEAMORBIT results related to the new NITS geometry are shown in Fig. 211, while the comparison between SLACCAD and BEAMORBIT is shown in Fig. 212 and Fig. 213.
From these figures it can be noticed that in this case the two codes are in better agreement for as regards both the beamlet divergence and the optimal extraction voltage.

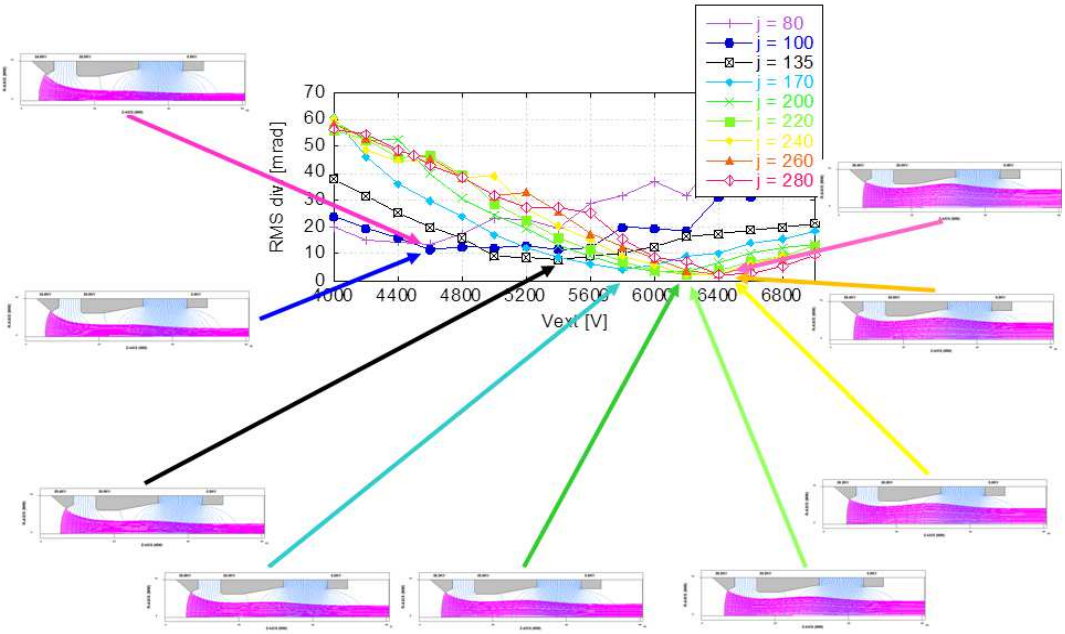

Fig. 211 Beamlet divergence calculated with BEAMORBIT on new NITS geometry. Enlarged view with beamlet trajectories.

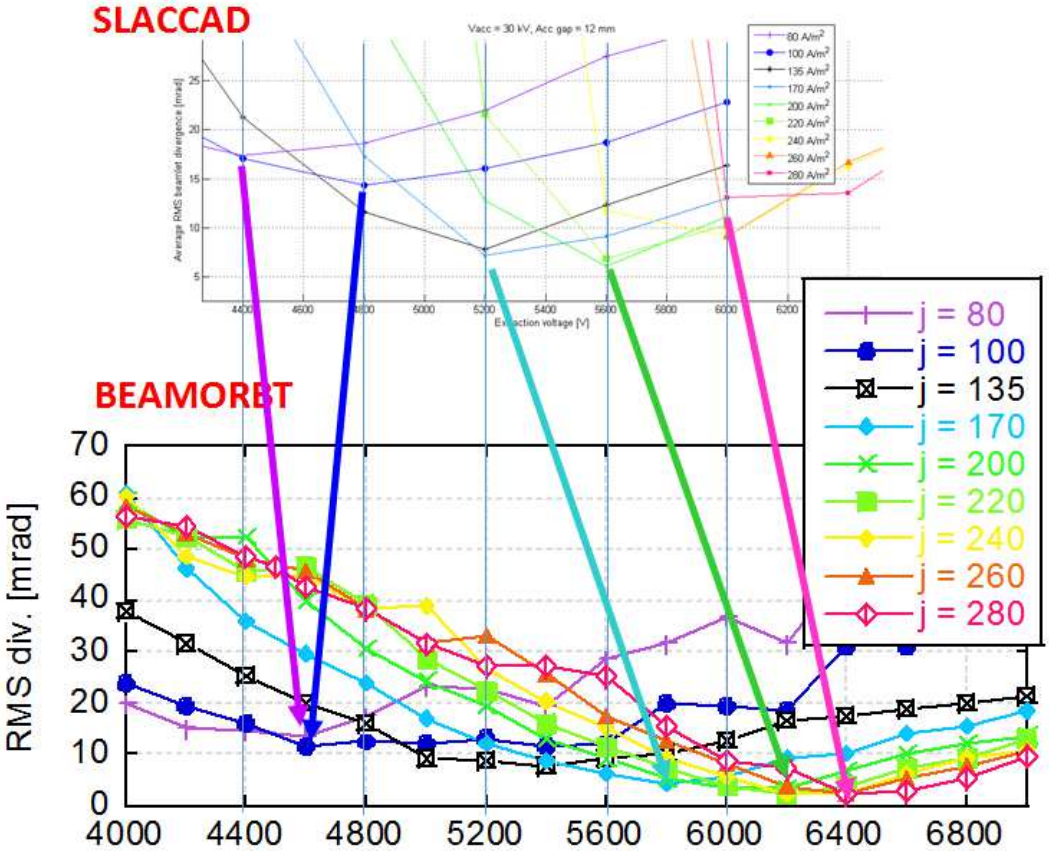

Fig. 212 Comparison between SLACCAD and BEAMORBIT on new NITS geometry.

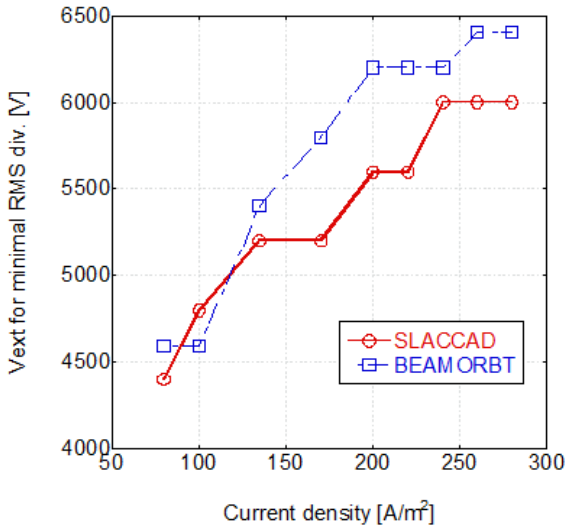

Fig. 213 Comparison between points with minimum divergence of SLACCAD and BEAMORBIT (new NITS geometry).

6.8. Calculation of ion deflection and ADCM optimization

6.8.1. Calculation of ion deflection using an analytical formula

Ion deflection under the combined effect of magnetic and electric field has been initially estimated with the "paraxial approximation" analytical formula reported below.

$$\delta = \frac{v_{x,exit}}{v_{z,exit}} = \frac{q\int_{z_0}^{z_{exit}} B_y\, dz}{m_{H^-}\sqrt{\frac{2qU_{exit}}{m_{H^-}}}} = \sqrt{\frac{q}{m_{H^-}}}\cdot\frac{\int_{z_0}^{z_{exit}} B_y\, dz}{\sqrt{2U_{exit}}}$$

(q and m are the ion charge and mass, U_{exit} is the electrostatic acceleration potential and z_0, z_{exit} are the initial and final axial coordinates of the ion trajectories).

Since the dependence of ion deflection on ADCM strength is almost linear, as previously observed in MITICA, three different cases (no ADCM, ADCM thickness = 0.2 mm, ADCM thickness = 0.6 mm) have been analyzed in NITS in order to obtain the optimal ADCM strength, i.e. the one producing a null ion deflection at accelerator exit.

All the parameters adopted for these simulations are reported in the next Table:

Parameter	**Value**	
ion species	Hydrogen	
ion starting position	3 mm upstream PG	
extraction gap	6	mm
extraction potential	optimal	kV
acceleration gap	12 or 23	mm
acceleration potential	30	kV
aperture vertical pitch	21	mm
aperture horizontal pitch	19	mm
CESM size	4.2x6.6x28.5 x4	mm^3
CESM magnetic remanence	1.1	T
ADCM size	[0 or 0.2 or 0.6]x6.6x16.5	mm^3
ADCM magnetic remanence	1.1	T

Tab. 36 Parameters adopted for the analytical calculation of ion deflection in NITS.

The calculated ion deflections depending on ADCM thickness and acceleration gap length are reported in Tab. 37:

Case	ADCM thickness [mm]	Acc Gap [mm]	Deflection @ 1m [mrad]
Acc gap 12 mm noADCM	/	12	3.6795
Acc gap 12 mm ADCM 0.2 mm	0.2	12	1.4549
Acc gap 12 mm ADCM 0.6 mm	0.6	12	-2.998
Acc gap 23 mm noADCM	/	23	3.714
Acc gap 23 mm ADCM 0.2 mm	0.2	23	1.491
Acc gap 23 mm ADCM 0.6 mm	0.6	23	-2.959

Tab. 37 Calculated ion deflections depending on ADCM thickness and acceleration gap length.

The linear dependence of ion deflection with respect to ADCM thickness is shown in the next two Fig., for the two different acceleration gap lengths. The red point indicates the optimal ADCM thickness in order to have an ion deflection equal to zero:

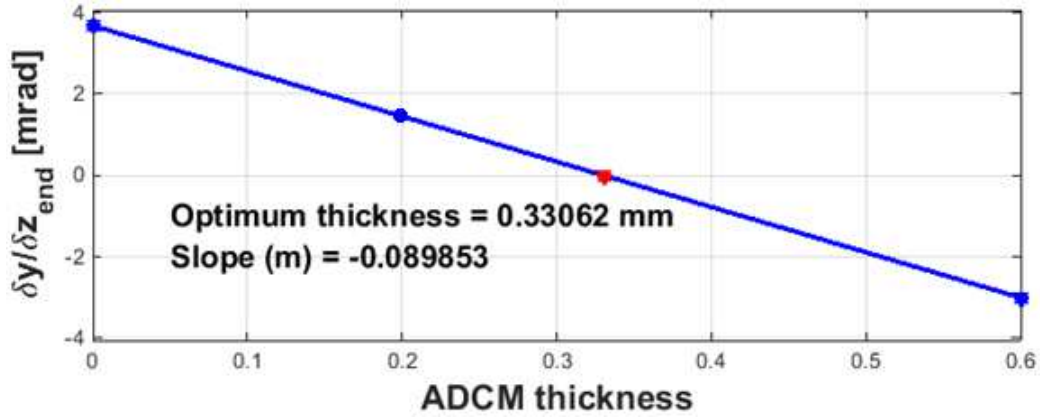

Fig. 214 Linear dependence of ion deflection with respect to ADCM thickness in case of acceleration gap = 12 mm. The optimal ADCM thickness corresponds to a deflection equal to zero.

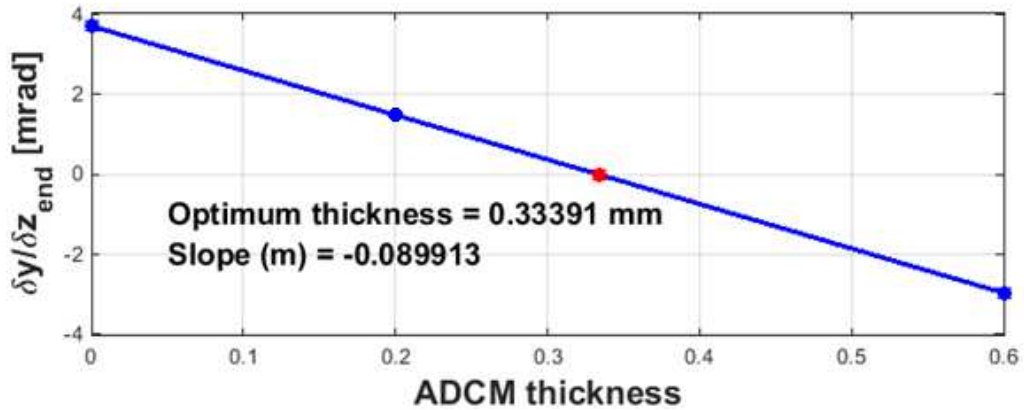

Fig. 215 Linear dependence of ion deflection with respect to ADCM thickness in case of acceleration gap = 23 mm. The optimal ADCM thickness corresponds to a deflection equal to zero.

From the last two Fig., it can be noticed that the dependence of ion deflection on the acceleration gap length is practically negligible. According to this calculation, the optimal ADCM thickness (being Br = 1.1 T) for cancelling the ion deflection at accelerator exit is about 0.33 mm

The vertical magnetic field, ion horizontal deflection, electric potential and electric field calculated along a beamlet in the case of ADCM thickness of 0.2 mm and acceleration gap length of 12 mm are shown in Fig. 216:

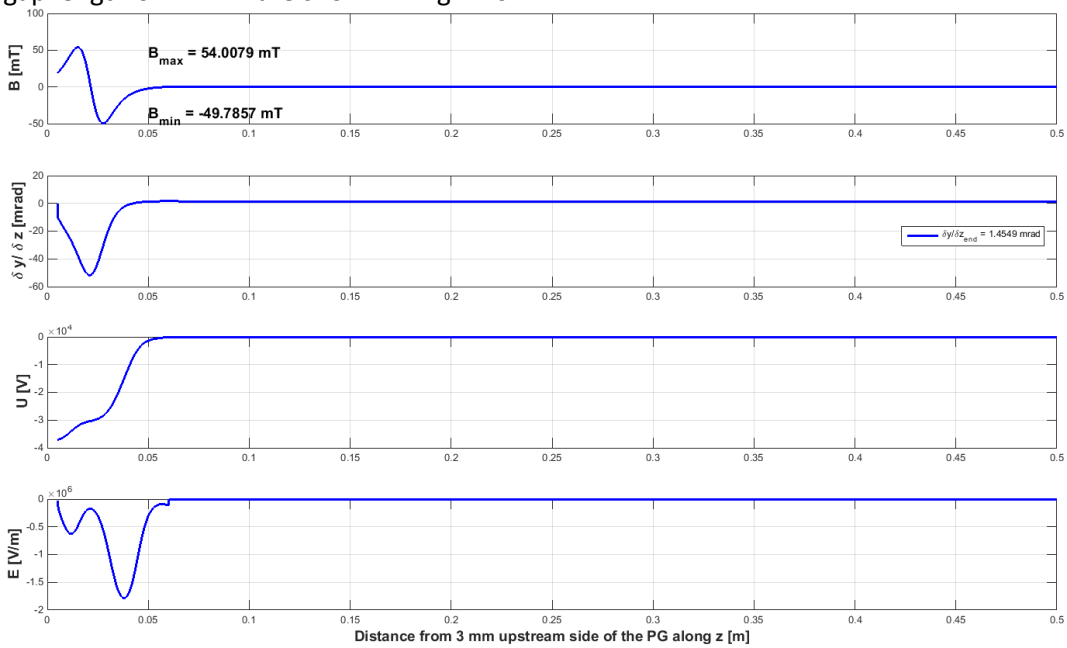

Fig. 216 Vertical component of the magnetic field, horizontal ion deflection, electric potential and electric field along the beamlet axis for the NITS configuration with 0.2 mm thick ADCM and 12 mm acceleration gap.

In conclusion, as already found for MITICA, a linear dependence of ion deflection with respect to ADCM thickness has been obtained in NITS. According to the results obtained with the analytical formula, the optimal ADCM thickness for cancelling the ion deflection is about 0.33 mm, with a magnetic remanence of Br = 1.1 T.

6.8.2. Calculation of Ion deflection calculation using OPERA

Analytical formula for ion deflection calculation is a fast and easy tool but doesn't take into account secondary effect like the electrostatic lenses and space charge. OPERA 3D, on the other hand, requires more computational time but provides more accurate results, since includes in the calculation all these secondary effects. A discrepancy between the ion deflection calculated with the formula and with OPERA had been already observed in MITICA, and for this reason the design of ADCM have to be based on the results of OPERA 3D only.

A single beamlet model of NITS has been modeled with OPERA and the ion deflection has been evaluated for different ADCM strength. Fig. 217 shows a case in which the ADCM thickness has been kept constant at 1 mm and the magnetic remanence Br has been varied from zero to 1.1 T. An extracted current density of 150 A/m^2 has been considered for this calculation. The ion deflection due to CESM only is about 10 mrad, against the 4 mrad calculated with the formula (see Fig. 215), while the optimal Br for having a deflection equal to zero is Br = 0.88 T.

It can be noticed how the optimal ADCM strength calculated with the formula is under-estimated more or less by a factor of two.

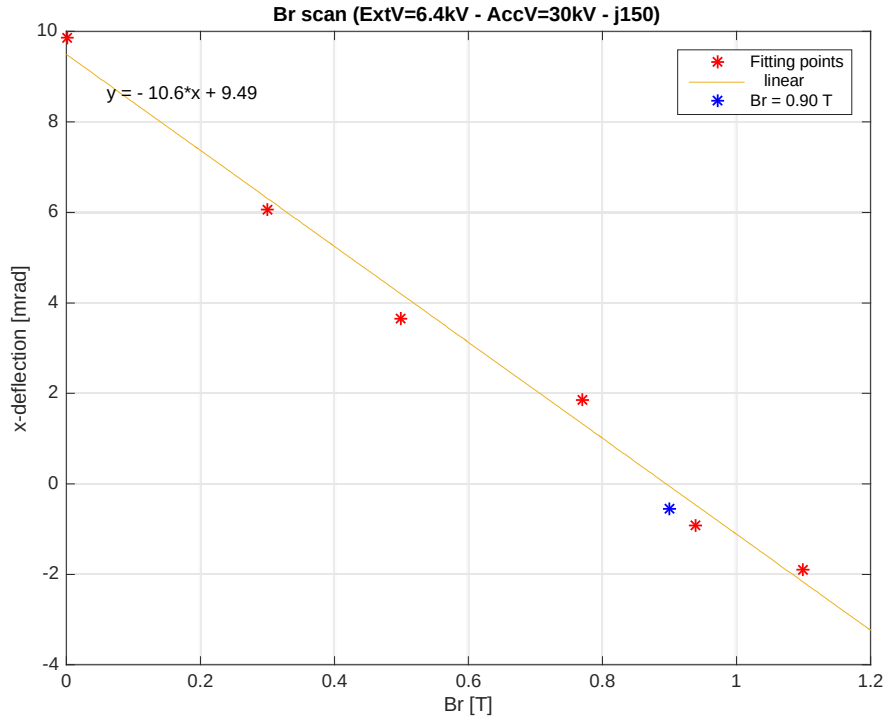

Fig. 217 Beamlet horizontal deflection at accelerator exit as a function of the ADCM remanence Br, calculated using OPERA 3D with: Jext= 150 A/m^2, Vacc=30 kV, gap_PG-EG= 6mm, gap_EG-GG= 12 mm, CESM (size 6.6x4.2 mm Br=1.1 T) and ADCM (size 6.6x16.4 mm, thickness 1.0 mm). The horizontal deflection is ≈ 0 for Br=0.88 T.

The next Fig. shows how the ion deflection varies inside the accelerator and how it becomes almost zero downstream the Grounded Grid under the combined effect of CESM and ADCM. Extracted current densities of 130 A/m^2 and 170 A/m^2 have been considered for this calculation. It can be noticed that the effect of CESM or CESM + ADCM is not much dependent on current density.

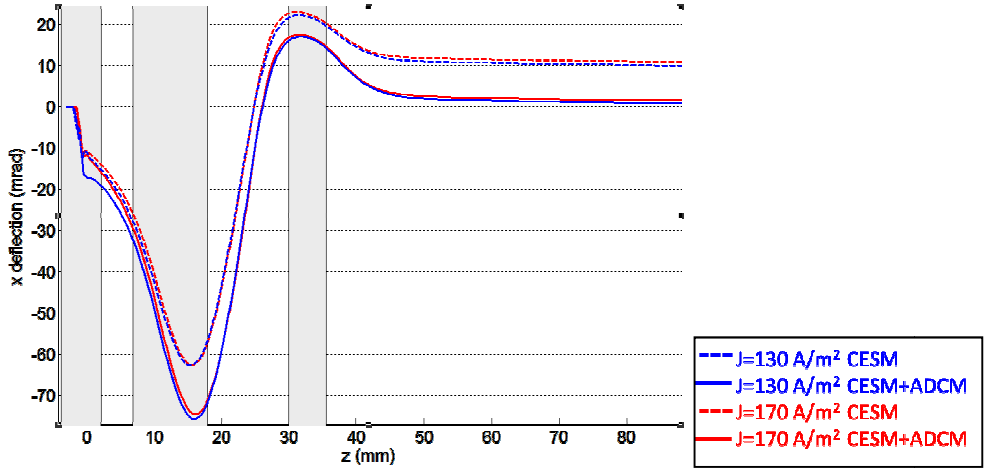

Fig. 218 Beamlet horizontal deflection along the NITS accelerator, calculated using OPERA 3D with Jext= 130 – 170 A/m2, Vacc=30 kV, gap_PG-EG= 6m, gap_EG-GG= 12 mm, CESM (6.6x4.2 mm, Br=1.1 T) and ADCM (size 6.6x16.4 mm, thickness 1.0 mm Br=0.88 T).

The ADCM thickness of 1 mm has been decided in order to have an optimal magnetic remanence of about 0.9 T. In this way, two additional sets of ADCM can be produced with a magnetic remanence ± 20% with respect to the optimum. In this way, if during

the experimental campaign it is found that for any reason (numerical errors, physical effects not included in OPERA, etc.) the nominal set is too weak or too strong, it can be substituted with the "reduced set" (Br - 20%) or with the "augmented set" (Br + 20%), remembering that 1.1 T is the maximum achievable magnetic remanence for SmCo permanent magnets.
In conclusion, the optimal ADCM strength has been determined using OPERA 3D, but two additional sets of ADCM with reduced or augmented strength will be produced for accounting any kind of error, as summarized in Tab. 38:

ADCM parameter		
size1	6.6	mm
thickness	1.0	mm
size2	16.4	mm
remanence (along 16.4 edge) (nominal set)	0.88	T
remanence (along 16.4 edge) (reduced set)	0.7	T
remanence (along 16.4 edge) (augmented set)	1.1	T

Tab. 38 Parameters of the three sets (nominal, reduced, augmented) of ADCM that will be produced for the Joint Experiments on NITS.

6.9. Mechanical design

In order to facilitate the assembly and disassembly of permanent magnets inside the grid, it has been chose to realize the new Extraction grid to be installed on NITS in two parts, the upstream one containing the grooves hosting the magnets and the second one being essentially a lid. The mechanical drawings of the upstream part, the downstream part and of the assembly are shown respectively in Fig. 219, Fig. 220 and Fig. 221.
The upstream part is a cylinder ϕ190mm x 11 mm and contains a series of vertical and horizontal grooves for hosting the CESM and the ADCM, and the initial part of the 34 apertures. The upstream and downstream parte are bolted together in six points, and they will be then installed on the EG support of NITS accelerator using 12 screws with conical head.
The downstream part is a cylinder ϕ210mm x 6 mm and contains the final part of the apertures and the interface for the assembly on the EG support.
Four apertures are used for alignment, see Fig. 193.
The material adopted is copper pure at 99,9%.
The two grid parts have been realized at Barco SrL [57]. Fig. 222 shows the two grid parts during the dimensional control.

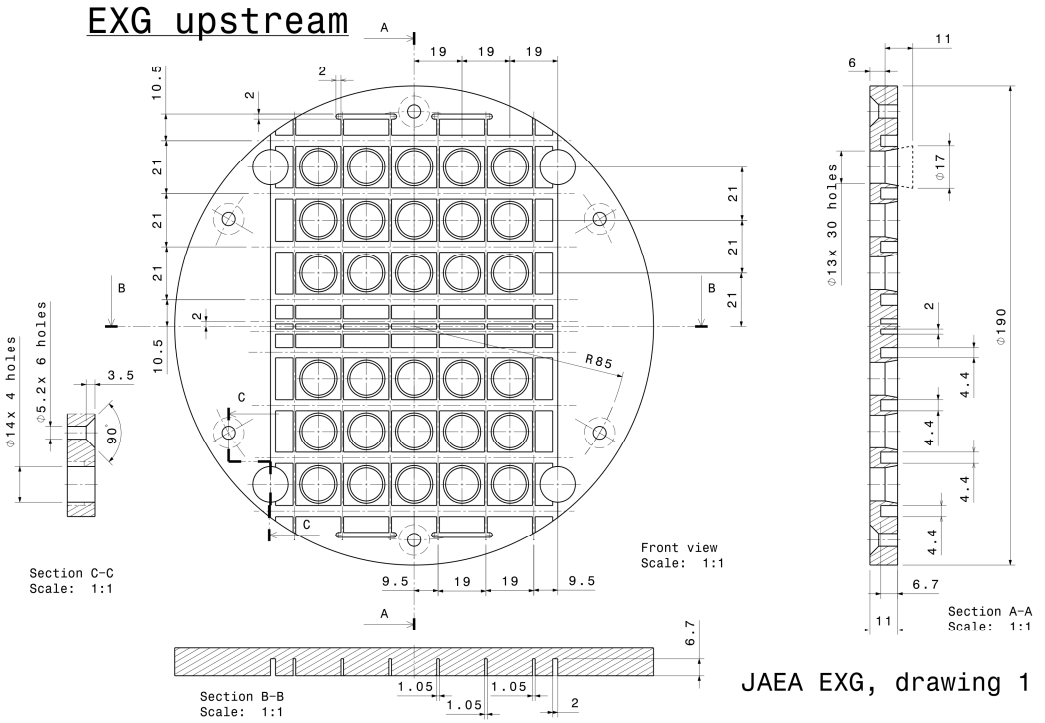

Fig. 219 Mechanical drawing of new EG for NITS, upstream part.

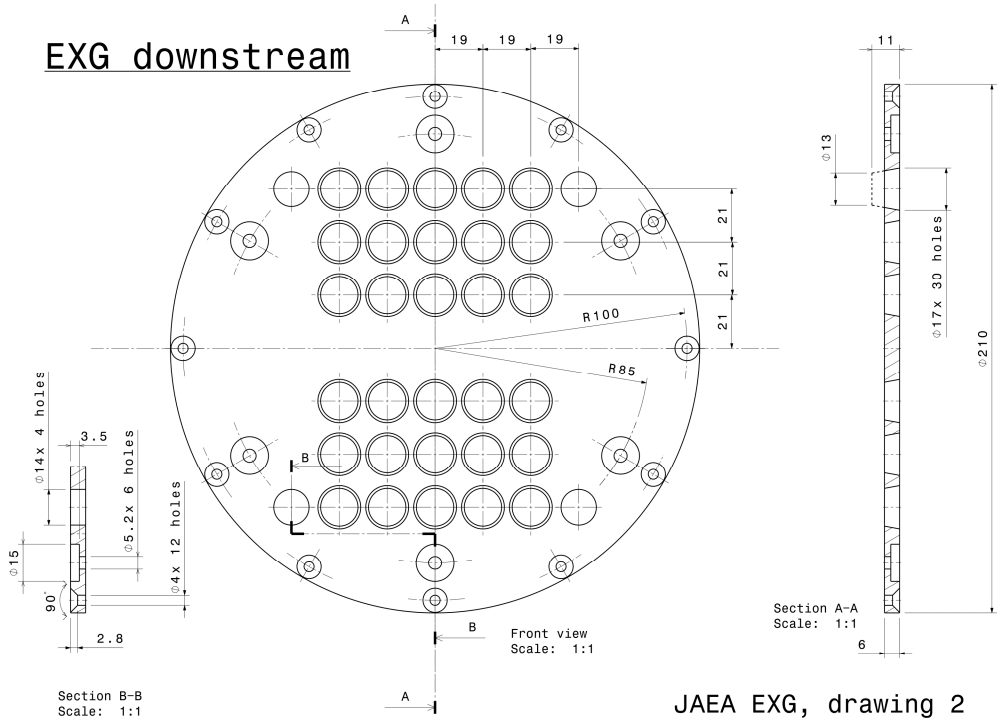

Fig. 220 Mechanical drawing of new EG for NITS, downstream part.

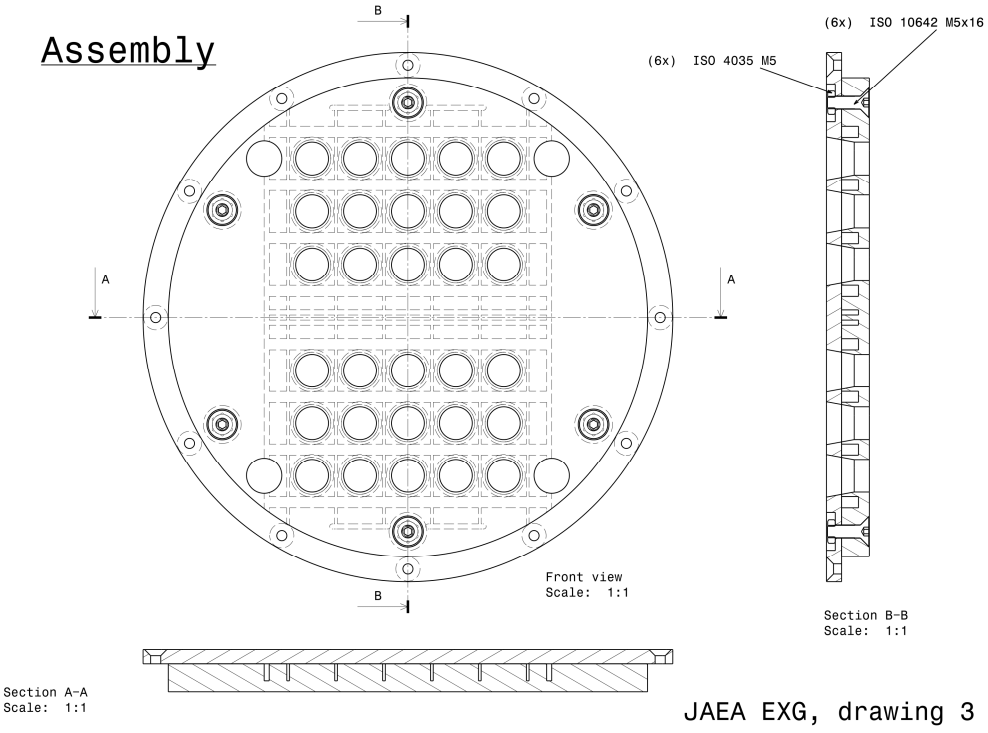

Fig. 221 Mechanical drawing of new EG for NITS, assembly.

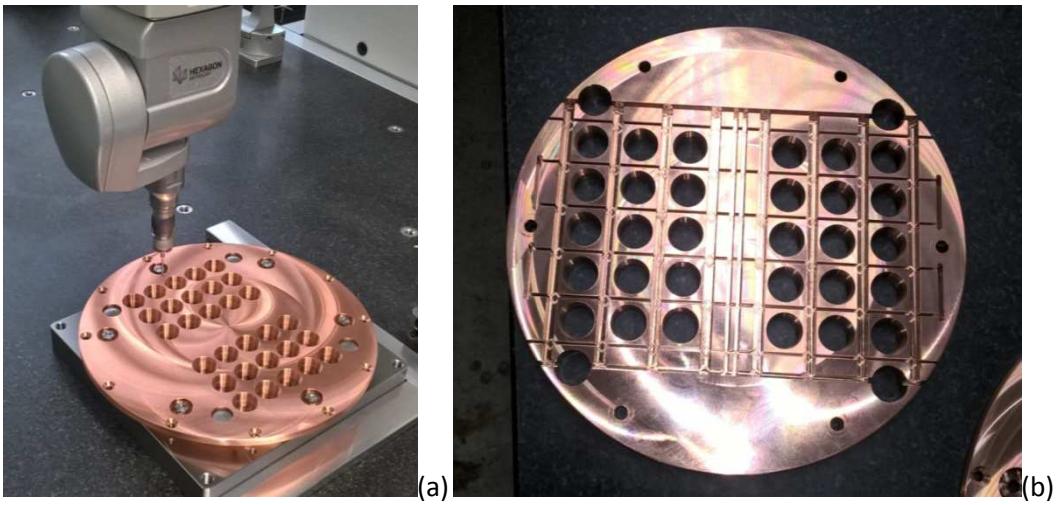

Fig. 222 (a) EG downstream part during dimensional control, (b) EG upstream part.

6.10. Conclusions

A new Extraction Grid to be installed on the accelerator NITS at JAEA Naka, Japan, has been designed and realized at Consorzio RFX and Barco SrL.

The purpose of this new grid is to test the reference magnetic solution for MITICA EG, developed at Consorzio RFX and never tested before, consisting in two sets of permanent magnets, the standard Co-extracted Electron Suppression Magnets (CESM) and the Asymmetric Deflection Compensation Magnets (ADCM).

The new grid has been optimized from the magnetic, electrostatic and mechanical point of view and will be tested on NITS during February 2016, under the framework of a scientific cooperation agreement between JAEA Naka Fusion Institute and Consorzio RFX.

7. Conclusions and future work

The final design of MITICA ion source and accelerator has started in 2010 and is now finished. The work presented in this thesis has coincided with the last three years of the design, in which important issues have been faced and solved.

Based on an idea developed at Consorzio RFX, a new magnetic configuration has been designed for MITICA accelerator, able to cancel the criss-cross ion deflection due to electron-suppression magnetic field. Magnetic simulations and beam simulations showed that this solution is more robust and effective with respect to the traditional electrostatic ion deflection correction, and for this reason it has been accepted as new reference design solution for MITICA and ITER HNB, see Par. 2.1.
This solution has been then implemented on a grid prototype present at Consorzio RFX and the produced magnetic field has been mapped using a gaussmeter and showing a good agreement with the simulations, see Par. 2.4.
Finally, an Extraction Grid featuring the new solution has been designed and will be tested on the NITS accelerator at JAEA Naka, Japan, during February 2016. The design of this new grid required a large amount of magnetic, electrostatic and beam simulations, and the results are promising. The calculated beam optics after several optimization steps of the electromagnetic fields seems to prelude a success of the experiments.
The mechanical design of the new Extraction Grid has been carried out evaluating the correct configurations and tolerances of the apertures and the magnet grooves in order to guarantee an easy assembly of the magnetic array inside the grid. A mechanical solution constituted by two grid parts has been chosen for this purpose.
The design of the new Extraction Grid is described in Chapter 6.

The design of the Transverse Magnetic Field Coils for MITICA has been updated, after a modification of the reference PG busbar layout, and further optimized, using an automatic optimization algorithm based on Simulated Annealing. Due to the new constraints, the TMFC performances are slightly decreased, but the new design requires lower driving current, 2500 A instead of the 30000 A of the previous design, as described in Par. 2.3.

The last phase of the MITICA accelerator design consisted of non-ideal, off-normal and failure operating condition analysis of the whole system, in order to identify and correct the possible flaws in the design, and to identify some detection and protection strategies in case of failure. This analysis was carried out considering a large variety of conditions such as: non ideal magnet position due to mechanical tolerances of grid grooves, demagnetization of permanent magnets, wrong value of PG current, non uniform gas density, non uniform extracted current and breakdowns between grids. This has required an extensive set of electromagnetic and beam simulations, reported in Chapter 4.
Some of the considered effects resulted to have negligible impact on the accelerator operation, but other ones (demagnetization, PG current fault, non uniform gas density/extracted current) can lead to a deterioration of beam optics with consequent increase of power loads on the components that have to be kept under control.

A magnetic sensor of the "flux-gate" type has been studied for application to MITICA and ITER HNB, as this kind of magnetic sensor seems to be the best candidate for operating in the ITER HNB environment, characterized by high neutron flux, relatively high stray magnetic field to be measured and necessity of remote control.
A numerical tool has been developed for predicting the performance of a fluxgate sensor depending on the hysteresis curve of the core material and other parameters. Basing on the prediction of the model, a fluxgate sensor prototype has been realized and tested at Consorzio RFX proving its operating principle and the possibility of extending its typical operating range until magnetic fields of the order of 10 mT and more, required for MITICA and ITER HNB, as presented in Chapter 5.
Complete characterization of the prototype as well as the comparison with the numerical model is still ongoing.

In parallel to the design activities related to MITICA, code improvement activities have been carried out on the magnetic code NBImag, used at Consorzio RFX. The main achievements are the validation of new routines for magnetic force and inductance calculation, presented in Chapter 3.

All the activities carried out during this Doctorate contributed to the formation of a solid background in the field of negative ion accelerators and Neutral Beam Injectors (NBI). Being two large projects under construction at Consorzio RFX, the ion source and accelerator SPIDER and the full NBI MITICA, this thesis has a natural continuation in this field, since lot of effort is still necessary for constructing and subsequently operating these two big experiments.

Finally, as the title itself suggests, the ultimate goal of this work and the achieved experience is to contribute to the successful operation of ITER, and maybe in the future of a Nuclear Fusion Power Plant.

References

[1] BP Statistical Review of World Energy 2015, bp.com/statisticalreview

[2] Emission Database for Global Atmospheric Research, http://edgar.jrc.ec.europa.eu/

[3] World Nuclear Association, http://www.world-nuclear.org/

[4] US Department of Energy, *What Are Greenhouse Gases?,* 2007.

[5] K.Miyamoto, *Plasma Physics for Nuclear Fusion*, The MIT press, 1989.

[6] W.K.Hogan. Nucl.Fusion, 44, 2004.

[7] M. Wakatani, *Stellarator and heliotron devices,* Oxford University Press, 1998.

[8] J. Wesson et al., *Tokamaks*, Oxford University, 2004.

[9] ITER Organization, http://www.iter.org

[10] V. Toigo, D. Boilson, T. Bonicelli, R. Piovan, M. Hanada… D. Aprile… et al, *Progress in the realization of the PRIMA neutral beam test facility,* Nuclear Fusion, 55 083025; doi:10.1088/0029-5515/55/8/083025, 2015.

[11] P. Agostinetti, D. Aprile, V. Antoni, et al., *Detailed design optimization of the MITICA negative ion accelerator in view of the ITER NBI*, Nucl. Fusion 56 016015, doi:10.1088/0029-5515/56/1/016015, 2015.

[12] H.P.L. de Esch, M. Kashiwagi, M. Taniguchi, , T. Inoue, G. Serianni…D. Aprile… et al., *Physics design of the HNB accelerator for ITER,* Nucl. Fusion 55 096001, doi:10.1088/0029-5515/55/9/096001, 2015.

[13] M. Bacal., *Physics aspects of negative ion sources*, Nucl. Fusion 46, S250, 2006.

[14] M. Bacal and G.W. Hamilton, *H- and D- production in plasmas*, Phys. Rev. Lett. 42, 1538, 1979.

[15] G. Chitarin, et. al., *Concepts for the magnetic design of the MITICA neutral beam test facility ion accelerator*, Rev. Sci. Instrum. 83, 02B107, 2012.

[16] G. Chitarin, et al., *Optimization of the electrostatic and magnetic field configuration in the MITICA accelerator*, Fusion Eng. Des. 88 507-511, 2013.

[17] N. Marconato, G. Chitarin, P. Agostinetti, N. Pilan, G. Serianni, *Simulation, Code Benchmarking and Optimization of the Magnetic Field Configuration in a Negative Ion Accelerator*, Fusion Eng. Des. 86 925-928, 2011.

[18] G. Chitarin, et al., *Flexible magnetic design of the MITICA plasma source and accelerator*, AIP Conf. Proc. 1515 217-226, 2013.

[19] N. Marconato, P. Agostinetti, G. Chitarin, *Magnetic and thermo-structural design optimization of the Plasma Grid for the MITICA Neutral Beam Injector*, presented at the SOFT 2014, to be published in Fusion Eng. Des.

[20] G. Chitarin, P. Agostinetti, D. Aprile, N. Marconato, P. Veltri, *Cancellation of the Ion Deflection due to Electron-Suppression Magnetic Field in a Negative-Ion Accelerator*, Rev. Sci. Instr. 85, 2, 02b317, 2014.

[21] J. C. Mallinson, *One-sided fluxes: A magnetic curiosity?*, IEEE Trans. Magn. 9(4), 678, 1973.

[22] K. Halbach, *Design of permanent multipole magnets with oriented rare earth cobalt material*, Nucl. Instrum. Methods 169, 1, 1980.

[23] S. M. Lund and K. Halbach, *Iron-free permanent magnet systems for charged particle beam optics*, Fusion Eng. Des. 32–33, 401, 1996.

[24] M. Taniguchi et al., Rev. Sci. Instrum. 83, 02B121, 2012.

[25] M. Kashiwagi et al., Compensations *of beamlet deflections for 1 MeV accelerator of ITER NBI*, AIP Conf. Proc. 1515, 227, 2013.

[26] M. Tanaka et al., Nucl. Instrum. Methods Phys. Res. A 449, 22, 2000.

[27] P. Agostinetti et al., *Construction and Testing of Grid Prototypes for the ITER Neutral Beam Injectors*, Proc. of 25th SOFE, San Francisco, 2013.

[28] G. Chitarin et al., *Experimental Mapping and Benchmarking of Magnetic Field Codes on the LHD Ion Accelerator*, AIP Conf. Proc. 1390, 381, 2011.

[29] G. Chitarin, N. Marconato, *Design of Trimming Magnetic Field Coils (TMFC) for MITICA accelerator*, RFX-MITICA-TN-239, 2013.

[30] S. Kirkpatrick, C. D. Gelatt; M. P. Vecchi, *Optimization by Simulated Annealing*, Science, Vol. 220, No. 4598, 1983.

[31] G. Chitarin, N. Marconato, *Adaptation and optimization of the MITICA PG bus-bar routing to the new magnetic field requirement*, RFX-MITICA-TN-268, 2014.

[32] G. Chitarin, P. Agostinetti, D. Aprile et al., *Off-normal and failure condition analysis of the MITICA negative-ion accelerator*, Review of Scientific Instruments 87, 02B311; doi: 10.1063/1.4933184, 2016.

[33] P Franzen et al., *Magnetic filter field dependence of the performance of the RF driven IPP prototype source for negative hydrogen ions*, Plasma Phys. Control. Fusion 53 115006D, 2011.

[34] P. Agostinetti et al., *R&D activities regarding the tests on accelerator grid samples*, RFX-MITICA-TN-242rev1, 2013.

[35] Magneti Permanenti Industriali, www.mpi.it

[36] M. Cavenago et al., *Development of versatile multiaperture negative ion sources*, AIP Conf. Proc. 1655, 040006, 2015.

[37] G. Akoun, Gilles and J. Yonnet, *3D analytical calculation of the forces exerted between two cuboidal magnets*, IEEE Transactions on Magnetics MAG-20.5, pp. 1962–1964, 1984.

[38] R. Ravaud, G. Lemarquand and V. Lemarquand, *Mutual Inductance and Force exerted between Thick Coils*, Progress In Electromagnetic Research, PIER 102, 367-380, 2010.

[39] M. W. Garrett, *Calculation of Fields, Forces, and Mutual Inductances of Current Systems by Elliptic Integrals*, Journal of Applied Physics, Vol. 34 n. 9, 1963.

[40] J. T. Conway, *Inductance Calculation for Circular Coils of Rectangular Cross Section and Parallel Axes using Bessel and Struve Functions*, IEEE Transactions on Magnetics, Vol. 46 n. 1, 2010.

[41] C. Akyel, S. I. Babic and M. M. Mahmoudi, *Mutual Inductance Calculation for non Parallel Coaxial Circular air Coils with Parallel Axes*, Progress in Electromagnetic Research, PIER 91, 287-301, 2009.

[42] S. Babic, C. Akyel and B. Babic, *Magnetic Force Calculation between Thick Circular Coil with Rectangular Cross Section and Thin Disk Coil (Differential Approach)*, International Journal of Engineering and Innovative Technology (IJEIT), Vol. 2 Issue 5, 2012.

[43] L.H. De Medeiros et al., *Comparison of Global Force Calculations on Permanent Magnets*, IEEE Transactions on Magnetics, Vol 34 n. 5, 1998.

[44] W. Robertson, B. Cazzolato and A. Zander, *Axial Force between a Thick Coil and a Cylindrical Permanent Magnet: optimizing the Geometry of an Electromagnetic Actuator*, IEEE Transactions on Magnetics, Vol. 48 n. 9, 2012.

[45] H. Allag, J. P. Yonnet and M. Latreche, *3D Analytical Calculation of Forces between Linear Halbach-Type Permanent Magnet Arrays*, Electromotion 2009 - EPE Chapter 'Electric Drives' Joint Symposiom, 2009.

[46] D. Yu and K. S. Han, *Self-Inductance of Air Core Circular Coils with Rectangular Cross Section*, IEEE Tansactions on Magnetics, Vol. mag-23 n. 6, 1987.

[47] F. W. Grover, *Inductance Calculations: Working Formulas and Tables*, Dover Publications Inc., 1962.

[48] T. R. Lyle, *On the Self-Inductance of Circular Coils of Rectangular Section*, Philosophical Transactions of the Royal Society of London, Series A, Vol. 213, pp. 421-435, 1914.

[49] K. Kajikawa and K. Kaiho, *Usable ranges of some expressions for calculation of the self inductance of a circular coil of rectangular cross section*, Cryogenic Engineering, Vol. 30, n. 7, 324 332, 1995.

[50] L. Svensson, *Magnetic field measurement at MITICA and at ITER HNB*, ITER Technical Specification IDM UID NNM5VQ.

[51] M. Marchesi, *Flux-gate Magnetic Sensor System for Electronic Compass*, PhD thesis.

[52] Pavel Ripka, *Review of flux-gate sensors*, Sensors and Actuators A, 33 129- 141, 1992.

[53] Ken Evans, *Flux-gate Magnetometer Explained*, INVASENS, 2006.

[54] Pavel Ripka, *Advances in flux-gate sensors*, Sensors and Actuators A 106 8–14, 2003.

[55] M. Kashiwagi et al., *Design Development of negative ion extractor in the high-power and long-pulse negative ion source for fusion application*, Review of Scientific Instruments 85, 02B320; doi: 10.1063/1.4852297, 2014.

[56] M. Kashiwagi et al., *High energy, high current accelerator development for ITER NBI at JADA*, 22nd IAEA Fusion Energy Conference (FEC), 2008.

[57] Barco SrL, www.barcofratelli.it

Acknowledgements

Thanks to

Giuseppe Chitarin (Bepi), my mentor, because he is simply outstanding.

Piero Agostinetti, Pierluigi Veltri, Nicolò Marconato, Emanuele Sartori and Gianluigi Serianni, for being exceptionally inspiring and for their very precious help in every situation.

All the other members of the NBI team, for their support and competency.

Consorzio RFX for giving me the opportunity of this PhD and for being an extremely friendly and pleasant working environment.

Paolo Bettini, coordinator and group leader, for his presence and his helpful advice.

M. Hanada, A. Kojima, M. Kashiwagi, J. Hiratsuka, M. Ichikawa, R. Nishikiori and M. Yoshida for their remarkable hospitality and for giving me the best professional and human experience of my life.

Matteo, Pietro, Nicolò, Ondra, Nisarg, Vadim and Paulo, my mates through this journey.

Carlo, Leonardo, Tautvydas, Yangyang, Marco G., Marco B., Giulio, Marco S., Matteo V., Daniele, Oisin, Nicola, Winder, Chiara and Cristina for making the office a place where it's impossible not to feel cheerful.

Finally, my family and Flavia for their unconditional love.